REPORT DOCUMENTATION PAGE

Form Approved
OMB NO. 0704-0188

1. AGENCY USE ONLY (Leave Blank)	2. REPORT DATE 12/20/1999	3. REPORT TYPE AND DATES COVERED Final Report, 10/1/96-8/31/1999

4. TITLE AND SUBTITLE
Visualization of High-Power Density Diesel Engine Spray and Combustion

5. FUNDING NUMBERS
DAAH04-96-1-0458

6. AUTHOR(S)
M.-C. Lai, N. A. Henein, T.-C. Wang, J.-S. Han, X. Xie, J. Qin

7. PERFORMING ORGANIZATION NAME(S) AND ADDRESS(ES)
Wayne State Universtiy
Detroit, MI 48202

8. PERFORMING ORGANIZATION REPORT NUMBER

9. SPONSORING / MONITORING AGENCY NAME(S) AND ADDRESS(ES)

U. S. Army Research Office
P.O. Box 12211
Research Triangle Park, NC 27709-2211

10. SPONSORING / MONITORING AGENCY REPORT NUMBER

ARO 36436.7-EG

11. SUPPLEMENTARY NOTES
The views, opinions and/or findings contained in this report are those of the author(s) and should not be construed as an official Department of the Army position, policy or decision, unless so designated by other documentation.

12 a. DISTRIBUTION / AVAILABILITY STATEMENT

Approved for public release; distribution unlimited.

12 b. DISTRIBUTION CODE

13. ABSTRACT (Maximum 200 words)

An experimental visualization study of spray and combustion processes under simulated high-power-density diesel (HPD) combustion conditions is carried out. The scope of work includes characterization of high-pressure injection on test rig, macroscopic and microscopic characterization of non-evaporative sprays in atmosphere ambient condition or in pressurized chamber, and direct visualization of spray and combustion processes inside a single-cylinder optically accessible research engine.

The results provide very interesting and dynamic information on spray structure, showing spray angle variations, primary breakup processes, and spray asymmetry under different combinations of injection systems and nozzle geometry. The injection systems tested included electronic unit injector (EUI), hydraulic unit injector (HEUI), and high-pressure common rail (HPCR) with both valve-covered orifice (VCO) and mini-sac nozzles. The near-field spray behavior is shown to strongly depend on the Some complementary numerical simulations using new transient schemes (space-time method) and primary breakup models (turbulent and cavitational) to better correlate spray and injector design are also discussed.

Combustion visualization inside an optically accessible diesel engine equipped with HEUI injection system capable of both single and multi-stage injections was also successfully conducted. Nozzle hole flow area, injection pressure, and length of rate-shaping pipe are the dominating parameters that control the injection rate. The results showed that ignition delay and heat release of pre-mixed combustion is significantly reduced with increase of charge air density and temperature, and with pilot injection.

14. SUBJECT TERMS
High-Pressure Diesel Fuel Injection, Electronic Control Unit Injector, High-Pressure Common Rail, High-Power Density Diesel Combustions, Spray Visualization, Microscopic Visualization, High-Speed Photography, Cavitation in Diesel Injection, Optical Accessible Engine, EUI, HEUI, HPCR, Combustion Analysis, Multi-zone combustion model.

15. NUMBER OF PAGES
280

16. PRICE CODE

17. SECURITY CLASSIFICATION OR REPORT UNCLASSIFIED	18. SECURITY CLASSIFICATION ON THIS PAGE UNCLASSIFIED	19. SECURITY CLASSIFICATION OF ABSTRACT UNCLASSIFIED	20. LIMITATION OF ABSTRACT UL

EXECUTIVE SUMMARY

An experimental visualization study of spray and combustion processes under simulated high-power-density diesel (HPD) combustion conditions is carried out. The scope of work includes characterization of high-pressure injection on test rig, macroscopic and microscopic characterization of non-evaporative sprays in atmosphere ambient condition or in pressurized chamber, and direct visualization of spray and combustion processes inside a single-cylinder optically accessible research engine.

The results provide very interesting and dynamic information on spray structure, showing spray angle variations, primary breakup processes, and spray asymmetry under different combinations of injection systems and nozzle geometry. The injection systems tested included electronic unit injector (EUI), hydraulic unit injector (HEUI), and high-pressure common rail (HPCR) with both valve-covered orifice (VCO) and mini-sac nozzles. The near-field spray behavior is shown to strongly depend on the nozzle geometry, needle lift dynamics, and injection pressure, which is a function of the injection system. Some complementary numerical simulations using new transient schemes (space-time method) and primary breakup models (turbulent and cavitational) to better correlate spray and injector design are also discussed.

Combustion visualization inside an optically accessible diesel engine equipped with HEUI injection system capable of both single and multi-stage injections was also successfully conducted. Nozzle hole flow area, injection pressure, and length of rate-shaping pipe are the dominating parameters that control the injection rate. The results showed that ignition delay and heat release of pre-mixed combustion is significantly reduced with increase of charge air density and temperature, and with pilot injection.

20001122 092

TABLE OF CONTENTS

CONTENTS   **Page**

APPENDICIES

vi

LIST OF TABLES

LIST OF FIGURES

CHAPTER 1

INTRODUCTION

1.1. GENERAL INTRODUCTION

The superior performance and efficiency of diesel engines make them the preferred power plant for many U. S. Army propulsion and power generation needs. The diesel's tolerance to fuel properties makes it most suitable for multi-fuel applications, with the potential for reducing both undesirable emissions and reliance on petroleum fuels. A compact high power deisel (HPD) engine is of particular interest to the U. S. Army, because of its wide variety of applications in tanks, armoured personnel carriers, standby power generations, and other compact high-energy-density powerplant applications. A successful HPD engine could also be more competitive and more desirable than a gas turbine engine.

The specifications of HPD engines are not definite. Niven and Webber (1996) define the overall HPD performance as follows:

Breake Mean Effective Pressure: $\geq$ 20 bar

Specific Volume: $\geq$ 300 kW/m^3

Specific Weight: $\leq$ 3 kg/kW

But the following performance goals are more relevant to the Army:

Low Heat Rejection: 10-13 BTU/BHP-min

Air Fuel Ratio: 22-26

Mean piston Speed: 13.5-15.5m/sec

Breake Mean Effective Pressure: 16-19 bar

Specific Fuel Consumption: 143-170g/ps-hr

These performance requirements pose a great challenge to engine designers. In addition to technologies developed over many years, new concepts and combustion optimization strategies must be devised to meet this challenge. Most engine developers have traditionally concentrated on general combustion chamber design parameters such as swirl, squish, fuel properties, turbo-charging, and intercooling. A detailed understanding of the fuel injection and combustion processes of the engines is required in order to reduce these products of combustion within the engine cylinder while not compromising engine fuel economy. In recent years, comprehensive research work has been carried out in the area of diesel injection and diesel spray characterization. Numerical, theoretical, and experimental studies all achieved important results that provide the guidelines for the design of injection and combustion systems [Ficarella et al., 1998]. Each approach of the studies has its own unique role and contributions. The experimental approach of the studies especially played as a role of discovering phenomena associated with new designs and new applications, and continuously providing data to correlate and validate with numerical models for improving the accuracy and efficiency of computer simulations. The experimental approach has been chosen to be the main method of this thesis work.

Recently, primarily because of regulations for simultaneously reducing soot and NOx emissions and the development of ceramic engine parts, more attention has been given to fuel injection, fuel-air mixing, and their optimization. Indeed, most of the recent progress in diesel engine combustion and advanced concepts is related to developments in diesel injection systems,

for example: high-pressure injection, injector geometry (e.g., VCO and VRD) and cavitation, injection rate shaping, multiple injection (e.g., pilot and split injection), utilization of wall impingement for enhanced mixing (e.g., OSKA-DH, NIT-MH, and TRB), and secondary gas injection (e.g., CCD). However, in addition to using available technology such as turbo-charging/intercooling, ultra-high fuel injection pressure, multiple injection and enhanced mixing, the military HPD engine must also incorporate ceramic parts for low-heat rejection.

High-pressure electronic-controlled fuel injection systems, such as Electronic Unit Injector (EUI), Hydraulic EUI (HEUI), and Common Rail (CR), are the heart of advanced diesel engines. These systems could provide features required by an advanced engine, such as more precise injection quantity, more flexible injection timing, and higher injection pressure comparing to the conventional mechanical injection systems. High injection pressure combined with small nozzle hole diameter can provide, 1) better spray formation which is due to finer initial drops exiting the nozzle with higher velocity, 2) better air entertainment and air-fuel mixing, and 3) more homogenous mixture with lower local equivalence ratio and fewer over-rich regions. These three factors have been reported as the keys to generate a low smoke combustion process [Kato et al., 1989]. Piperpont and Reitz (1995) also showed that at high load engine operating conditions increase of fuel injection pressure effectively reduces particulate emissions. Although the applications of electronic-controlled high pressure injection become popular in the diesel engine industry, some significant spray-related issues associated with high-pressure injection remain to be addressed, such as causes and

effects of hole-to-hole spray variability, spray breakup and atomization mechanisms, near nozzle exit spray dynamics, and how to optimize combustion chamber to cope with high pressure injection. Based on an in-cylinder visualization study of Rao and Winterbone (1993), the penetration and shape of the sprays were found non-uniform. A study of Ficarella et al.(1997) on a CR system with 5-hole axis-symmetry nozzle, also concluded that the general configuration of the spray is different for each hole and each hole has a particular way of injecting. The injection variability could penalize air utilization, fuel distribution, and combustion. The causes and effects need to be further investigated. Regarding the numerical spray calculation, the spray breakup and atomization sub-model supplies the initial conditions, such as drop sizes and velocities, of the calculation. The accuracy of the sub-model has significant impact on the final result of a numerical spray calculation. However, up to now the mechanisms of spray breakup and atomization are still not well understood [Reitz, 1996]. In recent studies, several close to nozzle exit spray investigations were conducted. Fath et al.(1997) proposed a new model in which both cavitation and aerodynamic interactions are considered as the most dominant mechanisms for atomization. Farrell et al.(1996) revealed that the near spray angles decreased from the start of injection to the end of injection and after the end of injection the near spray angle increased. In this thesis work near field observation will be conducted to further investigate the influence of injection pressure and type of injection system on the near field spray behavior. As to how to optimize combustion chamber to cope with high-pressure injection, in-depth understanding of the

cross influence between fuel injection and configuration of combustion chamber is inevitable. Using Optically Accessible Engine to directly observe the in-cylinder spray and combustion process has been recognized as a key technique to achieve that. This technique will be applied to the thesis work to analyze the effects of injection conditions and charge air temperature and pressure on in-cylinder spray and combustion processes.

Direct visualization, when combined with other cylinder pressure, heat release and fuel injection measurements, provides the most detailed description of the combustion processes. Therefore, direct visualization of the combustion process is greatly needed to provide the fundamental understanding and guide the design of this type of engines. While many diesel engine combustion visualization are available from rapid-compression machines and optically accessible engines (OAE), but the HPD combustion visualization data are very limited. This is because key components such as injection systems and durable engine parts are still being developed. The combustion chamber condition at the time of injection will be supercritical for the diesel sprays. In addition, the conditions to maintain HPD engine injection and combustion also make the experiments quite difficult.

Therefore, an experimental study of high HPD engine combustion visualization is proposed. It is expected that the results of this study will:

- help in the development of new and improved diesel injection systems and injection strategies for HPD engines,

- improve the accuracy and efficiency of diesel combustion simulation for HPD combustion process.

1.2. Previous Related Study

1.2.1. Review of Diesel Combustion and Emissions Formation Process

The diesel combustion process can be summarized and divided into five phases, fuel injection, ignition delay, pre-mixed combustion, mixing-controlled combustion, and late combustion. In diesel combustion the emissions formation process is strongly dependent on fuel distribution and how the distribution change with time. The characteristics of soot, NO_x, and HC formation can be summarized as follows. Soot first forms in rich unburned-fuel-containing cores of spray within flame region and later on oxidizes in the flame where there must be enough oxidizer. Soot could be reduced by promoting both fuel atomization and air entertainment into the fuel spray ,which can be enhanced by the increase of injection pressure. NO_x mainly forms in high temperature post flame region and the formation rate are highest in the close-to-stochiometric flame region. NOx could be reduced by decreasing the pre-mixed burning rate caused by the suppression of initial injection rate. HC is the unburned or incomplete burned fuel due to flame quenching on the walls, excessive lean mixture, or vaporized fuel from the sac volume. HC could be reduced by preventing fuel impingement on the combustion chamber wall or by decreasing the sac volume [Heywood, 1988].

1.2.2. Effects of Injection Pressure/Rate on Combustion and Emission formation

Kato et al. (1989), and Pierpont and Reitz (1995) conducted studies of the effects of injection pressure on diesel emissions and performance. The results showed that with other engine operating conditions unchanged, by

increasing the injection pressure from 45Mpa to 160Mpa, the engine smoke could be reduced by 80%. However, NO_x will increase due to higher heat release rate and higher local flame temperature. This kind of phenomena is known as NO_x-smoke trade-off of diesel combustion. To resolve the drawback associated with high-pressure injection, retarding the injection timing can let the auto-ignition start at lower bulk gas temperature and have lower local flame temperature that will result in lower NO_x formation rate. To maintain the NO_x at the same level, the retard of injection timing need to be increased as the injection pressure increased. However, the retard of injection timing also induces late combustion and decrease of thermal efficiency. According to the test results, if the injection timing retarded from 9 degree BTDC to 2 degree ATDC, the thermal efficiency will decrease about 2 %. Pierpont and Reitz (1995) showed that if injection pressure is high enough, for example, 160 MPa, the characteristics of NO_x-smoke trade-off will be far less significant than that of a lower pressure injection. With this situation, NO_x can be effectively reduced by retarding the injection timing without penalize too much on smoke emission. At part load operation condition, due to shorter injection duration, the injection pressure will not be able to reach its peak pressure. Particulate emission does not decrease as the injection pressure increased; nevertheless, NO_x increases with increase of injection pressure. The combustion process of part load condition is mainly pre-mixed combustion because injection duration is usually short and does not continue to mixing-controlled combustion phase. The high-pressure injection delivers fuel with higher fuel flow rate resulting in more fuel being accumulated during the ignition delay period. Once the auto-

ignition occurs and combustion starts, both heat release rate and gas temperature is high and more NO_x is formed. Therefore, at part load condition the rate shaping will have significant effect on emission formation. [Ryan et al., 1994, Acroumanis et al., 1996, Tsujimura, 1994]

1.2.3. Mechanisms of Atomization

Soteriou et al. (1995) reported that cavitation in the nozzle holes is the predominant mechanism causing atomization in the sprays. The cavitation is beneficial to spray atomization and causes atomization of the jet immediately on nozzle hole exit. There are two different mechanisms that cause cavitation in diesel fuel injection equipment. The cavitation that results from these mechanisms could be referred to as dynamically induced and geometry induced cavitation. The cavitation occurred in the holes of standard direct injection nozzles is categorized as geometry induced cavitation which could occur in steady state as well as in transient flow. It is initiated by local high velocities within separated boundary. The high velocities could result in sufficiently large reduction in local pressure to cause the formation of vapor bubbles. This cavitation process produces a homogenous opaque foam, rather than large voids. The intensity of geometry induced cavitation of an orifice could be indicated by a cavitation number which is defined as the ratio of a factor tending to create cavitation, such as average flow velocity or pressure drop across the orifice, to a factor tending to suppress it, such as down stream pressure. The intensity of cavitation increases with cavitation number. The jet from each nozzle hole diverges and atomizes when cavitation first occurs within the hole. The spray angle increases significantly once the cavitation

extends across and down to the bottom of the hole, and the flow consists of an opaque white form[Soteriou et al., 1995].

Hiroyasu et al. (1982) measured the break up length in the spray flow region by measuring an electrical resistance between the nozzle and a fine wire screen detector located in the spray jet. The injected liquid does not break up instantly after injection. There is some unbroken portion, which is referred to as the breakup length, in the spray. There is about 10-30 mm of breakup length, even if the injection pressure is higher than 20 MPa. Hiroyasu et al. (1995) also found that the breakup phenomena of liquid jets are controlled by both the internal turbulence in the nozzle and the interfacial force between the jet and the surrounding media. The main cause of disintegration from a smooth jet to a drop state is thought to be the surface instability expressed by Rayleigh's theory. In a wavy flow region, the instability of the jet increases with the turbulence in the nozzle. If the velocity of the jet further increases, interfacial forces, such as shear forces and pressure perturbations around the jet, become more important factors in the turbulence motion of the surface. As to the internal flow, the turbulence in the internal flow increases with an increase in the velocity. The increased velocity will finally result in a cavitation fixed at the entrance of the nozzle. This generates strong turbulence in the internal flow of the jet. This strong turbulence is amplified by the interfacial forces mentioned, and the jet disintegrates as quickly as in the spray region. The jet containing a fixed cavitation at the entrance of the nozzle appears as a spray jet. The breakup length in this situation decreases with an increase in

the velocity since turbulence generated by the cavity increases with the velocity increase.

As Arcoumanis et al.(1997) reported, three different atomization models had been used in their study; aerodynamic-induced atomization, jet turbulence-induced atomization, and cavitation-induced atomization. The models are briefed as follows. In the aerodynamic-induced atomization model, it was proposed that wave are developing on the surface of the liquid jet, caused by relative motion between the injected fuel and the gas. In terms of dimensionless parameters, the Weber number determines the grow rate of these waves and the disintegration of the jet into smaller droplet. In the jet turbulence-induced atomization model, it was proposed that for fully turbulence flow condition in the injection nozzle holes, the radial velocity component in the jet soon leads to disruption of the surface film, followed by general disintegration of the jet. Even when injected into vacuum, the jet will disintegrate solely under the influence of its own turbulence. In the cavitation-induced atomization model, it was proposed that the liquid jet emerging from the injection hole disintegrates due to the collapsing of the cavitation bubbles present at the exit of the holes. Since the pressure around the emerging jet is much higher than the pressure inside the cavitating bubbles, these bubbles gradually collapse while they are convected by the internal jet turbulence. This process causes perturbation to be formed on the surface of the liquid jet .The perturbations lead to jet disintegration and formation of smaller droplets at the time of total bubble collapse or at the time the bubble reach the jet surface. Based on the results of this study, it showed that the hole cavitation strongly

affects the injection velocity and droplet sizes and the cavitation-induced atomization model predicted the droplet sizes more accurately as compared to the other two models.

A recent study conducted by Fath et al. (1997) provided more in-depth investigation on atomization mechanism. They concluded that both cavitation and aerodynamic interactions are the most dominant mechanisms for atomization under the considered injection conditions. The primary mechanism seems to be cavitation. The effect of implosion of cavitation bubbles next to the nozzle exit creates a sudden increase in air entrainment and builds up a strongly increased interface for a stronger interaction by liquid and surrounding gas. By aerodynamic interaction the slightly cleft liquid column merges into a strongly cleft wave-like jet, whereby the first droplets are separated by the waves.

1.2.4. The Effect of Injection Pressure and Nozzle Configuration on Atomization

As mentioned previously, high injection pressure combined with small nozzle hole diameter can provide better spray formation, better air entrainment , better air-fuel mixing, and more homogenous mixture with lower local equivalence ratio and fewer over-rich regions. In the study of spray characteristics of a 250-Mpa high-pressure diesel injection, Minami et al. (1990) concluded that fuel droplet in the spray becomes finer with a increase of injection pressure, and even finer by using a smaller diameter nozzle hole. However, there are other ways to improve the spray atomization, such as

improvement of nozzle configuration. Su et al. (1995) pointed out that the nozzle configuration of an injector has important effect on the fuel atomization. The configuration includes the following factors: the area of a nozzle hole, the entrance shape of the hole, the number of holes, the length-to-diameter (L/D) ratio of the nozzle hole, the orientation of the nozzle holes with respect to the nozzle axis (i.e., injection angle), the nozzle discharge coefficient, and the sac volume. In their study of the configuration effects on atomization, two types of nozzle hole entrances, sharp-edged and round-edged inlet, were used. The type of nozzle tips was mini-sac. They concluded the study as follows. One, higher injection pressure results in longer spray tip penetration, narrower spray angles, and smaller droplet sizes for both types of nozzle entrances. Two, the difference in SMD becomes smaller as the injection pressure increase; and a higher injection pressure is required for the sharp-edged inlet tip to maintain the same injection rate under the same injection duration. Three, the sharp-edged inlet tip produces wider spray angle, smaller overall average SMD, and smaller value of particulate emission comparing to the round-edged inlet tip.

Atomization can also be improved by increase of fuel flow velocities in the nozzle holes. Yoda and Tsuda (1997) found that increase of the fuel flow velocity of the spray hole enables improvement of atomization without increasing the injection pressure. Also, improved atomization can be achieved through enlarging the chamfer at the spray hole inlet, which also improves the distribution of fuel flow velocity at the spray hole outlet.

Based on the study of Kampmann et al. (1996), increase of inlet radius can lead to a more symmetrical flow in the nozzle hole as a result the

turbulence intensity is reduced and average velocity of the injected flow is increased. The lower turbulence impedes the primary breakup mechanisms. However, the high flow speed enhances the interaction of spray with the gas and results in better atomization that takes place in a larger distance from the nozzle.

From the study of flow characteristics and the relation between fuel flow and spray [Date et al., 1992], it showed that the needle lift affects the internal flow of a nozzle and eventually will affect the atomization process. At small needle lift, the results showed a large turbulence in the sac chamber and vortexes near the sac wall, while at the large needle lift the turbulence becomes smaller and vortex disappears.

A study of the effect of nozzle opening pressure on atomization showed that with high (265 bar) - nozzle opening pressure- the start of injection occurs later and the end of injection is earlier as compared to the case of low opening pressure,190 bar. One possible advantage with increase of the needle opening pressure is that the larger drop sizes and their number density in the trailing regions of the spray are decreased. [Pitcher and Wigley, 1991]

1.2.5. Spray Characteristics

1.2.5.1. Spray Penetration

The speed and extent to which the fuel spray penetrates across the combustion chamber has an important influence on air utilization and fuel-air mixing rates. In multi-spray DI diesel combustion system, Over-penetration gives impingement of liquid fuel on cool surface which lowers mixing rates and increases emissions of unburned and partially burned species. Yet under-

penetration results in poor air utilization. The data taken by Hiroyasu et al. shows that the initial spray tip penetration increases linearly with time and, following jet breakup, then increases as $t^{1/2}$. Injection pressure has a more significant effect on the initial motion before breakup; ambient gas density has its major impact on the motion after breakup. [Heywood, 1988]

Farrel et al. (1996) reported that under high injection pressure (90 MPa), the ambient density, has less effect on the spray tip penetration than it has on that of low injection pressure (45 MPa) sprays. For multiple injection sprays, the second or third injection penetrates faster than the first split spray. The shorter the time spacing between the two split sprays the faster the following split spray can penetrate.

Naber and Siebers (1996) found that ambient gas density has a significantly larger effect on spray penetration and a smaller effect on spray dispersion than has been previously noted. The larger effect on penetration is caused by ambient gas density effects on spray dispersion. As ambient gas density increases, spray dispersion increases, which results in more entrained air in the spray. Based on conservation of momentum, the larger entrained mass leads to a slower penetration velocity and reduces penetration.

1.2.5.2. Spray Angle

The concept of near and far spray angles was proposed by Farrel et al. (1996). The near spray characteristic could be mainly dominated by the characteristics of the internal flow and has less influence from the ambient condition. While the far spray characteristic could be dominated mainly by the ambient conditions. Therefore, near and far spray angles measured within

different regions (near and far spray angles) provide more information on the spray transient characteristics than a single spray angle does. Higher backpressure or ambient density causes the sprays to have larger spray angle. Under high injection pressure (90 MPa), the backpressure (ambient density) has less effect on the far spray angle of sprays than it has on that under low injection pressure (45 MPa). The near spray angles decreases from the start of injection to the end of injection, and after the end of injection the near spray angle increases.

Dan et al. (1997) reported that the turbulence caused by seat region and the features in the sac region will dominate the jet dispersion at near region of the nozzle. This turbulent motion together with needle lifting and the cavitation phenomena in the sac chamber will have effect on the dispersing of sprays near the nozzle with distance within 10mm from the injector. The test results showed that in case of smaller needle lift, when the cross sectional area of the seat region becomes less than that of the hole region, the spray disperses more in the radial direction. And, once fuel emerges the nozzle exit within 2 to 10mm from the injector, the kinematic viscosity ratio between the fuel and the ambient gas determines the shearing phenomena to the turbulent liquid jet. On the other hand, for the spray far away from the injector, with distance of 20 to 40 mm from the injector, the kinematic viscosity of the ambient gas determines the dispersion of the spray in this spatial region.

Lowest drop sizes were measured at the leading edge of the spray, showing the capital importance of aerodynamic forces in the spray tip. Largest drop sizes were measured at the trailing edge of the spray; coalescence and

weaker aerodynamic interaction are responsible for this behavior. [Payri et al., 1996]

A study of local spray angle variation by Naber and Sieber (1996) showed that there is an initial transient which lasts about 0.5ms, the initial transient is then followed by a period with a relatively constant spray angle, and finally near the end of injection small increase in the spray angle is observed. It also showed that spray angles increase with an increase in the ratio of the ambient gas and fuel densities, and there is no significant effect of injection pressure on the spray dispersion angle for the range of injection pressures examined, ranging from 75 to 160 Mpa.

1.2.5.3. Initial Injection

Spray characteristics during initial injection are influenced by the existence of fuel in the sac as well as by the pressure in the sac. Initially injected fuel having a low momentum is pushed toward the spray periphery by fuel injected later. When injection is carried out with fuel remaining in the sac and with nozzle tip area wet with fuel, a protrusion shape like a needle can be seen. [Ishikawa and Niimura, 1996]

1.2.5.4. Spray Non-uniformity

Rao and Winterbone (1993), based on the results of their optically accessible engine spray combustion work, addressed that the penetration and shape of the sprays in the engine combustion chamber were found to be non-uniform. Arcoumanis et al. (1997) reported that considerable differences in the development of a five-hole spray were identified in terms of spray tip penetration. It was mainly attributed to differences in the hole inclination

angles. The smaller the inclination angle the smaller the injection rate from the hole and the higher the degree of cavitation. The nozzle used in the study was inclined, five-holes and sac type nozzle. It was concluded that the differences between the five sprays may be attributed to the non-symmetric orientation of the five holes relative to the sac volume, to the different length of the holes depending on their angle relative to the injector axis, and the manufacturing tolerances. [Arcoumanis et al.,1990]

Iiyama et al. (1992) performed a comprehensive study of the spray patterns produced by VCO (Valve-coveed-orifice) nozzles at low needle lift and had identified three distinct spray types. The work concluded that the inequalities of spray patterns are due to the eccentricity of the needle tip position. Soteriou et al. (1995) confirmed the results of Iiyama et al with regard to the three spray types identified. The first spray type has full cavitation in the hole and atomizes on exiting from the hole. The second spray type is a hollow cone spray of wide angle and with an air vortex at the center of the hole. There is no cavitation present. Although the jet angle is obviously diverging at the exit from the hole, it does not appear to be atomizing immediately on exit. The hollow cone spray is induced by an element of swirl as absorbed the fuel enters the hole as in the case of swirl injectors. The third spray type is produced by partial hydraulic flip. When this spray type is viewed from the side, it may be seen that the jet is directed more downwards and has a smaller cross sectional flow area. Unequal sprays from VCO nozzles at low needle lifts can be caused by partial hydraulic flip as well as by eccentricity of the needle tip. When the needle tip is eccentric, some holes have hollow cone sprays,

and at least one hole has partial hydraulic flip. Even when the needle tip is concentric, unequal sprays can occur because of partial hydraulic flip.

1.2.5.5. Overall Spray Structure

Ishikawa and Niimura (1996) described the mechanism of diesel spray formation from global structure point of view. They mentioned that the injected fuel is already atomized at the periphery near the nozzle hole exit. Instability generates near the nozzle hole exit in the shear layer between the spray and ambient gas. The instability grows as it moves toward the spray downstream and finally grows to form vortices at further downstream. In the ambient gas flow field near these vortices, air is induced into the spray periphery by streams and moves toward the spray axis. Meanwhile, due to the airflows toward the spray boundary fuel particles move outward the spray axis, form strip-shaped structure, and finally develop into branch-like structure. The branch-like structures turn out to be regions of higher and lower droplet number density. At higher fuel injection velocities, the generation of branch-like structures is dramatically increased.

1.2.5.6. Experimental Method

Single-hole nozzles are often used to study diesel spray as they could simplify experimental procedure. But, Hosoya and Obokata (1993) commented that the spray injected from the single-hole nozzle, which usually has a hole located at the tip of the sac, is shown to have very different characteristics from the sprays injected from multi-hole nozzles.

Based on the study of Soteriou et al. (1995), similar comment was found. They reported that single-hole nozzle does not produce spray which is

representative of those from standard multi-hole nozzles, and using such types of nozzle could produce misleading results, which is because the single-hole nozzle could not produce similar turbulence flow that could simulate those of multi-hole nozzles.

Regarding the measurement techniques for spray tip penetration, Hentschel (1996) addressed that the evaluation of the spray tip penetration from videos or films is independent of the measurement technique, which means the penetration data can be derived from the pictures quite straightforwardly, but evaluation of the spray angles depends on the measurement technique. Laser Schlieren and shadowgraphy high-speed film measurements result in significantly larger values for the spray angle than the light scatter measurement does. The results of former method represent the spray angle of vapor phase while these of the later method correspond to the spray angle of liquid phase.

1.2.6. Visualization of Spray and Its Combustion

Rao and Winterbone (1993) used a copper-vapor laser to provide 10-40 ns duration high energy pulses to study high pressure (120 MPa) diesel sprays in a swirling air single cylinder engine using a transparent piston with a quartz window. The fuel sprays were photographed at a framing rate of 20,000 frames/sec. The penetration and shape of the sprays were found to be non-uniform. The sprays impinged on the combustion chamber wall in less than 4.00 ms and most of the fuel was deposited on the wall, creating fuel rich zones, especially at high loads. The sprays were not deflected by the air even

at very high swirl levels even at low injection rates. Most of the fuel collected close to the combustion chamber wall is due to the high momentum flux of the injected fuel and the small radial distance from the injector to the combustion chamber wall. Most of the air close to the center of the bowl and injector tip was not utilized for combustion.

Maximum liquid-phase fuel penetration has been recognized as an important item of in-cylinder measurements. Because, it provides a measure of the fuel vaporization rate and has a significant influence on air utilization and fuel-air mixing. For designing the combustion chamber of small high-speed DI engines, special attention on liquid-phase fuel penetration is required. In low speed and low load conditions, avoiding the impingement of the liquid phase of sprays on the combustion chamber wall will be of benefit to hydrocarbon emission. In high speed and high load, matching the sprays with combustion chamber shape will reduce smoke emission. [Zhang et al., 1997]

Dec and Espey (1995) reported that the liquid-phase fuel penetration is determined by the rate of evaporation of the fuel and, under the specified test conditions, the liquid length remains fairly constant at 23 mm beyond 3 degree after start-of-injection. The engine operating conditions of the study were 1200-rpm engine speed, 95-degree C water/oil temperature, 11.5°-BTDC injection timing, and 68-MPa injection pressure. Beyond this 23mm liquid region, the jet consists of purely vapor-phase fuel (mixed with air). The limited liquid –phase fuel penetration is due solely to the evaporation induced by entrainment of hot ambient air into the fuel jet, and is not a result of combustion heating. Energy content of the in-cylinder air and the mixing rate

of the air with the liquid fuel are the two dominant factors of the penetration length. The liquid penetration length becomes shorter as combustion proceeds. Under the test condition of constant inlet air density, time to reach maximum penetration and maximum penetration length both systematically decrease with increasing TDC temperature. Liquid penetration lengths vary from about 30 mm at 800K to about 18 mm at 1100 K. For all temperatures, the initial fuel penetration rate is almost liner with time. Change in the air density can significantly impact the mixing rate of air with the liquid-phase fuel both by changing the droplet breakup rate and by changing the amount of air entrainment into the sprays and hence the energy available for fuel evaporation. Under the test conditions of constant inlet air temperature, the maximum liquid penetration lengths with increasing TDC density vary from 30 mm for 11.1 kg/m^3 (0.67-atm intake pressure) to about 13 mm for 33.3 kg/m^3 (2-atm intake pressure). Ignition delays vary from 7.5 degree at 11.1 kg/m to 1.5 degree at 33.2 kg/m3. The changes in TDC density have even more impact on maximum liquid penetration and ignition delay than changes in TDC temperature. Zhang et al. (1997) also reported that the penetration rate of liquid-phase fuel increases with injection pressure, while the maximum penetration is almost unchanged, because of the interaction of increased injection velocity and reduced drops average sizes. Fuel sprays injected at a high injection pressure reaches the cavity wall, collides against it and bounces from it, forming a good mixture before ignition occurs. The collision of fuel spray contributes much to the improvement of spray formation and of diffusion combustion. [Minami et al., 1990]

1.3. Introduction to Each Chapter

The characterization of the high-pressure injection is described in Chapter 2 in which all the characteristics required to proceed the visualization work is established and analyzed. Non-evaporative spray visualization can be divided into two parts, macroscopic and microscopic visualizations. Macroscopic visualization is included in Chapter 3 focused on spray penetration, spray uniformity, and global structure. Microscopic visualization is described in Chapter 4 focused on near nozzle exit spray dynamics. In cylinder spray and combustion visualization and analysis is described in Chapter 5. The conclusions are summarized in Chapter 6.

The numerical simulations using new transient schemes (space-time method) and primary breakup models (turbulent and cavitational) to better correlate spray and injector design are also discussed and are included in Appendix D (SAE paper: **1999-01-3554 and 1999-01-3555**) .

pressure, which is 345 bar for the nozzle used in the study. The schematic of the system is shown in Figure 2-3. A strain gage is installed on the surface of the rocker arm to for measuring the injection pressure.

2.2. Experimental Method

The items of injection characterization included injection pressure, injection rate, injector response time, and needle lift. Based on these measured characteristics, other useful information can be derived, such as injection quantity and dynamic discharge coefficients of the nozzles.

The experimental setup for the characterization of the HEUI system is shown in Figure 2-4. A Kislter 4067A2000 Piezo-resistive pressure transducer is installed at about 7 cm upstream of the inlet of the fuel injection nozzle holder. The measured pressure is upstream injection pressure. A Bosch type injection rate meter records injection rate by measuring the increase of pressure in a fuel-filled tube when the injector injects fuel into the tube. The rate of pressure increase in the tube corresponds to injection rate. A LVDT (linear variable differential transformer) displacement sensor with its ferromagnetic moving core mounted on the pressure pin of the injection nozzle holder detects needle lift of the nozzles. A special made nozzle tip is instrumented with pressure transducer, as shown in Figure 2-5, for the measurement of nozzle sac pressure that represents down stream injection pressure. By comparing the upstream and downstream injection pressures, pressure drop and fuel transportation time across the nozzle holder assembly

can be obtained. A Labview Data Acquisition and Controls system is implemented to operate the HEUI system with various requirements in terms of injection pressure, injection duration, and number of injections, and synchronization between injection and data acquisition. The Labview system is also used to record and analyze test data. The specifications of the nozzle tips used in this study are summarized in Table 2-1. The flow number, for example, 610 of the VCO nozzle, represents steady state volume flow rate in cubic centimeter within 30 seconds test period with 100 bar injection pressure.

Table 2-1 Specifications of the nozzle tips of HEUI system

Nozzle tip	No. of hole	Hole Diameter(mm)	Total hole flow area(m**2)	Cd (steady state flow)
610 VCO	6	0.218	2.24 E-7	0.58
620 Mini-sac	7	0.190	1.98 E-7	0.66
730 VCO	7	0.210	2.42 E-7	0.64

Similar approach and instrumentation is applied to the CR system for injection pressure and injection rate measurement. The injection pressure is directly measured at the fuel inlet of the injector by Piezo-resistive pressure transducer.

Table 2-2 shows the test conditions of the injection characterization of the fuel injection systems. As these three types of injection system are also used to deliver the high-pressure injections required by the spray and combustion visualization work, as described in chapter 3,4, and 5 respectively, the basic characteristics of these systems need to be well understood

beforehand. Therefore, the test conditions mentioned above have been arranged so that the requirement of the visualization work is met.

Table 2-2 Test matrix of the characterization of the injection systems

Injection Systems	HEUI	EUI	Common Rail
Operating conditions	Common rail pressures 380 and 275 bar	Cam speeds 300,400,500 and 600 rpm	Common rail pressures 350,800,and 1350 bar
Injection Duration	1.70 / 2.25 ms	10,15,20 and 25 degrees	from 0.35 to 1.2ms
Type of nozzle	VCO and Mini-sac	VCO	single/dual guided VCO
Rate shaping pipe	12" and 24"	n.a.	n.a.
Maximum injection pressures	1600 bar	1600 bar	1350 bar

2.3. Results and Discussions

2.3.1. Characteristics of HEUI Injection System

2.3.1.1. Injection Pressure

The injection pressure of HEUI system mainly depends on the common rail pressure and injection duration. As shown in Figure 2-6, at fixed injection duration of 2.25 ms, the injection pressures increase corresponding to the increases of the common rail pressure. With 2.25 ms injection duration and 380 bar common rail pressure, the system is able to issue injection with pressure up to 134 MPa. The intensified ratios, which is the ratio of injection pressure to common rail pressure, of the injector for three common rail pressure settings, 207, 276, and 380 bar, are 3.71, 3.80, and 3.44

respectively. Figure 2-7 shows the effect of injection duration on injection pressure; one millisecond increase of injection duration is corresponding to increase of 29 MPa in peak injection pressure. The thickness of the pressure adjusting shim also affects the peak injection pressure. With shim thickness increased from 1.95 to 3.24 mm, the peak injection pressure increases 4 to 6 %.

2.3.1.2. Injector Response Time

Injector response time, defined as the time between injection command and start-of-injection (SOI), is ranging from 1.4 to 2.0 ms. The injector response time consists of two parts; part one is the time required for energizing of the solenoid that drives the spool valve, and part two is the time required for the spool valve to move to the open position and the line pressure to build up. The former depends on the voltage of power supply applied to the driver of the solenoid; the latter depends mainly on the common rail pressure and length of the rate-shaping pipe. The injector is driven by peak-and-hold type driver. In this study, the voltage of the power supply to the driver is set at 70 volts.

The effects of shim thickness, common rail pressure, and length of rate-shaping pipe on injector response time are summarized in Table **2-3** and Table 2-4. The result shows that long rate-shaping pipe, low common rail pressure, and reduced pressure adjusting shim thickness increase the injector response time. On the contrast, short rate-shaping pipe, high common rail

pressure, and additional shim thickness shorten the injector response time.

Table 2-3 Effect of shim thickness on injector response time of HEUI system

Common Rail Pressure(bar)	Response time(ms)	
	3.1 mmShim Thickness	2.5 mm Shim Thickness
207	1.6	1.8
276	1.5	1.6
380	1.4	1.4

Table 2-4 Effect of length of the rate-shaping pipe on injector response time of HEUI system

Common Rail Pressure(bar)	Response time(ms)	
	24 inches shaping pipe	12 inches shaping pipe
207	2.0	1.8
276	1.7	1.6
380	1.5	1.4

2.3.1.3. Injection Rate and Needle Lift

Injection Rate mainly depends on the common rail pressure, needle lift, nozzle hole area, and length of the rate-shaping pipe. The common rail pressure has direct effect on the injection rate, as shown in Figure 2-8, higher injection rate corresponding to higher common rail pressure. Figure 2-9 shows the effect of length of the rate-shaping pipe on injection rate. With 24-inch rate-shaping pipe the pressure rising rate is reduced resulting in slower needle lift and lower peak pressure, as a result a in a lower injection rate. Figure 2-10 shows the effect of nozzle hole area on injection rate is obtained. As the nozzle flow area increases, the injection rate increases proportionally but there is little effect on the shape of the injection rate. With respect to other design or

operating variables such as Injection duration, type of nozzle tip (VCO or Mini-sac), and thickness of the pressure-adjusting shim, it is found that they have insignificant effect on the injection rate.

The characteristics of the needle lift in terms of maximum lift and lift speed are determined mainly by nozzle design and injection pressure. Maximum needle lift of the nozzles used in the tests is 0.31mm that is measured from needle seat to fully open position, which is pre-determined by the design and make of the nozzle tips. As to the effect of injection pressure, the pressure in the nozzle pressure chamber and the pressure applied to the top of the needle determine the behavior of the needle lift. In the case nozzles of HEUI system, the pressure applied to the top of needle is equivalent to the atmosphere pressure; therefore the pressure in the nozzle pressure chamber dominates the behavior of needle lift. As shown In Figure 2-9, with 12-inch rate-shaping pipe and 380 bar common rail pressure, it took 0.2 ms for the needle to reach fully open position. However, with (24 inch) injection rate-shaping pipe, and lower common rail pressure (276 bar), the needle lift time increases from a regular 0.2 ms to 0.6 ms. As far as the effect of shim thickness on needle lift, test result shows that increase of the thickness of the pressure adjusting shim reduces needle bounce.

2.3.1.4. Dynamic Discharge Coefficient

The steady-state Discharge Coefficients of the nozzles, as shown in Table 2-1 Specifications of the nozzle tips of HEUI system, are calculated

based on the nozzle data, steady-state flow rate and pressure, and following formula.

$$Cd = \frac{Q}{A \times \sqrt{\frac{2 \times P}{\rho}}}$$

Where, C_d = Discharge Coefficient

Q = Volume flow rate, m^3/sec

A = Nozzle flow area, m^2

P = Injection pressure, MPa

ρ = Fuel density, kg/m^3

On the other hand, the dynamic Discharge Coefficients of the nozzles can also be calculated by the same, but instead of using formula, the measured up-stream pressures and injection rates as the inputs. Figure 2-12 to Figure 2-14 show the calculated dynamic Discharge Coefficients for the nozzles used in the study associated with the measured injection pressure, injection rate, and needle lift. The C_d trace shown in the figures can be divided into three segments, which can be corresponding to three phases of the needle lift, opening, needle full lift, and closing, respectively. For example, in Fig 2-12, when the needle is in opening the Cd increases from 0 to about 0.57; Once the needle reaches the full lift position, the Cd gradually approaches value of 0.62 and maintains at the same value with some oscillation until needle starts to close; When the needle is closing, the Cd decreases from

0.62 to 0. As a remark, needle bouncing is observed in this example. The calculated dynamic Discharge Coefficient of the example, 0.62, at needle full-lifted condition is about 6% lower than the steady-state Discharge Coefficient, 0.66, for the 620 mini-sac nozzle. Similar results are applied to the other two types of nozzles, the 610 and 730 VCO.

2.3.1.5. Startup Transient

The HEUI system demonstrates significant transient in injection pressure and injection rate at system startup operating condition. Figure 2-15 and Figure 2-16 show the transient of injection pressure and injection rate at system startup. With common rail pressure maintained steadily at 380 bar, when the system is commanded to deliver injection, it takes 3 to 4 injections to fully establish the pressure in both the intensifier and the high-pressure line before a nominal injection can be issued. The injection pressure, injection rate, and injection quantity become stable and more repeatable after the 3rd injection is issued, as shown in Table 2-5. For the 1st injection, its pressure reaches 56% of the nominal pressure, (40 MPa), and its quantity reaches 71% of the nominal quantity, (101 mg). The injector response times of the first two injections are also longer than a nominal one.

2.3.1.6. Pilot Injection

The HEUI system is capable of delivering pilot injection, however the operating range of the pilot injection in terms of its duration and dwell time is

quite limited. The low limit of injection duration for pilot injection is 0.6 ms. The injector could not perform pilot injection with duration shorter than this duration. The dwell time, defined as the time between issue of pilot and main injection, could not be shorter than 0.6 ms. Figure 2-16 shows a typical measurement of the injection rate and needle lift for injection with pilot and main injection. The injection command is given at ' t = 0'. For the pilot injection, the injector response time is 1.4 ms and within 0.2 ms the needle reaches its full lift position. Figure 2-18 and Figure 2-19 show the effect of dwell time on main injection in terms of injection rate and needle lift. With shorter dwell time the peak pressure, rate, and quantity of an injection are lower than those of an injection with longer dwell time, which could be due to the slow recovery of the pressure in the common rail after a pilot is delivered. Figure 2-20 shows the effect of dwell time on injection quantity. As dwell time decreases, the injection quantity of the main injection decreases.

Table 2-5 Transient of HEUI injection during system startup period

Injection since engine start-up	injector delay time(ms)	Peak injection pressure(Mpa)	Injection Quantity(mg)
1st	1.5	80	72
2nd	1.44	127	90
3rd	1.38	143	99
4th	1.4	145	101
5th	1.38	140	101

2.3.1.7. Sac Pressure Measurement

In the characterization study of the HEUI system, the injection pressure

is measured at 7 cm upstream of the fuel inlet of injection nozzle holder. To understand the correlation between the upstream pressure and the sac pressure, the pressure in the sac chamber of nozzle tip, a special instrumented nozzle tip and adapter are made such that the pressure transducer can directly get access to the sac chamber of the nozzle tip. The upstream and sac pressures are measured at the same time associated with the command signal of an injection . The conditions and results of the test cases are summarized in Table 2-6. Figure 2-21 and Figure 2-22 show the pressure traces for two of the test cases. The pressure drops from the upstream to sac chamber are ranging from 5 to 10 MPa. It is believed that the pressure drop occurs mainly at the needle seat region where high-pressure and -velocity fuel flows through. The pressure transportation lag from the upstream to the sac chamber is in the range of 0.1 to 0.14 ms. There is no correlation found between the operating conditions, common rail pressure and injection duration, and the pressure drops and transportation lags.

Table 2-6 Summary of the sac pressure measurement of the HEUI system

Common Rail pressure(Mpa)	Injection Duration(ms)	Peak upstream pressure(Mpa)	Peak Sac Pressure(Mpa)	Pressure drop (Mpa)	Time Lag (ms)
380	2.25	158	149	9	0.12
380	1.70	126	121	5	0.14
276	2.25	114	108	6	0.14
276	1.70	101	91	10	0.1

2.3.2. Characteristics of CR and EUI Injections

Due to the difference in working principle between the CR and HEUI injection systems, the needle lift of the CR system is significantly different from that of the HEUI system. Unlike that of the HEUI system, the needle lift time of CR injector is much longer and is strongly affected by the injection pressure. As shown in Figure 2-23, the needle rising speeds are 0.25, 0.37, 0.56, and 0.81 mm per millisecond for injection pressure of 400, 800, 1100, and 1350 bar, respectively, which means the needle rises faster as injection pressure increases. For the case of 400-bar injection, it could take 1.15 ms for the needle to reach full lift position. Meanwhile, for the case of maximum injection pressure, it takes only 0.4 ms to reach maximum needle lift, which is shorter than that of the lower pressure case, but it is still twice as much of that of the HEUI system. The needle closing speed is 0.51 mm per millisecond and is independent of injection pressure. Figure 2-24 and Figure 2-25 show the injection rate and needle lift for the CR system with various injection duration's and pressures. Figure 2-26 shows the injection rates of injections with both pilot and main for various injection pressures. As shown in the figure, the pilot injection of 30 MPa barely appears, which demonstrates that 30 MPa is the low limit of system operating pressure.

The injection pressure of the EUI system is determined mainly by engine camshaft speed and injection duration. As shown in Fig 2-26, with 500-rpm camshaft speed, the pressure rising rate is 50 MPa per millisecond; with 25 crank angle injection duration, the peak injection pressure can reach 160

MPa. The injection pressure decreases as the speed of the camshaft decreases, as shown in Fig 2-27. The injector response time increase from 1.6 ms to 2.1 ms corresponding to the decrease of camshaft speed from 600 rpm to 300 rpm.

2.4. Concluding Remarks

The goal of this chapter is to characterize three types of high-pressure diesel injection systems, EUI, HEUI, and Common Rail, and evaluate the effects of design parameters and operating conditions on injection characteristics At the same time, all the characteristics required to proceed the visualization work is also established and analyzed in this chapter Specific findings for the HEUI system are summarized as follows.

- Common rail pressure and length of the injection rate-shaping pipe determine injection pressure, while pressure rising rate and injection duration determine peak injection pressure.

- Nozzle flow area, common rail pressure, and length of rate-shaping pipe are the main parameters that affect injection rate.

- The shape of injection rate is affected mainly by common rail pressure, especially its pressure rising rate, and length of rate-shaping pipe.

- Injection response time is in the range of 0.1 to 0.18 ms and mainly depends on common rail pressure, length of rate-shaping pipe, and shim thickness.

- Dynamic Discharge Coefficient derived from measured up-stream

injection pressure and injection rate is about 6% lower than steady-state Discharge Coefficient derived from steady-state flow data.

- .Injection transient at system startup is observed. At system startup, it takes 3 to 4 injections to establish line pressure in the high-pressure section of the system. Afterward, stable and repeated injection can be issued.

- .The pressure drop across nozzle seat flow area is in the range of 5 to 10 MPa and transportation lag between upstream and nozzle sac chamber is in the range of 0.1 to 0.14 ms, which is independent of common rail pressure and injection duration.

For CR system, it is found that the needle lift of the CR system is significantly different from that of the HEUI system. The needle lift time of CR injector is much longer and is strongly affected by the injection pressure. Due to the design and working principle, the injector is operating in partial needle lift condition regularly, especially for injection with short duration and low pressure.

For EUI system, the injection pressure is determined mainly by engine camshaft speed and injection duration. It is capable of delivering 200-MPa injection with high camshaft speed and long injection duration. Its injector response time is also affected by the camshaft speed significantly
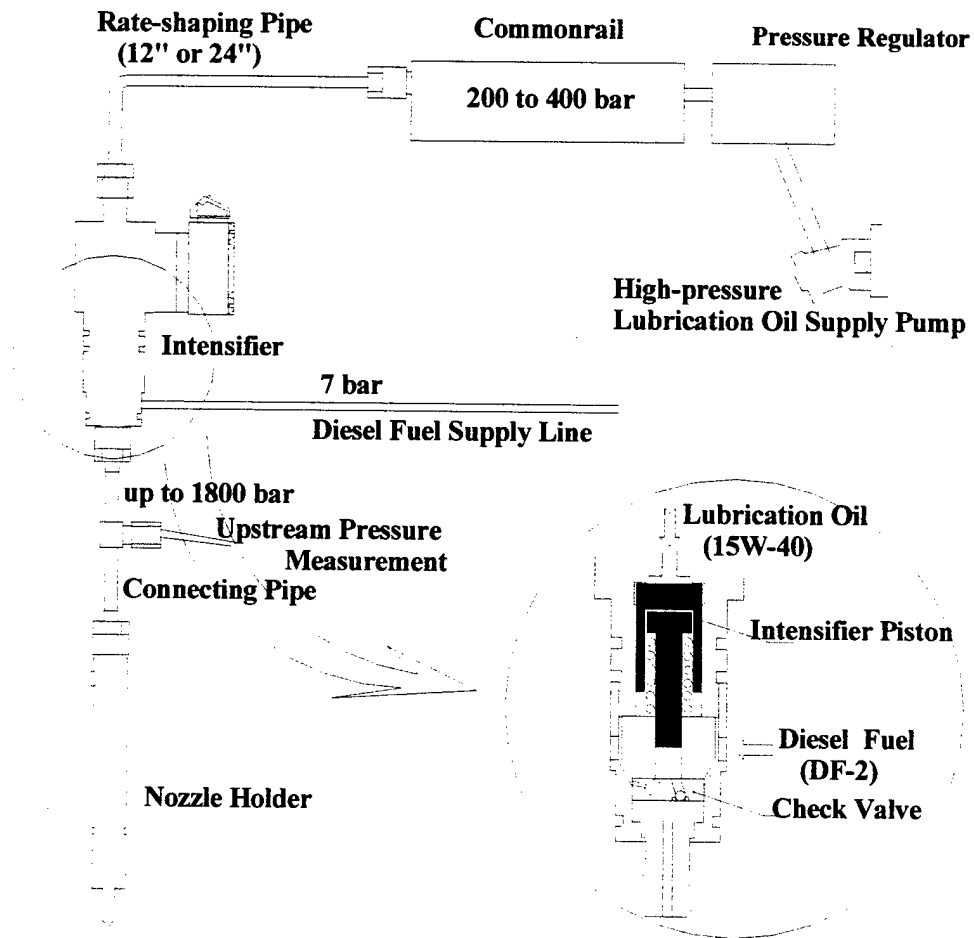
Figure 2-1 Schematic of HEUI injection system
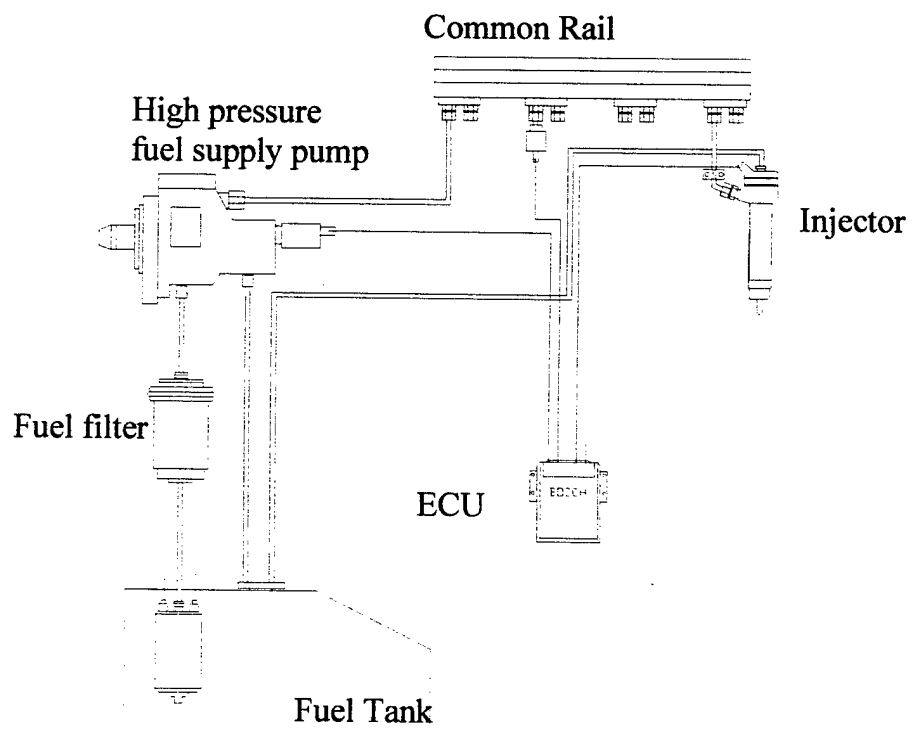
Figure 2-2 Schematic of CR injection system
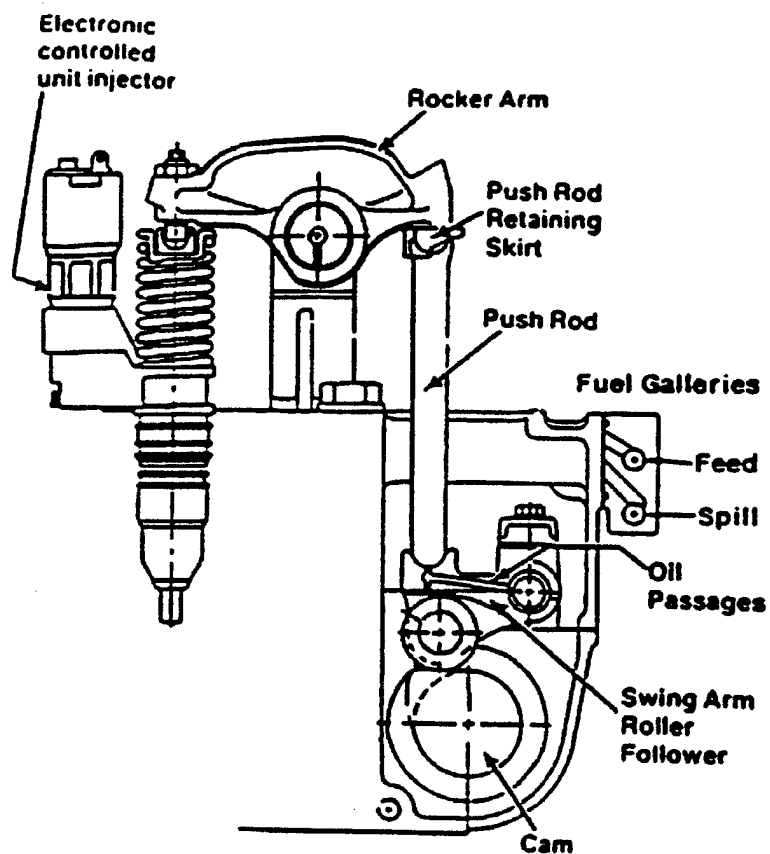
Figure 2-3 Schematic of EUI injection system
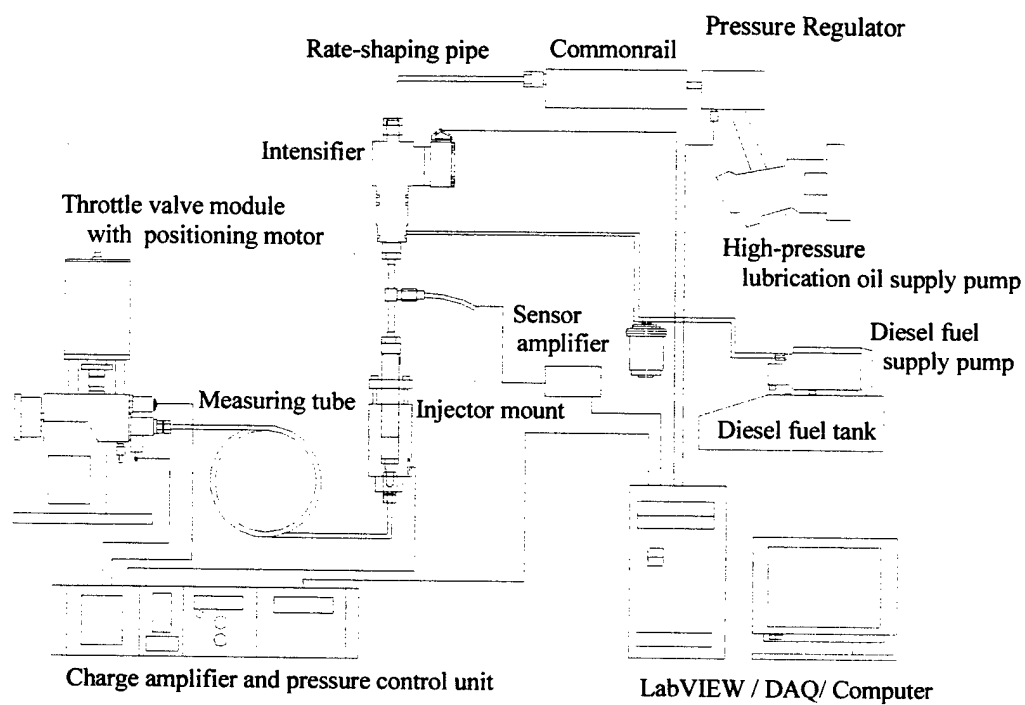
Figure 2-4 Schematic of experimental setup for the characterization of HEUI system
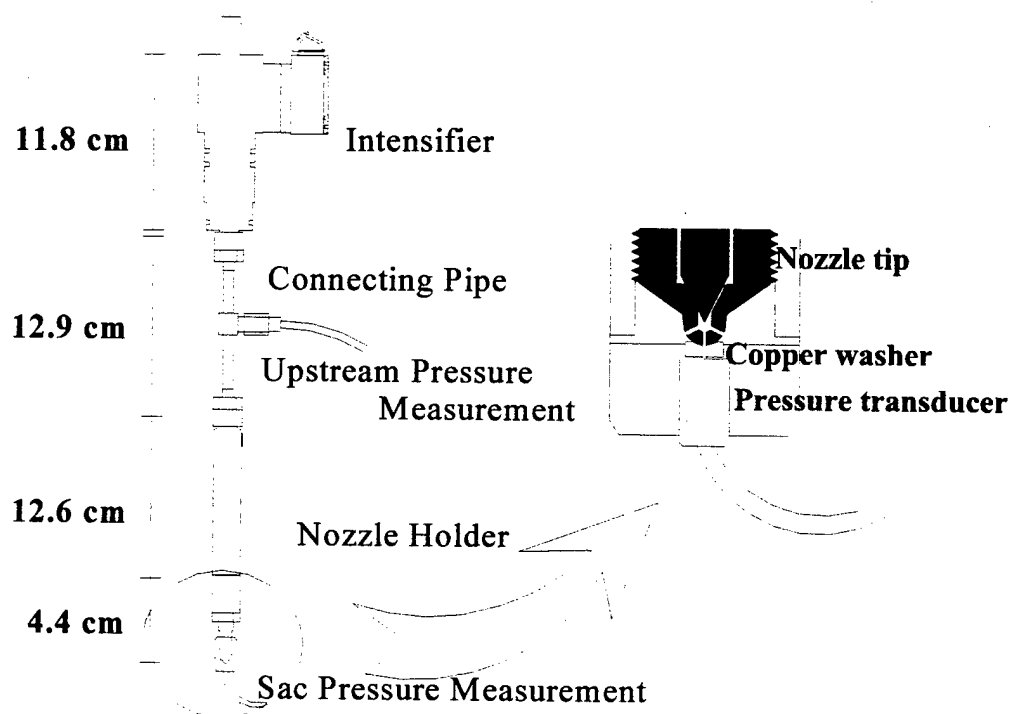
Figure 2-5 Schematic of the measurement of upstream and sac pressures
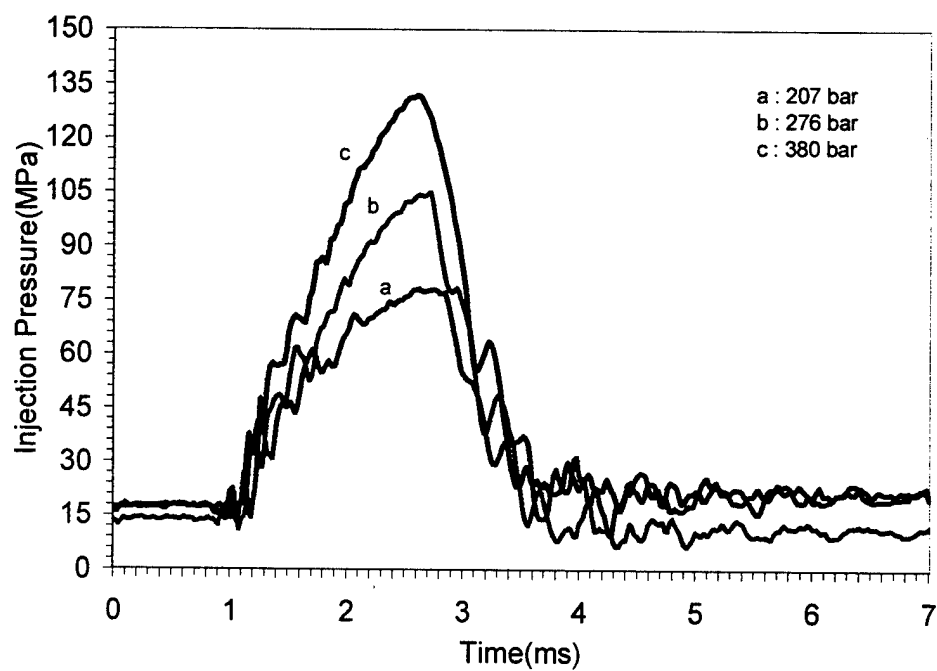
Figure 2-6 Effect of common rail pressure on injection pressure, with 2.25-ms
injection duration, 610 VCO nozzle, and 12-inch rate-shaping pipe
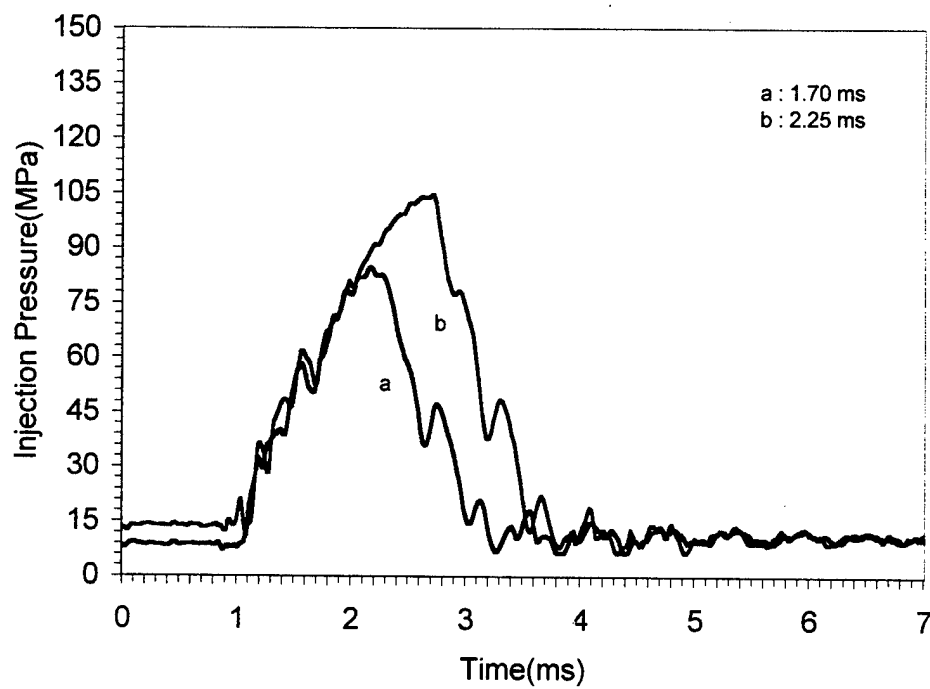
Figure 2-7 Effect of injection duration on peak injection pressure, with 276-bar common rail pressure, 610 VCO nozzle, and 12-inch rate-shaping pipe
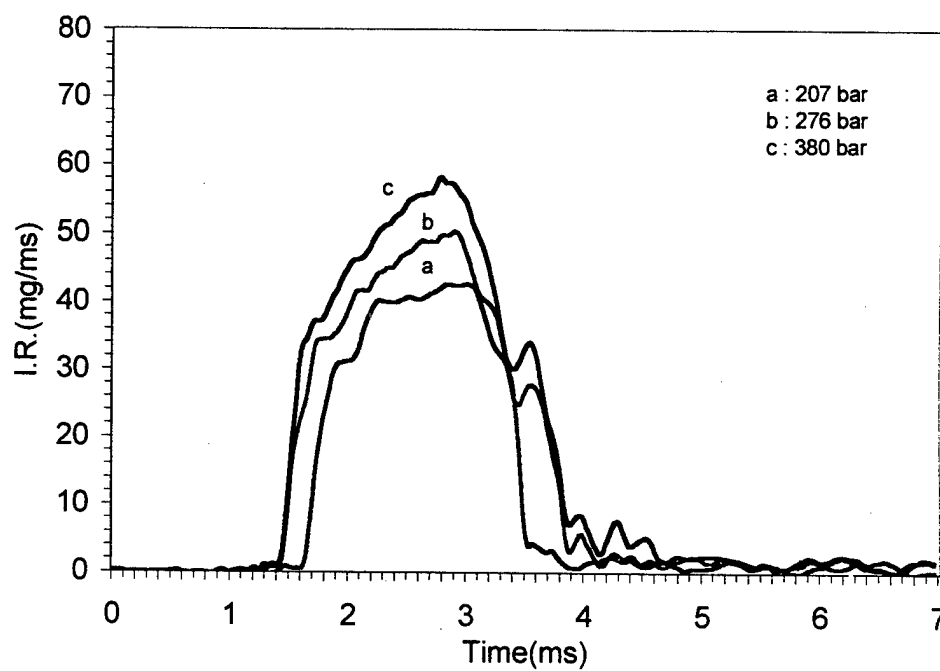
Figure 2-8 Effect of common rail pressure on injection rate, with 2.25-ms injection duration, 610 VCO nozzle, and 12-inch rate-shaping pipe
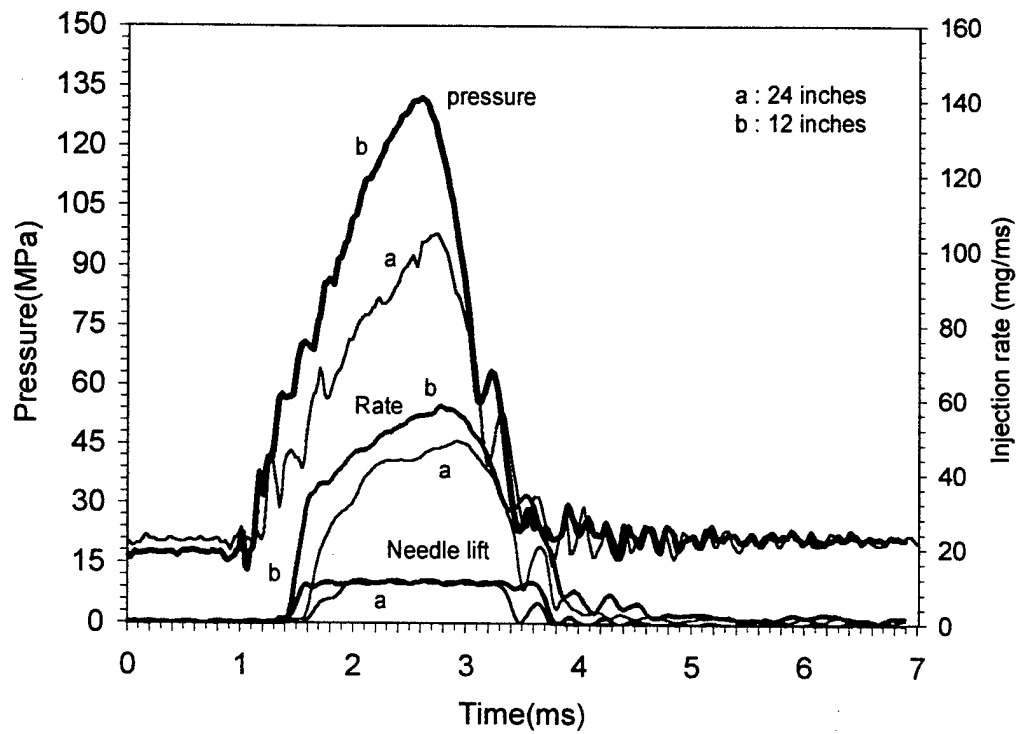
Figure 2-9 Effect of length of the rate-shaping pipe on injection rate, with 2.25-ms injection duration, 380-bar common rail pressure, and 610 VCO nozzle
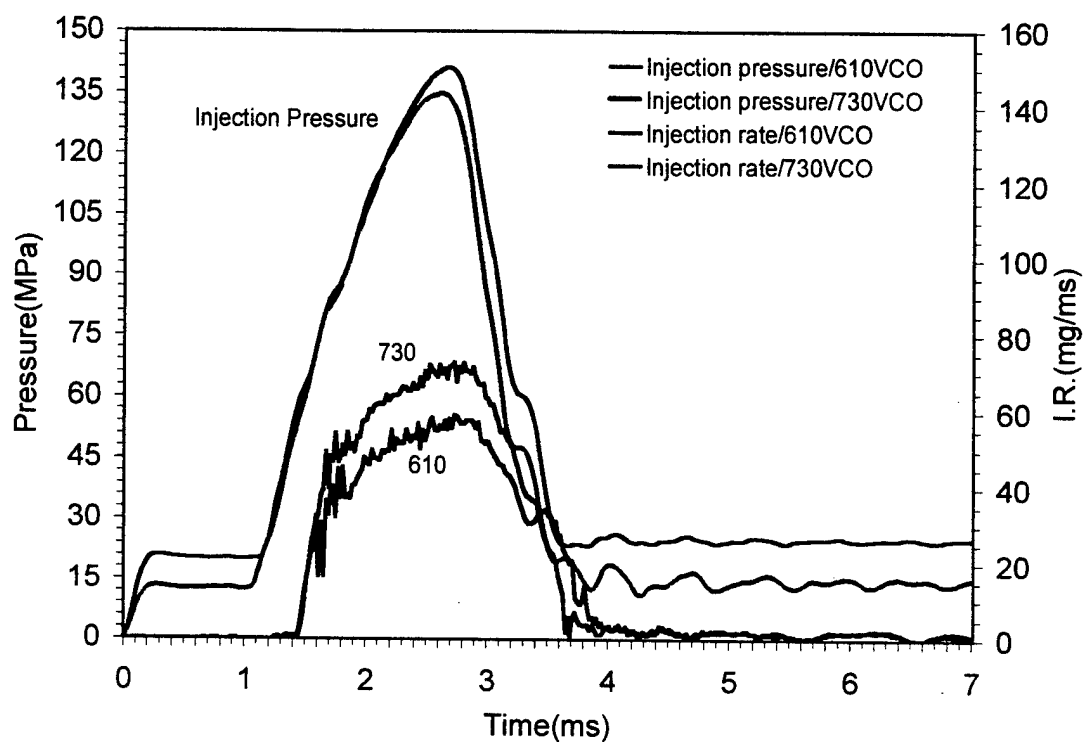
Figure 2-10 Effect of nozzle flow area on injection rate, with 2.25-ms injection duration, 380-bar common rail pressure, and 12-inch rate-shaping pipe
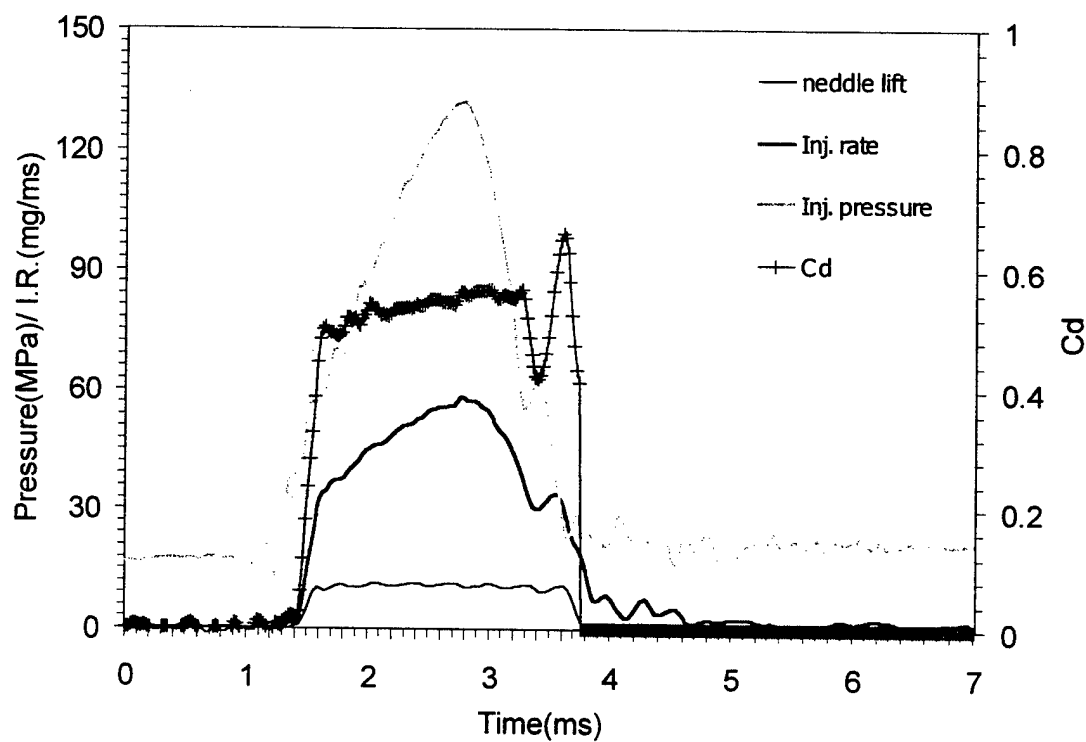
Figure 2-12 Dynamic Discharge Coefficient of 610 VCO nozzle, with 2.25-ms duration, 0.31-mm needle lift, and 0.58 steady flow Discharge Coefficient
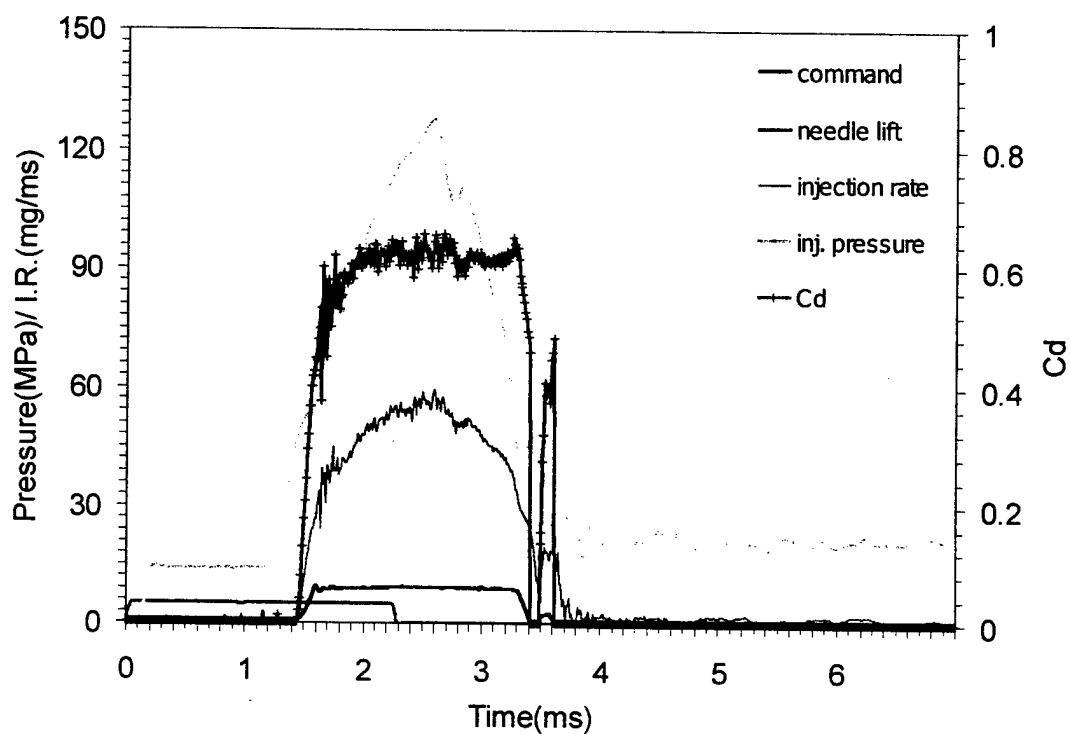
Figure 2-12 Dynamic Discharge Coefficient of 620 mini-sac nozzle, with 2.25-ms duration, 380-bar common rail pressure, 0.31-mm needle lift, and 0.66 steady flow Discharge Coefficient
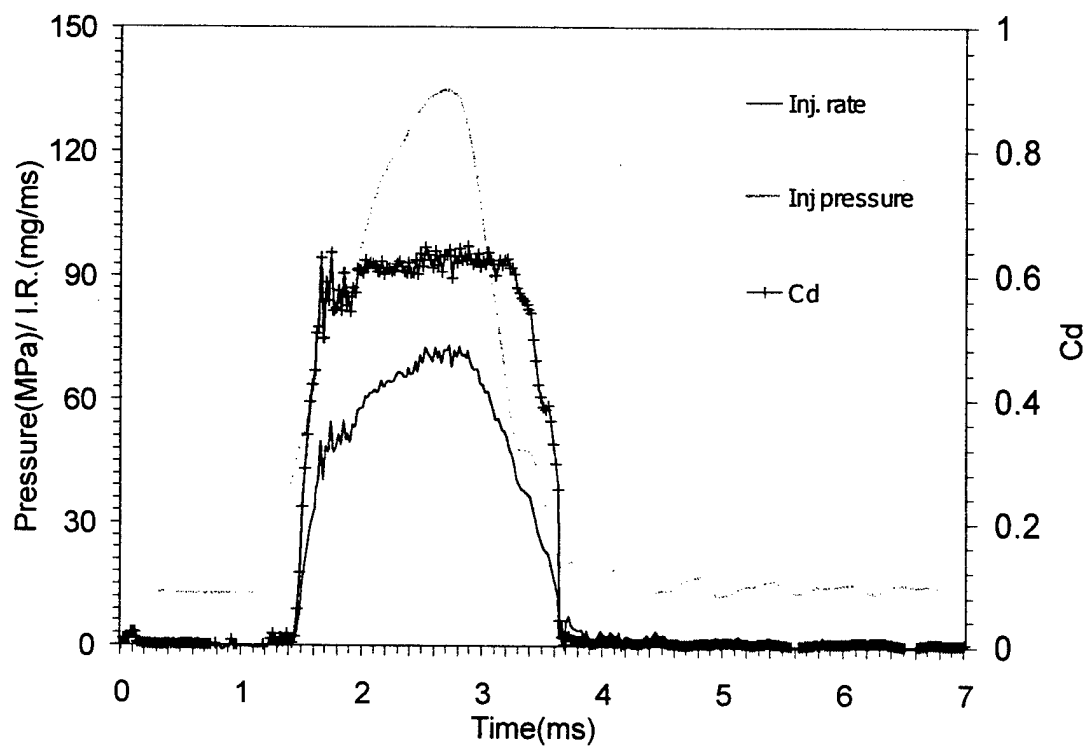
Figure 2-14 Dynamic Discharge Coefficient of 730 VCO nozzle, with 2.25-ms duration, 380-bar common rail pressure, 0.31-mm needle lift, and 0.64 steady flow Discharge Coefficient
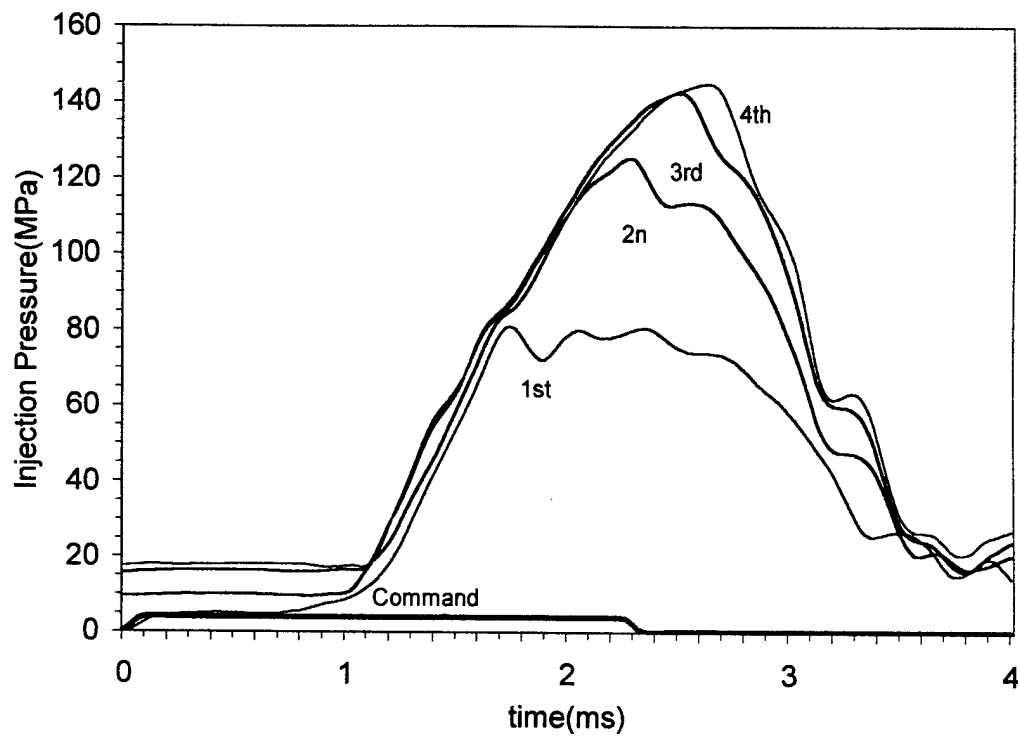
Figure 2-15 Transient of injection pressure of 4 consecutive injections at system startup , with 2.25-ms duration, 380-bar common rail pressure, 610 VCO nozzle, and 12-inch rate-shaping pipe
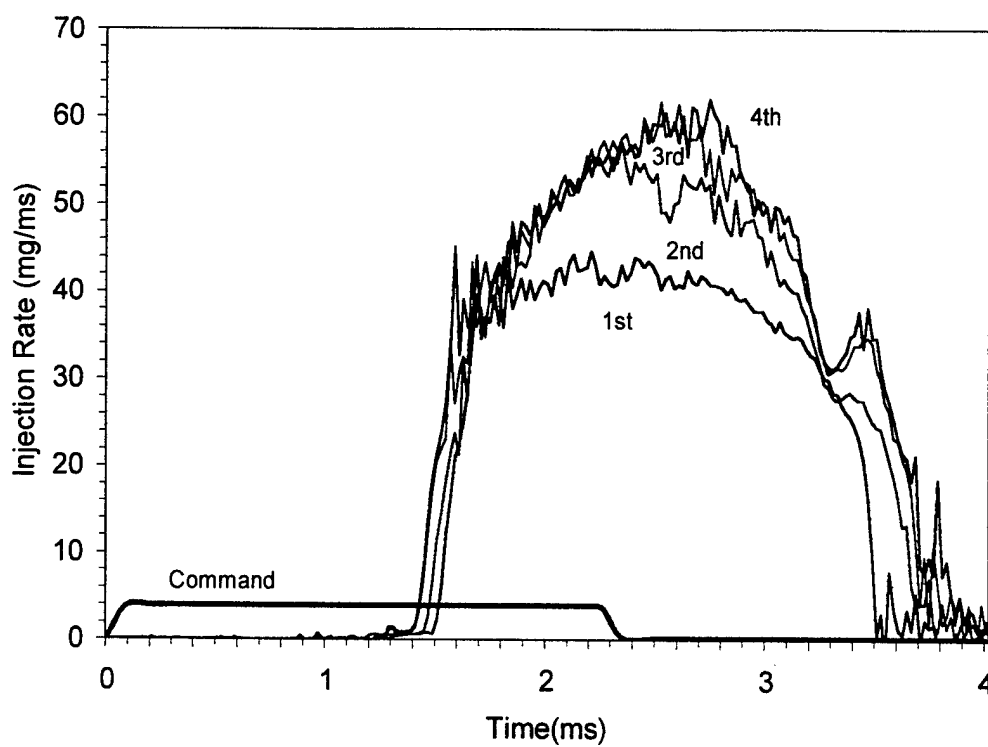
Figure 2-16 Transient of injection rate of 4 consecutive injections at system startup , with 2.25-ms duration, 380-bar common rail pressure, 610 VCO nozzle, and 12-inch rate-shaping pipe
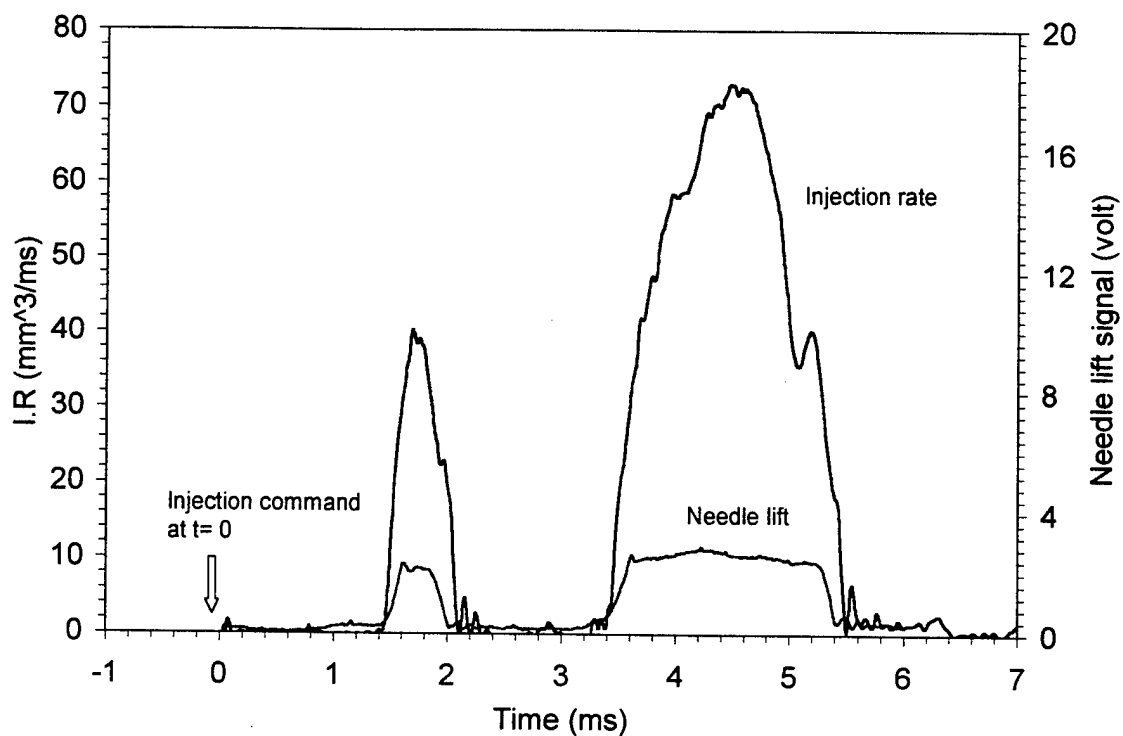
Figure 2-16 Injection rate and needle lift of HEUI pilot injection, with 380-bar common rail pressure, 620 mini-sac nozzle, 0.8-ms pilot, 2.25-ms main, and 1.2-ms dwell time
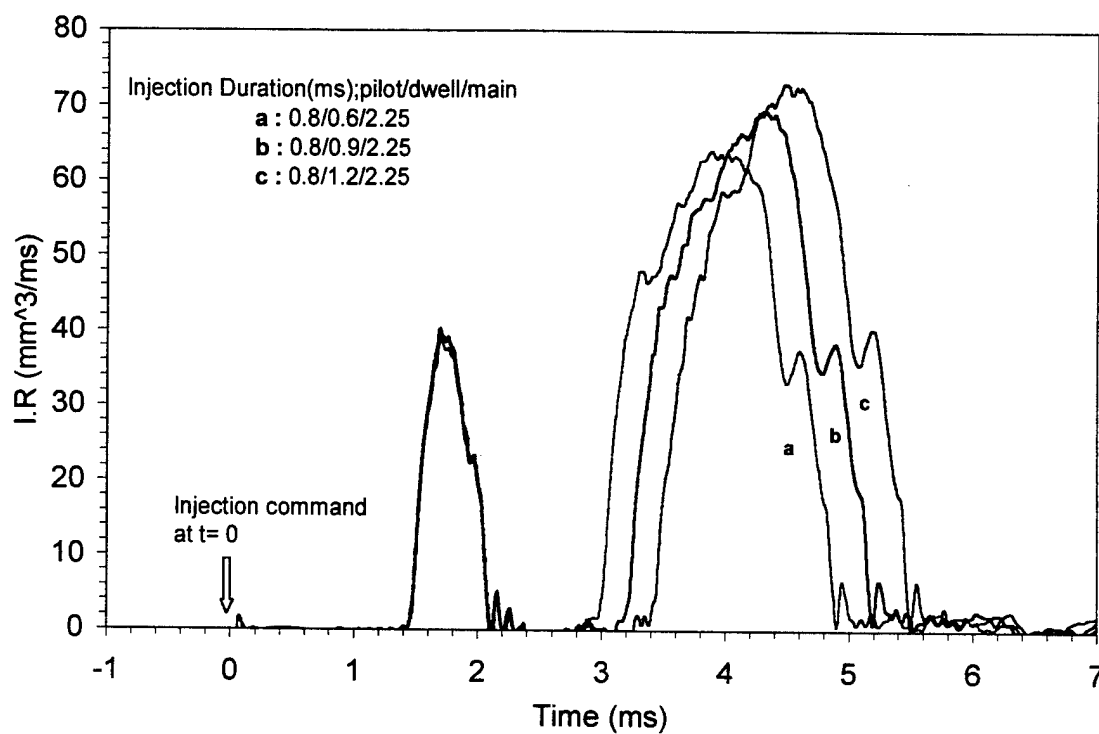
Figure 2-18 Effect of dwell time on injection pressure, with 380-bar common rail pressure, 620 mini-sac nozzle, 0.8-ms pilot, and 2.25-ms main injection
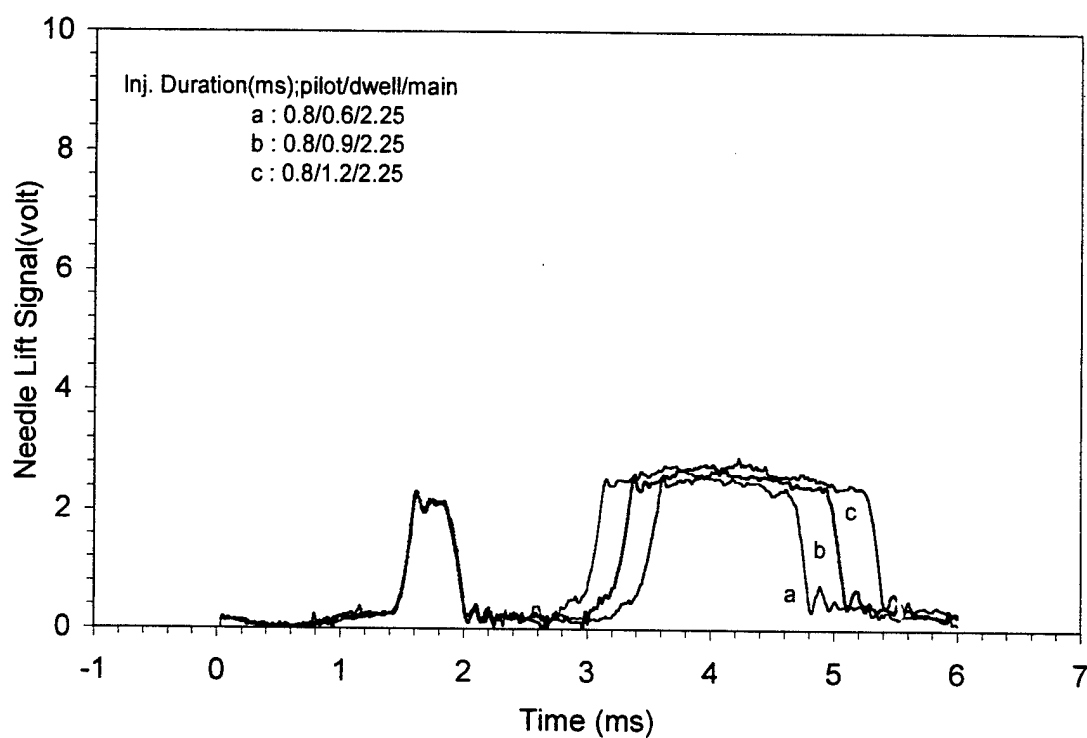
Figure 2-19 Effect of dwell time on needle lift, with 380-bar common rail pressure, 620 mini-sac nozzle, 0.8-ms pilot, and 2.25-ms main injection
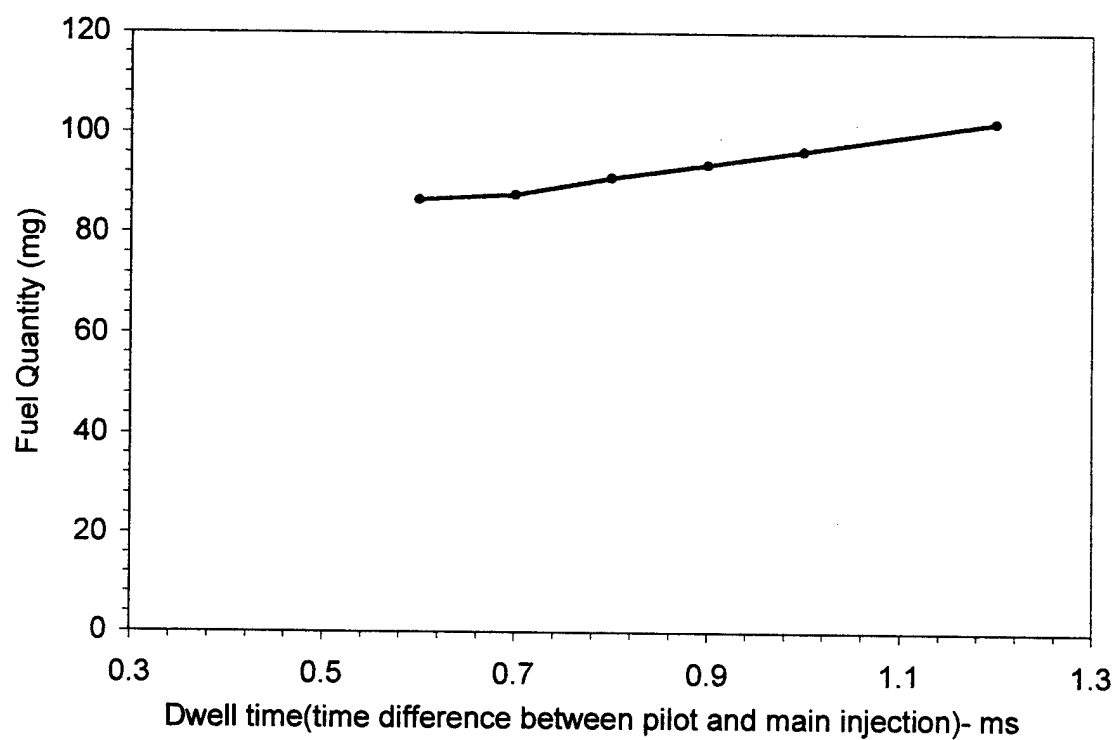
Figure 2-20 Effect of dwell time on injection quantity of the main injection, with 380-bar common rail pressure, 620 mini-sac nozzle, 0.8-ms pilot, and 2.25-ms main injection
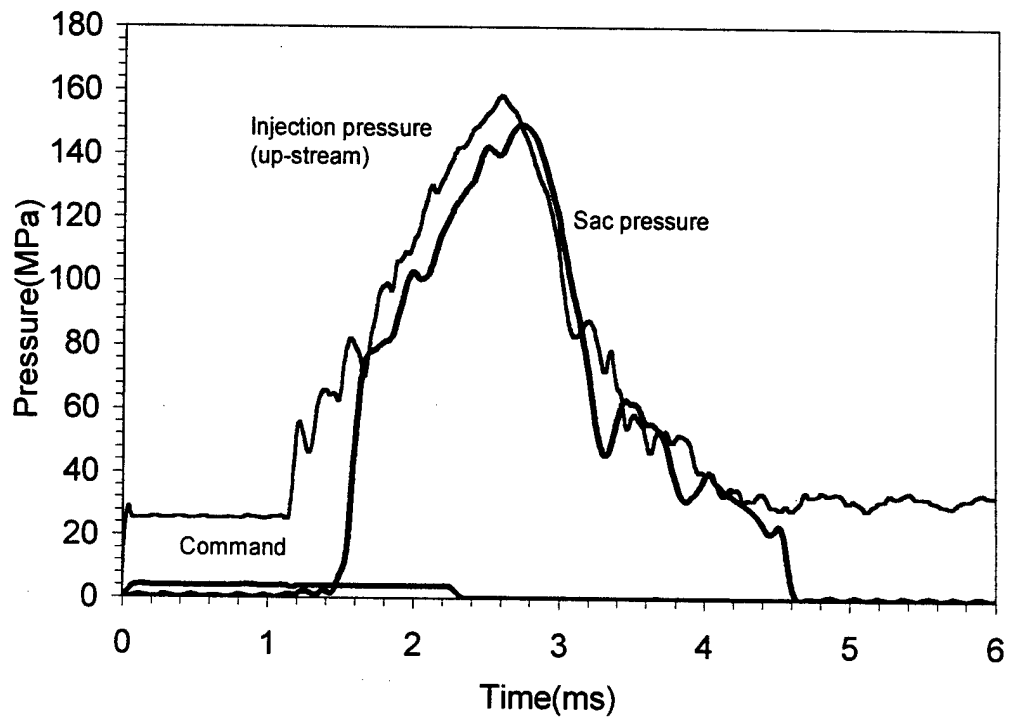
Figure 2-21 Comparison of upstream and sac pressure, with 380-bar common rail pressure and 2.25-ms injection duration
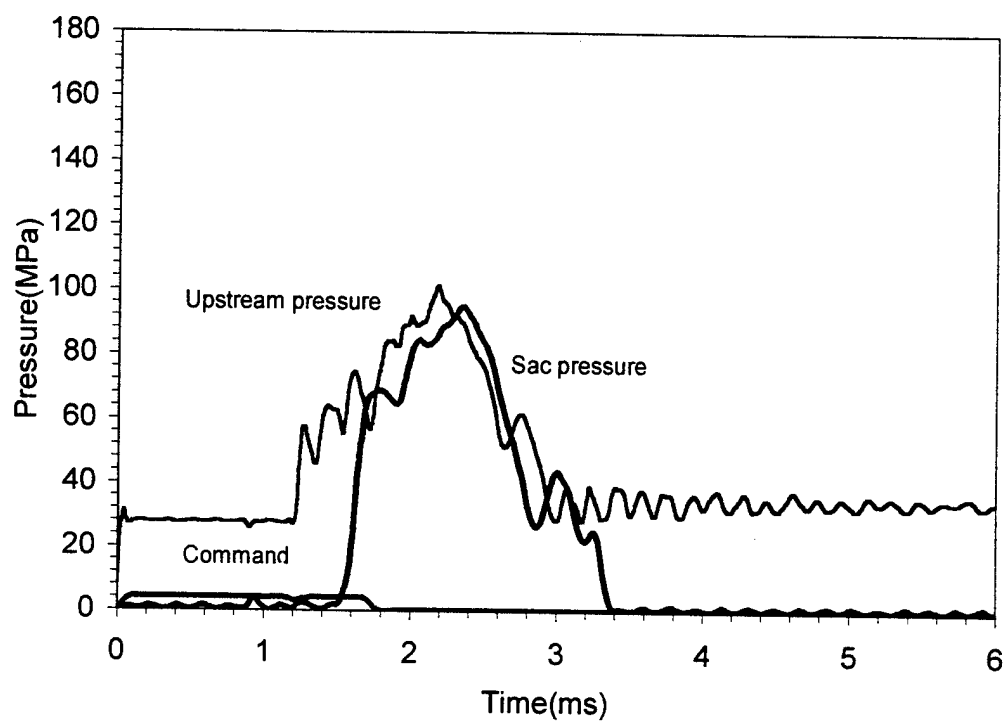
Figure 2-22 Comparison of upstream and sac pressure, with 276-bar common rail pressure and 1.70-ms injection duration
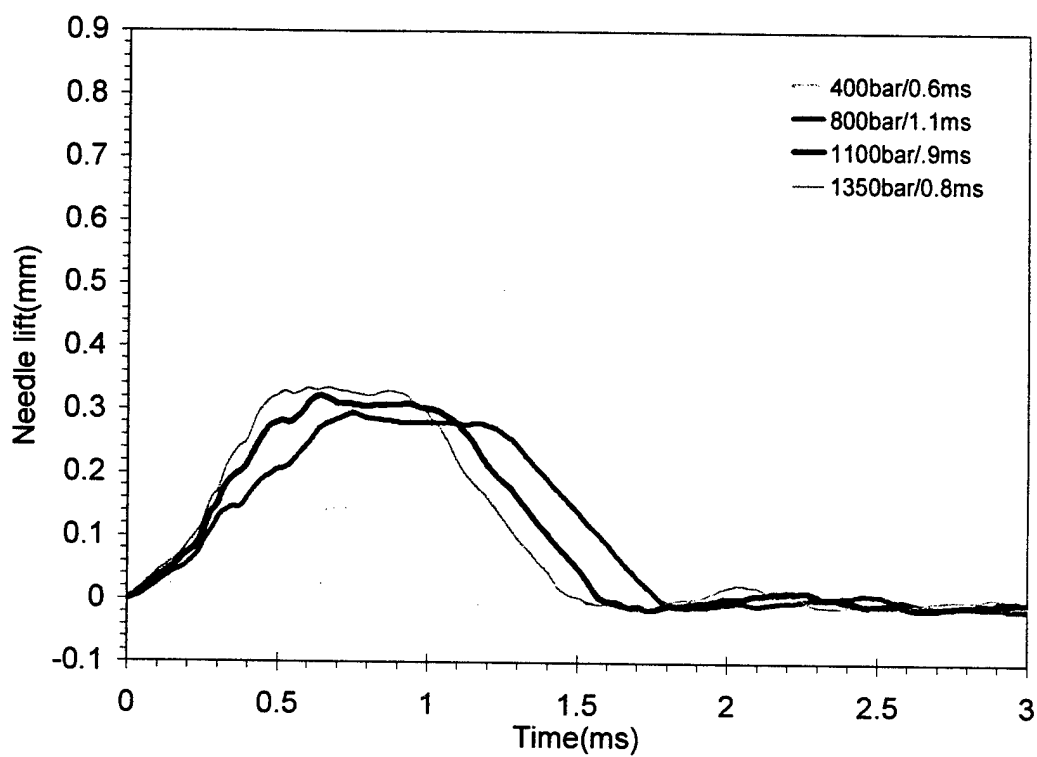
Figure 2-23 Effect of rail pressure on needle lift of the CR system, with 0.33-mm maximum needle lift, and 390 VCO nozzle (6 holes, 0.162-mm hole diameter, single-guide, and 6.173 L/D ratio)
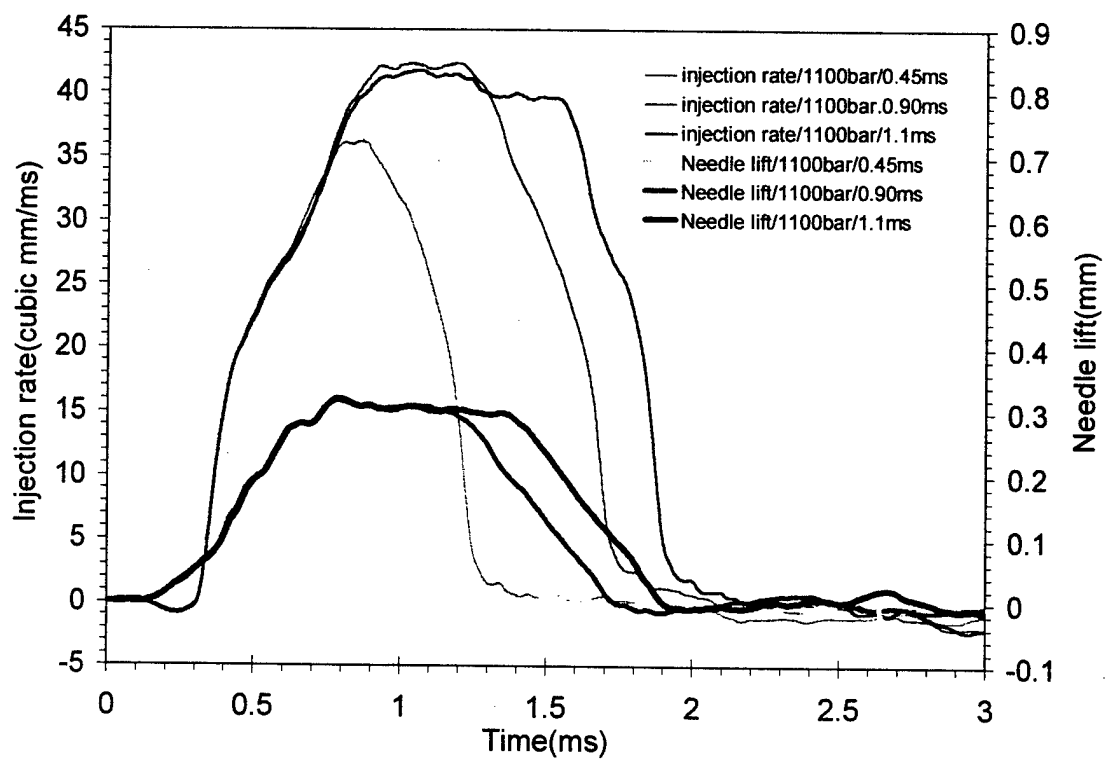
Figure 2-24 Injection rate and needle lift of the CR system under conditions of different injection duration with rail pressure of 1100 bar and 390 VCO nozzle
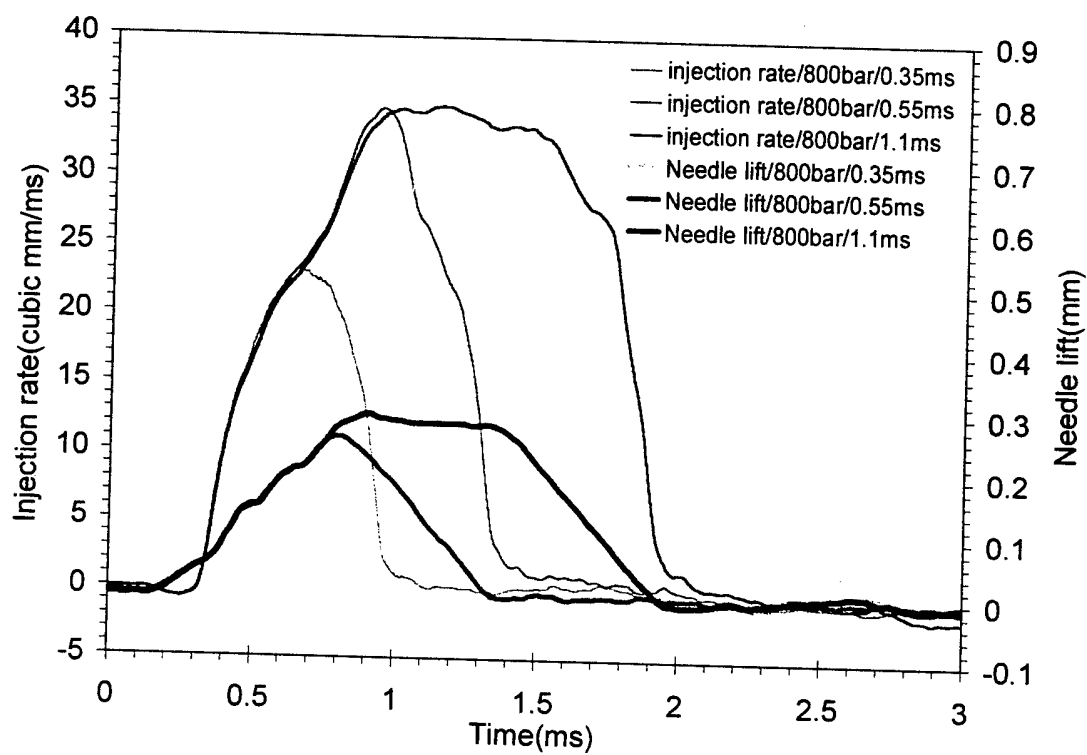
Figure 2-25 Injection rate and needle lift of CR system under conditions of different injection duration, with rail pressure of 800 bar and 390 VCO nozzle
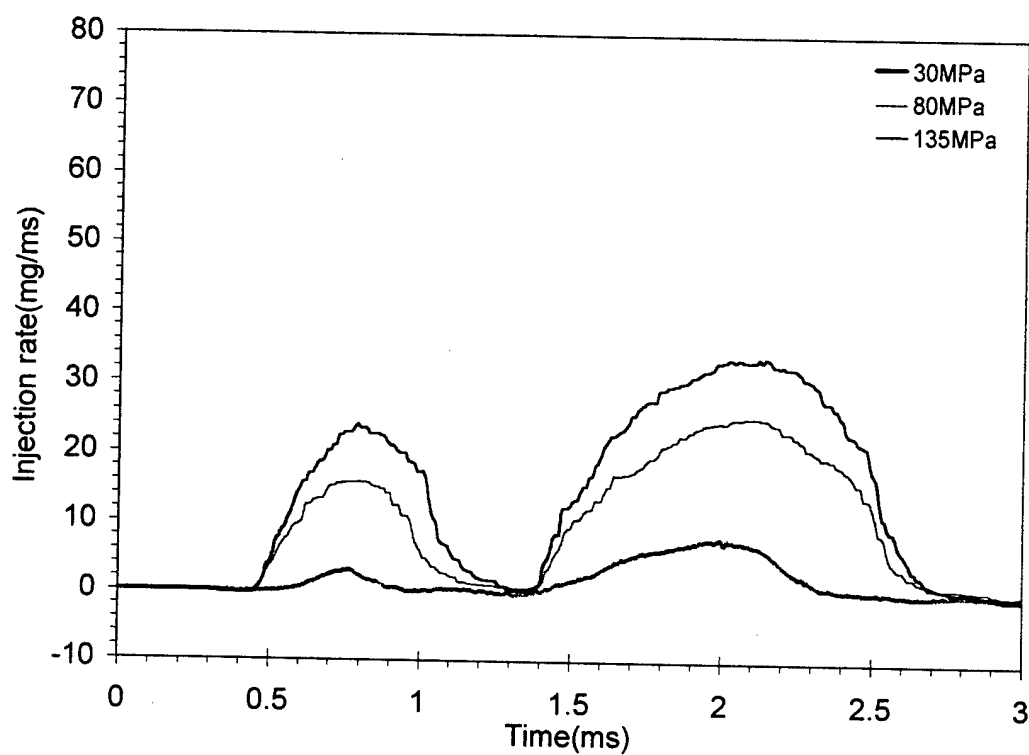
Figure 2-26 Injection rate of pilot and main injections, with various rail pressures and injection event: 0.35-ms pilot, 0.8-ms main, and 0.45-ms dwell time
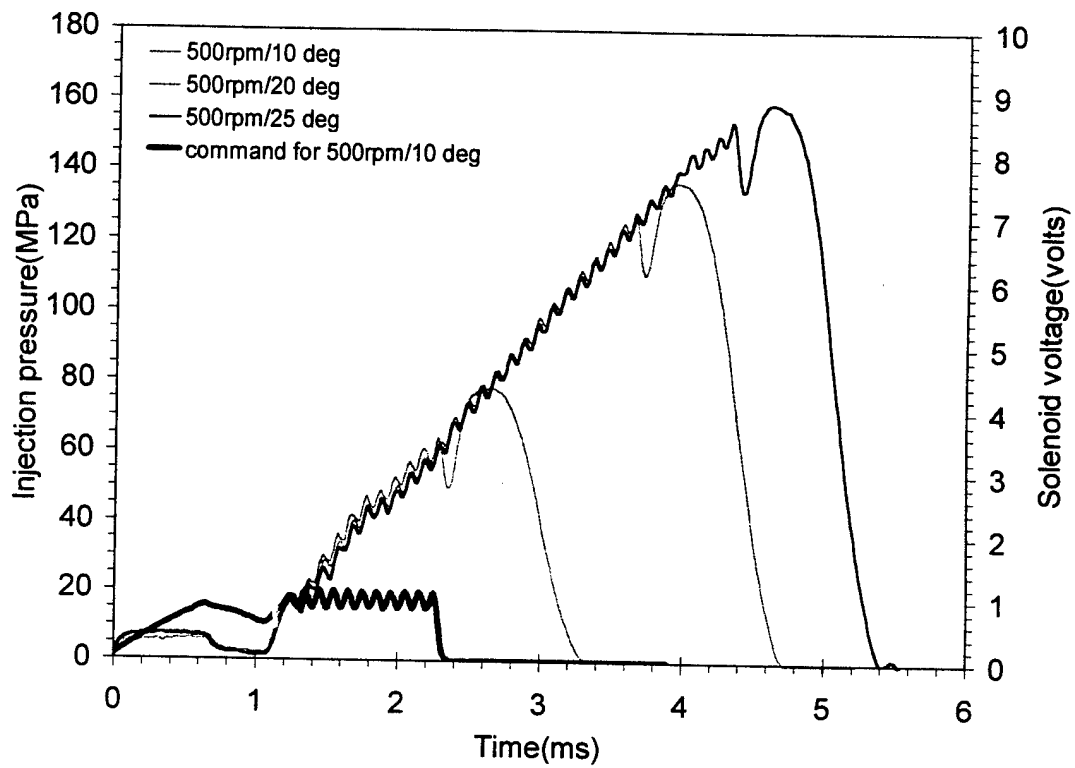
Figure 2-26 Injection pressure of EUI system, with various injection duration and 500-rpm camshaft speed
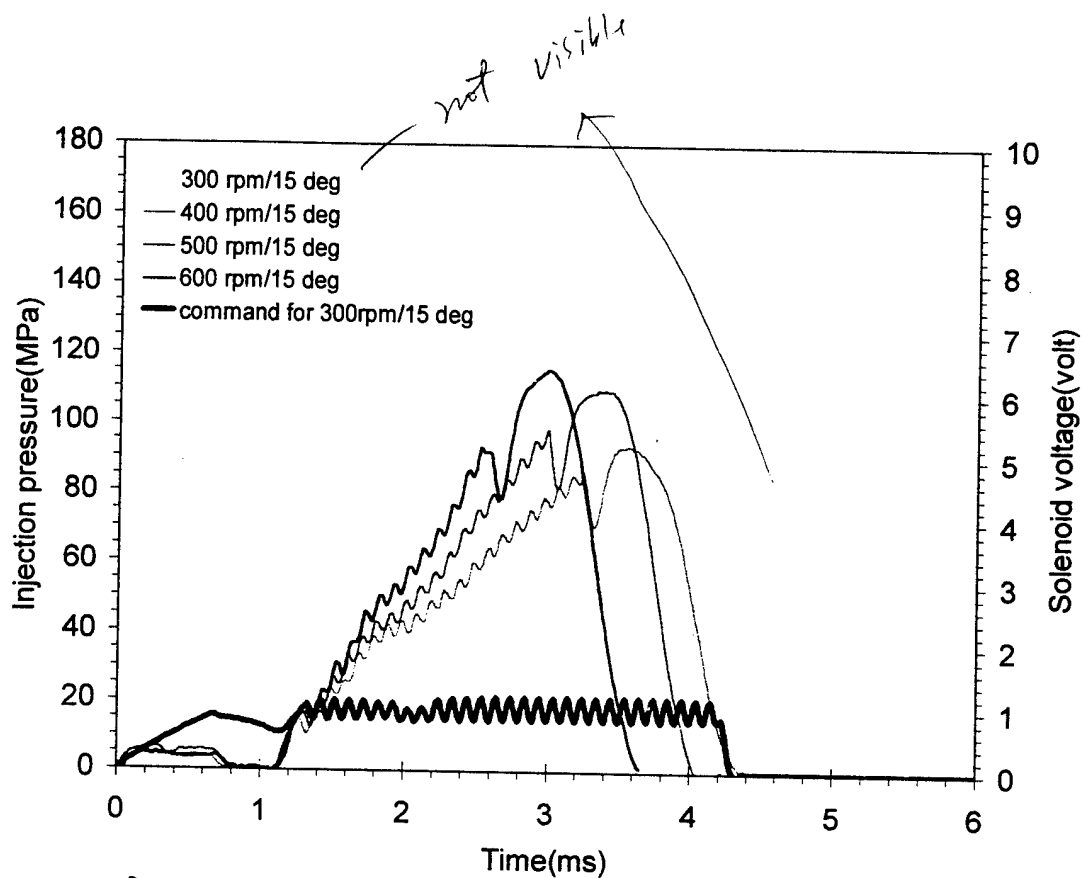
Figure 2-27 Injection pressure of EUI system, with various camshaft speeds and 15-degree injection duration

CHAPTER 3

SPRAY CHARACTERIZATION

3.1. Introduction

Spray characterization for the EUI, HEUI, and CR injection systems by macroscopic visualization method is the scope of work of this chapter. In the macroscopic visualization, the spray visualization is carried out by injecting fuel into a room-temperature nitrogen-filled pressurized chamber .The chamber pressure is adjusted to simulate the air density at the end of compression stroke of Compression Ignition engine. In a real engine operating condition, fuel is injected to combustion chamber at the timing closed to end of a compression stroke. Hence, it is reasonable to assume that the fuel sprays issued into the pressurized chamber encounters similar drag force as it did in a real engine. Since the chamber is filled up with room temperature nitrogen gas, the fuel sprays will mostly be in the form of liquid droplets and can be treated as non-evaporative sprays. By high-speed photography technique, the time-evolved structure and characteristics of non-evaporative fuel sprays could be recorded and analyzed. The characterization items carried out in this study include penetration, overall structure, and hole-to-hole variation. This method could be used to measure the performance of nozzle tip, injection unit, or injection system in terms of their capability of distributing fuel as far as temporal and spatial concerns. Although under same ambient density condition both the penetration and dispersion of a evaporative spray could be much less than those of a non-evaporative one, the characteristics obtained

from a non-evaporative test condition still provides good indication of the performance of a fuel injection.

The stability and asymmetry of the fuel sprays from high-pressure nozzles, especially the VCO type nozzle, has significant influence on the combustion and emission performance of diesel engines, mainly resulting from the decreased air utilization efficiency for the greater degrees of asymmetry. The variation in spray penetration and spray cone angle from hole to hole must be quantified both before and after the injector tip is utilized on the engine if emissions and combustion variations are to be understood and correlated.

The non-evaporative spray visualization is an intermediate step prior to the characterization of spray and its combustion in an Optically Accessible Engine (OAE). The experimental setup is convenient for optical access, the level of difficulty is lower , and the test conditions are more controllable as compared to the test situation of an OAE.

3.2. Experimental Method

The experimental setup includes copper-vapor laser system (Oxford CU15), a 35-mm still camera or high-speed drum camera, pressurized chamber and its peripheral, and Labview data acquisition and control system. The copper-vapor laser is expanded into a thin light sheet using cylindrical lens and functions as an optical shutter with 12.5kHz pulsing frequency and with exposure time as short as 10 ns. The drum camera is operating at 250

revolutions per second with 1/15-second shutter speed. A Labview Data Acquisition and Control System controls the fuel injection pressure, timing and quantity. At the same time, the Labview system also executes data acquisition and system synchronization among the laser, photography and fuel injection systems. The injection pressure is recorded along with injection and laser command signals, while the images are being taken by the photography system. The experimental setup is shown as Figure 3-1. The test conditions are arranged as Table 3-1.Two levels of chamber pressure, 17.2 and 27.6 bar, are used to evaluate the effect of ambient density condition on penetration and dispersion. For the study of CR sprays, both single- and dual-guided nozzle tips are tested to evaluate the effect of the design of needle guide on spray symmetry. Similarly, for the study of HEUI sprays, two types of nozzle with similar flow number, 620 mini-sac and 610VCO, are arranged in the test to analyze the effect of nozzle configuration on spray symmetry.

Calculated spray tip penetration based on the model proposed by Hiroyasu et al.(1980), as shown in equation(A1) and (A2) of Appendix A, is incorporated in the analysis to correlate with the measured data.

3.3. Results and Discussions

3.3.1. Spray Penetration and Correlation with Empirical Model

Both the ambient pressure and injection pressure affect penetration of the CR sprays. Figure 3-2 shows the effect of injection pressure and ambient condition on the tip penetration of the CR sprays. As shown in the figure, for

example, at the time of 0.4 ms after start of injection with 17.2 bar ambient pressure, the penetration increase from 17.5 to 32 mm corresponding to the increase of injection pressure from 30 to 135 MPa. Similarly, with fixed injection pressure of 80 MPa, at the time of 0.4 ms after start of injection the penetration decreases from 24.6 to 22 mm corresponding to the increase of ambient pressure from 17.2 to 27.6 bar. The result shows that both ambient and injection pressure have significant effect on spray tip penetration.

Table 3-1 Test conditions of the macroscopic spray visualization

Injection system	HEUI	Common Rail	EUI
Chamber Pressure(bar)	17.2 and 27.6	17.2 and 27.6	17.2 and 27.6
Injection pressure(bar)	1300	300, 800, and 1350	800
Injection duration(ms)	2.25 and 1.70	0.350 / 0.450 / 0.850	2.3
Nozzle tip/# of hole/hole diameter(mm)	620 mini-sac/7/0.190 and 610 VCO/6/0.218	390 VCO/6/0.162/single-guided and 430VCO/6/0.172/dual-guided	VCO/8/0.188

Figure 3-3 and Figure 3-4 also demonstrate how the tip penetration of HEUI and EUI sprays change with various ambient pressures. On average, increase of the ambient pressure from 17.2 to 27.6 bar reduces the penetration by 24 % for the HEUI sprays and by 10 % for the EUI sprays. Figure 3-5 shows the comparison of penetration between the HEUI and CR sprays under same ambient condition. Their penetrations are almost identical within 0.6 ms after SOI, which is due to both injections have similar injection velocity

Figure 3-6 to Figure 3-9 summarize the correlation between the measured and calculated penetration for the HEUI and CR sprays unaer various ambient conditions. For the CR sprays, the correlation is also reviewed under various injection pressures. The calculated penetration is based on empirical model proposed by Hiroyasu et al.(1983). Input data for the calculation include nozzle specifications, injection quantity, injection rate, density of ambient gas, and density of fuel. Value of 0.8 is used as the Coefficient of Spray Contraction for the calculation of average injection velocity, which is carried over from the study of Kuo (1987). To best fit with the measured data, 0.8 and 0.55 have been chosen as the values of Coefficient of Effective Injection Velocity for the calculation of penetration of CR and HEUI sprays., respectively. In general, the model correlate fairly well with the measured data. However, for the sprays of both injection systems, the model tends to over predict the early phase of the penetration and under predict that of the later phase. The calculated penetration of CR sprays with injection pressure of 30 MPa is far less than the measured data, which may indicate that the model does not apply to injection with low needle lift and low injection rate.

3.3.2. Hole-to-hole Spray Variation and Spray Structure

Figure 3-10 to Figure 3-16 show the penetration variation for the sprays of three injection systems under two ambient pressure settings. As summarized in Table 3-2, the variation of spray penetration depends on type

of injection system, nozzle configuration, and ambient pressure. Overall speaking, the EUI system equipped with VCO nozzle has the best performance in terms of penetration variation. The EUI system used in the test is for heavy-duty engine; it has a sturdy injector construction with a larger nozzle, which generally results into more symmetric spray. The CR system equipped with VCO nozzle has the largest penetration variation. As to the case of HEUI system, the variation of the Mini-sac nozzle is about 47% less than that of the VCO nozzle. The result also shows that increase of ambient pressure slightly reduces the magnitude of variation for all test cases.

Table 3-2 Comparison of hole-to-hole penetration variation of the injection systems

Injection System	Nozzle tip/ hole diameter	Ambient pressure(bar)	Variation of penetration (mm)
EUI	VCO/0.188mm	17.2	1.3
		27.6	1.0
HE'JI	Mini-sac/0.190mm	17.2	2.2
		27.6	1.8
HEUI	VCO/0.210mm	17.2	3.8
		27.6	3.7
CR	VCO/0.162mm	17.2	6.2
		27.6	5.4

Due to the large penetration variation of the CR sprays, special attention has been drawn to evaluate the correlation of penetration among the slowest, fastest, and average sprays. As the spray images of test cases with injection pressure of 80 and 135 MPa, as shown in Figure 3-19, the spray of 5-o'clock direction is the slowest one, while the spray of 10-o'clock direction is the fastest one. With 80-MPa injection pressure, the time lag between the

slowest and the average sprays is 0.08 ms that is equivalent to 2 crank-angle at 4200 rpm. The time lag could induce significant combustion variation among sprays. To study the penetration behavior of the fastest and slowest sprays, 0.08-ms time shift is applied to the penetration of the slowest spray to establish a comparison chart, as show in Figure 3-17. After the time shift, for both ambient pressure of 17.2 and 27.6 bar, the slowest spray shows same penetration pattern as that of the average, however the fastest spray shows 5 to 10 mm more penetration as compared to that of the average.

Figure 3-18 shows the comparison of spray structures of the mini-sac and VCO nozzle of the HEUI system. The mini-sac nozzle demonstrates more uniform spray penetration and structure compared to those of the VCO nozzle. Significant hole-to-hole variation in penetration and cone angle of the sprays of the VCO nozzle is observed, especially in the early stage of spray development. The fastest spray of the VCO nozzle appears in the 11 o'clock direction, while the slowest one is right on the opposite side in the 5 o'clock direction. In addition, puffy structure along the edges of the sprays is also observed for the 1-, 3-, 5-, and 7-o'clock sprays. Similar asymmetry and puffy structure are also observed on the sprays of the VCO nozzle of the CR system. As shown in Figure 3-19, with 30-MPa injection pressure, the 2- and 5-o'clock sprays do not appear for the whole injection period. Based on the data shown in Fig 2-25, with 30-MPa injection pressure, the needle just barely opens with little needle lift and injection rate; under this circumstance 4 holes are open, however the other two holes, 2- and 5-o'clock holes, remain covered

by the needle. This is an evidence of needle eccentricity. As injection pressure increases to 80 MPa, the injection rate and needle lift increase accordingly. The 5-o'clock hole starts to issue injection after a 0.16-ms lag time. Like what is observed on the sprays of VCO nozzle of the HEUI system, in the case of CR sprays, the fastest spray is also locating on the opposite side of the slowest spray. Therefore, it would be reasonable to conclude that the needle-to-seat eccentricity is most sever upon the 5 o'clock nozzle hole, which consequently reduces the flow area of the corresponding hole at the early stage of spray development. Puffy structure is observed on the 2-, 6-, 8- and 12-o'clock sprays. The puffy structure at the early development of these sprays may be categorized as hollow cone spray with characteristics of wide angle as the type of the spray Soteriou et al.(1995) identified in their study . As shown in Figure 3-19, these early-developed sprays with puffy structure are surpassed and penetrated by the later coming solid cone sprays after 0.24 to 0.32 ms from start of injection.

Figure 3-20 shows the comparison of spray structures of single-and dual-guide VCO nozzle of the CR system. Apparently, the dual-guide design does not improve the spray asymmetry. The fastest spray of the dual-guide nozzle is in 8-o'clock direction. Similar spray structure and asymmetry is observed. Figure 3-21 shows the effect of ambient pressure on spray structure. With higher ambient pressure, the penetration is reduced and the spray angle is wider.

3.4. Concluding Remarks

Specific findings obtained from the macroscopic visualization are summarized as follows.

- Both injection pressure and ambient pressure affect the spray tip penetration significantly. The penetration increases corresponding to increase of injection pressure or decrease of ambient pressure.

- The spray tip penetration model correlate fairly well with the measured data of HEUI and CR sprays under various injection and ambient pressures, except for the CR sprays with injection pressure of 30 MPa. Meanwhile, for the sprays of both injection systems, the model tends to over predict the early phase of the penetration and under predict that of the later phase.

- The variation of spray penetration depends on type of injection system, nozzle configuration, and ambient pressure. The large variation observed on the CR sprays could be caused by eccentricity of the VCO nozzle and exaggerated by the low needle lift under low injection pressure operating condition. From the visualization results of the HEUI sprays, the variation of mini-sac nozzle is 50% less than that of the VCO nozzle.

HEUI System

Pressurized Chamber

High Speed Drum Camera

Computer/ LabVIEW/ DAQ

Cr Vapor Laser
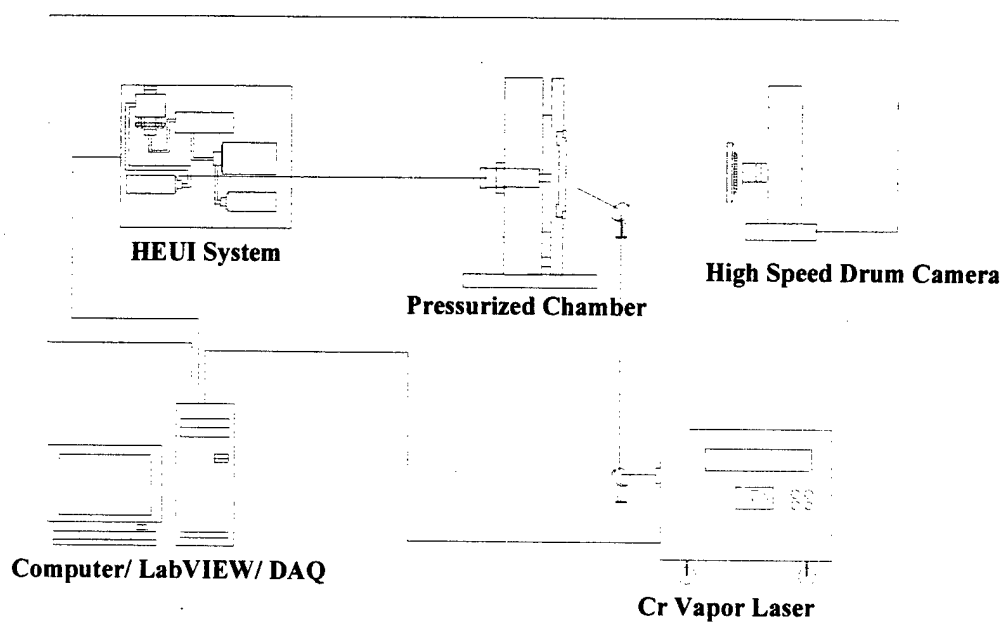
Figure 3-1 Schematic of the experimental setup of non-evaporative spray visualization
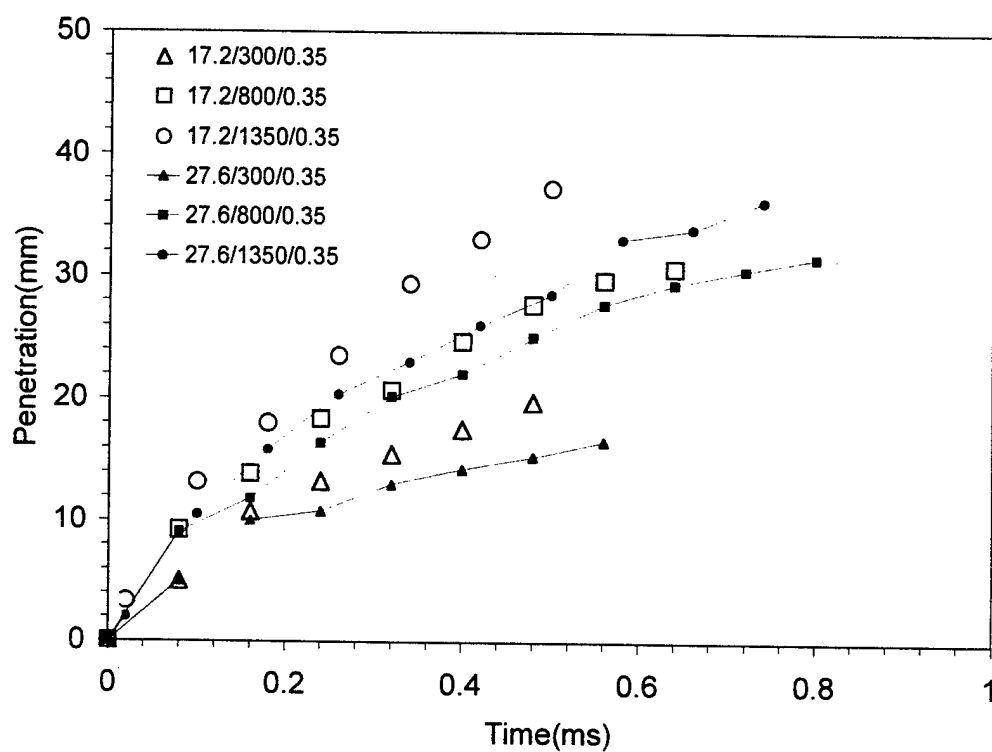
Figure 3-2 Effect of injection pressure and ambient pressure on the spray penetration of the CR system, with duration of 0.35 ms, ambient pressures of 17.2 and 27.6 bar, and injection pressures of 300, 800, and 1350 bar
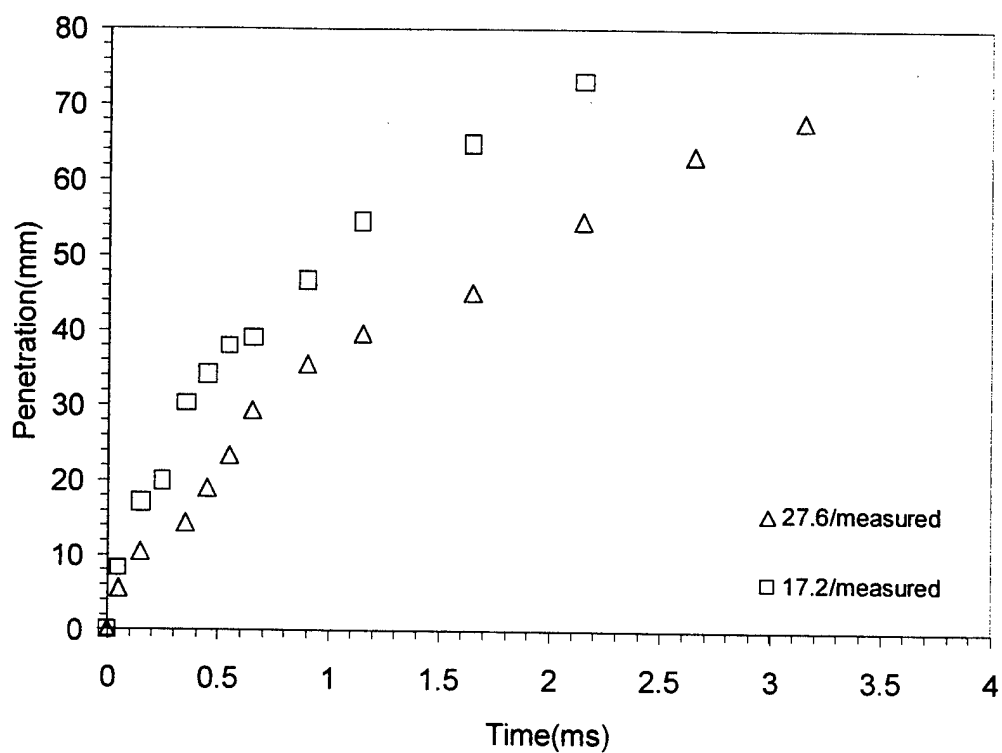
Figure 3-3 Spray penetration of the HEUI system, with 620 mini-sac
nozzle, duration of 2.85 ms, injection pressure of 77 MPa,
and ambient pressure of 17.2 and 27.6 bar
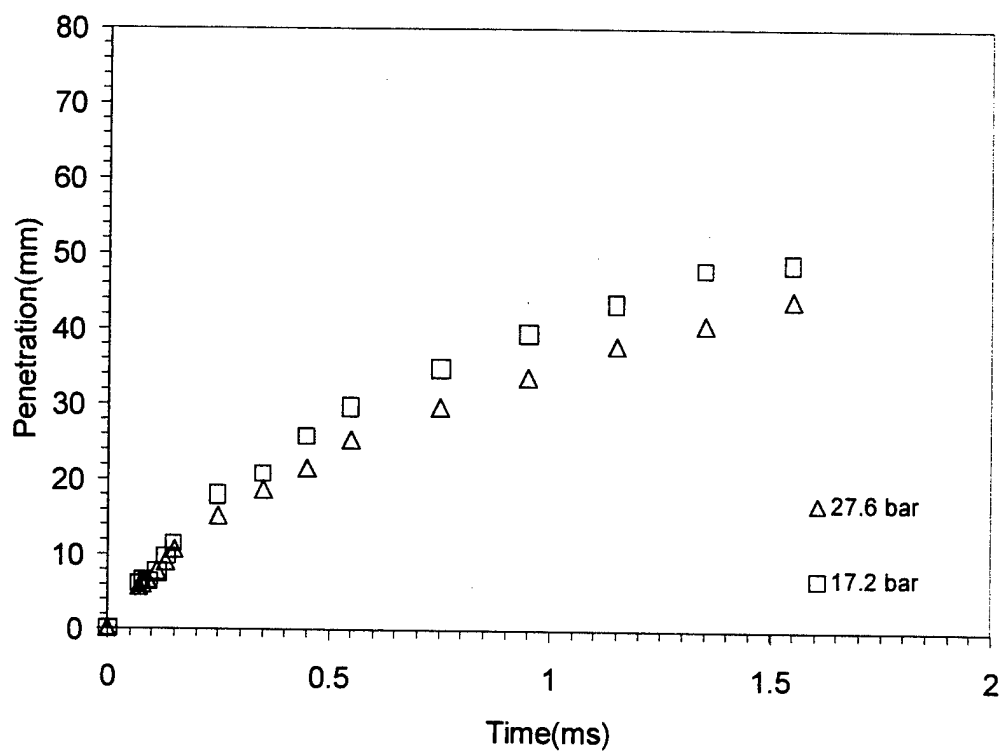
Figure 3-4 Spray penetration of the EUI system, with 480-rpm camshaft speed, injection duration of 15-degree crank-angle, VCO nozzle (with 0.188-mm hole diameter), and ambient pressures of 17.2 and 27.6 bar.
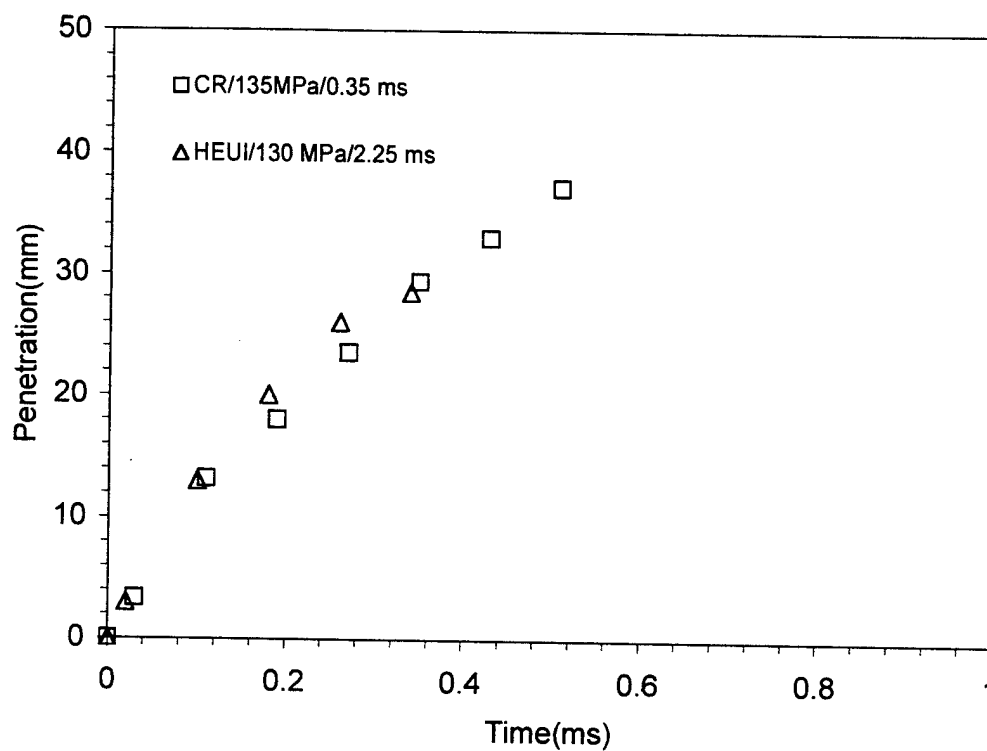
Figure 3-5 Comparison of the spray penetration of the HEUI and CR systems, with ambient pressure of 17.2 bar; HEUI system (pressure of 130 MPa, 620 mini-sac nozzle, duration of 2.25 ms); CR system(pressure of 135 MPa, 390 VCO nozzle, and duration of 0.35 ms)
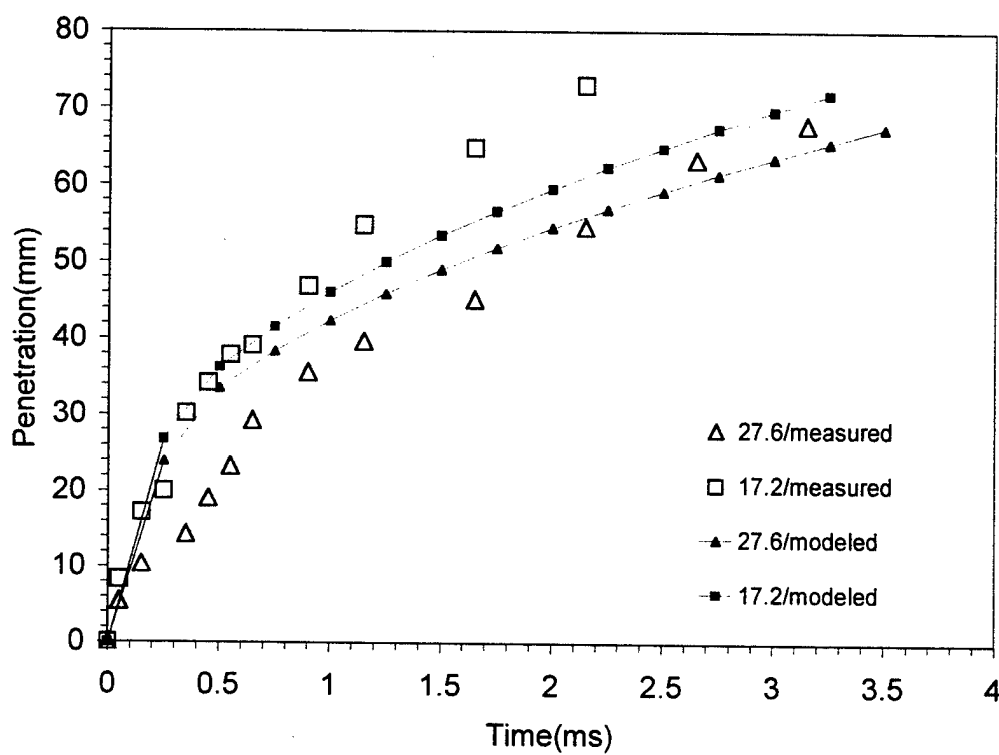
Figure 3-6 Correlation between measured and modeled penetration of the HEUI system, with pressure of 77 MPa, duration of 2.25 ms, 620 mini-sac nozzle, and ambient pressures of 17.2 and 27.6 bar.
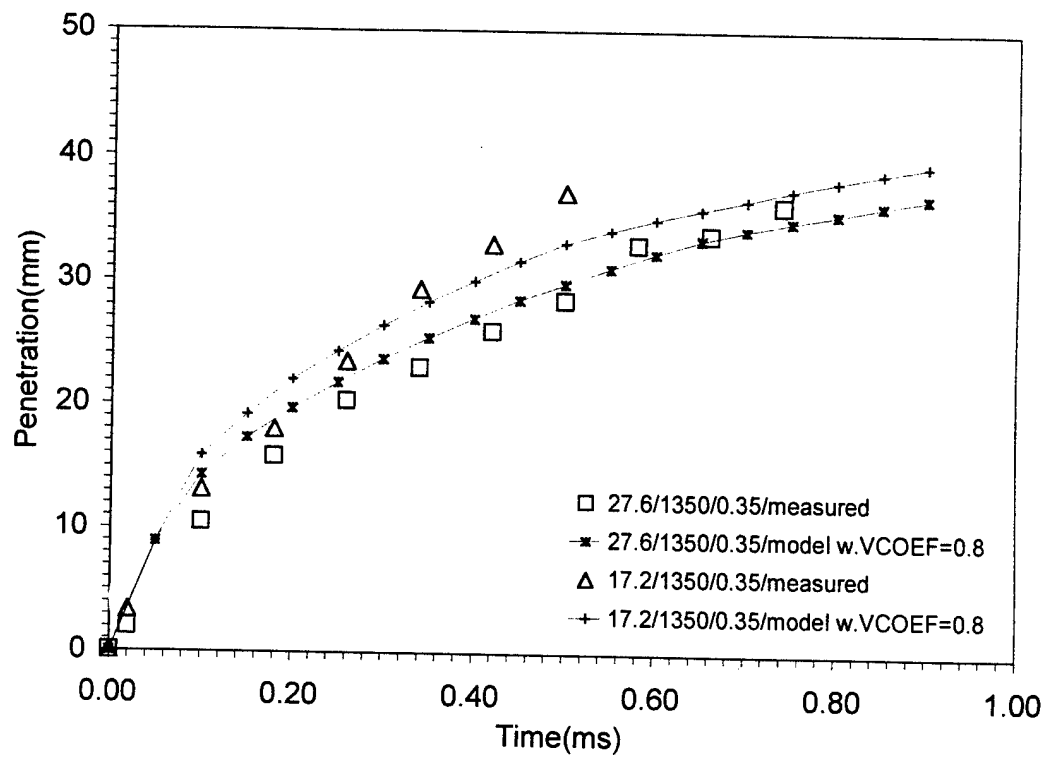
Figure 3-7 Correlation between the measured and modeled penetration of the CR system, with pressure of 135 MPa, duration 0f 0.35 ms, 390 VCO nozzle, and ambient pressures of 17.2 and 27.6 bar.
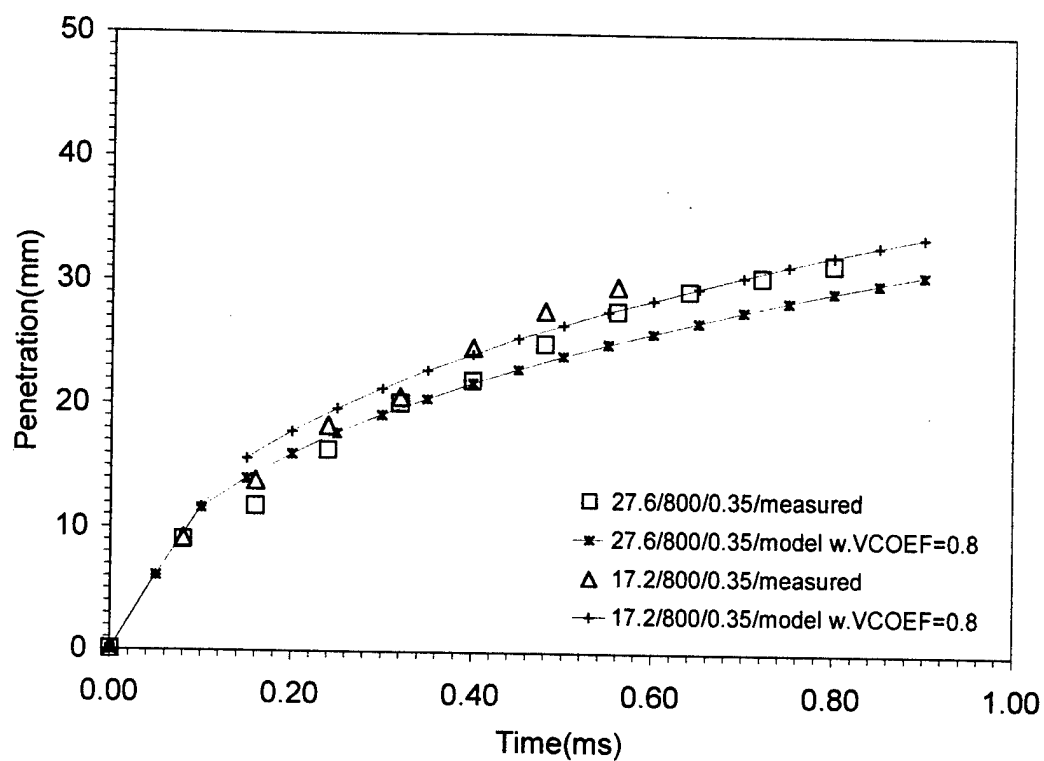
Figure 3-8 Correlation of measured and modeled penetration of the CR system, with pressure of 80 MPa, duration of 0.35 ms, 390 VCO nozzle, and ambient pressures of 17.2 and 27.6 bar.
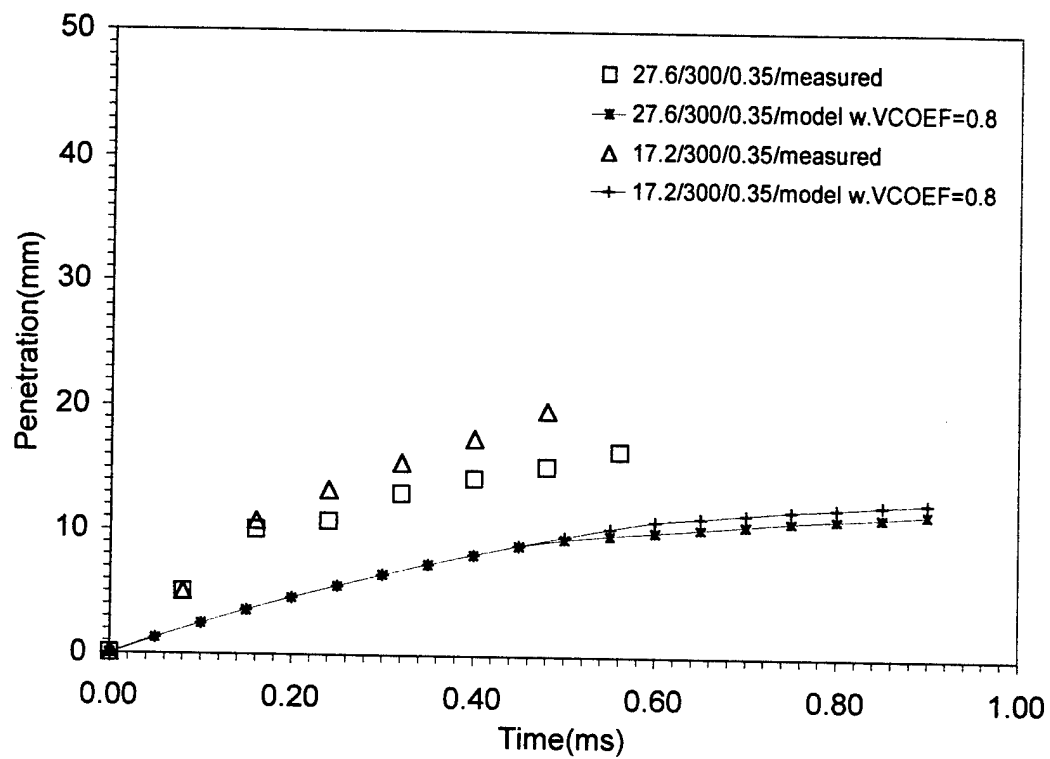
Figure 3-9 Correlation of measured and modeled penetration of the CR system, with pressure of 30 MPa, duration of 0.35 ms, 390 VCO nozzle, and ambient pressures of 17.2 and 27.6 bar.
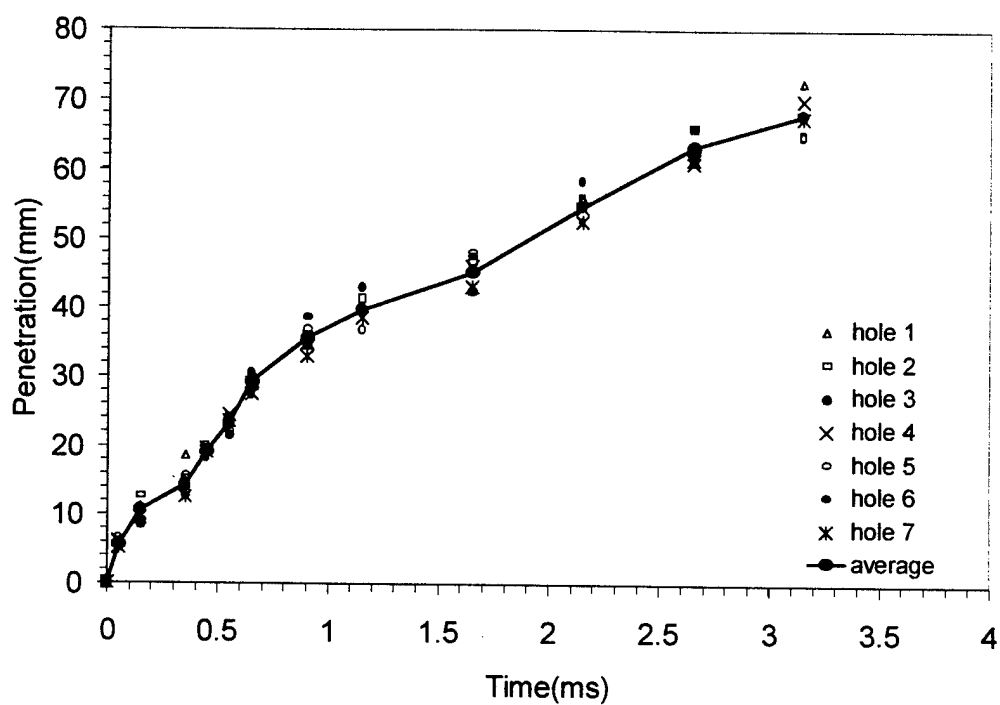
Figure 3-10 Hole-to-hole penetration variation of the HEUI sprays, with 620 mini-sac nozzle, pressure of 77 MPa, duration of 2.85 ms, and ambient pressure of 27.6 bar.
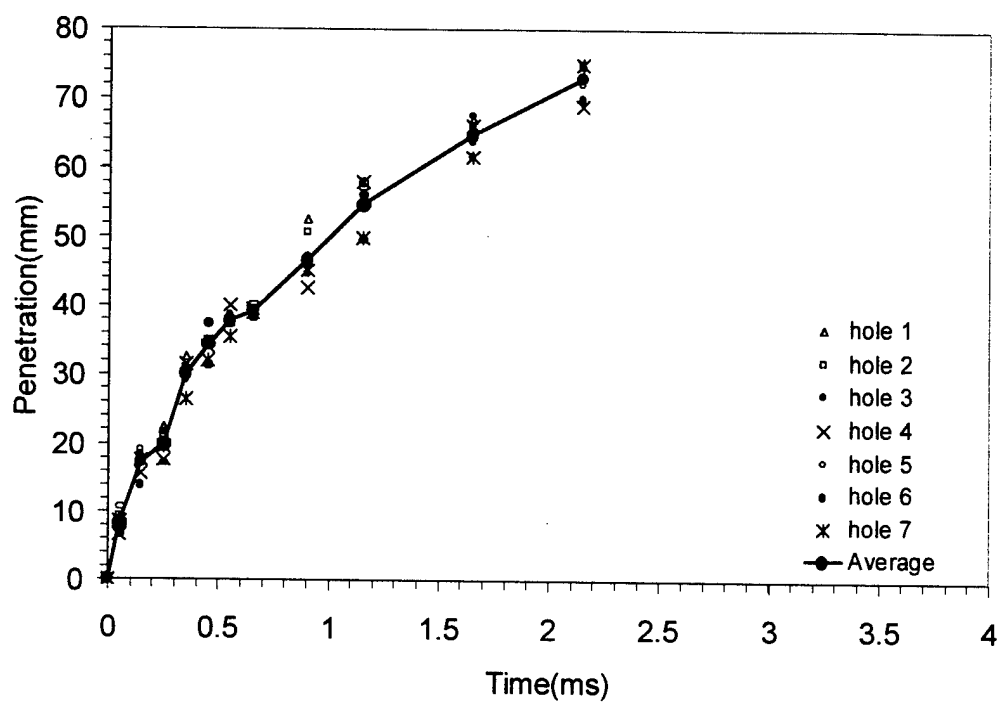
Figure 3-11 Hole-to-hole penetration variation of the HEUI sprays, with 620 mini-sac nozzle, pressure of 77 MPa, duration of 2.85 ms, and ambient pressure of 17.2 bar.
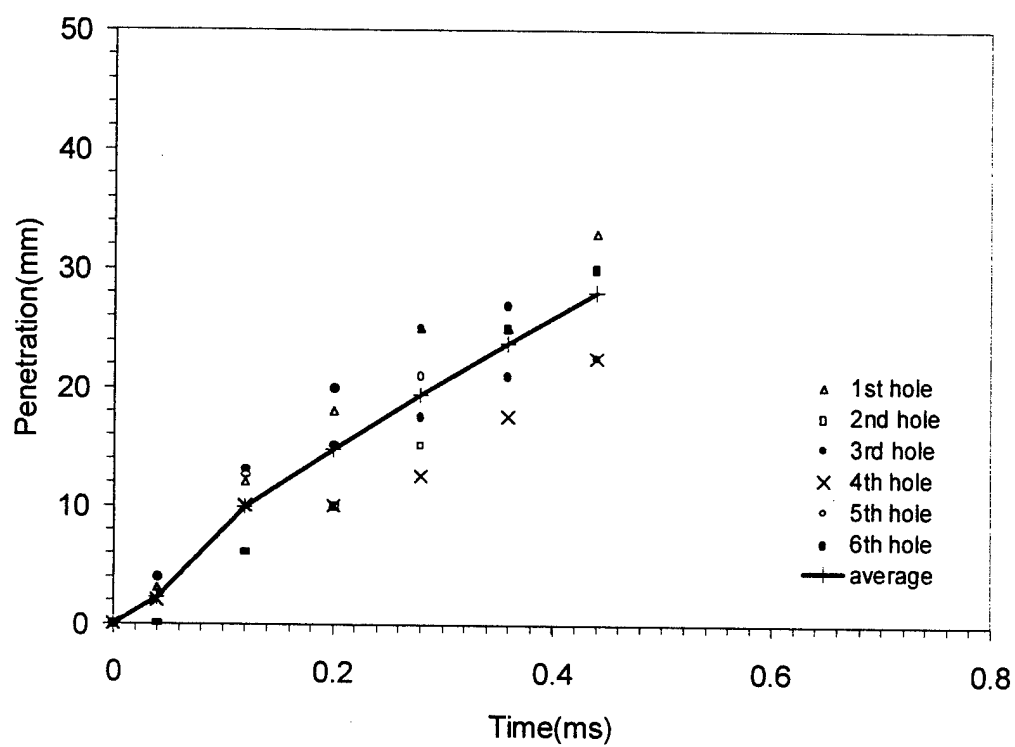
Figure 3-12 Hole-to-hole penetration variation of the HEUI sprays, with 610 VCO nozzle, pressure of 126 MPa, duration of 2.25 ms, and ambient pressure of 27.6 bar.
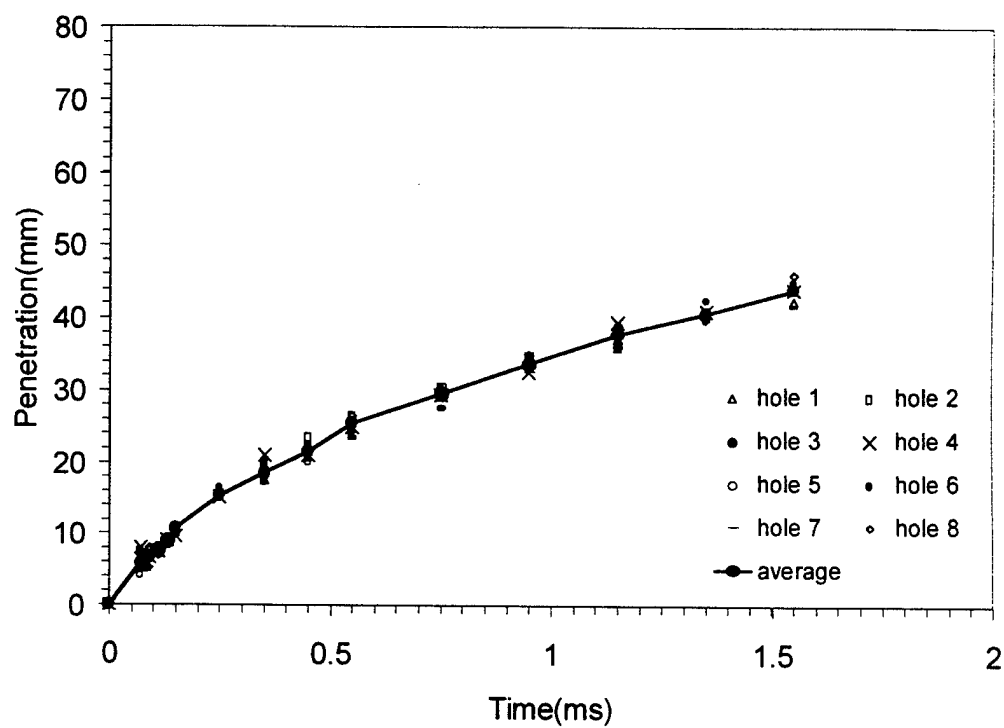
Figure 3-13 Hole-to-hole penetration variation of the EUI sprays, with 0.188-mm VCO nozzle, pressure of 80 MPa, duration of 2.3 ms, and ambient pressure of 27.6 bar
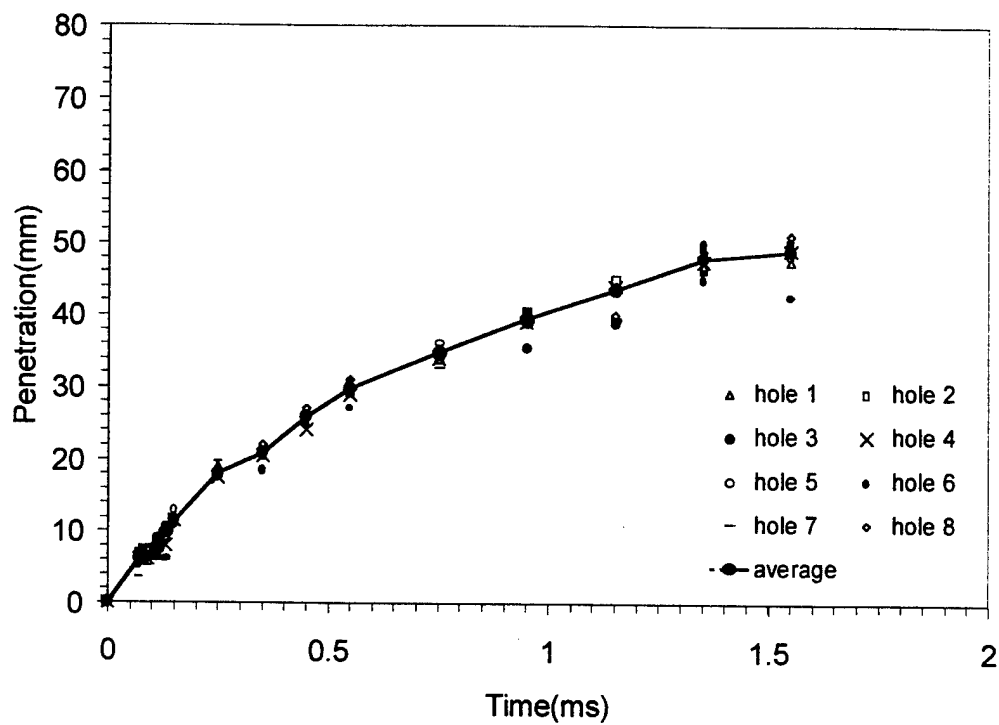
Figure 3-14 Hole-to-hole penetration variation of the EUI sprays, with 0.188-mm VCO nozzle, pressure of 80 MPa, duration of 2.3 ms, and ambient pressure of 17.2 bar.
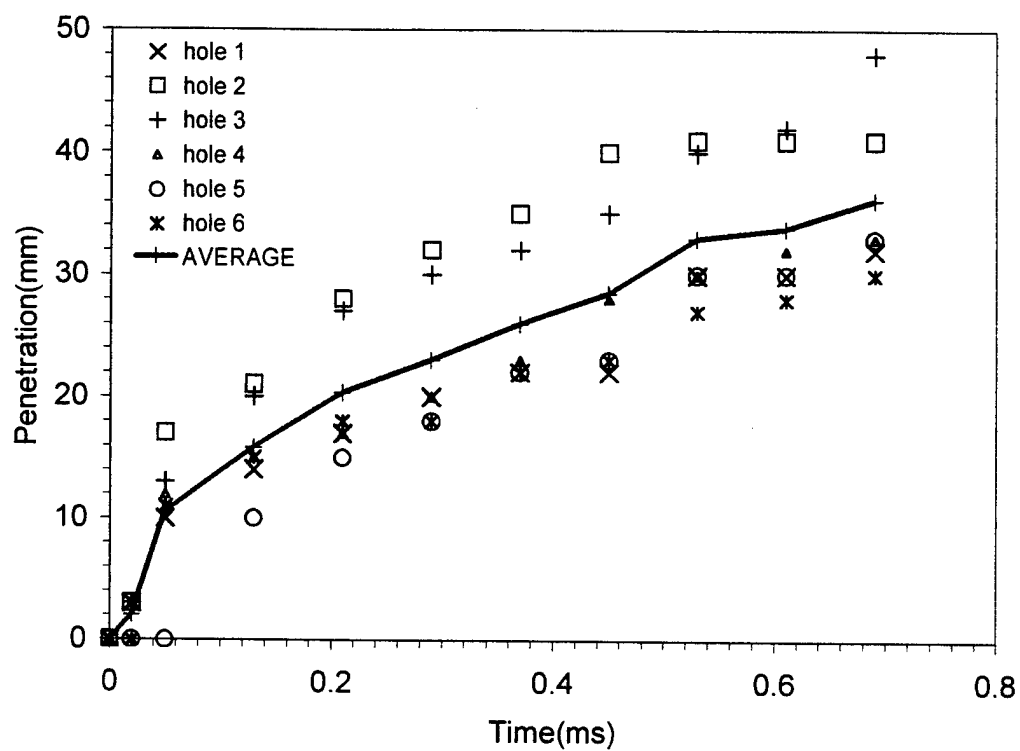
Figure 3-15 Hole-to-hole penetration variation of the CR sprays, with single-guide 390 VCO nozzle, pressure of 135 MPa, duration of 0.3 ms, and ambient pressure of 27.6 bar.
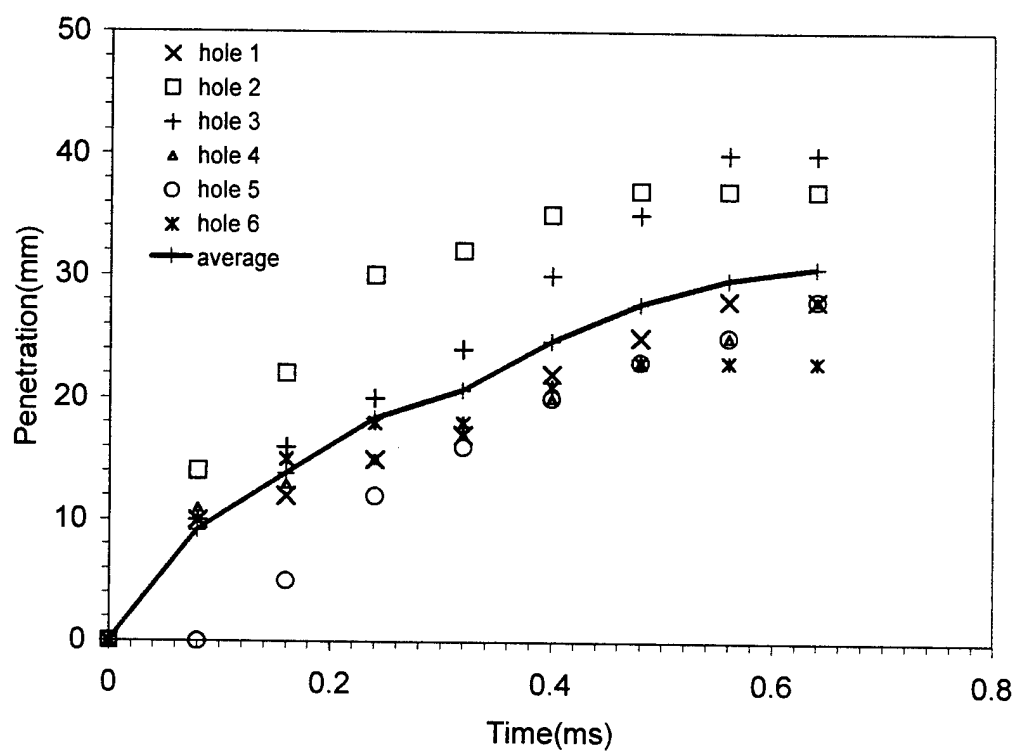
Figure 3-16 Hole-to-hole penetration variation of the CR sprays, with single-guide 390 VCO nozzle, pressure of 80 MPa, duration of 0.3 ms, and ambient pressure of 17.2 bar.
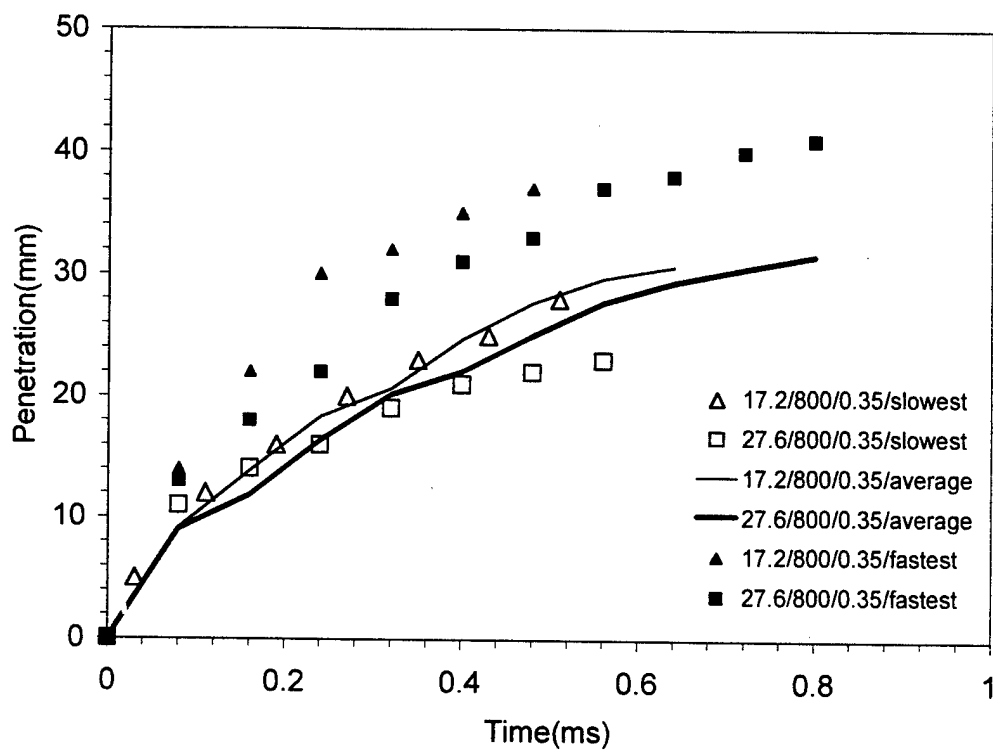
Figure 3-17 Comparison of penetration of the fastest, slowest, and average sprays under ambient pressures of 17.2 and 27.6 bar, with injection pressure of 80 MPa, and duration of 0.35 ms.
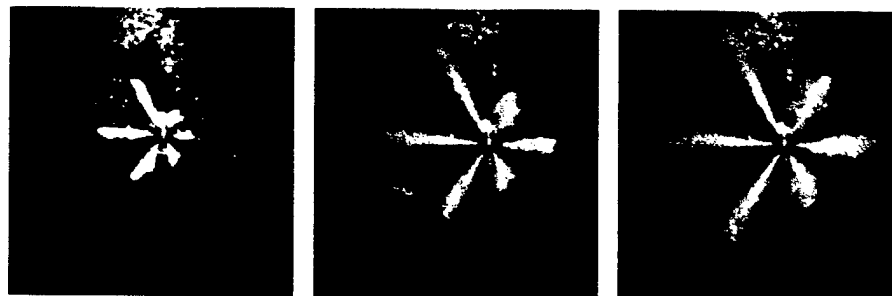
27.6 bar ambient pressure/ 1260 bar injection pressure/2.25ms duration. Images represent 0.08,0.16,and 0.24 ms after SOI. 610VCO with 0.218 mm hole diameter, L/D=3.67; actual picture size 4.5x4.5 cm.
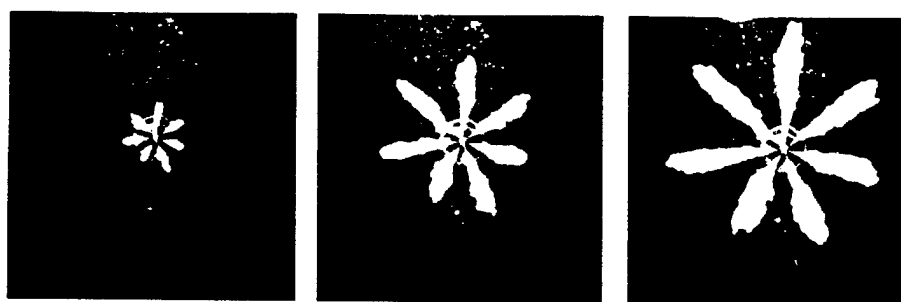
27.6 bar ambient pressure/ 1300 bar injection pressure/2.25ms duration. Images represent 0.08,0.16,and 0.24 ms after SOI. 620 mini-sac with 0.190 mm hole diameter, L/D=3.158; actual picture size 4.5x4.5 cm.

Figure 3-18 Comparison of spray structures of the VCO and mini-sac nozzles of the HEUI system; upper row images for VCO; lower row images for mini-sac; from left to right in sequence taken at 0.08, 0.16, and 0.24 ms after SOI
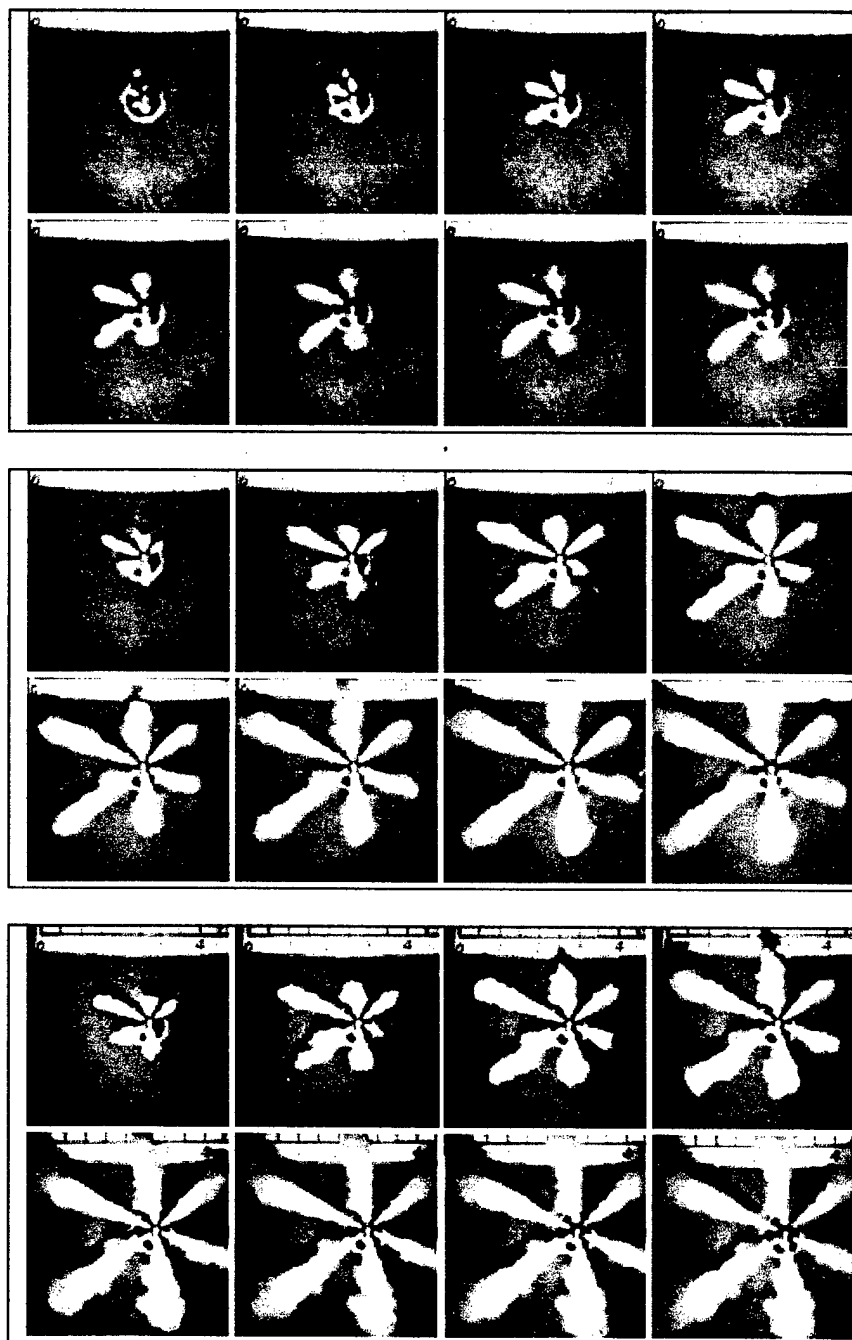
Figure 3-19 Sequences of development of the CR sprays, with single-guide 390 VCO nozzle, duration of 0.3 ms, and ambient pressure of 27.6 bar; upper rows for pressure of 30 MPa; center rows for pressure of 80 MPa; bottom rows for pressure of 135 MPa; 0.08-ms time interval between each frame
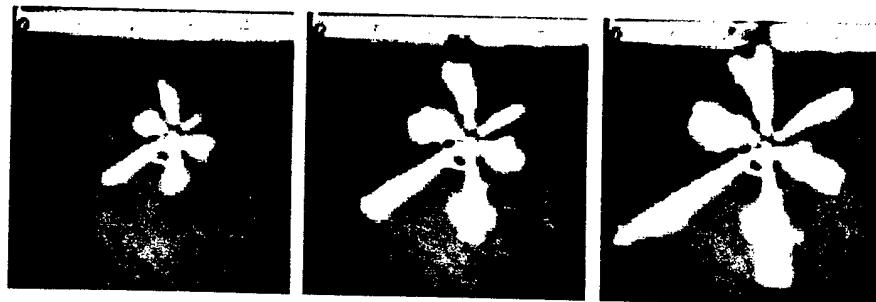
17.2 bar ambient pressure with 1350 bar injection pressure/0.35 ms duration. Images represent 0.08, 0.16,and 0.24 ms after SOI. Dual-guide /0.172mm hole diameter, L/D=5.81. Actual picture size: 5x5 cm.
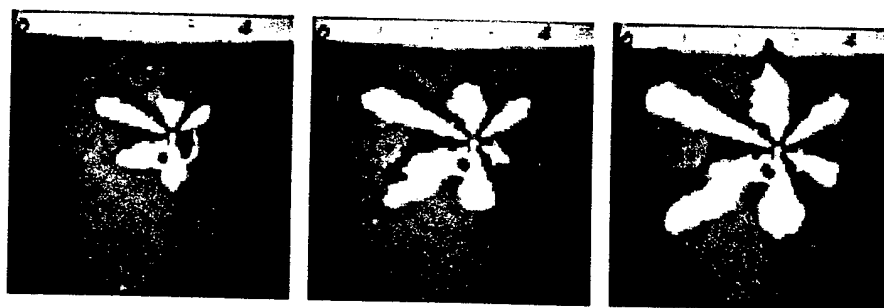
27.6 bar ambient pressure with 1350 bar injection pressure/0.35 ms duration. Images represent 0.08, 0.16, and 0.24 ms after SOI. Single· guide /0.162 mm hole diameter, L/D=6.17. Actual picture size: 5x5 cm.

Figure 3-20 Comparison of spray structures between single- and dual-guide nozzle of the CR system

| 17.2bar ambient pressure, with 1350bar injection pressure, 0.28ms after SOI; actual picture size: 5x5 cm. | 27.6 bar ambient pressure with 1350 bar injection pressure, 0.28ms after SOI; actual picture size: 5x5 cm. |
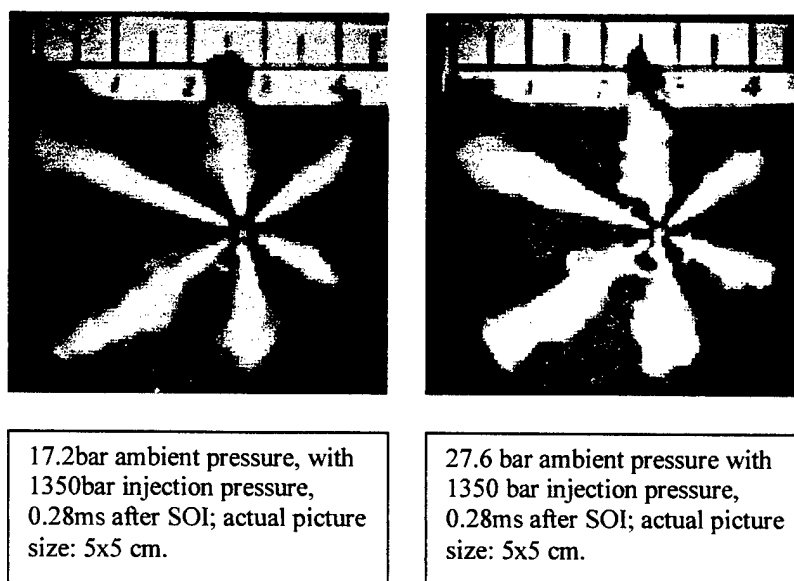
Figure 3-21 Effect of ambient pressure on spray penetration and cone angle.

CHAPTER 4

MICROSCOPIC SPRAY VISUALIZATION

4.1. Introduction

Recent implementation of laser diagnostics has been shown to provide insight into the diesel spray and combustion processes (e.g., Dec, 1997, Lai et al., 1995). The motivation of this research is to visualize the spray structure of advanced diesel injection systems very close to the nozzle exit in an attempt to correlate the microscopic spray structure to the injection system performance and nozzle design. In the microscopic observation, the spray visualization is carried out by injecting fuel into atmosphere ambient condition or a room-temperature nitrogen-filled pressurized chamber. Three types of modern High-pressure electronic-controlled fuel injection systems, EUI, HEUI, and CR, associated with two types of nozzle configuration, VCO and mini-sac, are incorporated in the study. Although some research has been carried out to characterize the near exit spray behavior, most previous work is limited to use single-hole nozzle which could not produce similar turbulence flow that could simulate those of multi-hole nozzles, or limited to scale-up models which could not exactly match the force-ratios and time scales in practical diesel sprays. As far as photograph technique concerns, most previous work is limited to single-image-per-injection photography technique, either using CCD or traditional still camera. To improve the situations, In this study, standard multi-hole nozzles are used to avoid misleading result; meanwhile both still camera and high-speed drum camera associated with long distance

microscope are applied to obtain more insight of near exit spray dynamics. The characterization items include initial spray break-up, spray at end of injection, spray at peak-pressure injection, and near-nozzle-exit spray cone angle.

4.2. Experimental Method

The optical system setup includes a long-distance microscope, copper-vapor laser (Oxford CU15), and still or high-speed drum camera. To obtain better image resolution, still camera photography with 35x24-mm photographic film, long-distance microscope, and single-shot laser as the light source is the method for the visualization of initial spray break-up, end of injection, and peak-pressure injection. To obtain more insight of spray dynamics, high-speed drum camera photography with 10x24-mm photographic film, long-distance microscope, and 25kHz pulsed copper laser as optical shutter is the method for near nozzle exit spray characterization.

The copper laser is expanded into a thin sheet with thickness less than 0.09mm using cylindrical lens. It is used as the optical shutter, one shot or 25-kHz shots, with the exposure time as short as 10 ns. The drum camera is operating at 250 revolution-per-second with 0.16 second shutter speed. The long-distance microscope, similar to the ones used by other researchers (Sjoberg et al., 1996; Fath et al, 1997), is used to magnify the diesel spray structure very close to the nozzle exit. With its lens 8.75 inches away from the observed object, the amplification factor is about 17.4. The diffraction-limit

resolution can be as small as 1-2 micron. The optical setup provides great resolution in both time and space, as shown in Figure 4-1.

The injectors examined include valve-covered-orifice (VCO) nozzles, from the CR, HEUI, and EUI systems, and a mini-sac nozzle from the HEUI system. The CR injection system tested is designed for high-speed small-bore diesel engine; it has a smaller injector body (17mm) and single-guide needle. The HEUI and EUI injection systems tested are for heavy-duty engine. Diesel fuel No.2 is used in this study. The test conditions of the microscopic visualization are summarized in Table 4-1.

Table 4-1 Test conditions of microscopic spray visualization.

Injection system	HEUI	Common Rail	EUI
Chamber Pressure (bar)	Atomsphere pressure	Atomsphere pressure / 17.2 and 27.6 bar	Atomsphere pressure
Injection pressure (bar)	640 to 1240	250,300, 800, and 1350	800 TO 2000
Injection duration (ms)	1.70 and 2.25	0.2 to 1.6	0.6 TO 1.4
Nozzle tip/flow number/ # of hole/hole diameter (mm)/ L/D ratio	Mini-sac/620/ 7/0.190/3.16 and VCO/610/6/0.210/3.67	VCO/390/6/0.162/6.17	VCO/n.a./8/0.188/n.a.

4.3. Initial Spray Breakup

In order to investigate the primary breakup mechanisms, single-shot microscopic visualization using 35-mm still camera is the method used to get higher resolution and to avoid the vibration effect which could be introduced by

the high-speed rotating drum camera. Figure 4-2 and Figure 4-3 show a collection of the microscopic photographs of EUI spray for initial spray development right after SOI, which are taken with a 35-mm still camera. The still-photography captures the overall spray boundary, and provides excellent contrast on black-and-white film. These close-ups are taken to catch the onset of spray formation, where the spray just exits the nozzle orifice. The photograph shows a very dynamic primary breakup processes very close to the injector. For the EUI injection system, the injection pressure and its rising rate are directly proportional to engine speed, as described in chapter 2. Figure 4-2 shows the primary breakup process of EUI spray with 750-rpm camshaft speed and 10- degree injection duration. At the earliest instant that the camera is able to capture the spray exiting the nozzle, the liquid column appears to have a translucent potential core wrapped around by a separating boundary layer that tends to mushroom and roll up, as shown on the 10-μs image of Fig 4-2. The asymmetry of the spray structure is obvious in the early spray development. Further into the spray development, at 40 μs after start of injection, the spray evolves to have a very large cone-angle; meanwhile, a cluster of fuel particles with sizes as large as 55 μm can be observed at the left bottom corner of the images. Fig 4-3 shows similar test case but with lower pressure rising rate resulting from reducing camshaft speed to 375 rpm. As the pressure rising rate reduced in a half, the early spray development process also slow down. The shape of the sprays in the early spray development is more irregular as compared to the case of 750 rpm. At this early spray

development, the spray penetration velocity is about 40 m/s, while the injection pressure is around or slightly higher than the needle opening pressure of 34.5 MPa.

Microscopic photographs of EUI spray at peak-pressure injection are shown in Figure 4-4 which are taken at the maximum injection pressure of 200MPa from four individual injections with 750-rpm camshaft speed and 25-degree injection duration. The spray shows a much smaller cone angle. The onset of spray breakup is immediately at the injector exit, indicating the presence of turbulent primary breakup (Dan and Lai, 1998). The bottom side of the spray shows some large droplet formation. The sizes of the droplet increase as the distance from the nozzle exit increases. Although some of which are not exactly focused, their diameters can be estimated to be 10-20% of that of the nozzle hole, corresponding to the turbulent integral scale within the nozzle. In comparison, the top side of the sprays does not show a symmetric and corresponding distribution of large droplets, but instead suggests the formation of a very fine mist, in spite of possible light attention across the spray. The nozzle internal flow direction is from top to bottom; therefore, the topside spray is directly downstream of the turn-around point, where nozzle internal flow passage dictates that fuel flow must negotiate a sharper inside turn into the VCO hole. The fine mist observed could be a direct confirmation of cavitation-enhanced breakup mechanism; however, more research is needed to verify these observations

For comparison, Figure 4-5 shows a collection of the close-ups of one of the spray from a HEUI mini-sac nozzle. At the onset of injection, the initially low-pressure fuel in the sac volume is squeezed out of the nozzle orifice like the shape of toothpaste. The initial liquid column has quite distinct and clear boundary, but it turns bubbly or milky, with a fussy boundary very quickly. Its surface also rolls up similar to that the eddy rollup processes observed in pure gas jet. Close examination of the fussy interface suggests formation of very fine droplets as a result of micro-explosion or busting of bubbles; however, some optical artifacts can not be completely ruled out. Comparing the mini-sac nozzle sprays with those of the VCO's show that sac-type nozzle has less turbulent primary breakup features, which is consistent with its internal flow characteristics.

At a compatible injection pressure as the opening pressure of the mini-sac nozzle case shown in Figure 4-5, Figure 4-6 shows two typical transient microscopic visualization of the CR injector with VCO nozzle at the rail pressure of 30 Mpa. A very fast transition from clear liquid column to milky spray is also observed, which, however, is not observed at higher-pressure cases. The penetration velocity of these early development sprays is ranging from 4 to 12 m/s.

4.4. Transient Spray Dynamics

4.4.1. Spray Cone Angle and Its Oscillation

High-speed microscopic visualization results of CR sprays are shown in Figure 4-7 to Figure 4-11 for various injection pressures. Figure 4-7 and Figure

4-8 are for the 12-o'clock spray in Fig.3-19 with pressure of 25 and 30 MPa respectively, which is the second slowest spray in terms of penetration. The copper vapor laser is operated at the frequency of 25kHz, *i.e.* each frame is 40 microsecond apart. The field of view extends from the nozzle exit to 1.2mm downstream. These injection events consist of a 0.2-ms or 0.3-ms pilot and a 1.0-ms main injection, with a 1.0-ms separation between the start of injection of the two events. Figure 4-7 shows that at the low injection of 25 MPa, the pilot barely made it out of the nozzle, resulting in an inconsistent and poorly atomized spray. As the injection pressure increases to 30 MPa, as shown in Figure 4-8, a proper pilot spray is observed, however both of the lower injection pressure cases shows poorer atomization and large-eddy structure inside and at the edge of the spray, as is evidenced by the less homogenous light intensity scattered. As the injection pressure go up to 80 and 135 MPa, as shown in Figure 4-9, Figure 4-10 and Figure 4-11, the pilot is much better atomized, but the 0.3-ms injection command results into an injection duration of more than 0.48 ms.

The visualization results in these microscopic visualization figures show rapid temporal variations of spray angle, which result into the puffy spray structure at the edge of the spray as observed in the macroscopic visualization in Figure 3-19. The results of the inclusive spray angles measured from all test cases of CR sprays are plotted in Figure 4-12 and Figure 4-13 for pilot and main injection respectively. Data of repeated tests with same injection pressure settings are included in the charts to evaluate injection-to injection

variability. Significant injection-to-injection variability is found for both pilot and main injections. As shown in Fig 4-12, for the case of pilot injection of 135 MPa, one test demonstrates large variation of spray angle, 70 degree at the early stage and 20 degree at the end of injection, but the other two tests with identical injection condition demonstrate fairly stable spray angles during the injection period of 0.52 ms. Similarly, for the main injections of 135 MPa, three tests demonstrate three types of spray angle oscillation pattern. To resolve the puzzle, the needle lift data of the CR system is introduced to enhance the analysis. As shown in Fig 2-22, due to the design and operating principle, the needle lift of CR injector is relatively slow as compared to those of HEUI or EUI injector. The time that required for the needle to fully open is also depending on injection pressure. The lower the pressure, the longer time it takes to reach full lift position. With the needle lift data applied to the analysis of the spray angle oscillation, the situation becomes clearer. Figure 4-14 shows spray angles of three tests with identical injection conditions. During the needle opening and closing period, there is no consistent spray cone angle as well as its variation, however, during the needle full open period, the spray angles stay fairly stable in the range of 30 to 50 degree. Similar result is found for the case of injection with 800 bar, as shown in Figure 4-15, during the needle full open period, the spray angle are stable and in the range of 20 to 40 degree. For both the case of main injection with low pressure, as shown in Figure 4-16, and the case of pilot injection with various pressures, the injection duration is not long enough for the needle to reach its full open position. As a

result, the needle is only partly open and could be operating at unstable situation at which the positioning of the needle in horizontal direction is not repeated for each needle opening. Hence, this inconsistency of spray angle oscillation could be attributed to uncertainty of needle positioning in horizontal direction that establishes inconsistent internal flow pattern of nozzle.

The ambient pressure does not dampen the spray cone angle oscillation; on the contrary, it seems to amplify it. This is shown in the Figure 4-17 for three ambient pressure cases with fixed injection pressure of 80MPa. The effect of ambient pressure on near spray angle is unidentifiable.

The variation of spray angle is not limited to one hole only. Figure 4-9 to Figure 4-11 are the results of microscopic visualization of the fastest penetrating spray (the 10-O'clock spray in Figure 3-19), which also show the similar behavior of spray cone-angle oscillation.

These spray cone-angle oscillation phenomena are also observed on the EUI and HEUI sprays. For the HEUI sprays, as shown in Figure 4-18, wider spray angle is observed at the early development of the injections, within 0.2 ms from start of injection, for injection pressures of 64, 80, and 124 MPa. As refered to data of Fig 2-9, with 12-inch rate-shaping pipe, the time for needle full open is about 0.2 ms, which is in line with period of time in which wider spray cone angle is observed. Hence, it can be concluded that the wider spray cone angle at early development of the spray is induced by needle opening. The result can also be verified with Fig 4-19, which shows that under the condition of same pressure rising rate, even with different injection

duration's and types of nozzle, all three cases show wider spray cone angle at the early development of the sprays that is about 0.2-ms period after SOI. Similarly, for the case of EUI spray, wider spray cone angle is observed at the early development as well as prior to the end of injection; as shown in Figure 4-20 and Figure 4-21, the sprays start with 80-degree cone angle. Within 0.2 ms after start of injection, their cone angle decrease to about 20 degree and stabilize at the same angle through the mid-injection period until the end of injections at which the cone angles kick up to about 30 degree. Fig 4-22 shows the microscopic visualization result of EUI sprays with two injection conditions. As a conclusion of the analysis on the spray cone angle oscillation of EUI and HEUI injection, it is suggested that the opening and closing of needle induce the wide spray cone angle. , In the mid-injection period, both EUI and HEUI sprays are devoid of the significant oscillation as observed in the CR injector case, which may be attributed to their quick needle opening and settling at the full open position.

4.4.2. Spray Characteristics at End of Injection

In the microscopic visualization, spray trickles down and forms larger drops or liquid ligament is observed at end of injections. Figure 4-23 shows the end of injections of EUI sprays for four injection conditions. All images in the figure show that at the end of injection, the spray trickles down and forms larger drops. Fig 4-24 shows the captured images by still camera with better resolution, which are taken just prior to end of injection of two individual EUI

injections with 750-rpm camshaft speed and 10-degree duration. Both Figure 4-23 and Figure 4-24 show that large drops are formed at the edges of spray as well as and in the spray. The size of the larger drops could be as large as 100 μm ; these large drops are moving with slow speed that could be as low as 12 m/s.

Figure 4-25 shows the end of injection of CR injections with pressure of 30, 80, and 135 MPa respectively. Significant liquid ligament sustaining for long period of time, about 0.32 ms, is observed in the case of low pressure injection. Large size drops moving with low velocity, about 6 m/s, are also observed. As the pressure increase to 80 and 135 MPa, the situation is improved. Both of the number and sizes of drops and the hanging-around period of liquid ligament are reduced as the injection pressure increases.

Figure 4-26 and Figure 4-27 compare the end of injections of the mini-sac and VCO nozzles of the HEUI system. The mini-sac nozzle tends to produce larger ligaments and drops at end of injection (and consequently higher HC emission in engine tests); the VCO nozzle shows some improvement. For both injection conditions, pressure of 70 and 98 MPa, secondary injection due to needle bouncing are observed. As a result, the period of injection with poor atomization is extended. As shown in Figure 4-27, the width of the ligament formed at end of injection of a mini-sac nozzle is about 110 μm that is 60% of the size of the nozzle hole. On average, the moving velocity of the drops formed at end of injection of HEUI injection is about 3 to 4 m/s.

4.5. Concluding Remarks

The microscopic visualization results provide very interesting and dynamic information on spray structure, showing spray angle variation, injection-to-injection variation, and primary breakup processes not observed using conventional macroscopic visualization techniques. The near-field spray behavior is shown to be highly transient, strongly depend on the injector design, nozzle geometry, needle lift and vibration, and injection pressure which is a function of the injection system. Specific conclusions are as follows:

The spray cone-angle observed for the injector of the EUI system is larger at the early transient stage of needle lift. For the high-pressure common rail system tested, the spray cone angle shows conspicuous oscillation during pilot or main injection period, possibly due to needle eccentricity and oscillation.

At the mid-injection period where injection is quasi-steady, spray breakup is shown commence at the nozzle exit, exhibiting behavior due to turbulent primary breakup. Therefore, future spray modeling should consider the effects of transient three-dimensional turbulent flow and cavitation on the spray breakup processes.

Direction of fuel flow

1.38 mm

Nozzle tip surface

Amplification factor: 17.4
Film size: 35x 24 mm
VCO nozzle
Width of hole exit=0.223mm
Nozzle hole diameter=0.188mm

Laser sheet with thickness less than 0.09 mm
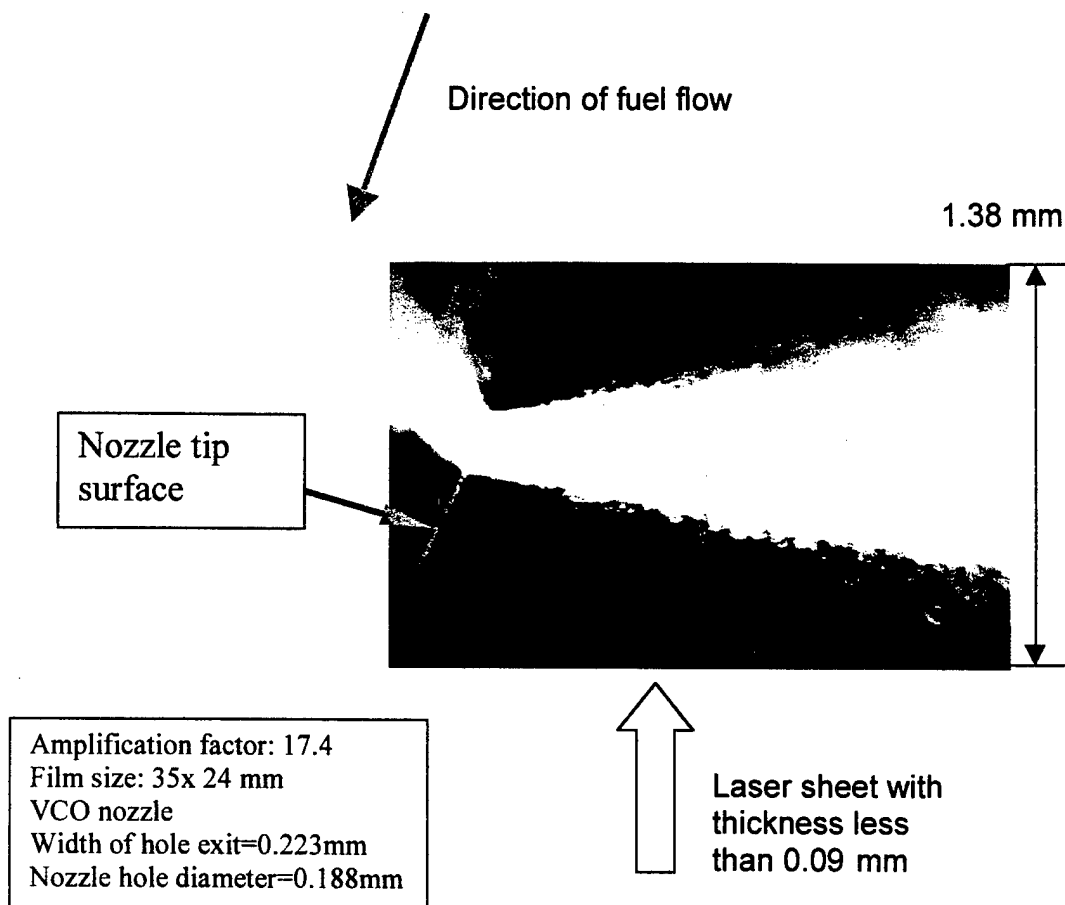
Figure 4-1 Schematic of microscopic visualization of VCO nozzle of the EUI system

SOI
(Start of
Injection)

10 μs
after
SOI

20 μs
after
SOI

30 μs
after
SOI

40 μs
after
SOI
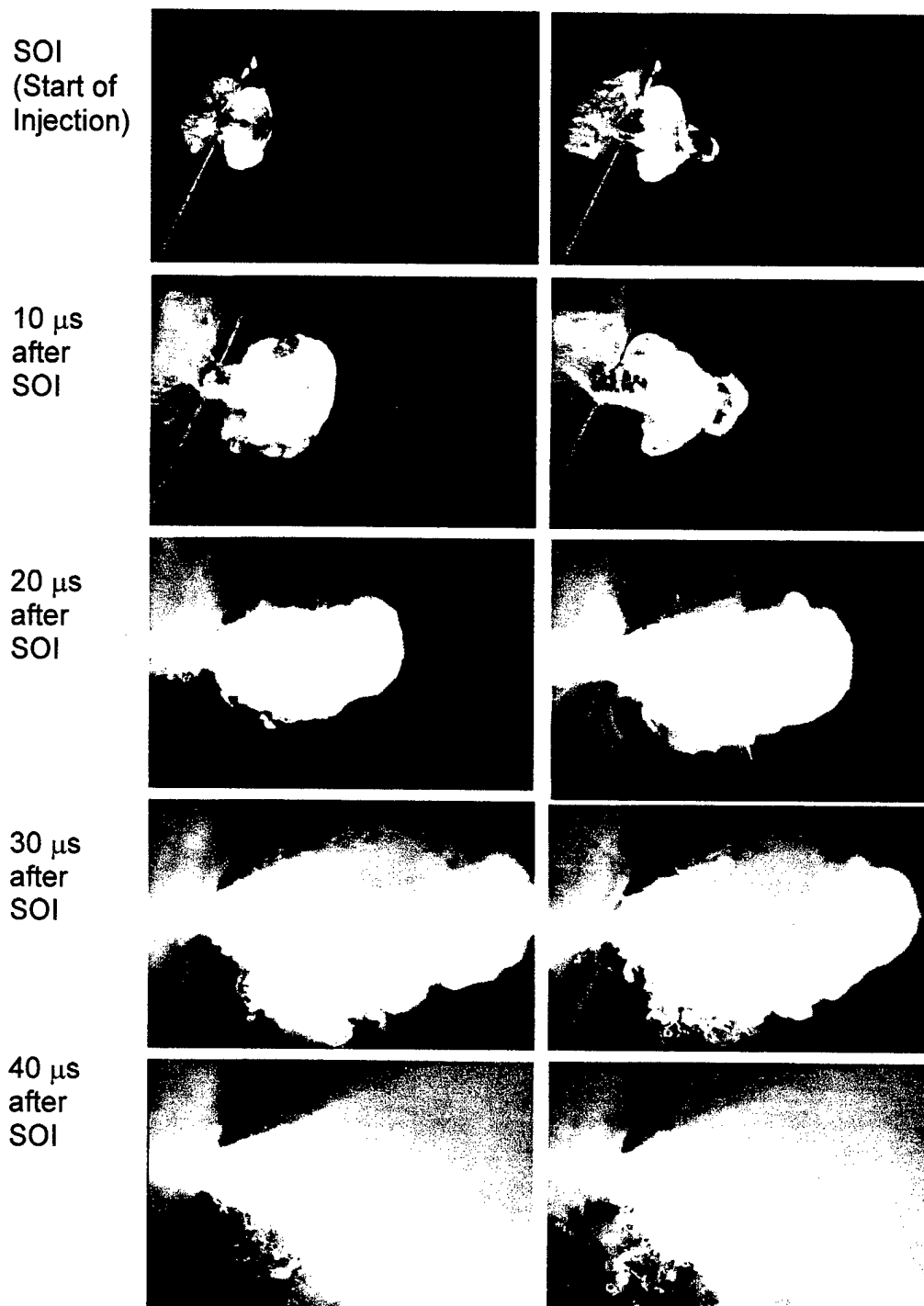
Figure 4-2 Still photographs of early development of EUI sprays, with 0.188-mm VCO nozzle, 1500-rpm engine speed, and injection duration of 10 degree.
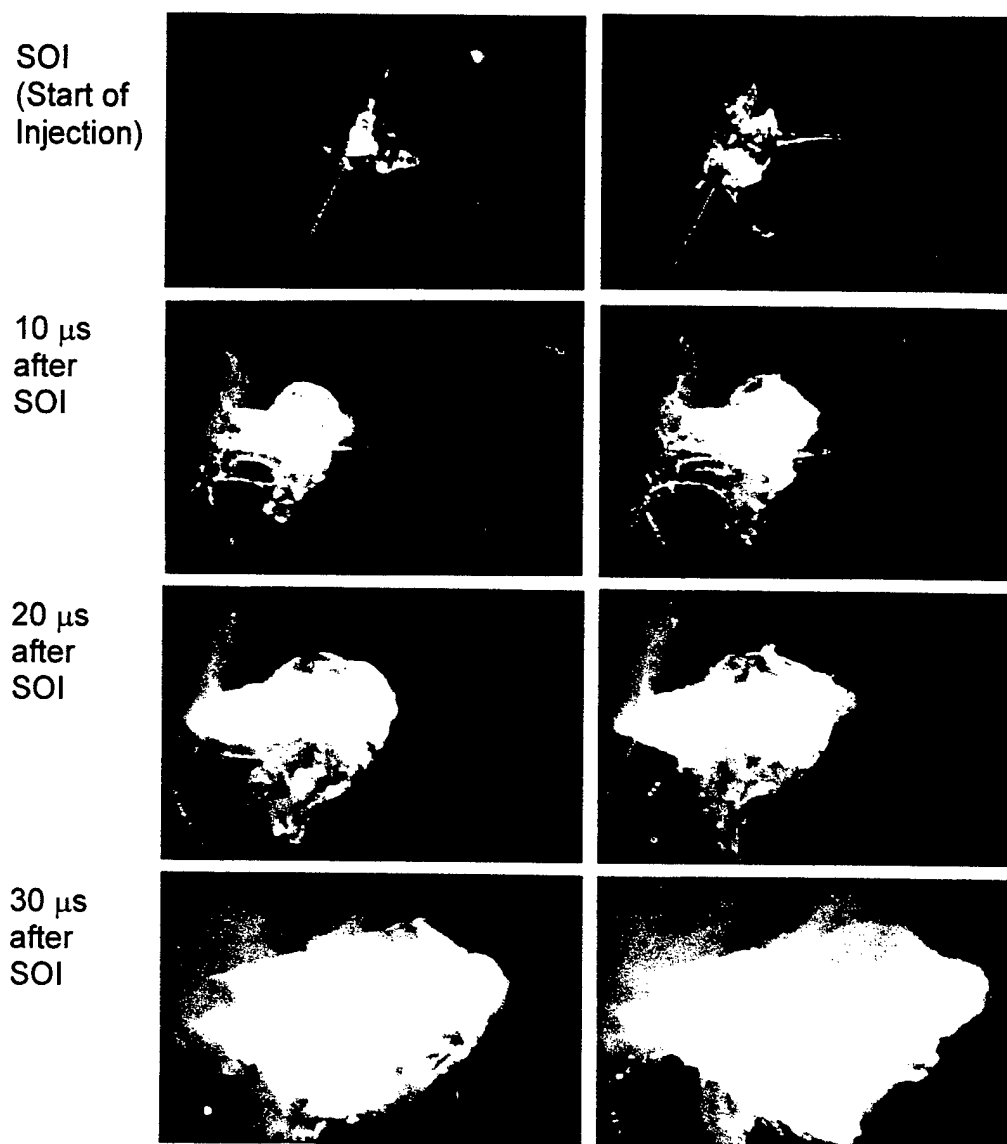
Figure 4-3 Still photographs of early spray development of EUI sprays, with 0.188-mm VCO nozzle, 750-rpm engine speed, and injection duration of 10 degree.

Figure 4-4 Still photographs of EUI spray at peak injection of 200 MPa, with 1500-rpm engine speed and injection duration of 25 degree
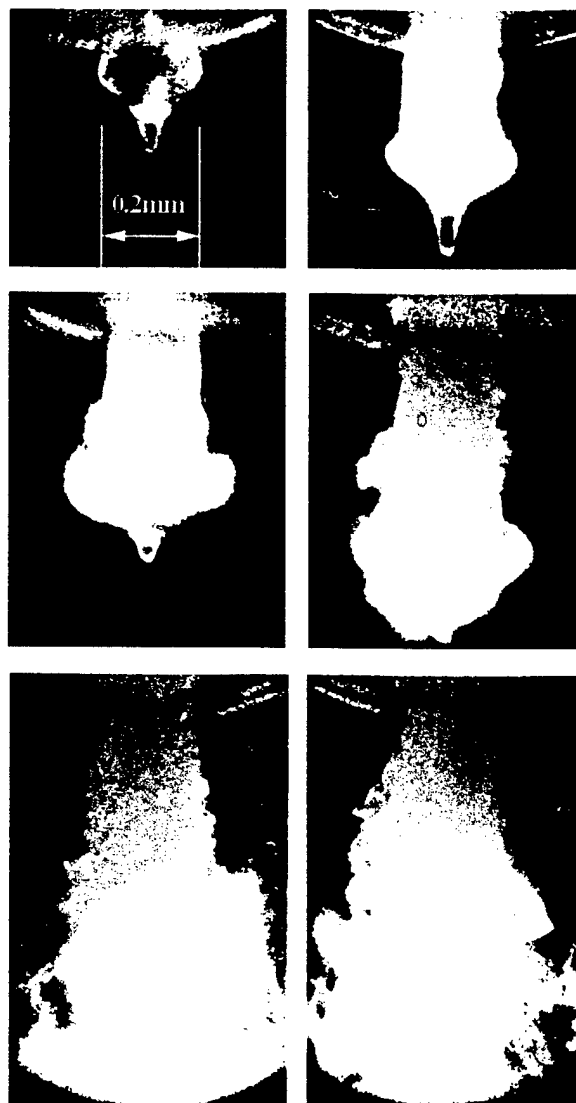
Figure 4-5 Early spray breakup photographs of HEUI sprays (mini-sac nozzle)
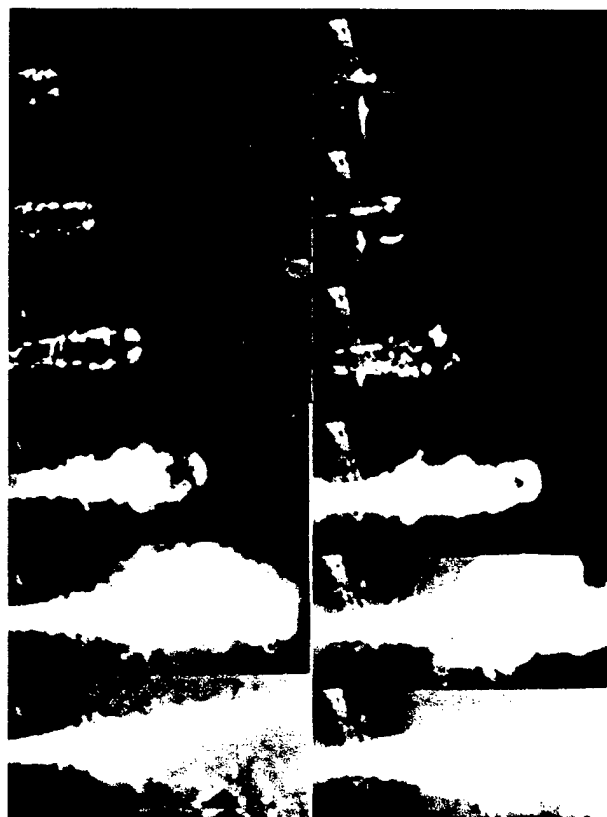
Figure 4-6 Initial spray breakup of CR spray, with injection pressure of 30 MPa; injection event: 0.3ms-pilot/0.45ms-dwell/1.2ms-main; time between frame: 0.04 ms
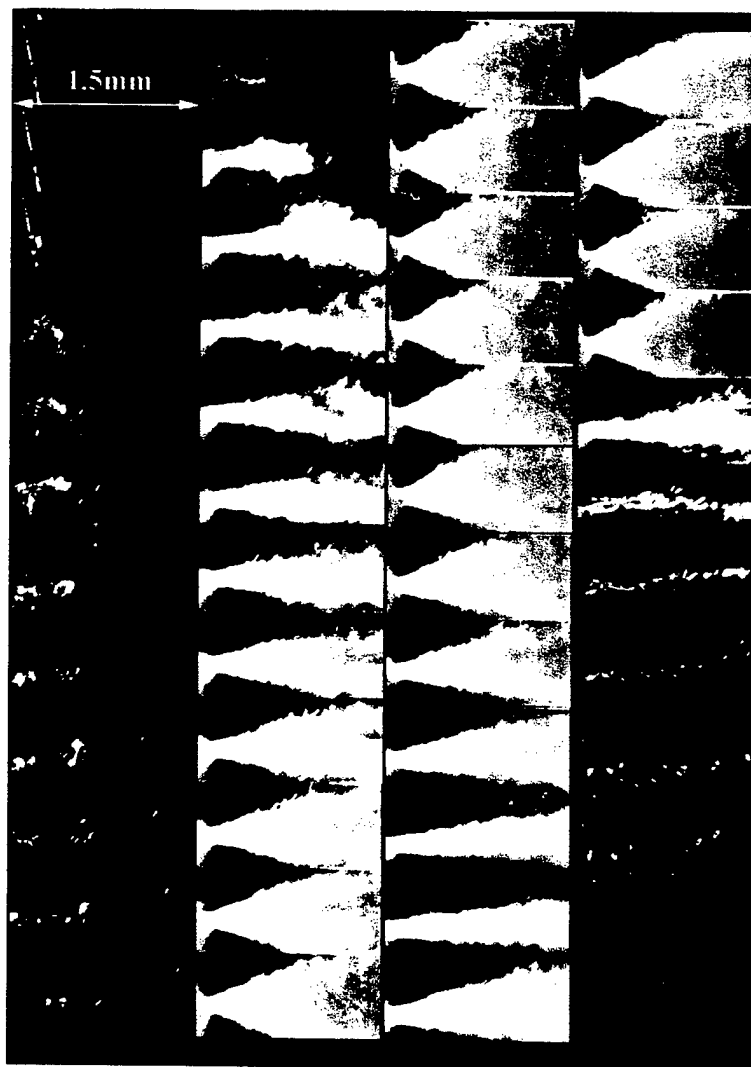
Figure 4-7 Microscopic visualization of CR spray; Injection pressure: 25 MPa, Injection event: 0.2ms-pilot/1.0ms-dwell/1.0ms-main, and time between frame: 0.04 ms (frame 13-23 between pilot and main skipped)
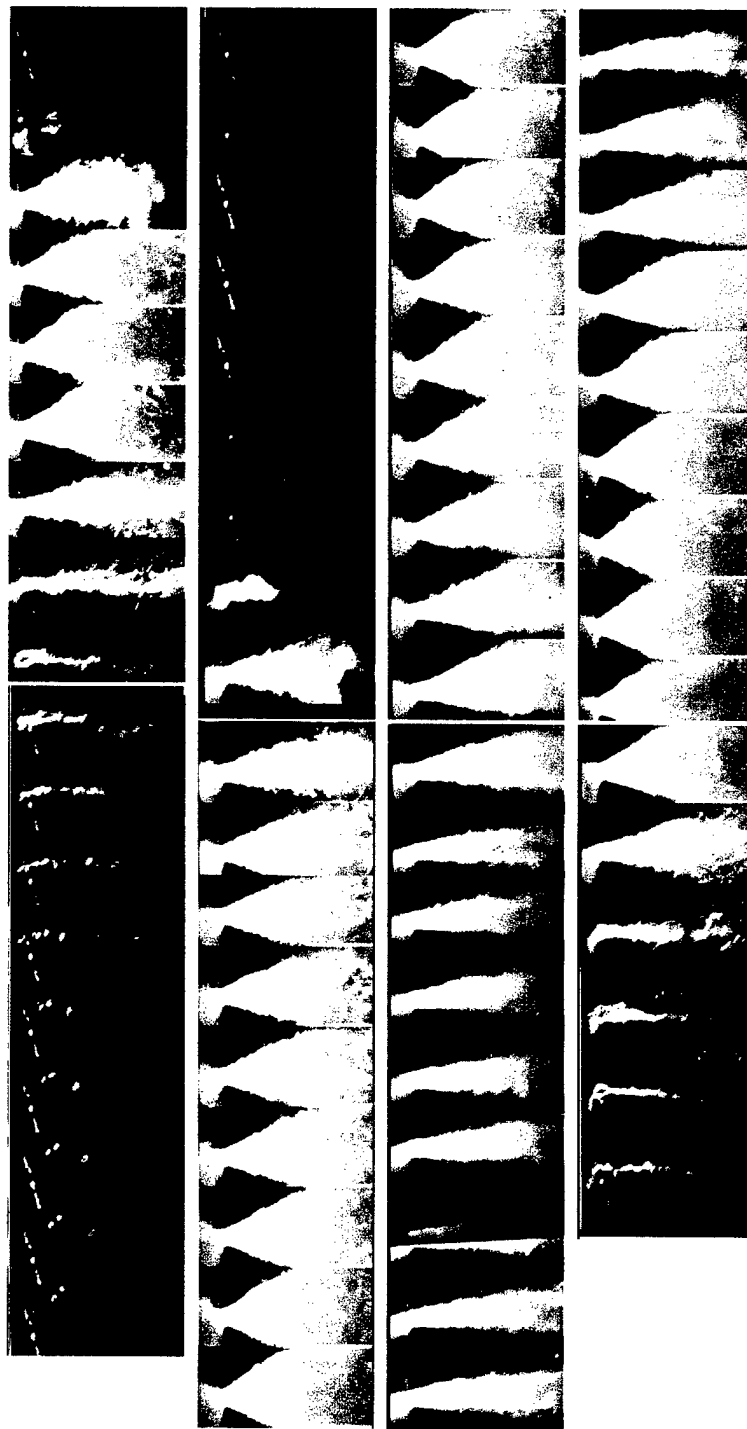
Figure 4-8 Microscopic visualization of CR spray; injection pressure: 30 MPa, injection event: 0.3 ms-pilot/ 1.0 ms-dwell/ 1.2 ms-main; time between frame: 0.04 ms (frame 19 to 24 skipped)
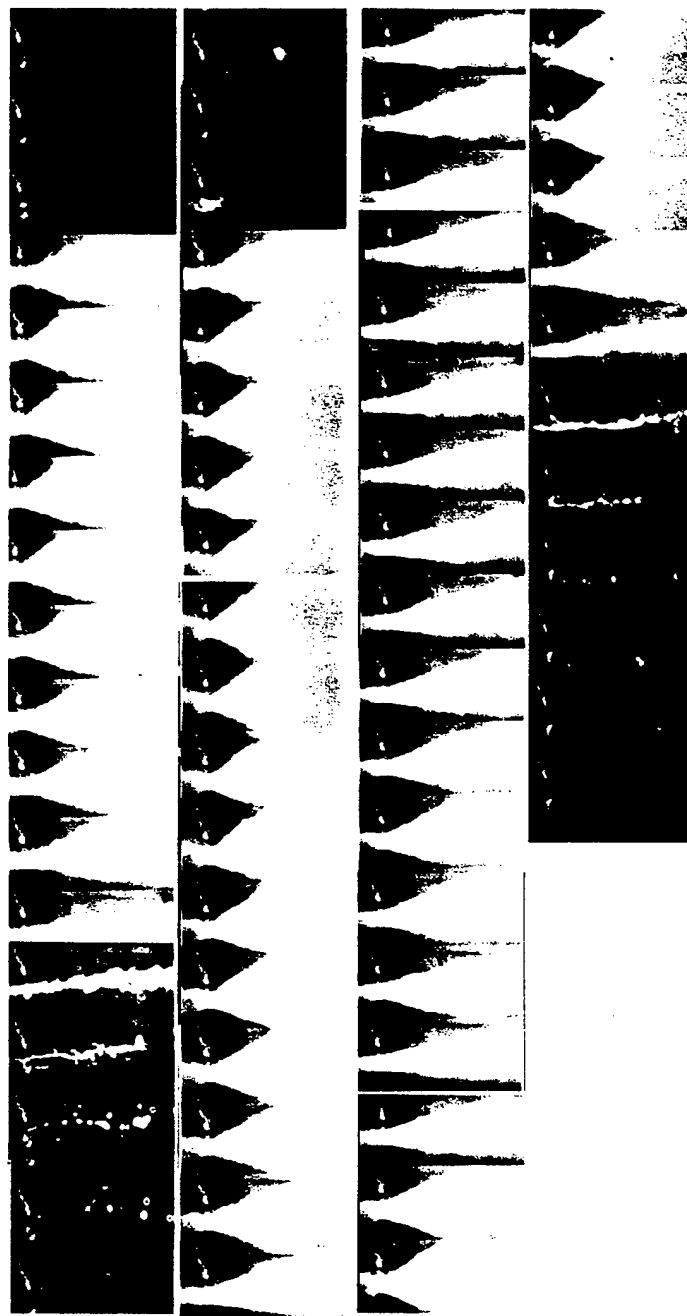
Figure 4-9 Microscopic visualization CR spray; injection pressure: 80MPa, injection event: 0.3ms-pilot/0.45ms-dwell/1.2ms-main, and time between frame: 0.04 ms
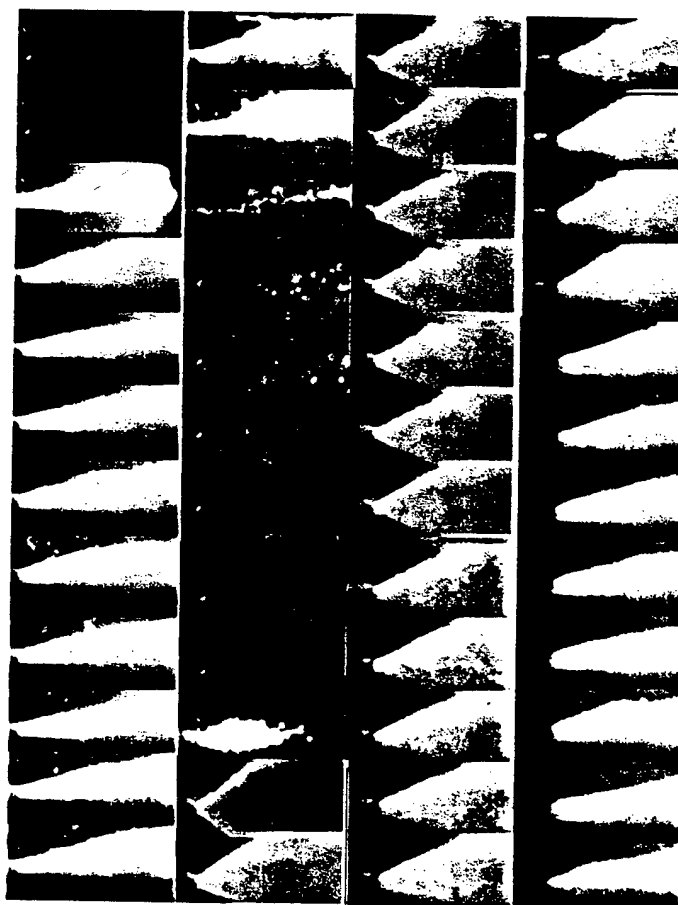
Figure 4-10 Microscopic visualization of CR spray; injection pressure: 135MPa, injection event: 0.3ms-pilot/1.0ms-dwell/1.2ms-main, and time between frame: 0.04 ms (frame 13 to 28 between pilot and main skipped)
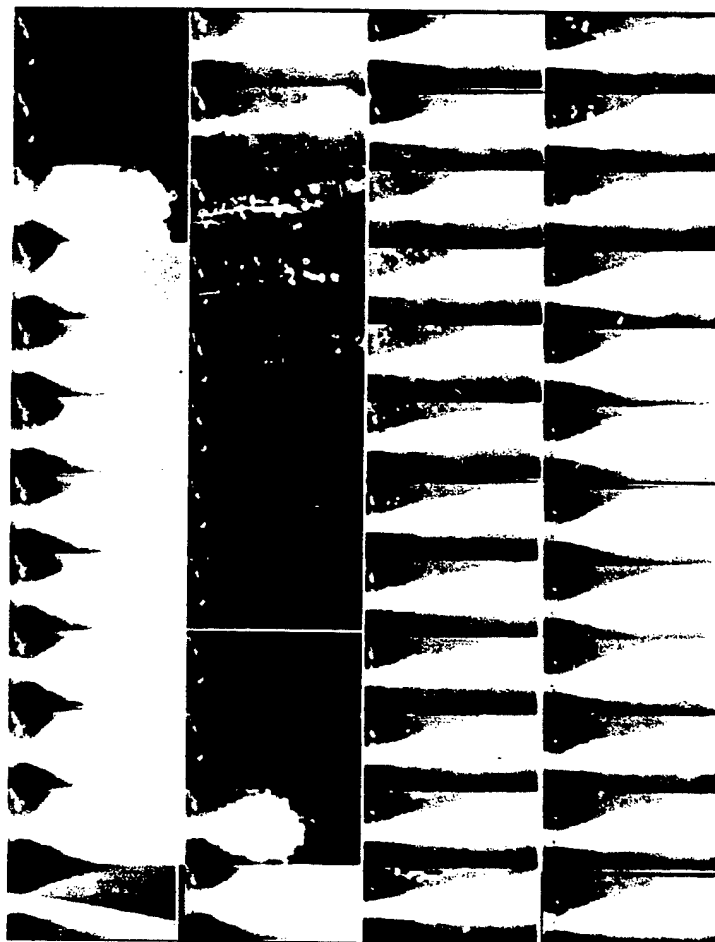
Figure 4-11 Microscopic visualization of CR spray under same condition as Figure 4-10
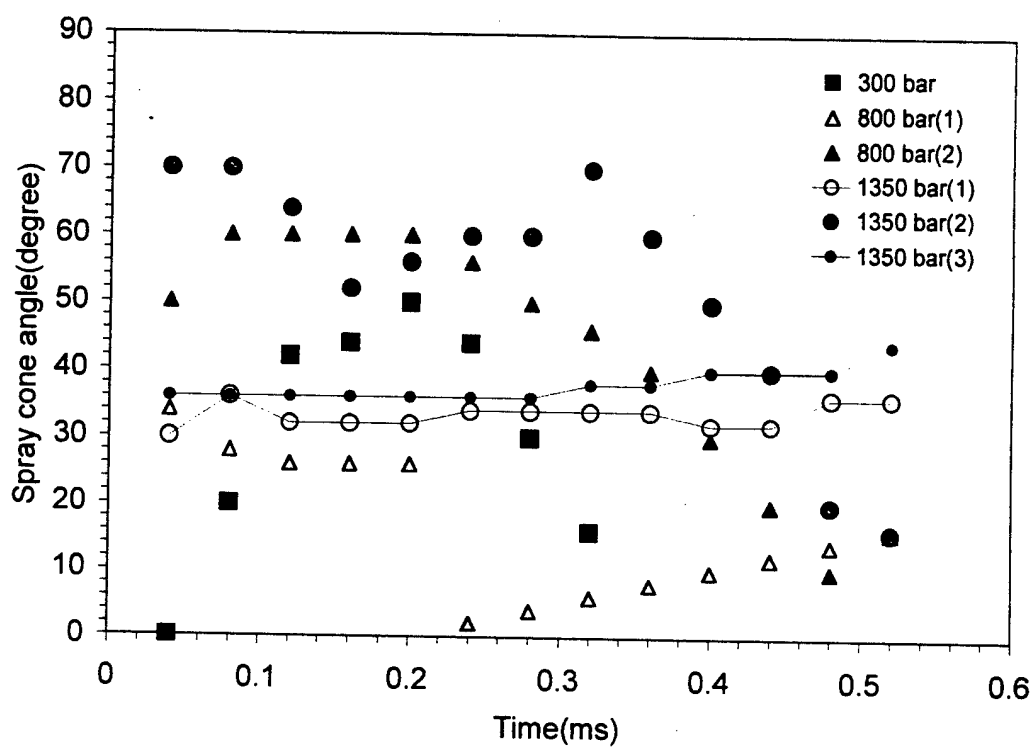
Figure 4-12 Spray cone angle of pilot injection sprays of CR system, with duration of 0.3 ms and various injection pressures, 30, 80, and 135 MPa.
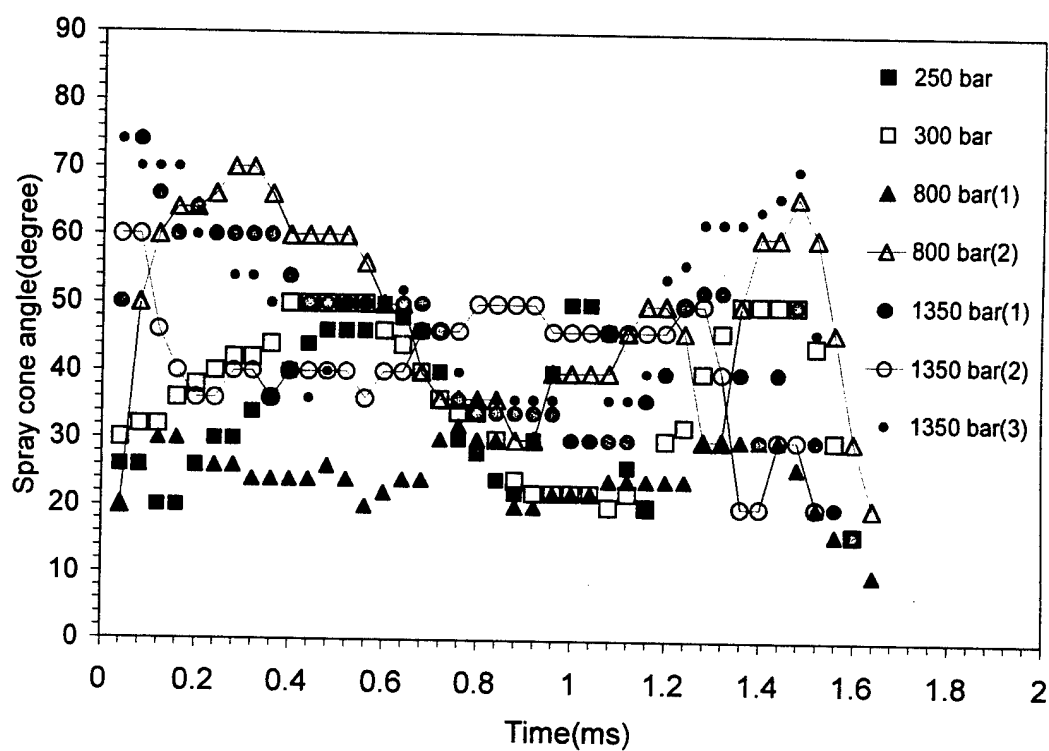
Figure 4-13 Spray cone angle of main injections of CR system, with duration of 1.2 ms and various injection pressures, 25, 30, 80, and 135 MPa.
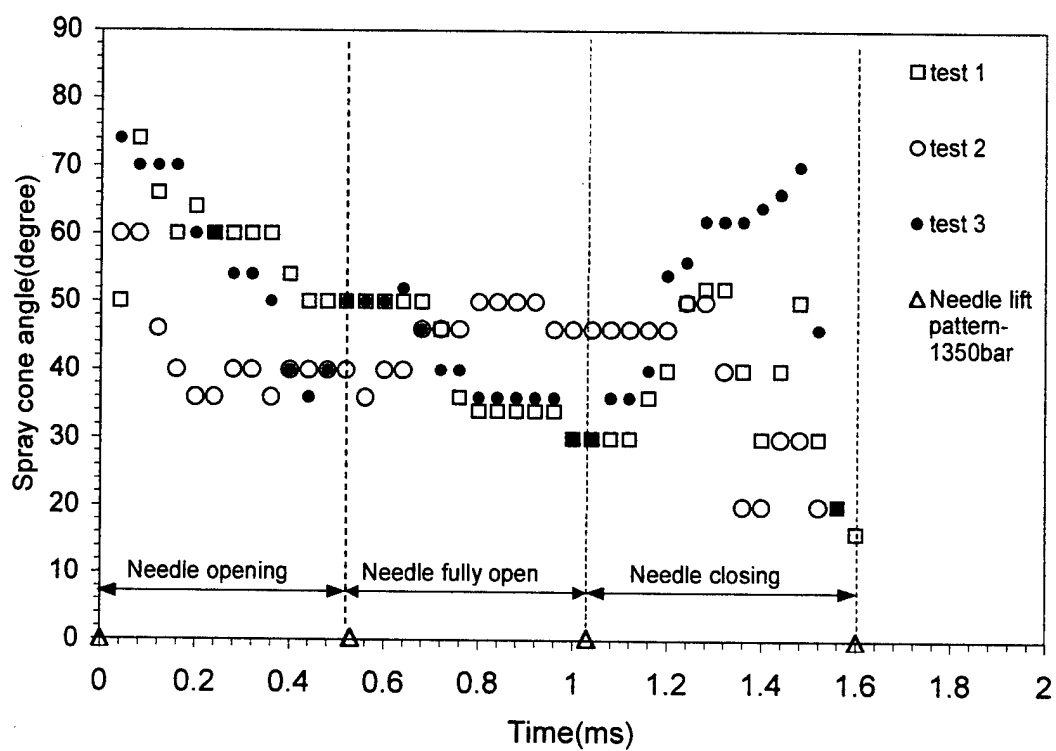
Figure 4-14 Correlation between spray cone angle and needle lift of CR injections, with pressure of 135 MPa and duration of 1.2 ms.
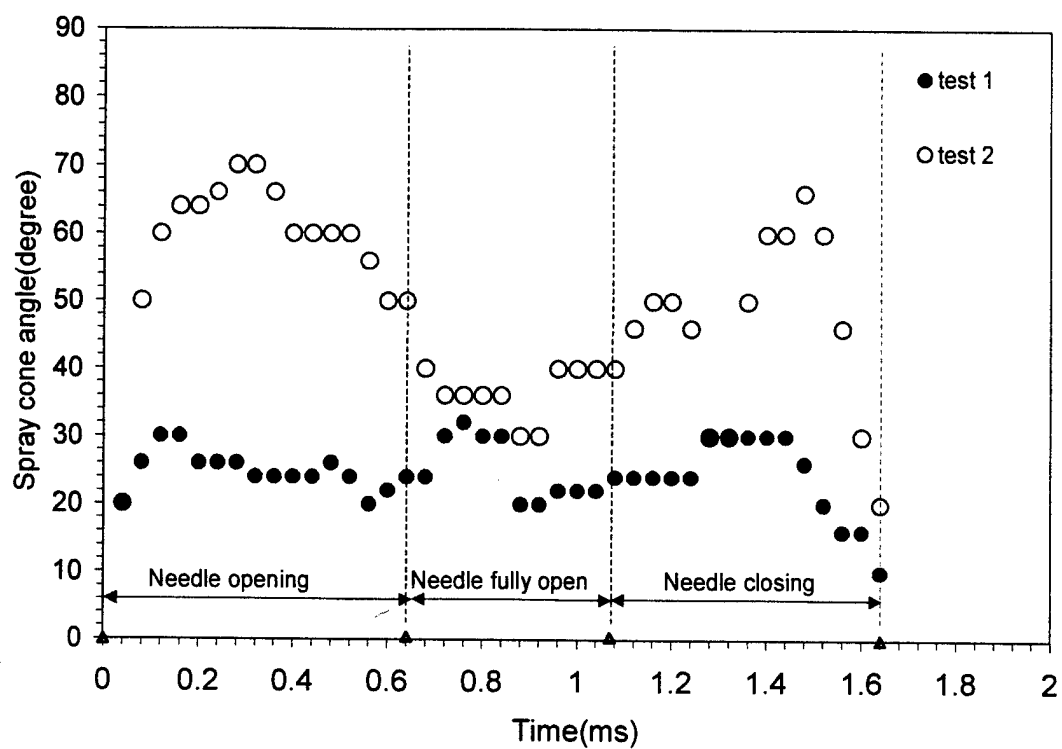
Figure 4-15 Correlation between spray cone angle and needle lift of CR injections, with pressure of 80 MPa and duration of 1.2 ms
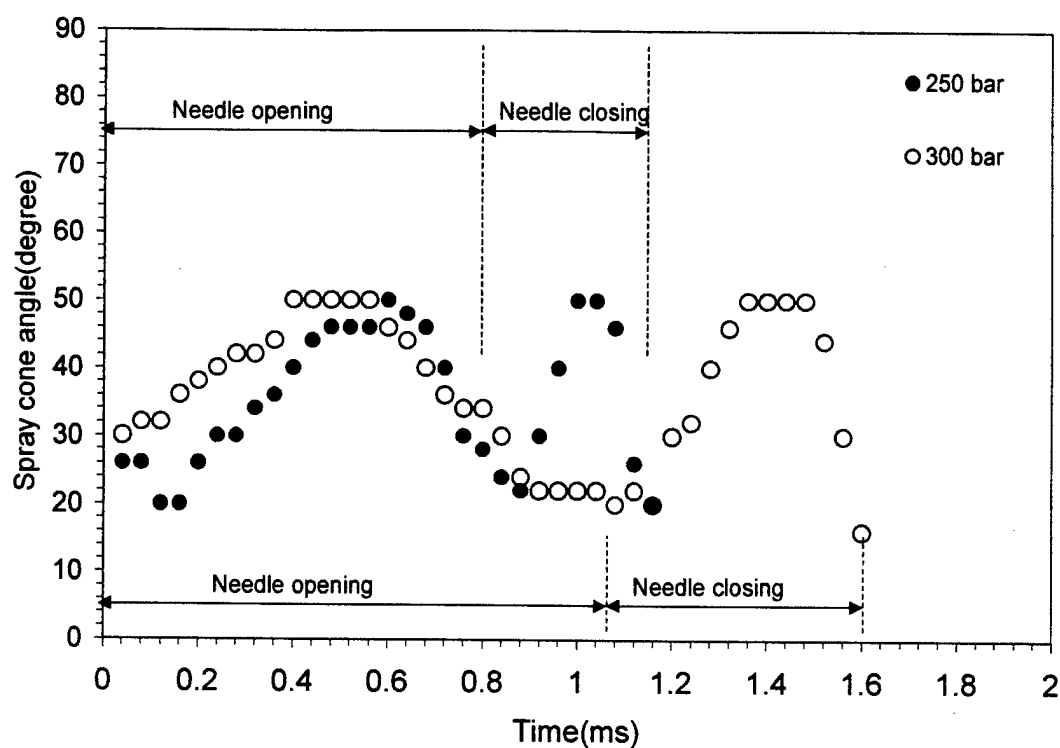
Figure 4-16 Correlation between spray cone angle and needle lift of main injections of CR system, with pressures of 25 and 30 MPa and duration of 1.0 and 1.2 ms.
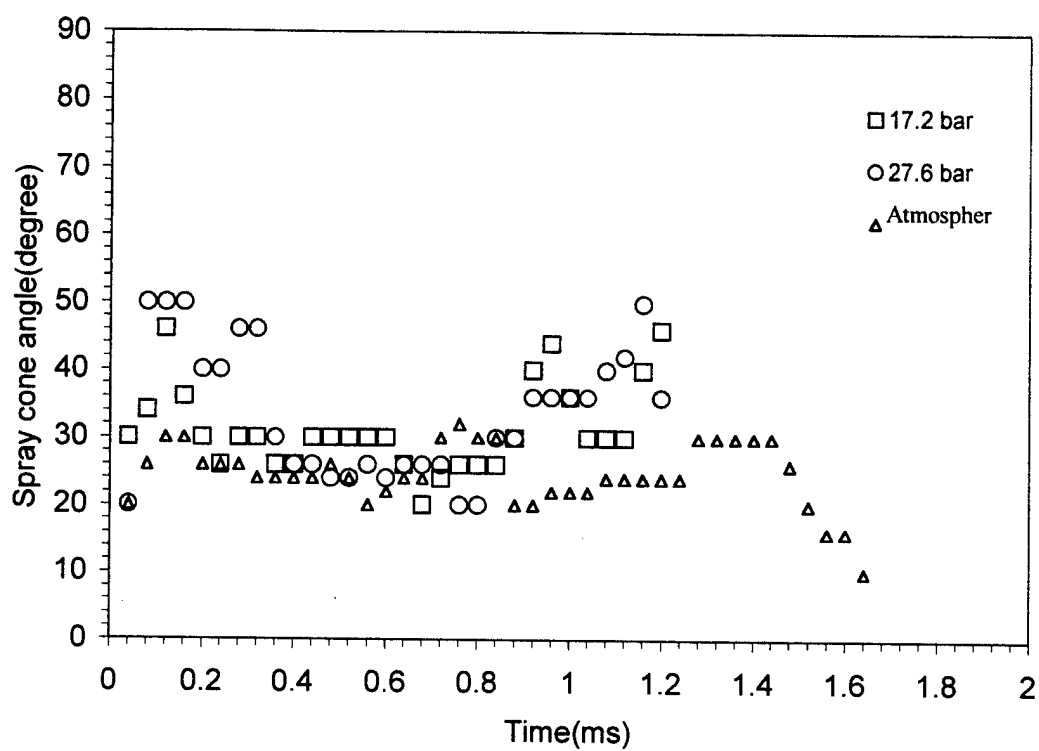
Figure 4-17 Effect of ambient pressure on spray cone angle of CR
sprays, with pressure of 80 MPa and duration of 0.8 ms
(1.2 ms for the case of atmosphere)
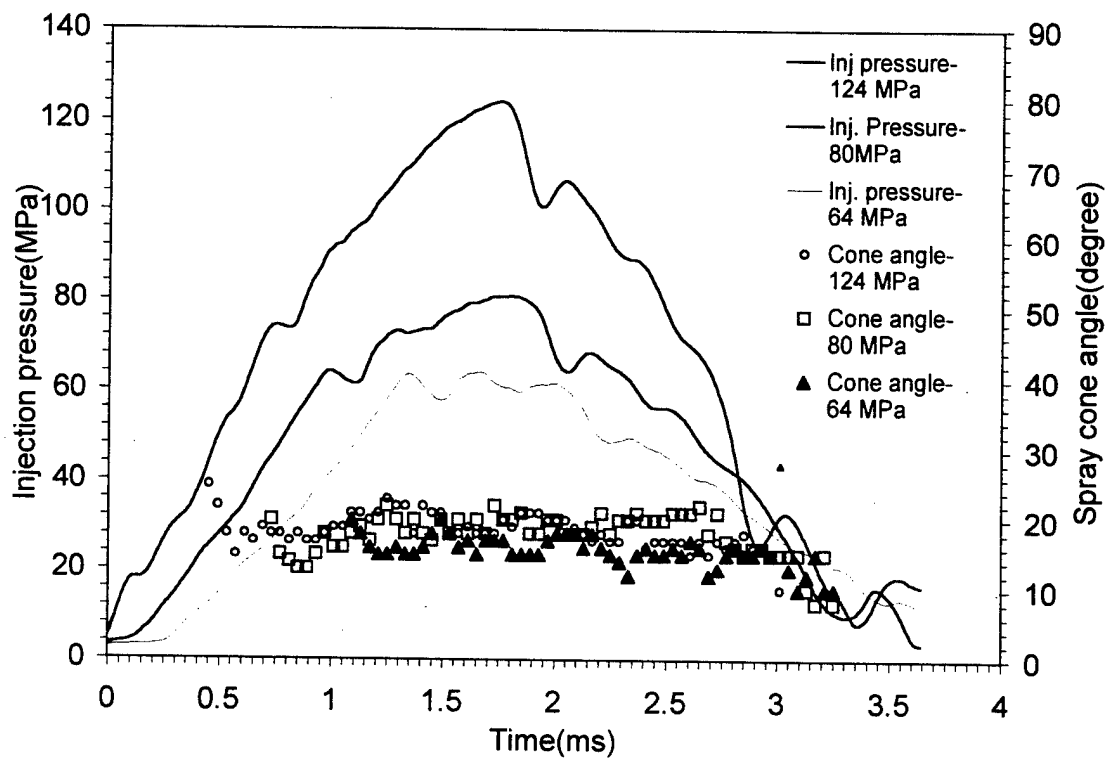
Figure 4-18   Spray cone angle and injection pressures of HEUI spray, with fixed duration of 2.25 ms and 610 VCO nozzle
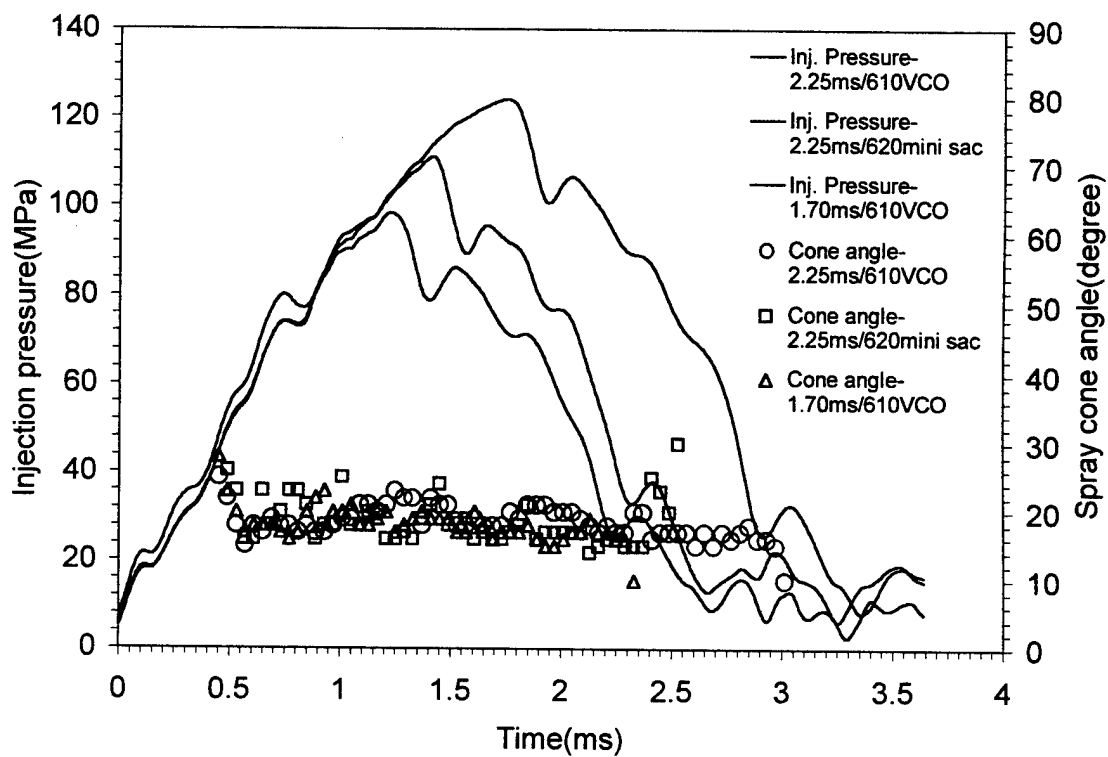
Figure 4-19 Spray cone angle and injection pressures of HEUI spray, with fixed common rail pressure of 379 bar
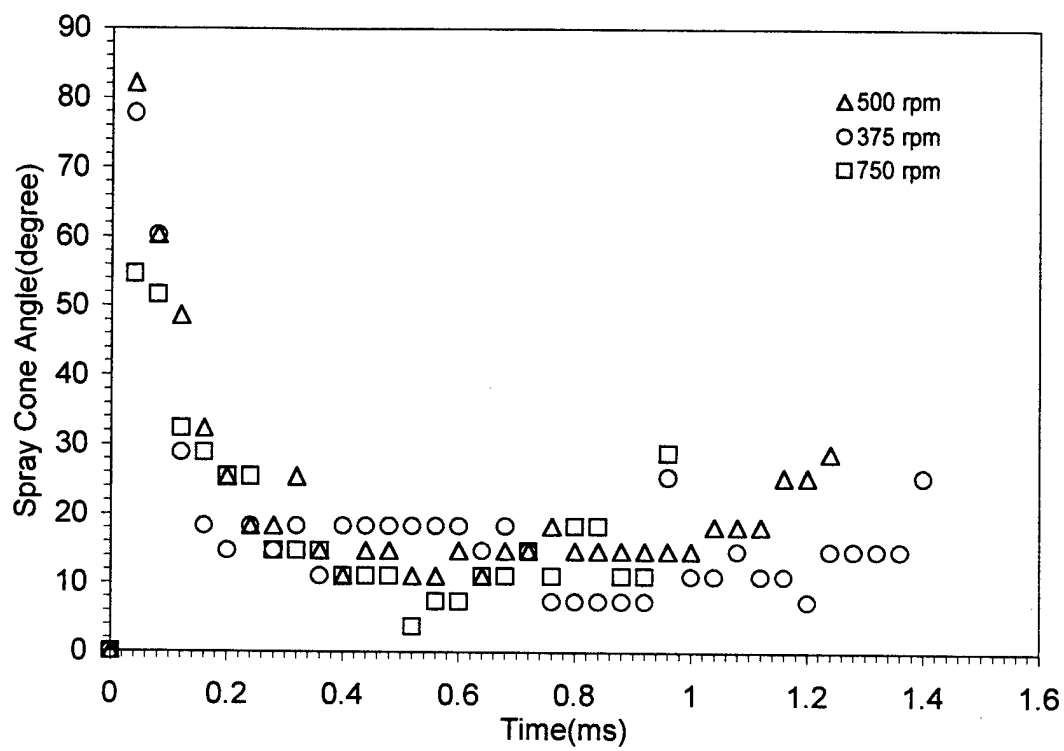
Figure 4-20 Spray cone angle of EUI spray with various camshaft speeds
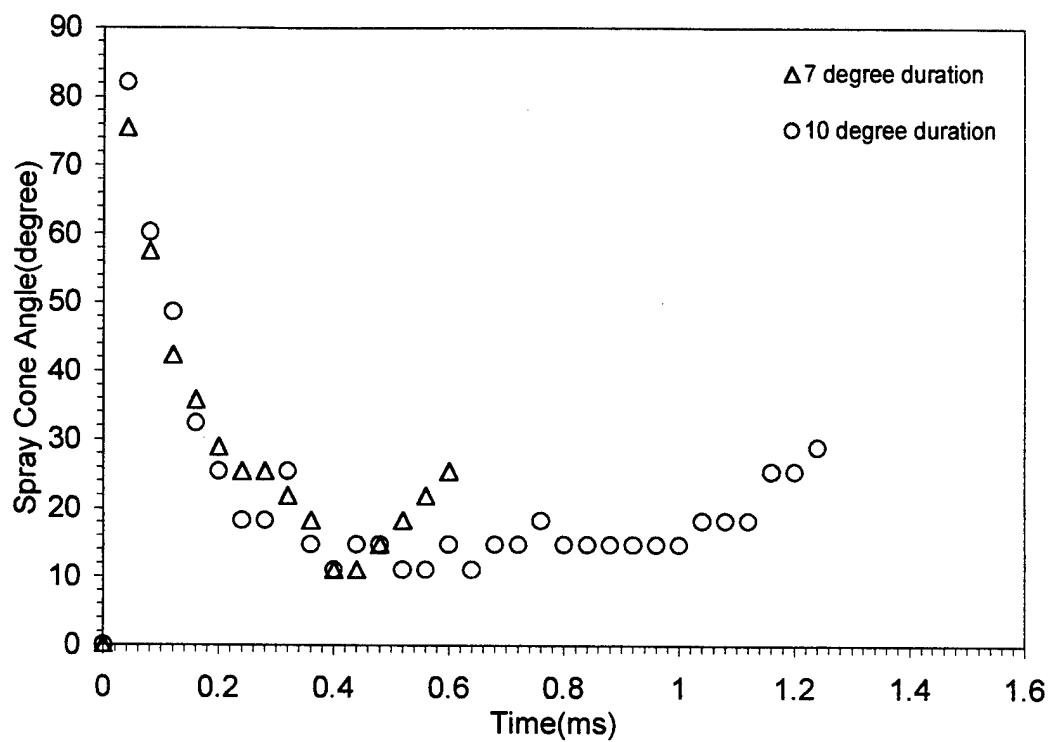
Figure 4-21 Spray cone angle of EUI spray with fixed camshaft speed of 500 rpm and injection duration of 7 and 10 crank-angle degree

| 375-rpm camshaft speed and 7-degree duration | 750-rpm camshaft speed and 10-degree duration |
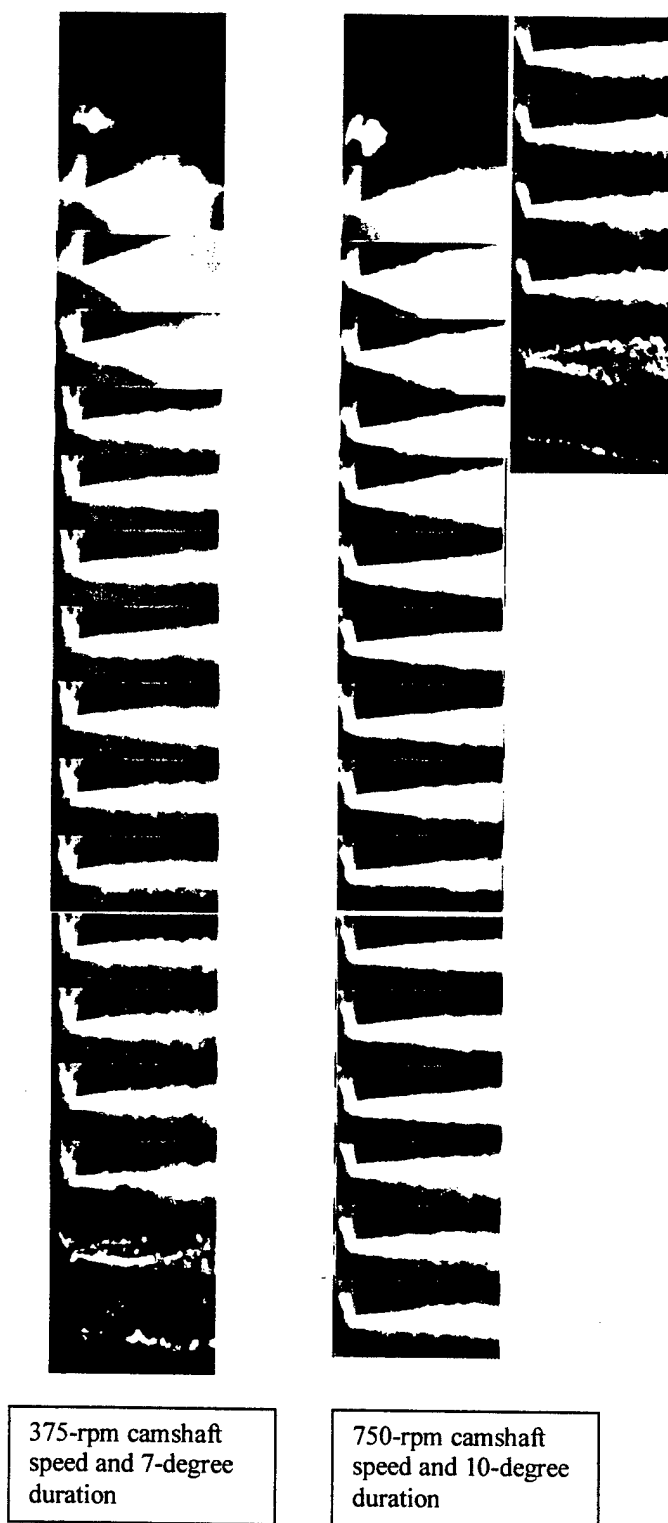
Figure 4-22 microscopic visualization of EUI spray.

750 rpm / 7 degree

375 rpm / 7 degree

750 rpm / 10 degree

500 rpm / 10 degree
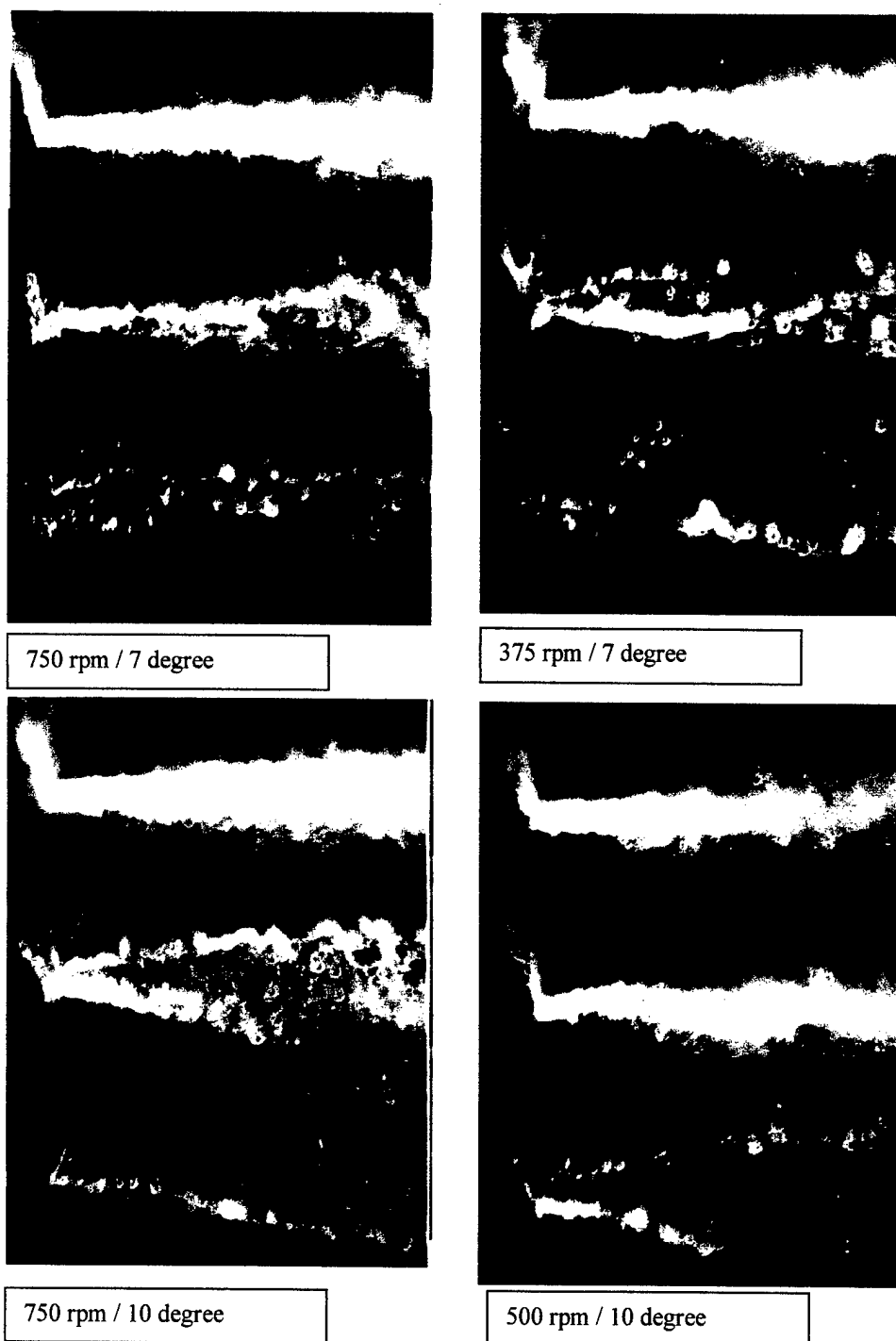
Figure 4-23 End of injections of EUI system under various camshaft speeds and injection duration

Figure 4-24 Still photographs of end of injection of EUI system, with 750-rpm camshaft speed and 10-degree duration.

1350 bar

800 bar

300 bar
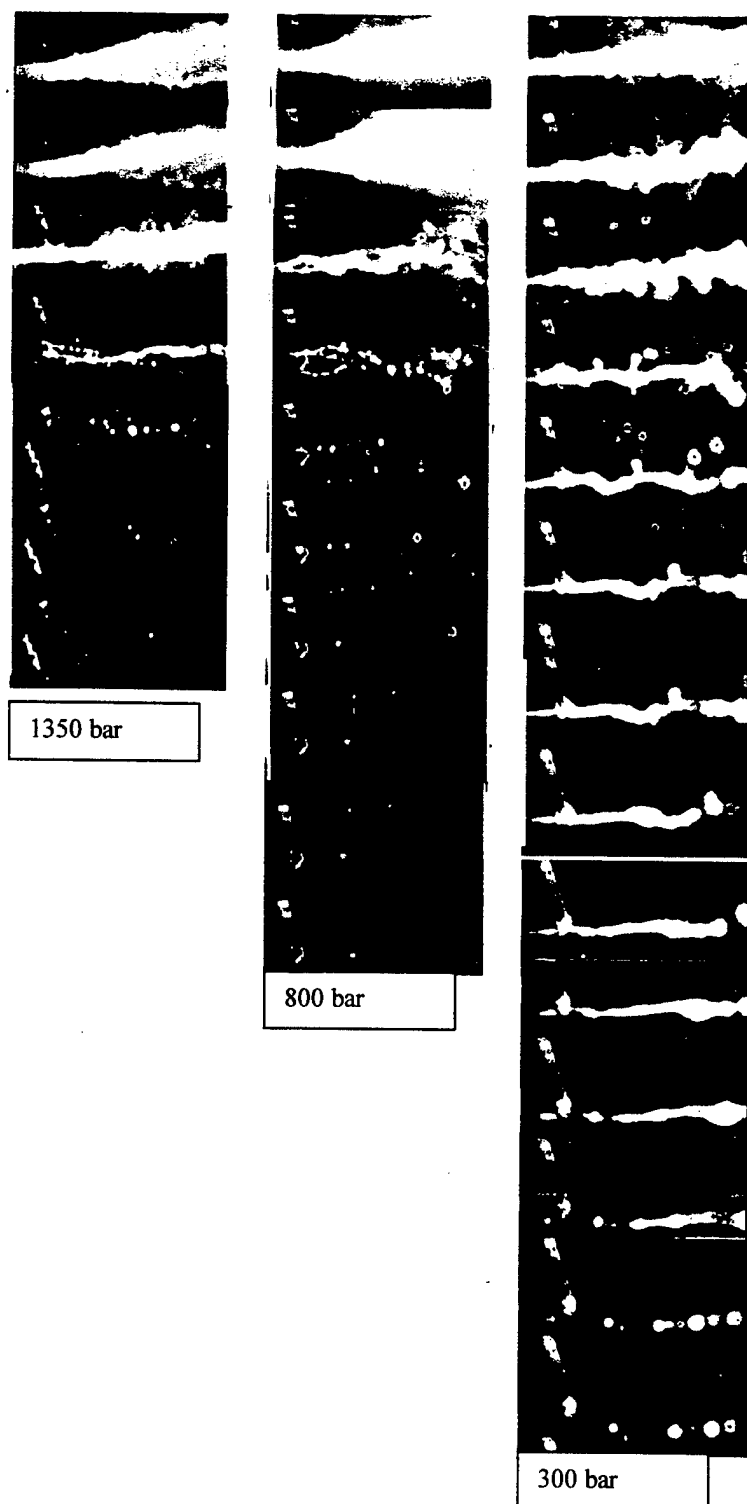
Figure 4-25 Effect of injection pressure on end of injection of the CR system
with 390 VCO nozzle and injection duration: 1.2ms-main

610 VCO nozzle, 98 MPa peak injection pressure, 1.7 ms duration

620 Mini-sac nozzle, 97 MPa peak injection pressure, 1.7-ms duration
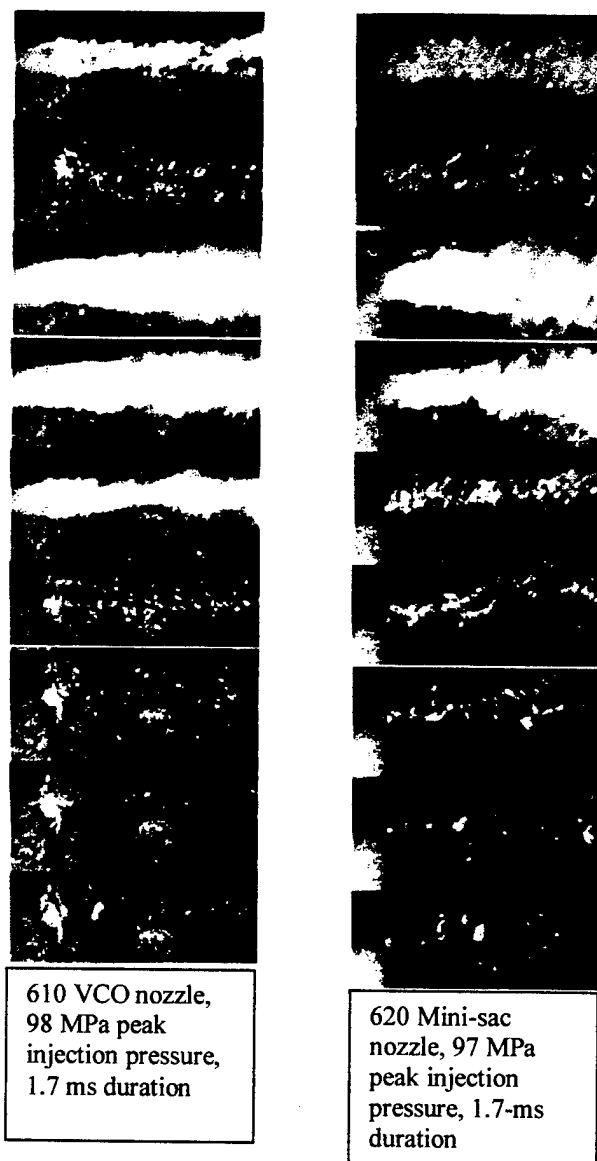
Figure 4-26 Effect of nozzle configuration on end of injection of the HEUI system (610 VCO vs.620 mini-sac) with common rail pressure of 379 bar

610 VCO nozzle, 69-MPa peak injection pressure, and 1.7- ms duration

620 Mini-sac nozzle, 71-MPa peak injection pressure, and 1.7- ms duration
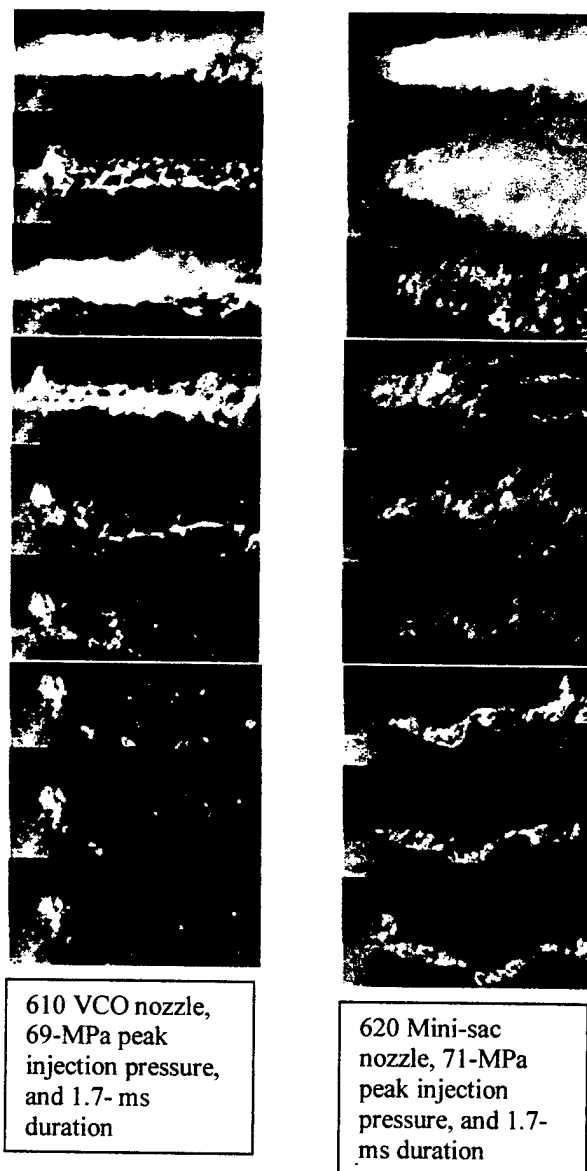
Figure 4-27 Effect of nozzle configuration on end of injection of the HEUI system (610 VCO vs. 620 mini-sac) with common rail pressure of 276 bar

CHAPTER 5

IN-CYLINDER SPRAYS AND COMBUSTION VISUALIZATION

5.1. Introduction

The objective of this work is to visualize and analyze in-cylinder spray and combustion process and evaluate the effects of fuel injection and engine operating conditions on the process. In this study, an AVL single-cylinder optically accessible engine is used to visualize spray and combustion process directly from the engine bottom through a quartz window inserted in the piston top. The in-cylinder spray characterization items include penetration, structure, and uniformity of liquid-phase fuel in the combustion chamber under conditions of various charge air temperatures and pressures. Based on visualization, the effects of engine and injection operating conditions on ignition delays, ignition locations, and combustion process are addressed and analyzed. The injection command, injection pressure, cylinder pressure, and temperature and pressure of charge air, are the data need to be acquired at the same time as the visualization photographs are being taken by the high-speed camera. Therefore, timing control and events synchronization is the most crucial feature of the experimental setup. Intensive injection characterization has been conducted, as described in chapter 2, prior to the in-cylinder spray and combustion visualization to obtain the characteristics of the injectors, nozzle tips, and the fuel systems used in the study. The injection characterization items included injector response time, injection pressure,

injection quantity, and injection rate. Based on the results of injection characterization, proper sets of injection conditions are then identified and designed to match with the intent engine operating conditions in terms of the timing and duration of the injection command. Non-evaporative spray visualization has also been conducted beforehand, as described in chapter 3, to gain knowledge of the sprays issued by the injection system in terms of spray penetration, spray symmetry, and characteristics of start and end of injection. The injection characterization and non-evaporative spray visualization, both are deemed as necessary and important preparation work to assure a successful in-cylinder spray and combustion visualization. Since cylinder bulk gas temperature is not available from direct measurement in the visualization test, a multi-zone combustion model is incorporated to calculate the temperature. A blow-by term is included in the calculation to address the effect of gas leakage through the ring-end gaps, the ring-side clearance, and the crevice between piston and liner. As a measure of the accuracy of the temperature calculation, the calculated cylinder pressure is compared and correlated with the measured pressure.

5.2. Experimental Method

The experimental setup for the in-cylinder spray and combustion visualization consists of a bottom-viewed optically accessible engine (OAE), 16-mm high-speed movie camera, HEUI fuel injection system, copper-vapor laser system, and Labview data acquisition and control system. The optically

accessible engine modified from an AVL single cylinder engine is as shown in Figure 5-1. The schematic at the top shows the basic structure of the OAE engine while the one at the bottom shows the details of setup of quartz window and the injection system. The specifications of the OAE engine are summarized in Table 5-1.

Table 5-1 Specification of the OAE engine

Bore x Stroke (mm)	120 X 120	IVO (degree, BTDC)	13
Compression Ratio	16.7	IVC (degree, ABDC)	26
No. of valves	4	EVO(degree, BBDC)	48
Combustion chamber (mm)	66.5 (diameter)	EVC(degree, ATDC)	6
bowl-in-piston(mm)	16.5(deep)	Swirl Number	2.1

The instrumentation of the engine includes a Kistler 6043A60 cylinder pressure transducer installed on the cylinder head, 72-ticks-per-revolution shaft encoder installed on the camshaft, and charge air temperature and pressure transducers mounted on the intake manifold. The charge air is supplied from a 100-psig shop air system, then accumulated in a 200-liter tank. It is heated by a 40kW air heater before delivered to the engine An additional 50-liter surge tank is installed in-line to the engine induction system to stabilize engine intake pressure. The air induction pipeline beyond the heater outlet, including the surge tank, is covered by thermal-insulated material to minimize the heat loss of the heated air to the ambient. A Kislter

4067A2000 Piezo-resistive pressure transducer is installed in the high-pressure fuel line at 7 cm upstream of the fuel inlet of the injection nozzle holder. The measured injection pressure is upstream injection pressure. The Labview system is implemented to operate the HEUI system to the required injection conditions such as injection pressure, timing, duration, and number of injections. The copper-vapor laser is operated at 25-kHz pulsing frequency to illuminate the in-cylinder spray from bottom of the piston through the quartz window. The high-speed movie camera is operated at 5-kHz framing speed for about 2 second of picture-taking period after triggered by a synchronization signal. The synchronization logic among the operating of the engine, injection system, high-speed camera, and data acquisition is implemented by the Labview programming and the associated hardware consisting of a Pentium computer system and National Instrument's PC compatible I/O devices such as timer/counter and data acquisition boards.

Figure 5-2 describes the controls and synchronization logic. The TDC signal is the reference for generating injection timing and duration signals. It is also the signal used to synchronize the high-speed camera. A gate signal is generated after a delay time is expired. The period of the delay time is about 1 second, which allows the high-speed camera to accelerate to the required rotational speed before the pictures can be taken. The number of fuel injection issued is determined by the period of the gate signal.

Cylinder pressure, injection pressure, and charge air pressure and temperature are acquired and recorded for each crankangle degree while the

spray and combustion pictures are being taken by the high-speed movie camera. The visualization films are developed by traditional film-developed method, then digitized by scanner for further process and analysis.

Table 5-1 Test conditions of in-cylinder spray and combustion visualization

Engine speed	750 rpm
Injection timing (command signal)	10 degree BTDC
Inlet Conditions(pressure/temperature)	1.5bar/75 C and 1.85 bar/110 C
Common Rail Pressure	27.6 MPa and 37.9 MPa
Injection duration	1.70 ms and 2.25 ms
Length of rate shaping pipe	12 inches and 24 inches
Nozzle tip type	610VCO,620mini-sac,and 730VCO

The specifications of the nozzle tips used in this study are summarized in Table 2-1. The flow number- for example, the 610 of the VCO nozzle-represents steady state volume flow rate in cubic centimeter within 30-second test period with 100-bar injection pressure. The test conditions are summarized in Table 5-1. For all of the test cases, the engine speed and injection timing are kept unchanged at 750 rpm and 10 degree BTDC respectively. However, other test variables, such as charge air conditions, Common Rail pressure, injection duration, length of rate shaping pipe, and type of nozzle tip are changed according to the test requirement. Table 5-3 details the conditions for each of the 7 test cases. Case A to E simulate full-

load engine operating condition with air-to-fuel ratio set to about 20 to 1, while Case F and Case G simulate 65% load condition. In addition to the test conditions mentioned above, a test is also arranged to study the spray and combustion process of a multi-stage fuel injection.

Table5-3 Detail of test case A to G

Test case	Inj. Duration (ms)	Peak Inj. Pressure (MPa)	Inlet Temp. /Pressure (deg C/bar)	Type of Nozzle Tip	Length of Rate Shaping Pipe (inches)
A	2.25	101	110/1.85	620mini-sac	24
B	2.25	101	75/1.5	620mini-sac	24
C	2.25	106	75/1.5	610VCO	24
D	2.25	134	75/1.5	610VCO	12
E	2.25	84	75/1.5	730VCO	12
F	1.7	75	75/1.5	730VCO	12
G	1.7	109	75/1.5	610VCO	12

5.3. Calculation of In-Cylinder Gas Temperature

Like the cylinder pressure and fuel injection pressure, the bulk gas temperature of combustion chamber is a valuable information for analysis of the data obtained from the spray and combustion visualization. However, in the study the bulk gas temperature is not available from direct measurement due to availability of instrument at the time when the tests were conducted. To improve the situation, a multi-zone combustion model is implemented to estimate the average bulk gas temperature in the cylinder during compression, combustion, and expansion strokes. Detailed discussion, evaluation, and applications of the model had been conducted by Hiroyasu and Kadota (1976), Kuo(1987),and Yoshizaki et al(1993). The features of the model

include the modeling of spray penetration, fuel distribution, droplet size assignment, air entrainment, fuel droplet evaporation, ignition, heat release, and heat loss. Detailed information with respect to the equations used in the model is given in Appendix A. Since the blow-by of the OAE engine used in this study is relatively higher than a normal metal engine, a blow-by term is incorporated in the equation of cylinder pressure calculation, as shown in equation A21, which is based on the derivation of Ferguson (1986). The blow-by rate in equation A21 can be obtained from a crevice-flow model originally developed by Namazian and Heywood(1982) for a study of flow into and out of the piston top-land of a squared-piston spark ignition engine. In the crevice-flow model, the crevice flow through the ring-side clearance is treated as compressible, laminar, and isothermal at a temperature that is the average of the piston, cylinder, and ring temperatures; the crevice flow through the ring end gap is treated as orifice jet flow [Shih and Assanis, 1994]. The equations used to calculate the crevice flows are also included in Appendix A.

Beside the engine and nozzle specifications, for each test case the injection pressure, injection rate and blow-by rate are the main inputs to the program. The injection pressure and rate are measured data while the blow-by rate is calculated from the blow-by model using the measured cylinder pressure, engine specifications, and ring specifications as the main inputs. To reflect the characteristics of the HEUI system used in the study, the Coefficient of Effective Injection Velocity has been modified from 0.8 to 0.55 based on the spray penetration result of chapter 3. All of the other coefficients required for

the calculation are carried over from the study of Kuo et. Al.(1986) and remained unchanged.

Figure 5-3 and Figure 5-4 show the calculated bulk gas temperatures and the correlation between the measured and calculated cylinder pressure for four test cases. For case A, B, and D, the measured peak pressures are 9%, 15%, and 13% lower the calculated results respectively. For case G, the measured peak pressure is 2% higher than the calculated result. For case A, the case of high charge air temperature and pressure, the model well predicts the timing of start of combustion, however for other three cases the calculated timing is about 4 degree earlier than the measured data.

5.4. Results and Discussions

5.4.1. Evaporative and Non-evaporative Sprays

Figure 5-5 and Figure 5-6 show the comparison between non-evaporative and evaporative spray for two types of nozzle tip, 620 mini-sac and 610 VCO. As shown in Figure 5-5, the image at the top is originated from the visualization result of Case B, which is taken from OAE combustion chamber around 0.2 to 0.3 ms after start of injection which corresponding to 1 crank-angle degree BTDC at which the cylinder pressure and temperature are 50 bar and 922 K respectively. The image at the bottom is taken at 0.24 ms after start of injection with the sprays issued into a Nitrogen-filled pressurized chamber with pressure of 27.6 bar and temperature of 298 K. The injection conditions of these two test cases are identical in terms of their pressure, rate,

and duration. Similar comparison is made for VCO type nozzle, as shown in Figure 5-6.

The comparison show that the evaporative sprays have much less penetration and width of liquid-phase fuel, as compared to those of the non-evaporative sprays. Both the penetration and width of the sprays are reduced in half. In the evaporative ambient condition, the mini-sac nozzle still performs better in terms of penetration uniformity of the sprays. On the contrary, the highly spray asymmetry of the 610 VCO nozzle at the early phase of injection are observed in both non-evaporative and evaporative conditions. The spray asymmetry in combustion chamber could result in difference in ignition delay and air utilization among the sprays. Due to evaporation of fuel droplet, the puffy spray structure of the slow sprays of VCO nozzle is not observed in the evaporative condition.

5.4.2. Locations of Ignition and Start of Combustion

The asymmetry of VCO nozzle affects the characteristics of Ignition and Start-of-Combustion. Figure 5-7 shows the ignition and start-of-combustion of three consecutive cycles with injections issued by the 610 VCO nozzle. With the spray asymmetry, the ignition and start-of-combustion tend to occur at the edges of the fast sprays, the 3-and 5-o'clock sprays, because of their longer time of exposure to and mixing with the air in the cylinder and their higher penetration velocity that enhances the air-fuel mixing.

Figure 5-8 shows the images of ignition and start-of-combustion of three consecutive cycles with injections issued by the 620 Mini-sac nozzle under the operating condition of the Case A. Swirl is introduced in the clockwise direction. The images in both Figure 5-7 and Figure 5-8 associated with visualization results from other test cases demonstrate that with high injection pressure and swirl air, the Ignition and start-of-combustion mostly occur at the downwind sides of the sprays where the air-fuel mixing is apparently enhanced by the swirl air.

5.4.3. Effect of Charge Air Temperature and Pressure

The Case A and Case B are made as comparing cases to evaluate the effect of charge air condition on in-cylinder spray and combustion process. Figure B-1 and Figure B-2 in Appendix B are the visualization results of Case A and Case B. Figure 5-9 shows the traces of cylinder pressure and apparent heat release rate of both cases. The apparent heat release rate shown in the figure is calculated from the measured crank-angle-based cylinder pressure data according to the first law of thermodynamics.

As shown in the figure, for Case B, most of the energy is released by pre-mixed combustion and only small portion of that is released by diffusion-controlled combustion. As shown in Figure B-2, the fuel delivery to the cylinder is started at about 2 degree BTDC and according to the measured injection pressure data, the injection is ended at about 8 degree ATDC. First visible flame started at about 3.3 degree ATDC at the downwind edges of the 3-and

8-o'clock sprays near the wall of the combustion bowl. The in-cylinder air swirl is in the clockwise direction. The direction of gas motion could be clearly observed in an animated movie. As mentioned previously, at the downwind side of each spray the air and fuel mixing is enhanced by the swirl air and, as shown in the picture of the 4.4 degree ATDC, those regions are the locations where the ignitions and initial stage of combustion occur. At 6 degree ATDC, the heat release reached its peak. At 7degree ATDC, the cylinder pressure reached its maximum pressure, 83.5 bar. Soot flame is observed in both the spray overlapping and the wall impingement regions. After 46 degree ATDC the flame becomes invisible.

As compared to Case B, Case A has much lower level of pre-mixed combustion heat release and most of the energy is released by diffusion-controlled combustion, which is a much more favorable combustion process in terms of reduction of NO_x emissions and combustion noise. As shown in Figure B-1, the fuel is introduced to the combustion chamber at about 2 degree BTDC and ended at about 8 degree ATDC. The ignitions and initial flames start at the downwind sides of the sprays, but as opposed to Case B they do not appear at the near wall regions. At 3.3 degree ATDC, Soot flame is observed at the spray wall impingement regions. At 6.0 degree ATDC, soot flame also appears in the spray overlapping regions. Most soot oxidizes after 8.7 degree ATDC. After 30 degree ATDC, the flame becomes invisible. As compared to Case B, the increase of temperature and pressure of the charge air has significant influence on the spray and combustion process. The higher

charge air temperature and pressure condition enhances further breakup of the liquid fuel droplet as the sprays proceed outward away from nozzle exit, and also accelerates the evaporation of the liquid fuel droplet, as a result the atomization, fuel distribution and air-fuel mixing are improved. The combustion of Case A is more uniformly across the combustion chamber while the combustion of Case B is more concentrating toward the near wall region and appears in a circular shape of combustion flame. Both cases have portion of air at the center region near the nozzle exit not being fully utilized.

Figure 5-10 compares the process of sprays and early development of combustion. As shown in the figure, the ignition delay of Case A has been reduced by about 0.6 ms. Table 5-1 summarizes the comparison. It shows the thermal efficiency of Case A is higher than that of Case B by 5 %, which could be attributed to shorter ignition delay and better fuel distribution, air-fuel mixing, and air utilization.

5.4.4. Effect of Injection Pressure

The Case D and E are used as the comparing cases to evaluate the effect of injection pressure on sprays and combustion process. For both cases, the injection pressures and nozzle specifications are carefully selected such that their injection quantity and injection rate are identical or closed enough to make a good base for case comparison. The average injection velocity of Case D is about 15% higher than that of Case E, due to the higher injection pressure.

Table 5-4 Comparison of Case A and Case B

Test Conditions and Results	Case A	Case B
Engine speed(rpm)	750	
Charge air conditions	110 deg C / 1.85 bar	75 deg C/ 1.5 bar
Peak motoring pressure(bar)	64	50
Injection timing (BTDC)	2	
Injection pressure(MPa)	101	
Injection Quantity(mg)	92.4	96.7
Ignition delay(ms)	0.6	1.2
Total heat release(kJ)	2.07	1.96
Thermal efficiency	0.52	0.47
Peak heat release rate(kJ/ degree)	0.265	0.615
Maximum liquid fuel penetration(mm)	21	27
Liquid phase fuel penetration rate(m/sec)	26	26

Figure 5-11 shows the comparison of cylinder pressure and apparent heat release rate. Figure B-4 and Figure B-5 in Appendix B are the visualization results of these two cases. Both cases show similar heat release pattern. The combustion of Case E is about 3 crank-angle degree later than that of Case D, which is attributed to longer injector response time and longer ignition delay. The ignition delay of Case E is about 0.2 ms longer that that of Case D. Both of the longer injector response time and ignition delay result from the lower injection pressure. Basically, sprays of higher injection pressure leave the nozzle holes with higher velocity and momentum. The higher velocity

sprays induces higher level of dispersion, and consequently better atomization and air/fuel mixing; more importantly when the higher momentum sprays collide with the wall of the combustion bowl higher level of spray rebound is generated, which enhances air entrainment rate. As shown in Fig B-5, for the case of lower injection pressure, the air utilization at the center region of the combustion bowl is very poor. Heavy soot flame is observed in the spray wall impingement region and spray-overlapping region. It is an evident that most of the vaporized fuel is distributed to and stagnant around the near wall region. Table 5-5 summarizes the comparison between Case D and Case E.

Similar situation can be found on the comparison of Case F and Case G. As shown in Fig B-7, with lower injection pressure, most of the combustion occur around the near wall region.

Table 5-5 Comparison of Case D and Case E

Test condition and results	Case D	Case E
Engine speed(rpm)	750	
Charge air condition	75 C and 1.5 bar	
Peak motoring pressure(bar)	57	
Injection timing (BTDC)	3	2
Injection pressure(MPa)	134	84
Injection Quantity(mg)	109	100
Ignition delay(ms)	1.2	1.4
Total heat release(kJ)	2.39	2.05
Thermal efficiency	0.51	0.48

5.4.5. Effect of Nozzle Type, Injection Rate, and Duration

The effect of nozzle configurations on spray and combustion is evaluated using two types of nozzle tip , 7-hole mini-sac and 6-hole VCO. The cases made for the comparsion are Case B and Case C. Non-uniform spray penetration of liquid phase fuel is observed at the early stage of injection of the VCO nozzle. However, within short period of time, about 0.4 ms or 2 crankangle degree, the spray penetration of liquid fuel becomes as uniform as that of the mini-sac nozzle. There is no difference found between these two types of nozzle in terms of the in-cylinder spray and combustion characteristics.

Case C and D are used to evaluate the effects of injection rate shape on spray and combustion process. The rate shape of HEUI injection is changed by changing the length of the rate shaping pipe which is a piece of high pressure steel tube connected the intensifier and the nozzle holder. The injection rate shape becomes smoother with increase of the length . In this study, 12" and 24" pipe are used for comparison. With increase of the length from 12" to 24", the rate of injection pressure decreases from 72 MPa/ms to 54 MPa/ms. The gradient of injection rate of Case D is about 15% higher than that of Case C. Figure 5-1 shows the comparison of cylinder pressure and heat release rate between the cases. Beside the difference in injector response time and injection quantity, there is no distinguishable difference found from the visualization. The late combustion of Case C is mainly due to the longer injector response time resulting from slower pressure rising rate.

Figure 5-13 shows the effect of injection duration on combustion and heat release rate for Case D and G, while Figure 5-14 is for comparison between Case E and F. The results show that longer combustion duration and higher cylinder pressure result from longer injection duration, but there is no change on the heat release pattern

5.4.6. Sprays and Combustion with Pilot Injection

Figure B-8 shows the visualization result of a two-stage injection. The engine operating condition is 1000 rpm with charge air of 80 degree C and 1.48 bar . As shown in Figure 5-15, the pilot is issued at 13 degree BTDC and ended at 9 degree BTDC, with duration of 0.8 ms and quantity of 13.4 mg that is accounted as 16 % of the total injection quantity. It is followed by a 2.25-ms and 70.5-mg main injection issued at 3 degree BTDC and ended at 10 degree ATDC. The dwell time between the pilot and the main is 0.6 ms. The injection rate is shown as trace "a" in Figure 2-17. The peak injection pressures of the pilot and main are 65 MPa and 110 MPa respectively. After end of the pilot at 8.2 degree BTDC, the ignition and start-of-combustion of the pilot injection occur simultaneously at several spots near the center of the combustion bowl. The combustion occurred mainly along the spray paths and as it proceeds its shape is changed and twisted slightly by the clockwise swirl air. Combustion in the spray wall impingement region is weak. At 3 degree BTDC the main injection is issued directly into the pilot flame, the main combustion starts almost immediately , and the pilot flame decays partially due to the issue of

the main injection. After 5 degree ATDC, several heavy soot combustion zones are observed at the spray wall impingement regions due to oxygen deprivation by the pilot flame. The cylinder pressure and heat release curves of the pilot-injection combustion along with needle lift signal are shown in Figure 5-16. It demonstrates that a mild pre-mixed combustion followed by a strong and smooth diffusion-control combustion is realized by the application of two-stage injection. The application of pilot injection significantly reduces the peak heat release rate of the pre-mixed combustion. However, to optimize the combustion process, the timing, quantity, and dwell time of the pilot injection need to be further refined.

5.4.7. Recommendations on the Design of High IMEP Combustion

Based on the results and experience obtained from the study, recommendations on the design of fuel Injection and combustion system to achieve high IMEP combustion are described as follows..

Increase of charge air density and fully utilization of the air available in the cylinder are known as the approaches to achieve a high IMEP combustion. (Chen et. Al.,1997). High-pressure injection has also been reconiged as a requirement of the injection system for high IMEP combustion system.However, as observed in this study, with high pressure injection the air in the center of the combustion chamber ihas not been fully utilized . For combustion system with high-pressure injection, how to effectively use the air in the center of the combustion chamber is one of the key to achieve high

IMEP combustion. One of the approach could be let the ignition start as earlier as possible at the center of combustion chamber near the nozzle exit and have the combustion start from center and proceed toward the wall region.To realize the approach, high injection pressure with small nozzle hole diameter and pilot injection , along with high-density and -temperature charge air and slight swirl air, are the features recommended for the design of high IMEP combustion system. With high injection pressure, the amout of fuel required to fully utilize the air available in the cylinder can be delivered within short period of time to avoid late combustion. The application of small nozzle hole associated with high injection pressure reduces the droplet sizes and increase the velocity and momentum of the droplet, as a result atomization and air-fuel mixing can be enhanced. With pilot injection, a small amount of fuel is issued to the cylinder close to the end of compression stroke;after evaporation, air-fuel mixing, and ignition delay, a small scale of combustion starts prior to the issue of the main injection. With pilot flame appears in the chamber, the combustion chamber is conditioned with higher bulk gas temperature and radicals, hence the main combustion can occur right after the injection is issued with very limited delay. COnosequently, the high pre-mixed heat release will no more appear. In stead, a fast and smooth combustion can be achieved.

An ideal pilot woulb be a small amount of fuel being delivered with high prssure and short duration at the timing that can be changed according to engine speed. The CR injection system can be the one that meet this requirement in terms of injector response time and in-time availability and

flexibility of injection pressure, if its asymmetry fuel distribution, especially at the circumstance of low needle lift operating condition, and peak operating pressure can be improved.

High density and temperature charge air can reduce ignition delay and enhance atomization, evaporation, and air-fuel mixing. However, the charge air temperature need to be carefully selected to minimize the impact on volumetric efficiency.

With respect to the spray characteristics, uniform hole-to-hole spray penetration and minimized spray cone angle oscillation are the basic requirement for injection system of high IMEP combustion.
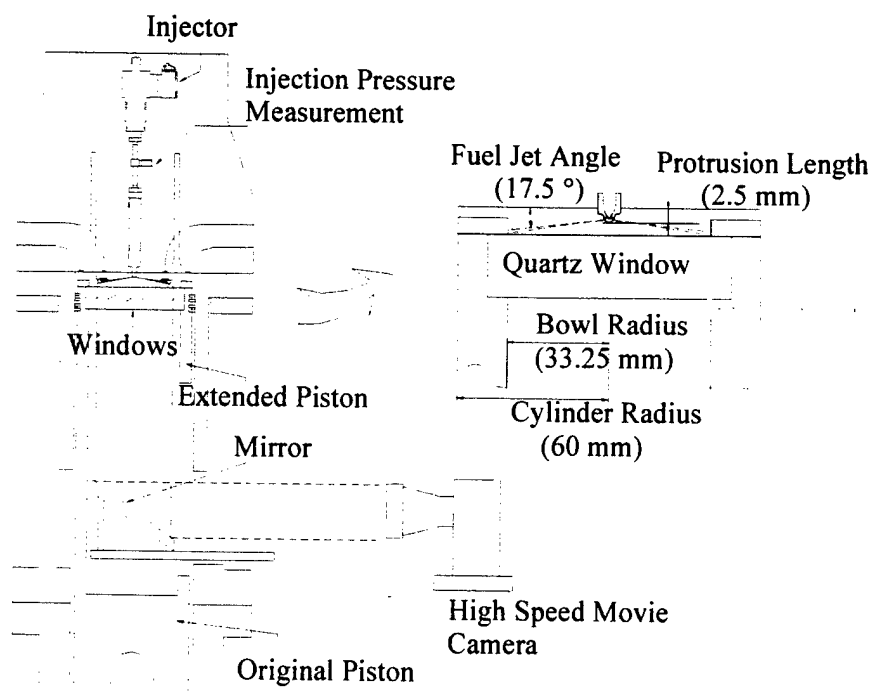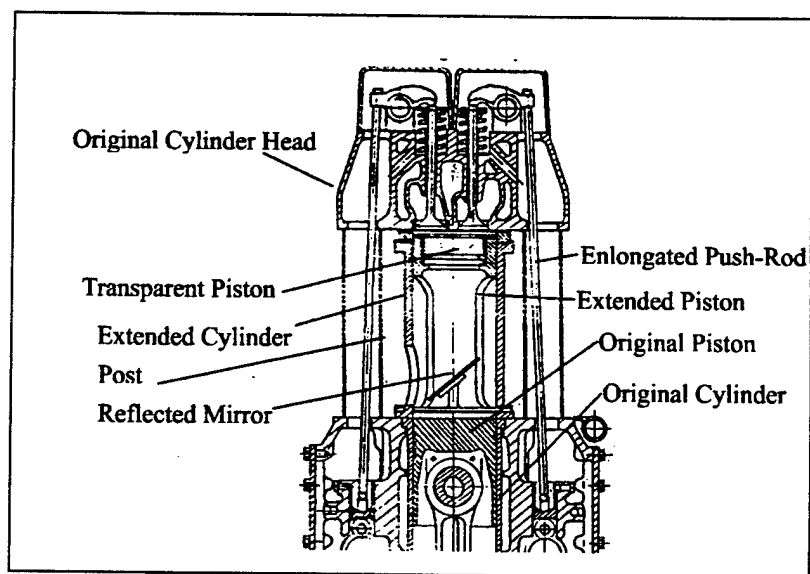
Figure 5-1 Schematic of the basic structure of the OAE engine(as top) and the experimental setup for in-cylinder spray and combustion visualization (as bottom)
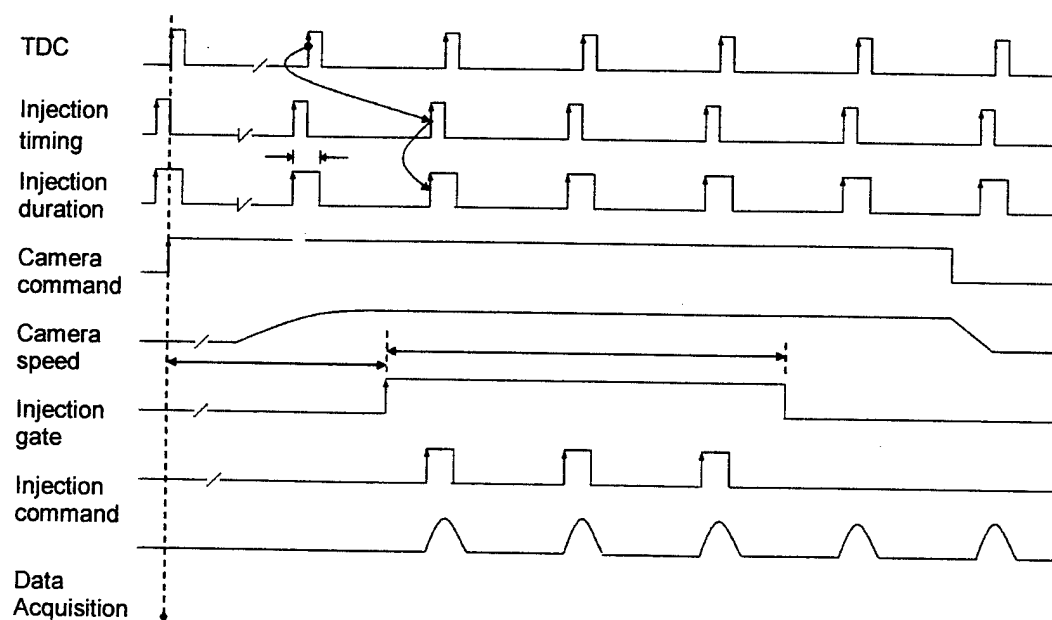
Figure 5-2 Control and synchronization logic for the test of OAE spray and combustion visualization
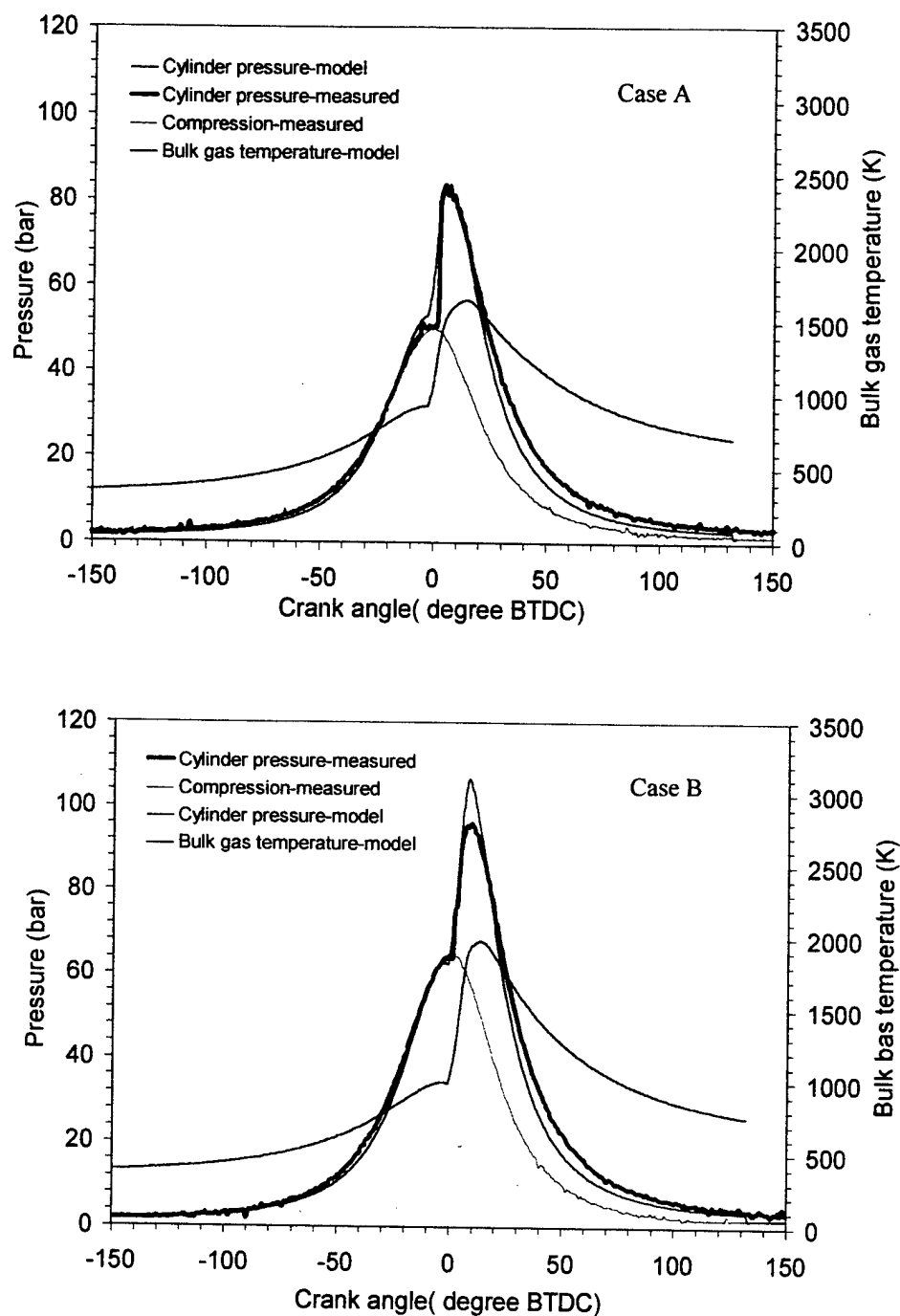
Figure 5-3 Calculated bulk gas temperature and correlation between calculated and measured cylinder pressures; chart at top for Case A and bottom one for Case B.
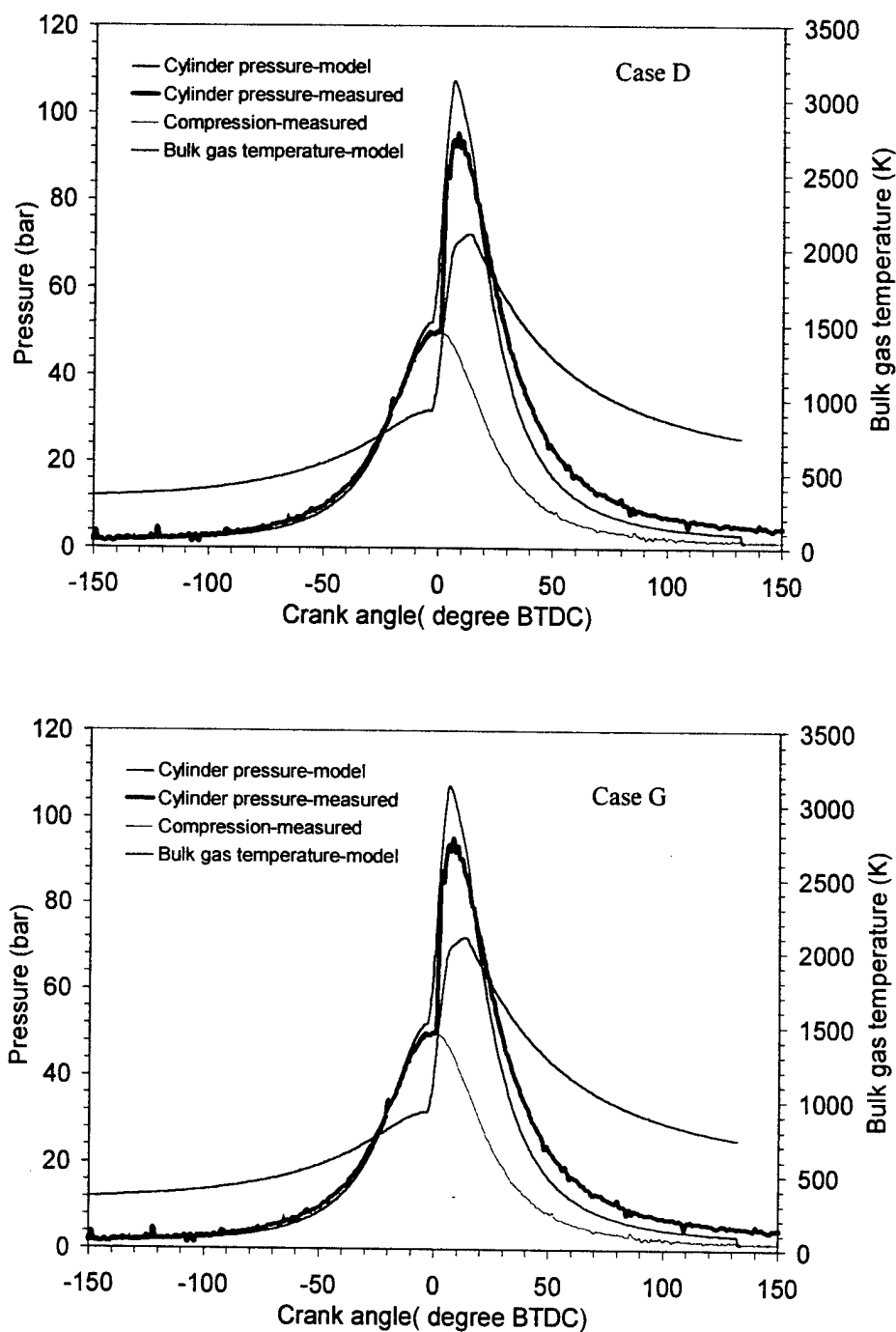
Figure 5-4 Calculated bulk gas temperature and correlation between the calculated and measured cylinder pressures; chart at top for Case D and bottom one for Case G.

620 mini-sac nozzle

In-cylinder spray visualization
Image is taken at 1 degree BTDC- about 0.2 ~0.3 ms after SOI, with 50-bar cylinder pressure and 922-K cylinder bulk gas temperature.

Nitrogen-filled pressurized chamber spray visualization
Image is taken at 0.24ms after SOI – with 27.6-bar ambient pressure and 298-K ambient temperature.
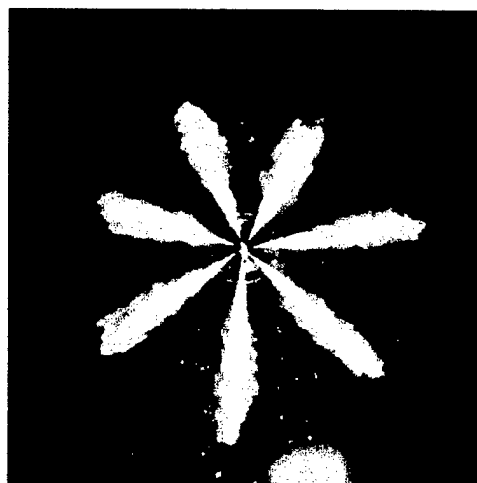
48 mm

Figure 5-5 Comparison of non-evaporative and evaporative sprays of the HEUI system with 620 mini-sac nozzle

610 VCO

In-cylinder spray
visualization
 Image is taken at 1
degree BTDC- about
0.2 ~0.3 ms after SOI,
with 50-bar cylinder
pressure and 922-K
cylinder bulk gas
temperature.
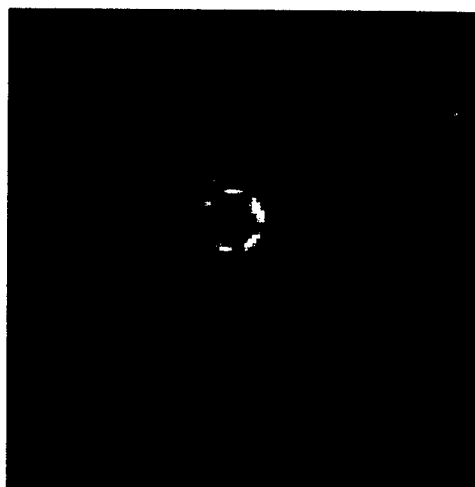
Nitrogen-filled
pressurized chamber
spray visualization
Image is taken at
0.24ms after SOI – with
27.6-bar ambient
pressure and 298-K
ambient temperature.
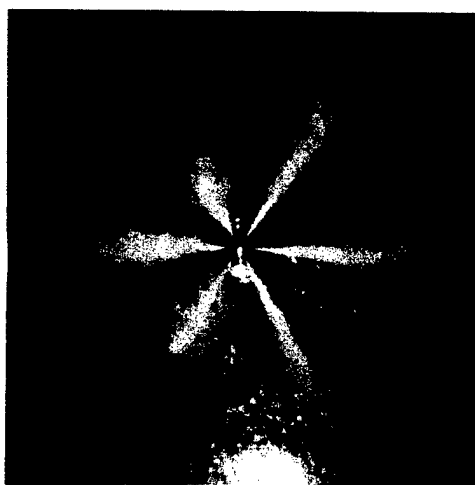
48 mm

Figure 5-6 Comparison of non-evaporative and evaporative sprays of
the HEUI system with 610 VCO nozzle.
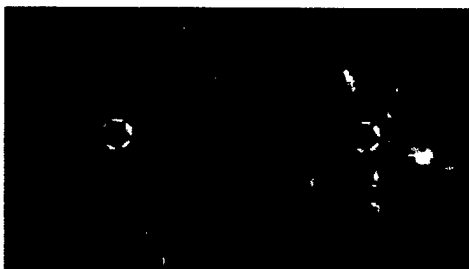
Figure 5-7 Ignition and start of combustion, with test condition of Case D (610 VCO nozzle)
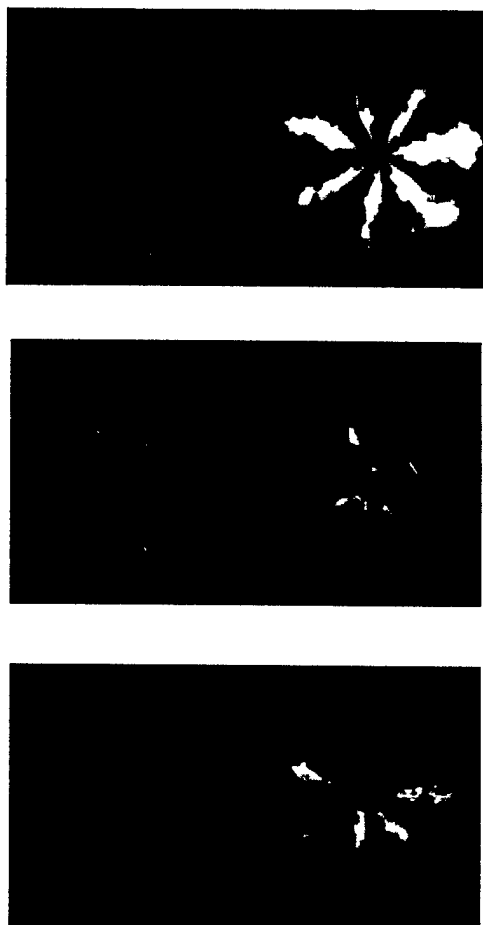
Figure 5-8 Ignition and start of combustion, with test condition of Case A (620 mini-sac nozzle)
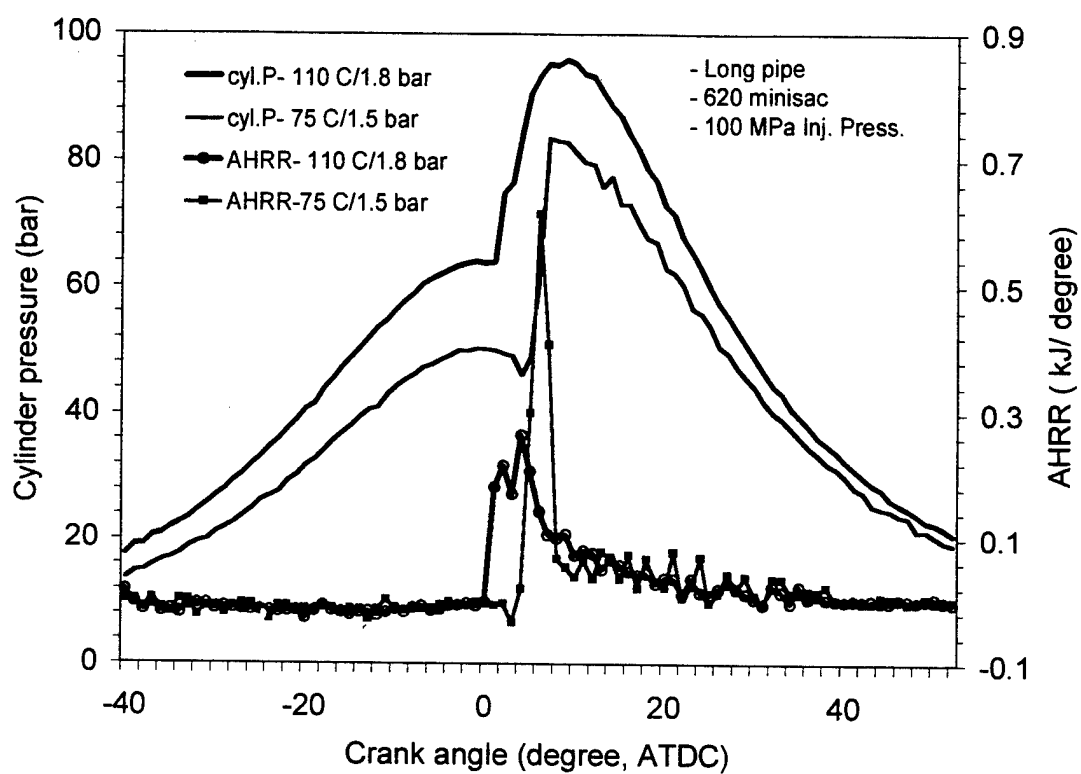
Figure 5-9 Comparison of cylinder pressure and heat release rate of Case A and Case B.

SOI at 2 degree BTDC, 62.6-bar cylinder pressure and 999-K cylinder
gas temperature
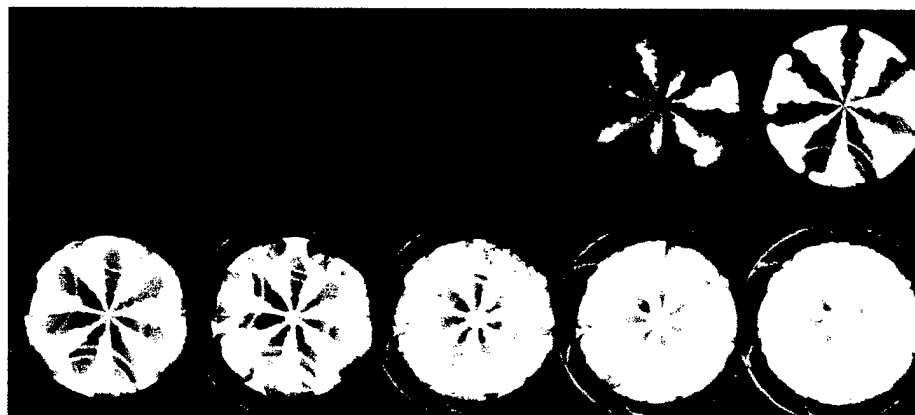
SOI at 2 degree BTDC, 49.5-bar cylinder pressure and 928-K
cylinder gas temperature
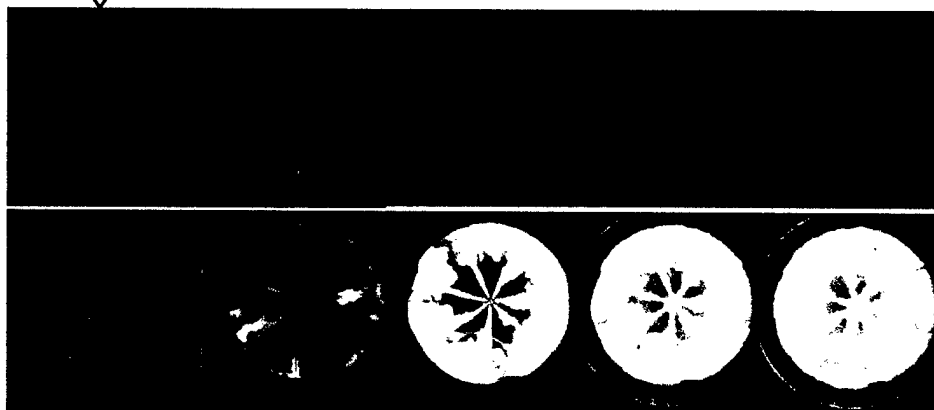
Figure 5-10 Comparison of spray and combustion process of Case A
and Case B.
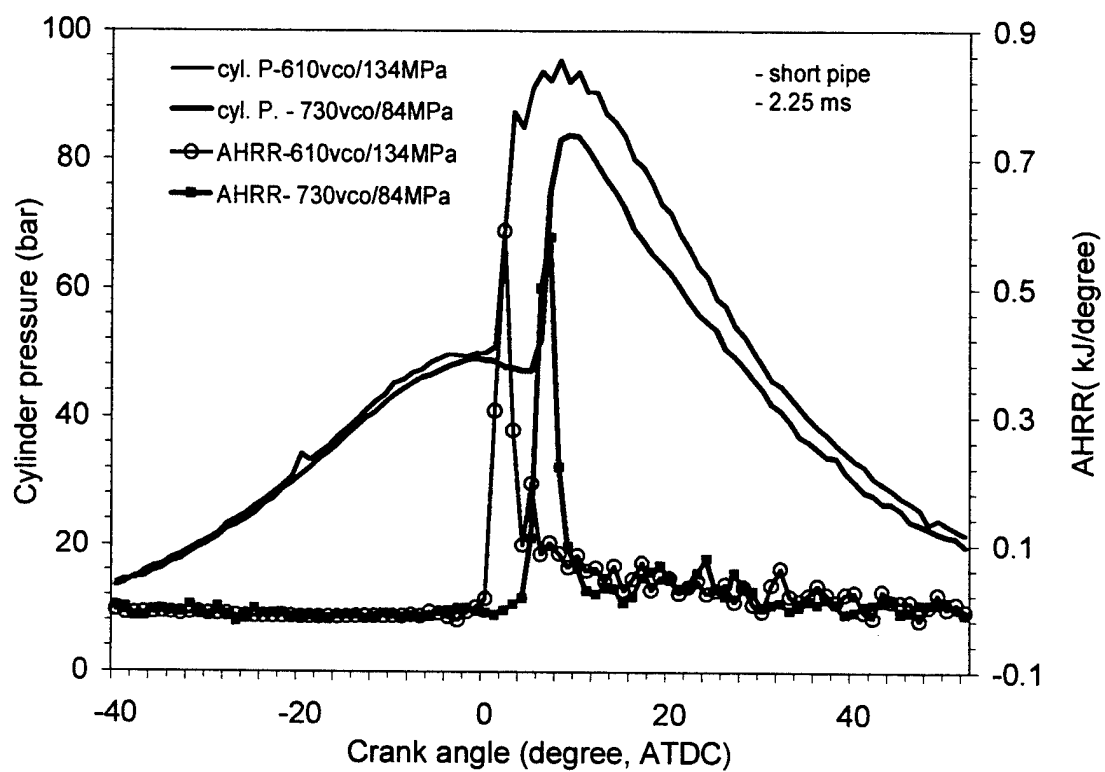
Figure 5-11 Comparison of cylinder pressure and heat release rate of Case D and Case E.
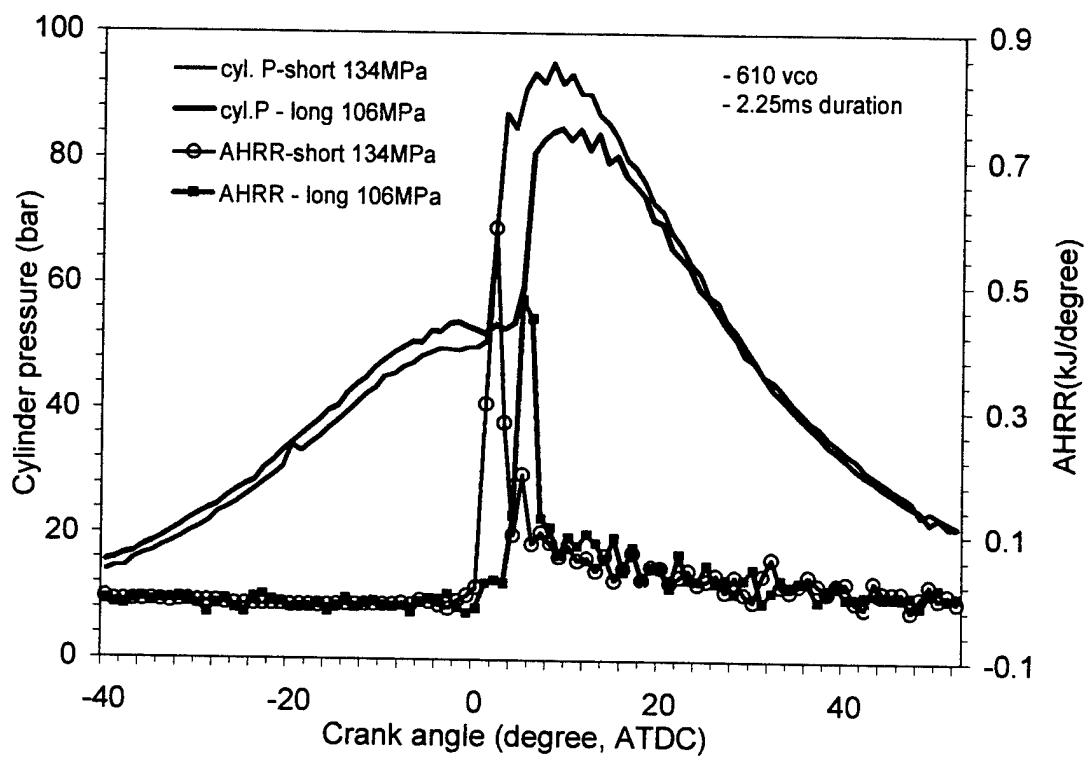
Figure 5-12 Comparison of cylinder pressure and heat release rate of Case C and Case D.
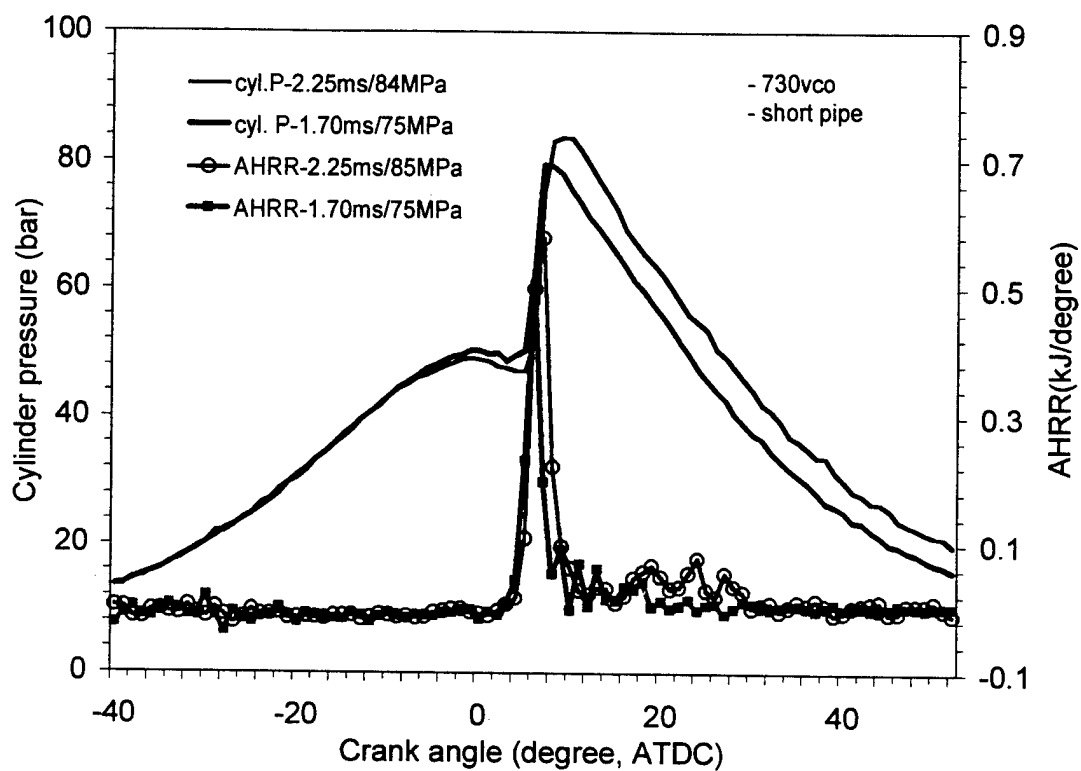
Figure 5-13 Comparison of cylinder pressure and heat release rate of Case D and Case G.
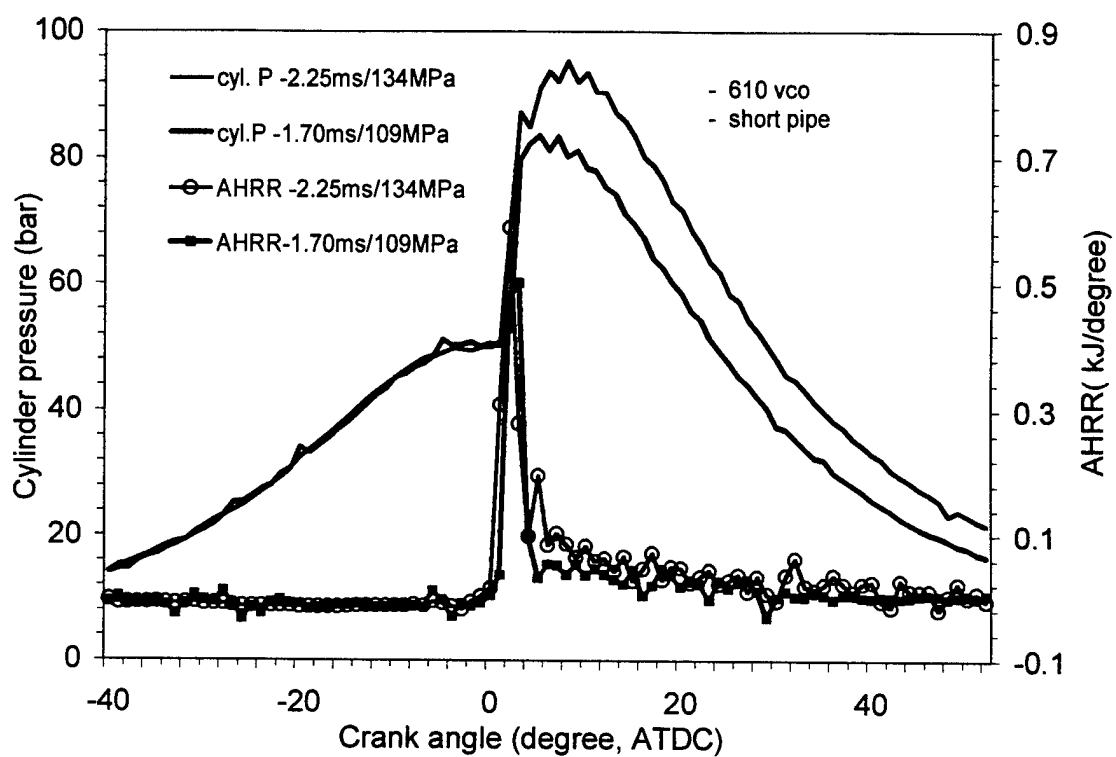
Figure 5-14 Comparison of cylinder pressure and heat release rate of
Case E and Case F.

Pilot injection is issued at 13 degree BTDC with pressure of 65 MPa (about half of the main injection) and injection quantity about 16 % of the total injection quantity.

After the pilot injection stops, Ignition starts at several spots near the center of combustion bowl. Weak wall impingement combustion is observed. The combustion occurs mainly along the spray paths and is twisted by the swirl air.

Main Injection Starts at 3.3 degree BTDC. The sprays are issued into the pilot flame.
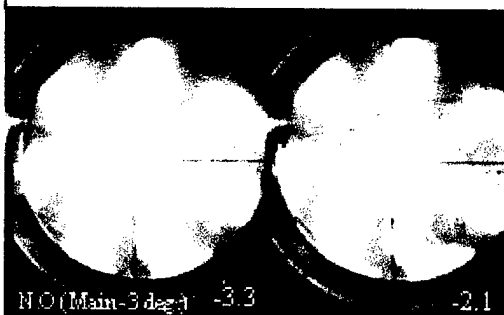
Pilot flames decay. Combustion of the sprays of the main injection starts with soot flame formed in several spots

Figure 5-15 Spray and combustion visualization of combustion with pilot injection
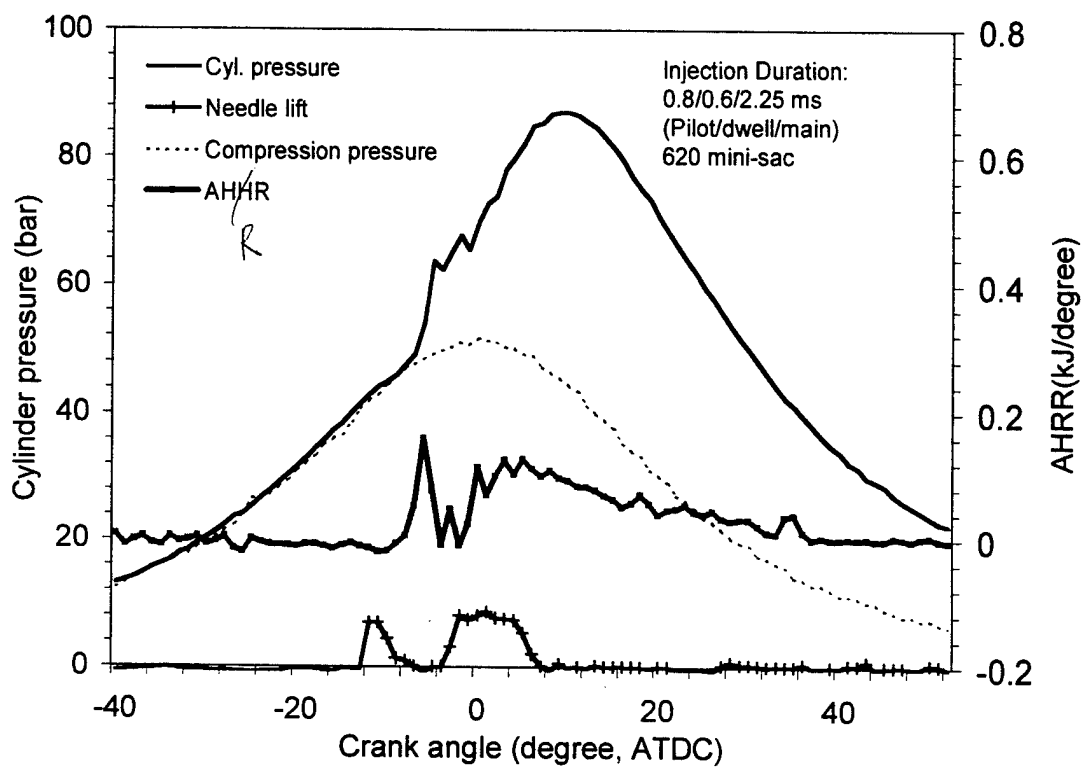
Figure 5-16 Cylinder pressure and heat release rate of combustion with pilot injection; injection event: 0.8ms-pilot/0.6ms-dwell/2.25ms-main.

CHAPTER 6

CONCLUSIONS AND RECOMMENDATIONS

6.1 Conclusions

Injection characterization of three types of modern high-pressure diesel injection system, EUI, HEUI, and Common Rail system, has been conducted to evaluate the effects of design parameters and operating conditions on injection characteristics such as injector response time, needle lift, pressure, rate, and quantity. The needle lift of the CR system is significantly different from that of the HEUI system. The needle lift time of CR injector is much longer and is strongly affected by the injection pressure. Due to the design and operating principle, the system is operating in partial lift condition regularly, especially for short injection duration and low injection pressure.

Both macroscopic and microscopic visualization methods have been applied to visualize the behavior of non-evaporative sprays of the injection systems. The methods provide a good measure for the fuel distributing performance of specific nozzles or injection system in terms of penetration, cone angle, structure, and hole-to-hole variation of the diesel sprays. The microscopic visualization results provide very interesting and dynamic information on spray structure, showing spray angle variations, injection-to-injection variation, and primary breakup processes not observed using conventional macroscopic visualization techniques In this study, specific findings are summarized as follows.

- Both injection pressure and ambient pressure affect the spray tip penetration significantly.

- The variation of spray penetration depends on type of injection system, nozzle configuration, and ambient pressure. The large variation observed on the CR sprays could be caused by eccentricity of the VCO nozzle and exaggerated by the low needle lift under low injection pressure operating condition. From the results HEUI spray visualization, the mini-sac nozzle has 50% less variation than that the VCO nozzle

- The near-field spray behavior is shown to be highly transient, which strongly depends on the injector design, nozzle configuration, needle lift and vibration, and injection pressure.

- The spray cone-angle observed for the injector of the EUI system is larger at the early transient stage of needle lift. For the CR system, the spray cone angle shows conspicuous oscillation during pilot or main injection period, possibly due to needle eccentricity and oscillation.

Direct in-cylinder visualization of global sprays and combustion process of single and multi-stage high-pressure direction injection has been conducted in this study. The visualization results associated with measured cylinder pressure and calculated apparent heat release rate provided useful information for studying of Diesel combustion. Especially, this method could be applied to optimizie the application of pilot injection in terms of injection

rate, quantity, and timing to best match it with the main injection under various engine operating conditions. Specific findings are summarized as follows.

- At high load condition the pilot injection significantly reduces the peak heat release rate of the pre-mixed combustion, which is favorable to the reduction of NOx emissions and combustion noise. With pilot injection, the pre-mixed combustion of the main injection is not observable. It is seemed that the diffusion-controlled combustion of the main injection got started right after the main injection is issued. How would the sprays of main injection interact with pilot flame would be an interesting subject for future study.

- By increase of pressure and temperature, up to 1.85 bar and 110 degree C, of the charge air, the maximum liquid fuel penetration is reduced by about 20% for the case of injection with 100 MPa peak pressure, and the air utilization of the combustion is also improved. Therefore, it could be an effective approach to avoid liquid fuel impingement on the wall of combustion bowl and to improve fuel distribution, atomization, and air-fuel mixing, especially for high load and high-pressure injection engine operating condition.

- At 65% load condition, with charge air of 1.5 bar and 75 degree C the high pressure injection tends to distribute the fuel to the near wall region, which could cause rich combustion around the wall and

lean combustion at the center region. The situation is getting worse by adopting nozzle with larger hole flow area.

- With high-pressure injection the ignition and start of combustion most likely occurred at the sprays' downwind where the air-fuel mixing is enhanced by swirl air.

6.2 Recommendations for Future Work

Large spray cone angle variation is observed on CR and EUI sprays. Large drops and liquid ligament forms at end of injection are observed on all of the three types of injection system. Further research on how would this transient spray behavior affect HC and Particulate emissions could be beneficial to refinement of diesel engine emissions.

The CR system demonstrate high potential and capability to deliver fuel for advanced diesel engine in terms of its short injector response time and in-time availability and flexibility of high-injection pressure. However the highly asymmetry and large and inconsistent spray cone angle of the VCO sprays need to be improved.

The application of pilot injection significantly reduces the peak heat release rate of the pre-mixed combustion. It demonstrates that a mild pre-mixed combustion followed by a strong and smooth diffusion-control combustion is realized by the application of two-stage injection. However, to

optimize the combustion process, the timing, quantity, and dwell time of the pilot injection need to be further refined.

APPENDIX A

EQUATIONS FOR COMBUSTION MODELLING

(A) Governing Equations for Heat-Release Model

Spray Tip Penetration in Quiescent Air

(a) For packages on the spray centerline

$$S = C_V \sqrt{\frac{2\Delta P}{\rho_l}} t \qquad , 0 < t < t_b \qquad (A1)$$

$$S = 2.95 (\frac{\Delta P}{\rho_a})^{1/4} \sqrt{d_0 t} \, , t \geq t_b \qquad (A2)$$

where $C_V = 0.55,$ Coefficent of Effective Injection Velocity

$$t_b = 28.65 \frac{\rho_l d_0}{\sqrt{\rho_a \Delta P}}$$

S = penetration

ΔP = injection pressure

ρ_l = density of fuel

ρ_a = density of ambient gas

d_0 = diameter of nozzle hole

(b) For packages in the radial direction away from the spray centerline

$$S_L = S \times \exp(-4.403 \times 10^{-3} \times (L-1)^2) \qquad (A3)$$

where $L = 2,3,....,$ denotes number of packages
injected per injection interval.

Spray Tip Penetration in Swirling Air

$$S_s = C_s \times S$$

$$C_s = (1 + \frac{\pi \, r_s \, nS}{30 U_i})^{-1} \qquad \qquad \text{(A4)}$$

where r_s = swirl ratio

n = engine speed

U_i = Initial spray - tip penetration velocity

Air Entrainment Rate

$$m_a = m_f \times (U_0 \frac{dt}{dS} - 1) \qquad \qquad \text{(A5)}$$

where U_0 = spray injection velocity

m_a = mass of air

m_f = mass of fuel

(a) Before start of combustion and wall impingement

$$\frac{dm_{ae}}{dt} = \frac{dm_a}{dt} \qquad \qquad \text{(A 6a)}$$

(b) After start of combustion but before wall impingement

$$\frac{dm_{ae}}{dt} = C_f \frac{dm_a}{dt} \qquad (A\,6b)$$

where $C_f = 0.7$

(c) After wall impingement

$$\frac{dm_{ae}}{dt} = C_w \frac{dm_a}{dt} \qquad (A7)$$

where $C_w = 1.5$

Spray Deflection in the Swirl Direction

$$r_{def} = S(\frac{m_a}{m_a + m_f})(\frac{\frac{n}{60} r_s 2\pi S}{\frac{U_0 + U}{2}}) \qquad (A8)$$

where r_s = swirl ratio

n = engine speed

U_0 = initial injection velocity

U = injection velocity

Droplet and Spray Evaporation

- Injected-Droplet Sauter Mean Diameter(SMD)

$$SMD = 23.9(\Delta P)^{-0.135} \rho_a^{0.12} B^{0.131} \qquad (A9)$$

where B = quantity of fuel injection per stroke

- **Single-Droplet Evaporation Equations**

$$\frac{dT_l}{dt} = \frac{1}{m_l C_{Pl}}[\pi D_l h(T_2 - T_l) + \lambda \frac{dm_l}{dt}] \qquad (A10)$$

$$\frac{dD_l}{dt} = \frac{2}{\pi D_l^2 \rho_l}[\frac{dm_l}{dt} - \frac{\pi D_l^3}{6}\frac{d\rho_l}{dt}] \qquad (A11)$$

$$\frac{dm_l}{dt} = -\pi D_l^3 k(\frac{Y_{f0} - Y_{f2}}{(1+\xi)Y_{f0}}) \qquad (A12)$$

$$m_{fg} = \frac{\pi}{6}(\rho_{l0}D_{l0}^3 - \rho_l D_l^3)N \qquad (A13)$$

where T_l = temperature of liquid fuel

$\quad C_{pl}$ = specific heat at constanrt pressure

$\quad D_l$ = diameter of liquid droplet

$\quad h$ = heat transfer coefficient between droplet and air

$\quad T_2$ = bulk gas temperature

$\quad Y_{f0}$ = mass fraction of vaporized fuel, surface

$\quad Y_{f2}$ = mass fraction of vaporized fuel, bulk

$\quad m_{fg}$ = mass of vaporized fuel

$\quad \xi$ = transfer number

$\quad k$ = mass transfer constant

Ignition Delay of Gaseous Fuel

$$\phi_g = \frac{m_{fg}}{m_g F_{st}} \qquad (A14)$$

$$\tau = 2.0 \times 10^{-2} P^{-2.5} \phi_g^{-1.04} \exp(\frac{4000}{T_2}) \qquad (A15)$$

$$\int_0^{\tau_i} \frac{1}{\tau_i} dt = 1 \qquad (A16)$$

where ϕ_g = equivalence ratio for vaporized fuel

$\quad F_{st}$ = stoichiometric air - fuel ratio

$\quad \tau$ = ignition delay, ms

Heat Release Rate

$$\Delta m_{fi} = \Delta m_{fui} \quad ,(\phi \leq 1)$$
$$\Delta m_{fi} = \Delta m_{fci} \quad ,(\phi > 1) \tag{A17}$$
$$\Delta Q_b = H_u \sum_{i=1}^{n} \Delta m_{fi} \tag{A18}$$

where Δm_{fi} = mass of fuel burned in the package

Δm_{fui} = mass of fuel evaporated in the package

Δm_{fci} = mass of fuel burned at stoichimetric ratio

H_u = fuel heating value

Heat Loss due to Heat transfer to the wall

$$Q_w = A h_w (T - T_w) \tag{A19}$$

where $h_w = 265 \times B^{-0.2} P^{0.8} V_p^{0.8} T^{-0.53}$

A = combustion chamber wall area

h_w = heat transfer coefficient between burned gas

and cylinder wall

B = engine bore size

P = cylinder pressure

V_p = instaneous piston velocity

Net Rate of Heat Release and Pressure Change

$$\frac{dQ}{d\theta} = \frac{dQ_b}{d\theta} - \frac{dQ_w}{d\theta} \tag{A20}$$

$$\frac{dP}{d\theta} = \frac{1}{V}[(k-1)\frac{dQ}{d\theta} - kP\frac{dV}{d\theta}] - k\frac{C}{\omega}P \tag{A21}$$

$$\text{where } k = \frac{C_p}{C_v}$$

$$C = \frac{\dot{m}_b}{m}, \text{Blow - by rate}$$

$\dot{m}_b$ = mass blowby rate

m = air mass in the cylinder

ω = crank shaft angular velocity

Q_b = net heat release

Q_w = net heat transfer

(B) Equations used in the Crevice Flow Model for Blow-by Calcualtion

<u>The Orifice Flow Equation for the calculation of mass flow rate through ring gap</u>

$$\dot{m} = C_d A_g \rho c \eta \qquad\qquad (A22)$$

where $C_d = 0.86$, disch arge coefficient

A_g = Ring gap area

ρ = upstream gas density

c = speed of sound

η = compressibility factor for isentropic flow

$$= \left\{ \frac{2}{\gamma - 1} [(\frac{P_u}{P_d})^{2/\gamma} - (\frac{P_u}{P_d})^{\frac{\gamma+1}{\gamma}}] \right\}^{1/2}, \text{for } \frac{P_u}{P_d} > 0.52$$

$$= (\frac{2}{\gamma + 1})^{\frac{\gamma+1}{2(\gamma-1)}}, \text{for } \frac{P_u}{P_d} \leq 0.52$$

where γ = specific heat ratio of the gas

P_u = Upstream pressure

P_d = Downstream pressure

Mass flow rate through the ring-side clearance

$$\left(\frac{\dot{m}}{A}\right) = \frac{h^2}{24w_r} \frac{1}{\mu_{gas}RT}(P_u^{\,2} - P_d^{\,2}) \qquad (A24)$$

where h = Ring side clerance

w_r = ring width

μ_{gas} = viscousity of gas

A = Flow area

APPENDIX B

HIGH-SPEED PHOTOGRAPHS OF COMBUSTION VISUALIZATION

Spray and combustion visualization results for eight test cases are included in this appendix. Detail of test condition of each test case is described in the text box at the bottom of each figure.
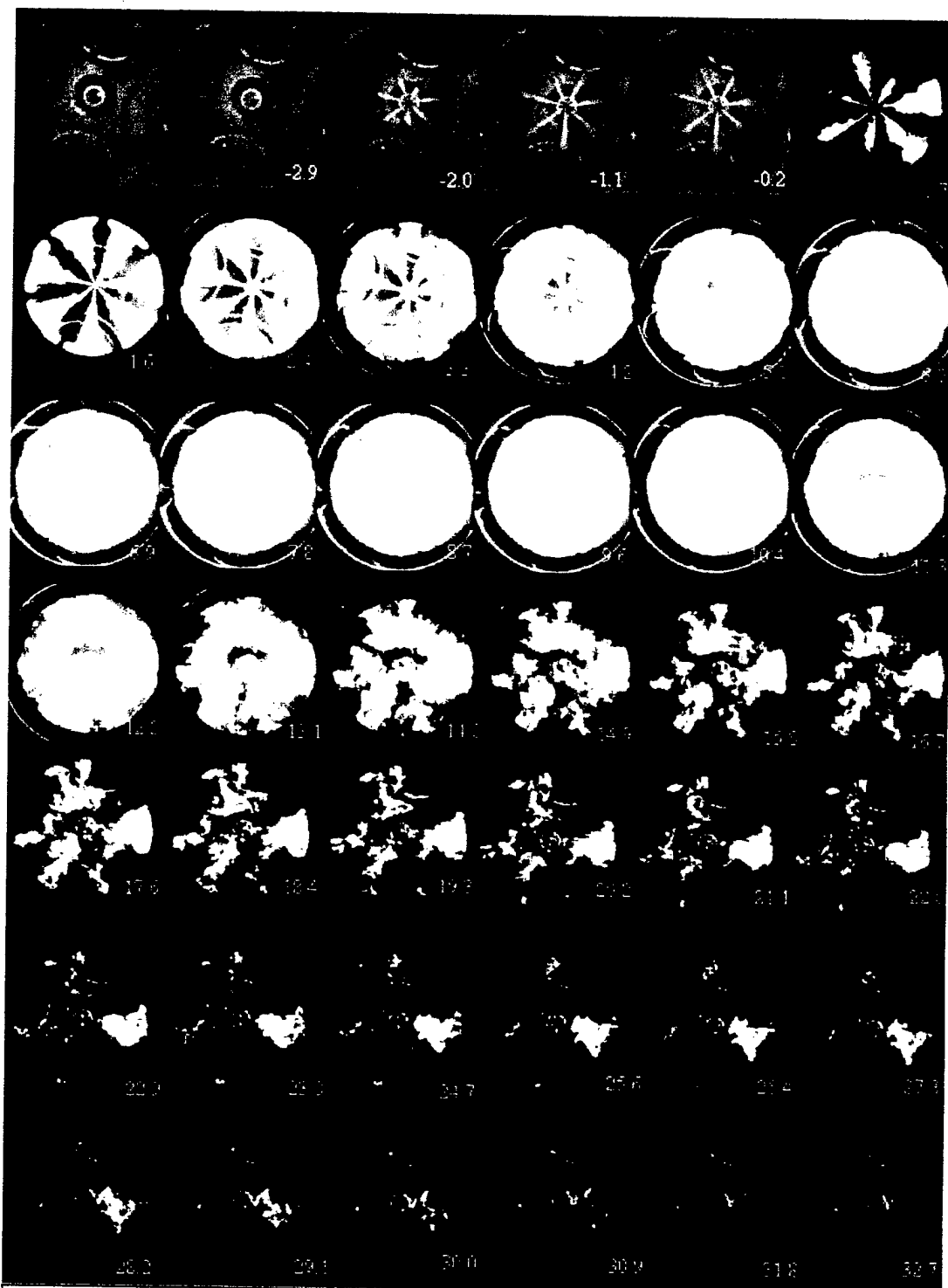
Figure B-1 Combustion images – Case A
Test condition: 750 rpm, 10-degree BTDC injection timing, 2.25-ms injection duration, 110 C/ 1.85 bar charge air, 101-MPa peak injection pressure, 620 mini-sac nozzle, and 24" rate shaping pipe.
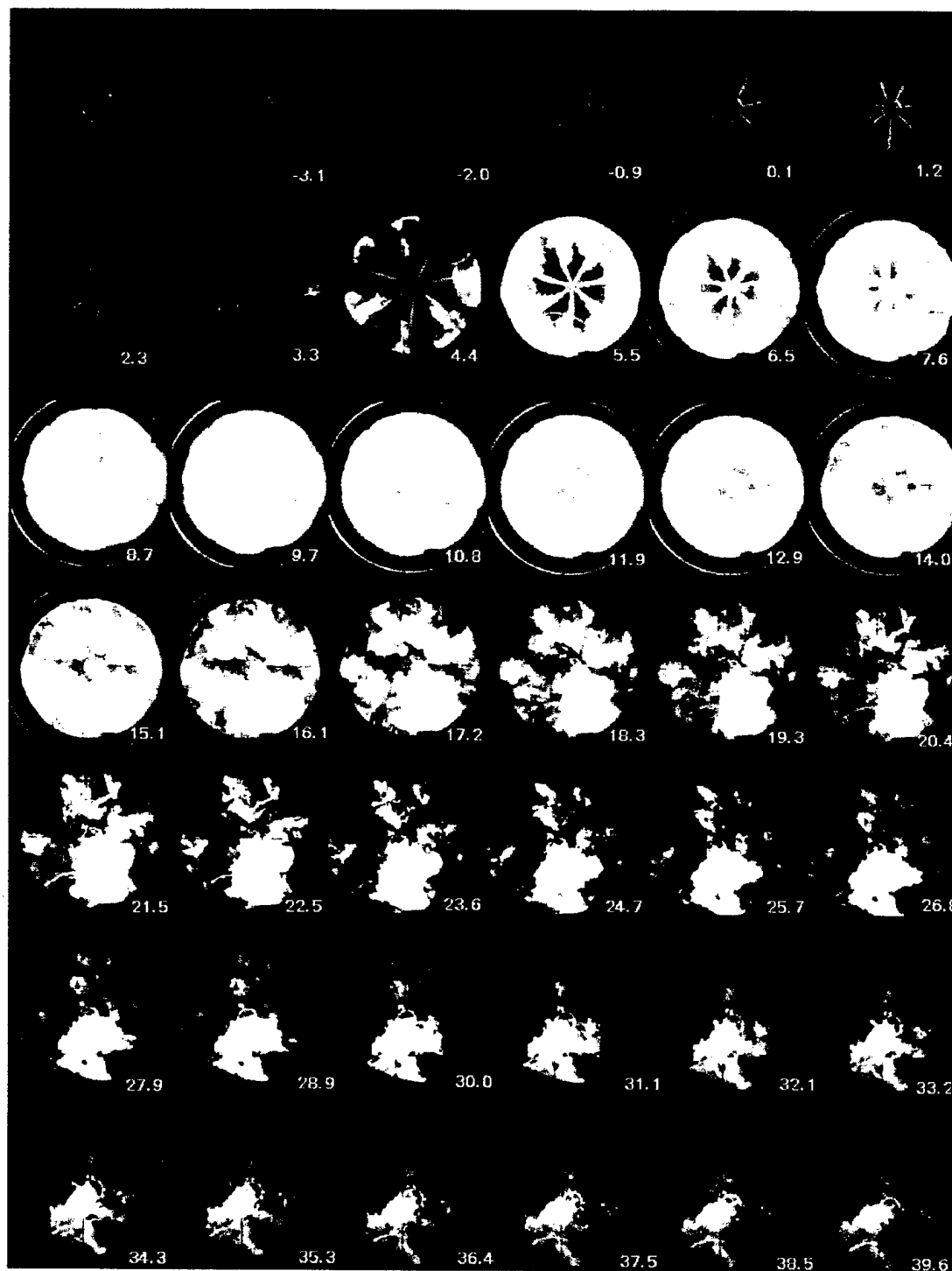
Figure B-2 Combustion images – Case B
Test condition: 750 rpm, 10-degree BTDC injection timing, 2.25-ms injection duration, 75 C/ 1.50 bar inlet air, 101-MPa peak injection pressure, 620 mini-sac nozzle, and 24" rate shaping pipe.
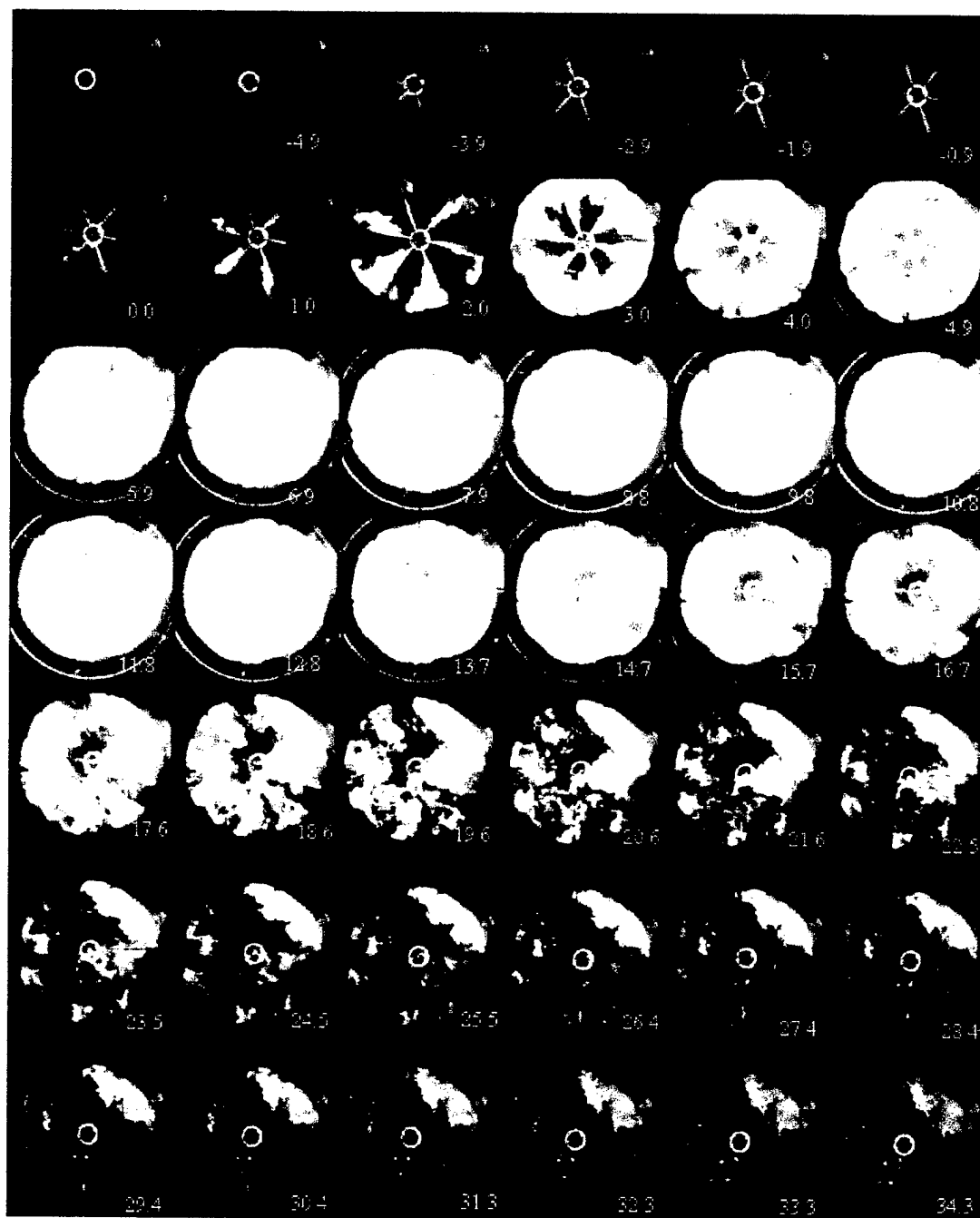
Figure B-3 Combustion images – Case C
Test condition: 750 rpm, 10-degree BTDC injection timing, 2.25-ms injection duration, 75 C/ 1.50 bar inlet air, 134-MPa peak injection pressure, 610VCO nozzle, and 24" rate shaping pipe.
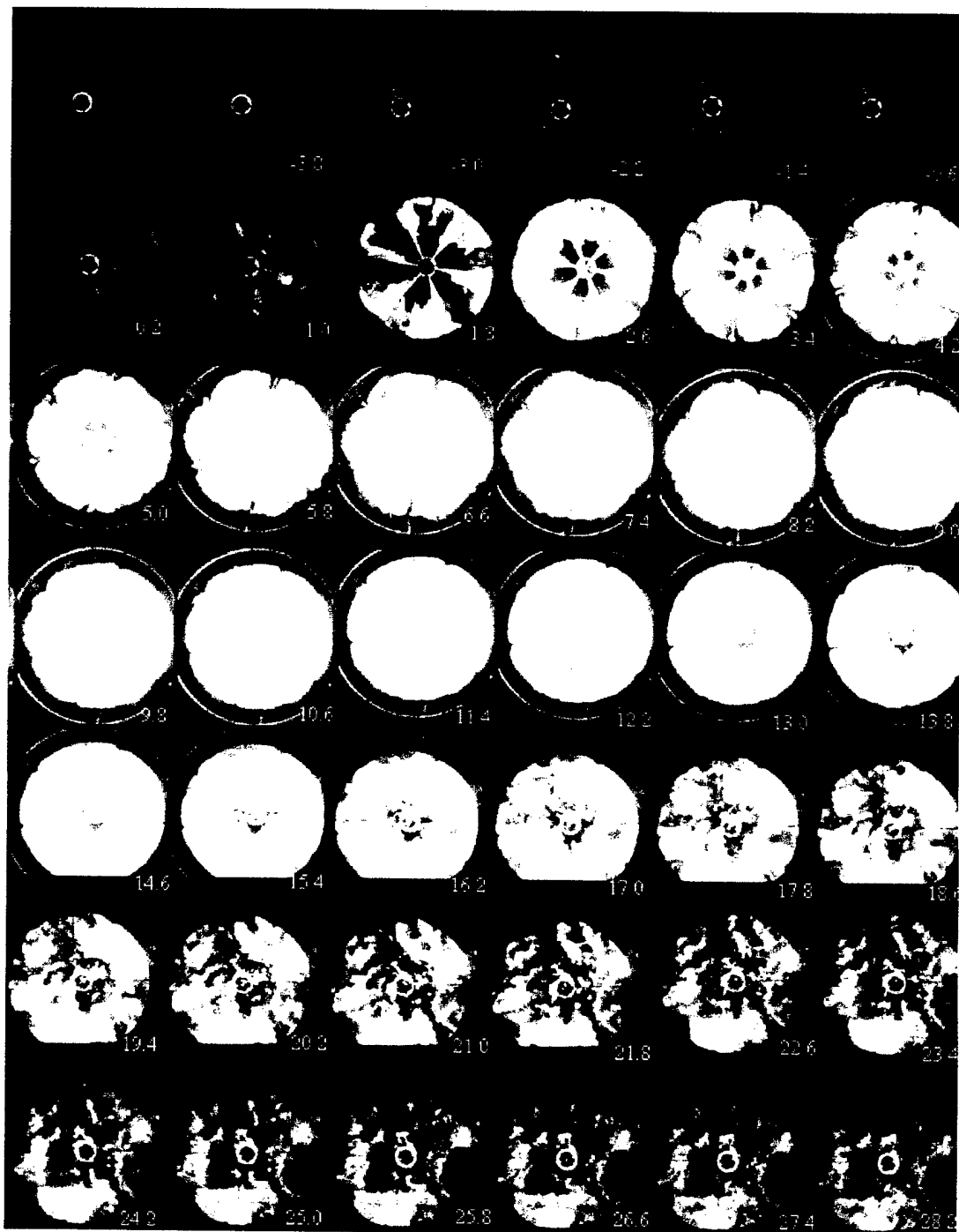
Figure B-4 Combustion images – Case D
Test condition: 750 rpm, 10-degree BTDC injection timing, 2.25-ms injection duration, 75 C/ 1.50 bar charge air, 134-MPa peak injection pressure, 610VCO nozzle, and 12" rate shaping pipe
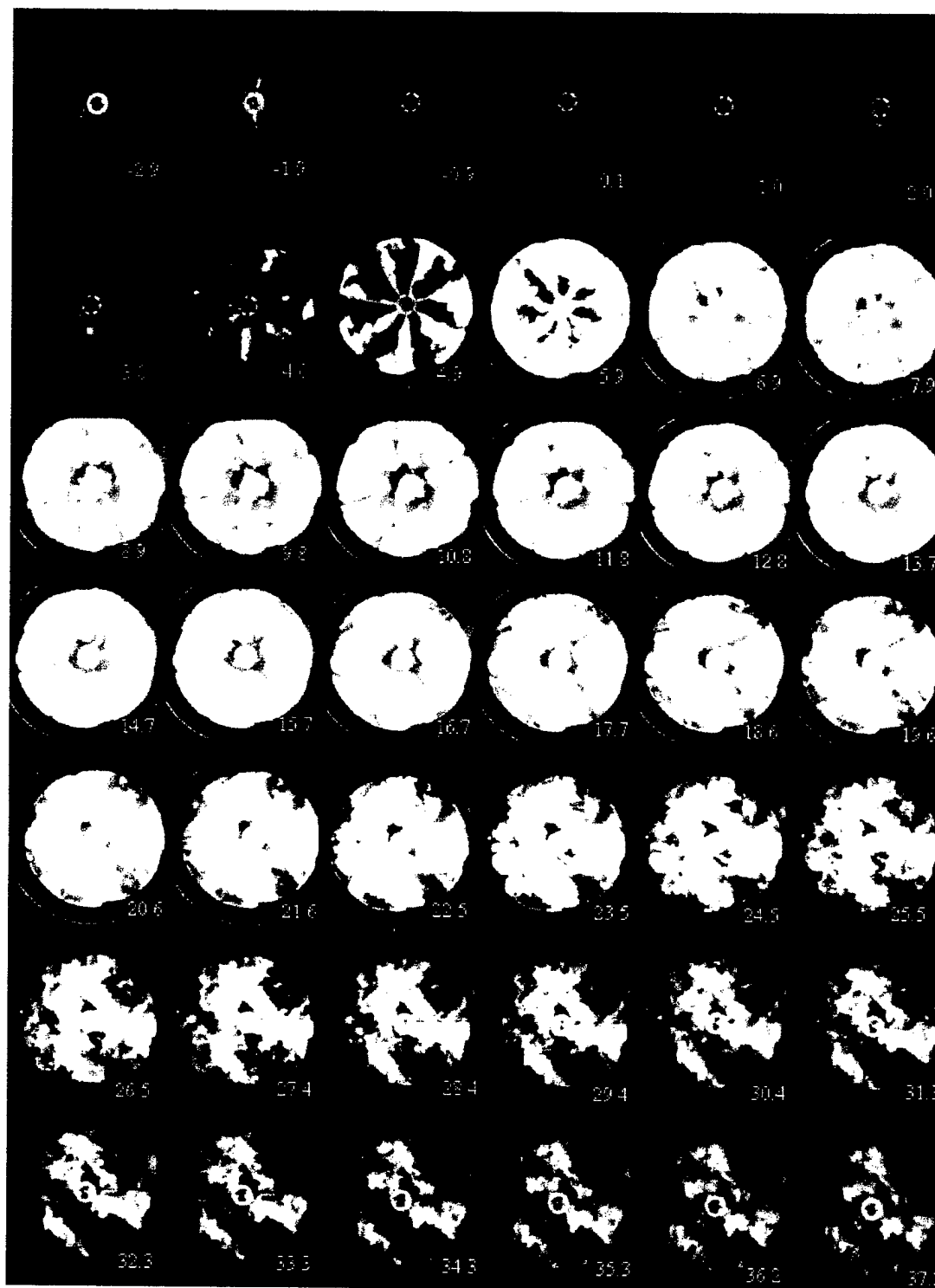
Figure B-5 Combustion images – Case E
Test condition: 750 rpm, 10-degree BTDC injection timing, 2.25-ms injection duration, 75 C/ 1.50 bar charge air, 84-MPa peak injection pressure, 730VCO nozzle, and 12" rate shaping pipe
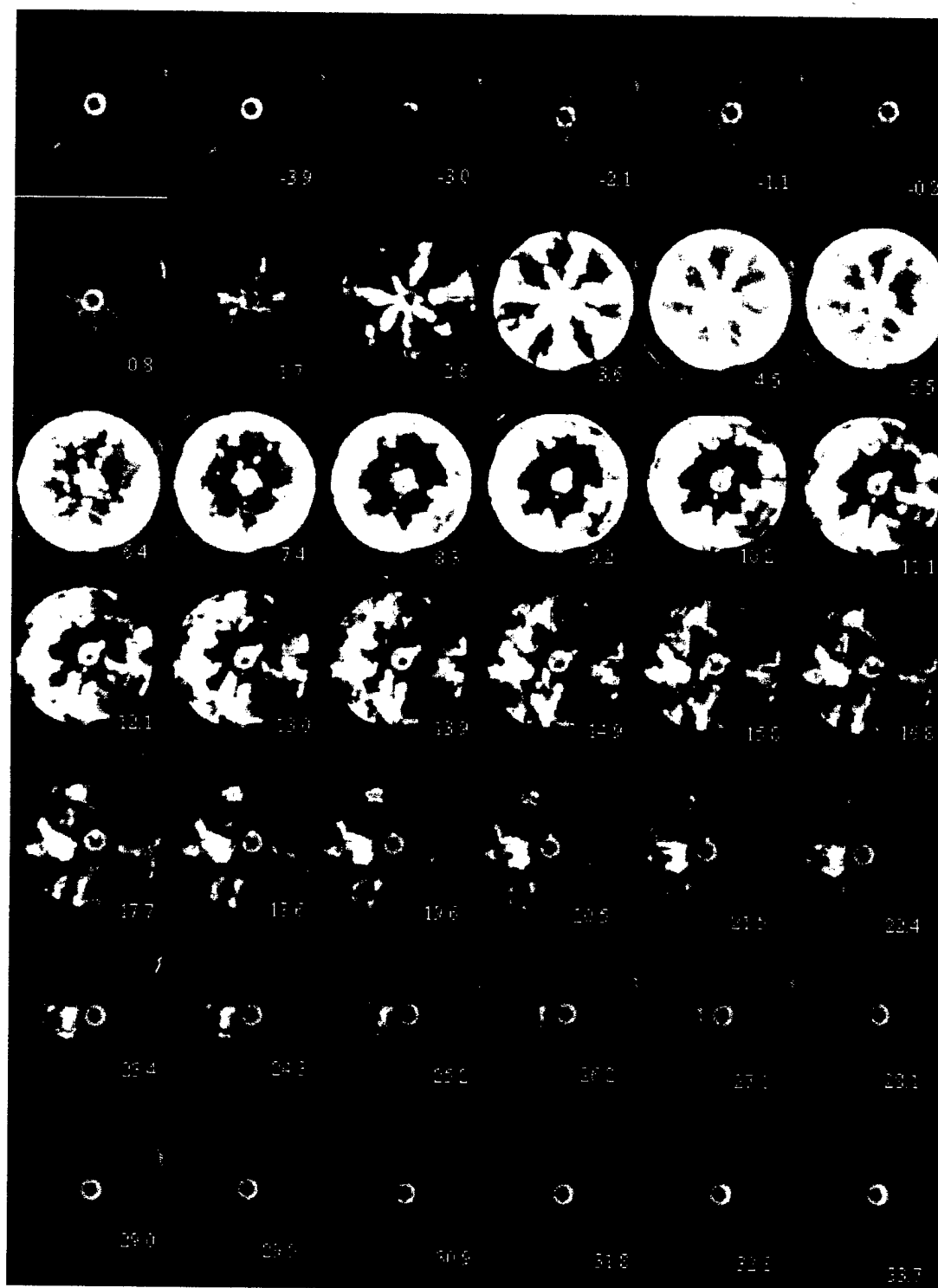
Figure B-6 Combustion images – Case F
Test condition: 750 rpm, 10-degree BTDC injection timing, 1.70-ms injection duration, 75 C/ 1.50 bar charge air, 75-MPa peak injection pressure, 730 VCO nozzle, and 12" rate shaping pipe
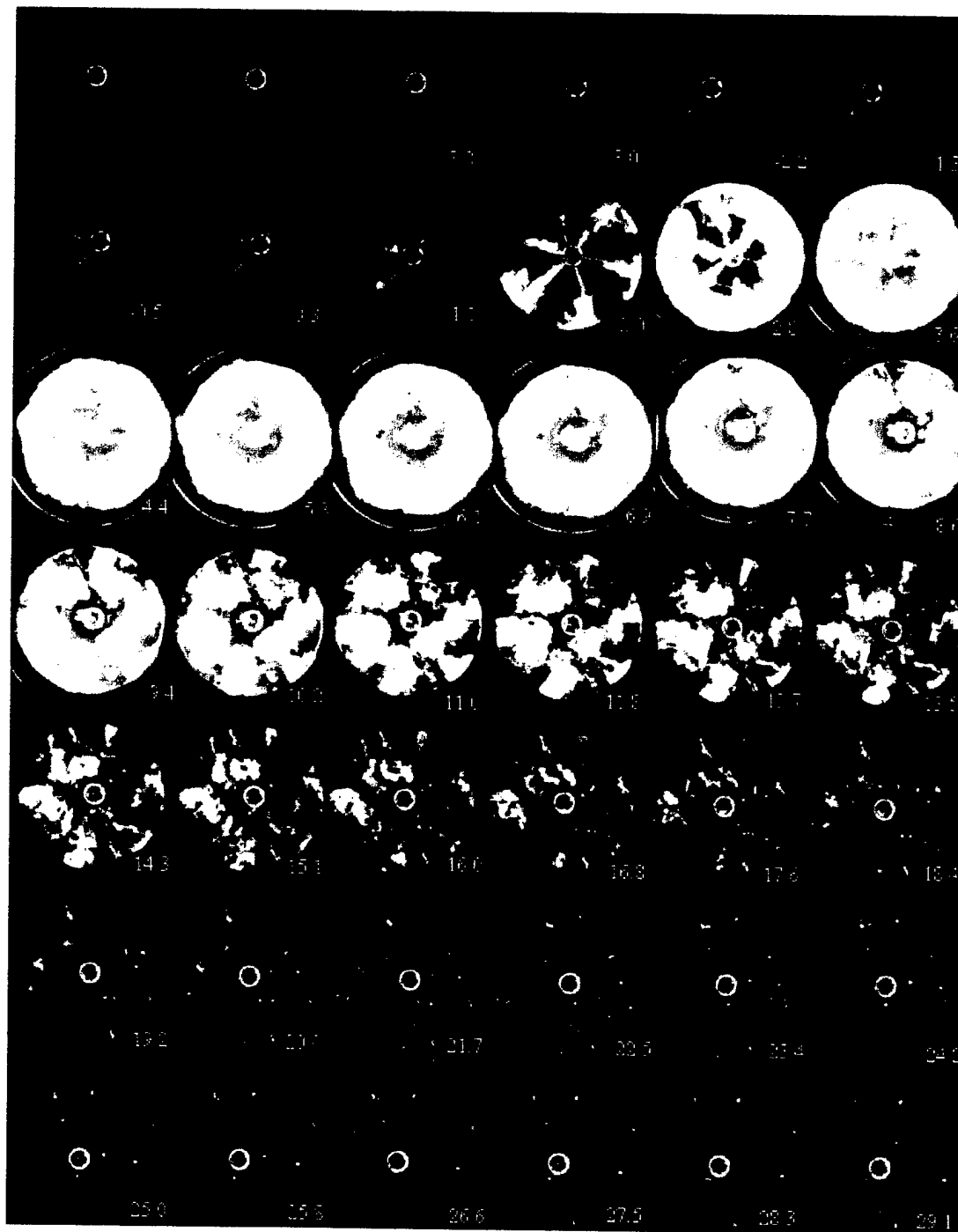
Figure B-7 Combustion images – Case G
Test condition: 750 rpm, 10-degree BTDC injection timing, 1.70-ms injection duration, 75 C/ 1.50 bar charge air, 109-MPa peak injection pressure, 610VCO nozzle, and 12" rate shaping pipe
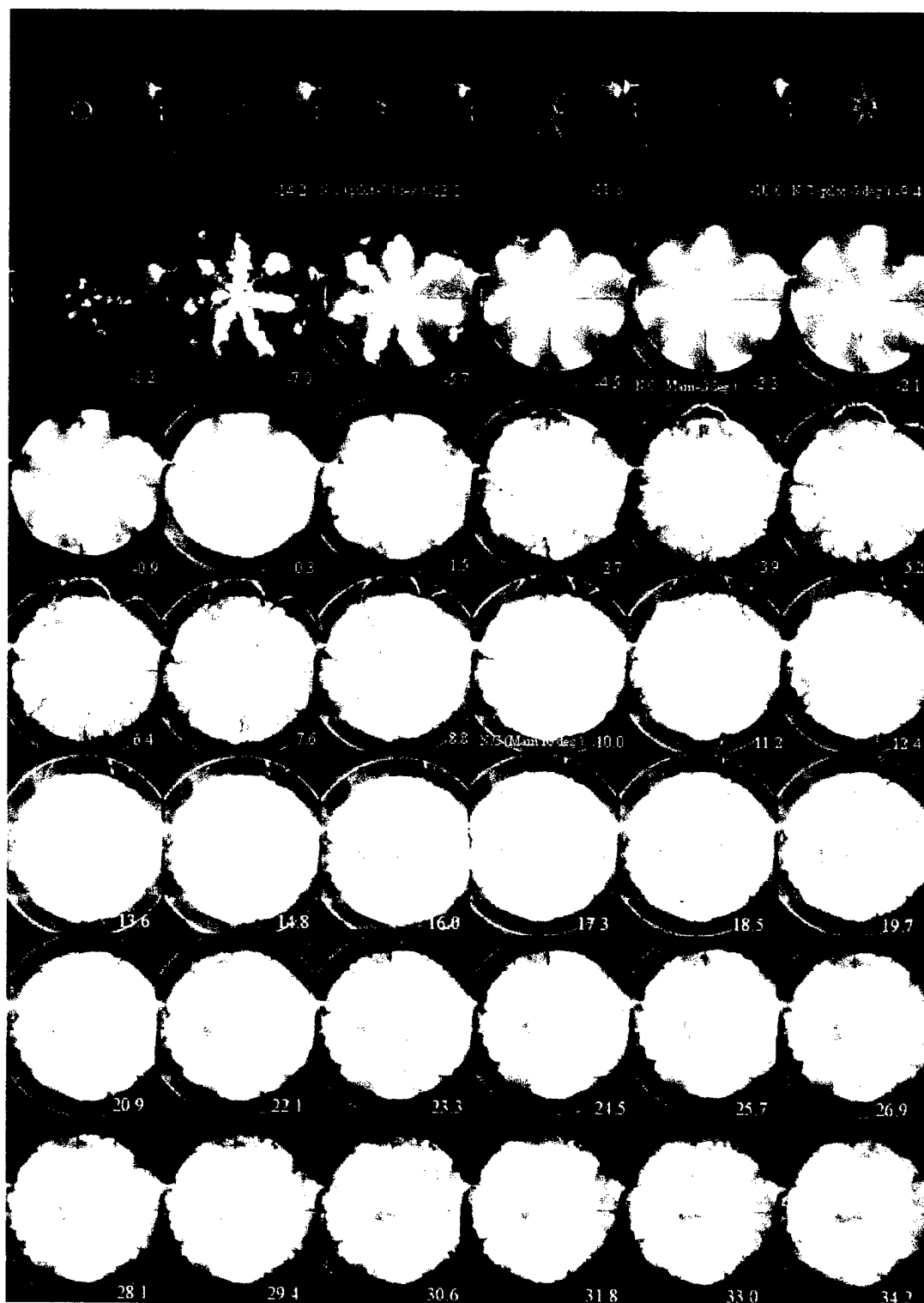
Figure B-8 Combustion images – combustion with pilot injection
Test condition: 1000 rpm, 20-degree BTDC injection timing, injection event:
0.8ms-pilot/0.6ms-dwell/2.25ms-main, 80 C/ 1.60 bar charge air, 620 mini-sac
nozzle, and 12" rate shaping pipe

APPENDIX C

PUBLICATION LIST

Lai, M.-C., Wang, T.-C., and Xie, X. (1998) "Microscopic Visualization of the Diesel Spray Behavior," *ILASS AMERICAS '98*, pp. 38-42, Sacramento, May 17-20, 1998.

Dan, T., and Lai, M.-C. (1998) "Modeling Primary Turbulent Breakup Processes in Diesel Sprays," *ILASS AMERICAS '98*, pp. 48-52, Sacramento, May 17-20, 1998.

*Lai, M.-C., Wang, T.-C., Xie, X., Han, J., Henein, N. A., Schwarz, E., and Bryzik, W., (1998) "Microscopic characterization of Diesel Sprays at VCO Nozzle Exit" *J. Fuels & Lubricants*, SAE Transc. 107(4), pp. 1283-1293, SAE 982542.

Han, J.-S., Wang, T. C., and Lai, M.-C., (1999) "Common-Rail Diesel Fuel Injection System Dynamics and Spray Characterization," Proceedings of *ILASS-Americas '99*, pp. 201-205, , Indianapolis, IN, May 16-19, 1999

Qin, J., Dan, T., Lai, M.-C., (1999) "Correlating the Diesel Spray Behavior to Nozzle Design," Proceedings of *ILASS-Americas'99*, pp. 455-457, Indianapolis, IN, May 16-19, 1999.

Qin, J., Yu, S.-T., Lai, M.-C., (1999) "Direct Calculations of Cavitating Flows in Fuel Delivery Pipe by the Space-Time CE/SE Method," Proceedings of *ILASS-Americas'99*, pp. 459-461, 12th Annual Conference on Liquid Atomization and Spray Systems, Indianapolis, IN, May 16-19.

*Wang, T. C., Han, J.-S., Lai, M.-C., Henein, N. A., Schwartz, and Bryzik, W., (1999) "Direct Visualization of High-Pressure Diesel Spray and Engine Combustion," SAE 1999-01-3496, in SAE SP-1484, *Diesel Engines Combustion and Emissions*, pp. 107-122, SAE Int'l Fuel & Lub. Meeting, Toronto, Oct. 1999.

*Qin, J., Yu, S.-T., Lai, M.-C., (1999) "Direct Calculations of Cavitating Flows in Fuel Delivery Pipe by the Space-Time CE/SE Method," SAE 1999-01-3554,

in SAE SP-1480 *Modeling and Diagnostics in Diesel Engines*, pp. 73-78, SAE Int'l Fuel & Lub. Meeting, Toronto, Oct. 1999.

*Qin, J., Dan, T., Lai, M.-C., Savonen, C., Schwartz, E., and Bryzik, W., (1999) "Correlating the Diesel Spray Behavior to Nozzle Design," SAE 1999-01-3555, in SAE SP-1480 *Modeling and Diagnostics in Diesel Engines*, pp. 79-93, SAE Int'l Fuel & Lub. Meeting, Toronto, Oct. 1999.

*Han, J.-S., Wang, T. C., Lai, M.-C., Henein, N. A., Miles, P., and Harrington, D. L., (2000), "Dynamics of Multiple-Injection Fuel Sprays in a Small-Bore HSDI Diesel Engine," SAE 2000-01-1256, to be presented in SAE Int'l Congress, Detroit, MI., March 6-9, 2000.

*Wang, T. C., Han, J.-S., Lai, M.-C., Henein, N. A., Schwartz, and Bryzik, W., (2000) "Parametric Characterization of High-Pressure Diesel Fuel Unit Injection Systems," to be presented in ASME ICED Spring Technical Conference, San Antonio, April 9-12, 2000.

* included in Appendix D.

Microscopic Characterization of Diesel Sprays at VCO Nozzle Exit

Ming-Chia Lai, T.-C. Thomas Wang, Xingbin Xie,
Jong-Sub Han and Naeim Henein
Wayne State Univ.

Ernest Schwarz and Walter Bryzik
U. S. Army TARDEC

Microscopic Characterization of Diesel Sprays at VCO Nozzle Exit

Ming-Chia Lai, T.-C. Thomas Wang, Xingbin Xie, Jong-Sub Han and Naeim Henein
Wayne State Univ.

Ernest Schwarz and Walter Bryzik
U. S. Army TARDEC

ABSTRACT

A long-distance microscope with pulse-laser as optical shutter up to 25kHz was used to magnify the diesel spray at the nozzle hole vicinity onto 35-mm photographic film through a still or a high-speed drum camera. The injectors examined are high-pressure valve-covered-orifice (VCO) nozzles, from unit injector and common rail injection systems. For comparison, a mini-sac injector from a hydraulic unit injector is also investigated. A phase-Doppler particle analyzer (PDPA) system with an external digital clock was also used to measure the droplet size, velocity and time of arrival relative to the start of the injection event. The visualization results provide very interesting and dynamic information on spray structure, showing spray angle variations, primary breakup processes, and spray asymmetry not observed using conventional macroscopic visualization techniques. The near-field spray behavior is shown to strongly depend on the nozzle geometry, needle lift dynamics, and injection pressure, which is a function of the injection system.

INTRODUCTION

The stability and asymmetry of the fuel sprays from high-pressure VCO nozzles has an important influence on the combustion and emission performance of diesel engines, mainly resulting from the decreased air utilization efficiency for the greater degrees of asymmetry. The variation in spray penetration and spray cone angle from hole to hole must be quantified both before and after the injector tip is utilized on the engine if emissions and combustion variations are to be understood and correlated. Similarly, the additional spray parameters of drop size and drop velocity distributions are important characteristics that also influence diesel combustion, and should be quantified for nozzles that are used in diesel combustion test programs.

High-pressure electronic-controlled fuel injection systems, such as electronic unit injector (EUI), hydraulic EUI (HEUI), and common rail (CR), are the heart of advanced diesel engines. Although extensive research has been carried out to characterize and simulate diesel sprays, most previous work is limited to the conventional low-pressure mechanical systems. Many significant spray-related issues remain; e.g., spray breakup mechanisms, effects of cavitation. Although scale-up models have been used to study the flow characteristics, it is impossible to match the force-ratios (as represented by Reynolds, Weber, Ohnesorge, and cavitation numbers) and time scales in practical diesel sprays. On the practical side, issues such as injector-to-injector, injection-to-injection and hole-to-hole variability, and pilot repeatability, have very important impacts on our capability to design and simulate advanced diesel engines to meet their combustion and emission goals.

Recent implementation of laser diagnostics has been shown to provide insight into the diesel spray and combustion processes (e.g., Dec 1997, Lai et al., 1995). The motivation of this research is to visualize the spray structure of advanced diesel injection systems very close to the nozzle exit in an attempt to correlate the microscopic spray structure to the injection system performance and nozzle design.

EXPERIMENTAL SETUP

The optical system setup includes a long-distance microscope, a copper-vapor laser (Oxford CU15), and a still or a high-speed drum camera, both using 35-mm photographic film. The copper laser is expanded into a thin sheet using cylindrical lens and is used as the optical shutter, up to 25kHz with the exposure time as

short as 10 ns. The long-distance microscope, similar to the ones used by other researchers (Sjoberg et al., 1996; Fath et al, 1997), is used to magnify the diesel spray structure very close to the nozzle exit. The diffraction-limit resolution can be as small as 1-2 micron. The optical setup provides great resolution in both time and space, as shown in Figure 1.
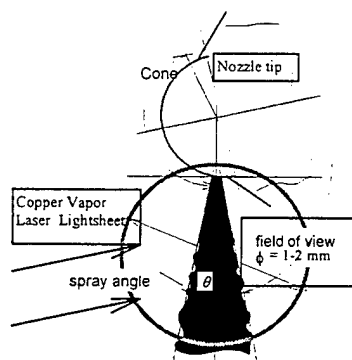
Fig. 1 Microscopic Visualization Field of View

The injectors examined are valve-covered-orifice (VCO) nozzles, from either a CR or an EUI (6-hole nozzle, system. The CR injection system tested is designed for high-speed small-bore diesel engine; it has a smaller injector body (17mm) and single-guide needle. For comparison, a mini-sac injector from a HEUI system is also investigated. Diesel fuel No.2 was used in this study. Unless otherwise noted, the results presented in this paper are carried out in atmospheric ambient conditions. The injection system properties are summarized in Table1.

Table 1 Summary of Injection Systems Tested

System	Nozzle	Opening Pressure (MPa)	Max. Pressure (MPa)
CR	.16mm ϕ, 6-hole VCO 90°-Needle,156°-Spray	-	150
EUI	.18mm ϕ, 2-hole VCO 60°-Needle,145°-Spray	34	200
HEUI	.18mm ϕ,6-hole mini-sac	28	180

A phase-Doppler particle analyzer (PDPA) system with an external digital clock was used to measure the droplet size, velocity and time of arrival relative to the start of the injection event. The measurement location is at 25mm downstream of the nozzle hole.

RESULTS AND DISCUSSIONS

MACROSCOPIC SPRAY BEHAVIOR   Figure 2 shows the macroscopic visualization of the early spray development of the CR diesel spray injected into a

pressurized chamber. This time sequence photograph is taken with the drum camera with the laser pulsing at 12.5kHz. Significant hole-to-hole variation in the penetration and the spray angle is observed, especially in the early stage of spray development. This type of spray asymmetry is usually associated with poor machining tolerance of the nozzle (Harrington and Lai, 1998). In addition, puffy structure along the edge of the spray is observed.
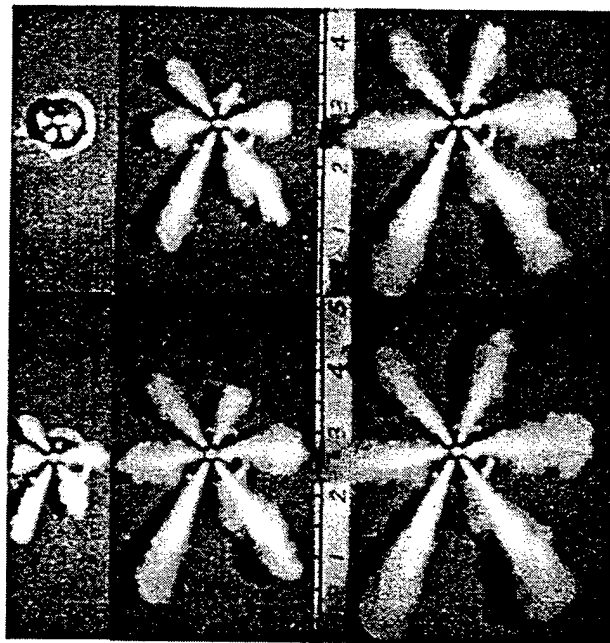
Fig. 2 Early development of high-pressure CR spray. P_{inj}=135MPa, P_{amb}=2.8MPa(nitrogen), Time between frame: 0.08ms, from top to bottom, left to right.

POOR PILOT AND END OF INJECTIONS
Typical high-speed microscopic visualization results are shown in Figures 3 and 4 for the 9-o'clock CR spray in Fig. 2, which is the second slowest spray in terms of penetration. The copper vapor laser was operated at the frequency of 25kHz, i.e. each frame is 40 microsecond apart. The field of view extends from the nozzle exit to 1.2mm downstream. These injection events consist of a 0.2-ms pilot and a 1.0-ms main injection, with a 1.2-ms separation between the start of injection of the two events. Figure 3 shows that at the low injection of 25MPa, the pilot barely made it out of the nozzle, resulting in an inconsistent and poorly atomized spray. At the injection of 135 MPa, the pilot is better developed, but the 0.2-ms injection command results into an injection duration of more than 0.3 ms.

Both figures show that at the end of injection, the spray trickles down and forms larger drops. However, compared with sac nozzles that tend to produce even larger ligaments at end of injection (and consequently higher HC emission in engine tests), the VCO nozzle shows considerable improvement. The lower injection

2

pressure case in Figure 3 also shows poorer atomization and large-eddy structure inside and at the edge of the spray, as is evidenced by the less homogenous light intensity scattered.

SPRAY ANGLE OSCILATION The visualization results in Figures 3 and 4 also show rapid temporal variations of spray angle, which result into the puffy spray structure at the edge of the spray as observed in the macroscopic visualization in Figure 2. The results of the inclusive spray angles measured from Figures 3 and 4 are plotted in Figures 5 and 6 respectively, together with the injection line pressure simultaneously measured right at the injector inlet. At the high injection pressure of 135 MPa, the spray angles at the start of injection are larger than those of during the mid-injection period; there is also a slight increase at the end of injection. However, the low-pressure spray shows pronounced oscillation in spray angles even during the mid-injection period. The frequency of the oscillation is on the order of a couple of kHz.

Fig. 3 Microscopic Visualization of CR spray. P_{inj}=25MPa, Injection Event: 0.2ms-pilot/1.0ms-dwell/1.0ms-main, Time between Frame: 0.04ms (frame 13-23 between pilot and main skipped).
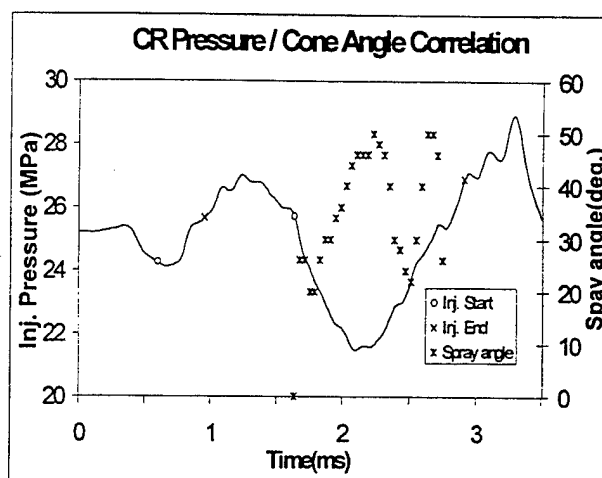
Fig. 5 Injection pressure and spray angle variation for the CR spray shown in Fig. 3.

Fig. 6 Injection pressure and spray angle variation for the CR spray shown in Fig. 4.

Fig. 4 Microscopic Visualization of CR spray. P_{inj}=135MPa, Injection Event: 0.2ms-pilot/1.0ms-dwell/1.0ms-main, Time between Frame: 0.04ms (frame 13-28 between pilot and main skipped).
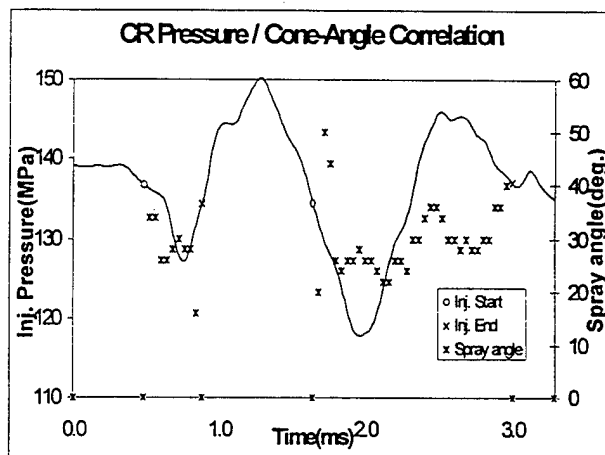
Since the spray angle does not correlate very well with injection pressure, the spray angle oscillation is due to other factors. Needle oscillation is a probable candidate, because it potentially sets up swirling flow motion within the injector hole (Arcoumanis et al, 1998). Similar behavior, however, has also been

3

observed for a dual-guided VCO nozzle in our test. Another possibility is due to oscillation of cavitation bubble inside the injector (Schmidt, D. P., 1997). The ambient pressure does not dampen these oscillations; on the contrary, it seems to amplify it. This is shown in the Figure 7 for three ambient pressure cases with a injection pressure of 800MPa.
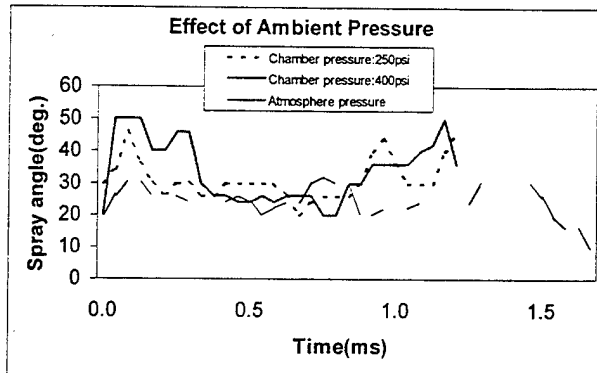
Fig. 7 Effect of ambient (nitrogen) pressure on the spray cone-angle. Injection pressure is 800MPa.

These spray cone-angle oscillation phenomena are not limited to one hole only. Figures 8-12 are the results of transient microscopic visualization of the fastest penetrating spray (the seven-O'clock spray in Figure 2), which also show the similar spray cone-angle oscillation behavior.
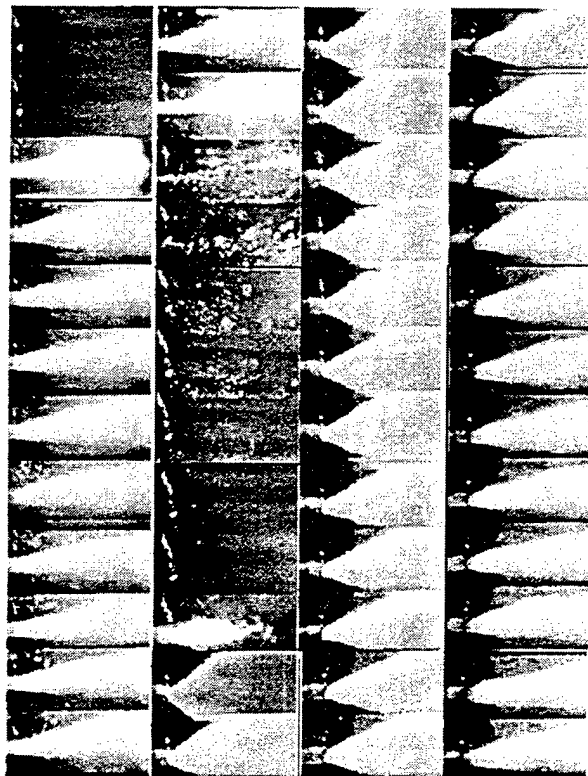
Fig. 8 Microscopic Visualization of CR spray. P_{inj}=135MPa, Injection Event: 0.3ms-pilot/0.45ms-dwell/1.2ms-main, Time between Frame: 0.04ms.
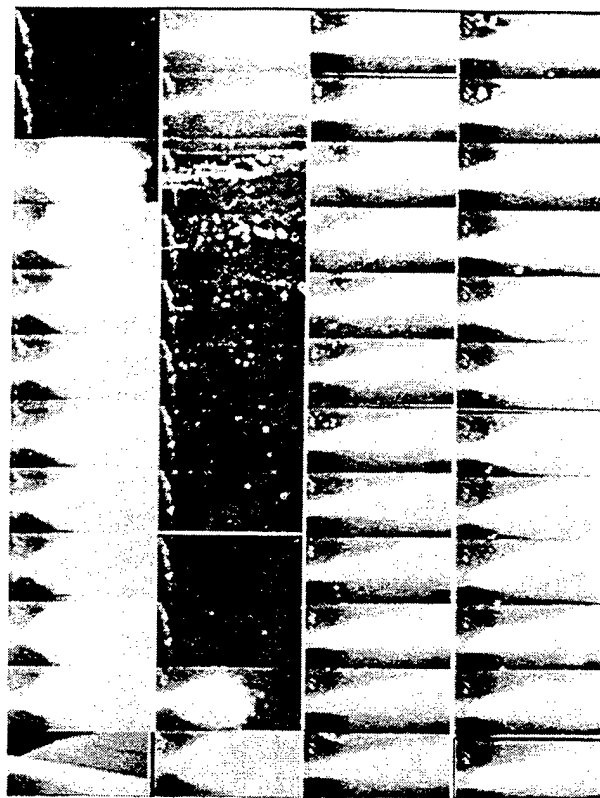
Fig. 9 Microscopic Visualization of CR spray under the same condition as Figure 8.

HOLE-TO-HOLE AND INJECTION-TO-INJECTION VARIABILITY Both Figures 8 and 9 are for the same injection pressure of 135Mpa and the same injection event of 0.3ms-pilot/0.45ms-dwell/1.2ms-main. Both show spray-cone angle oscillation for the same spray (the fastest penetration spray in Figure 2), but they also show injection-to-injection variability. For example, the pilot injection in Figure 8 has much smaller spray-cone angle than that of Figure 9; the oscillation history of the main injection is also different. Similar injection-to-injection variability is also observed for other test conditions.

EFFECT OF INJECTION SYSTEM: A typical visualization high-speed microscopic visualization result of the EUI spray is shown in Figure 10. The EUI system is integrated with the cylinder head; thus the condition in Figure 10 is for a speed of 1500 rpm and a injection duration of 7 crank angle degrees. The EUI system used in the test is for heavy-duty engine; therefore it has a sturdy injector construction with a larger nozzle, which generally results into more symmetric spray. Lower needle opeing pressure also stabilize the spray. Figure 11 summarizes the spray cone-angle as visualized using the microscope. It shows that the spray cone angle is usually very large initially, but it quick stabilizes and only kicks up at the end of injection. In the mid-injection period, it is devoid of the significant oscillation as observed in the CR injector cases.

4
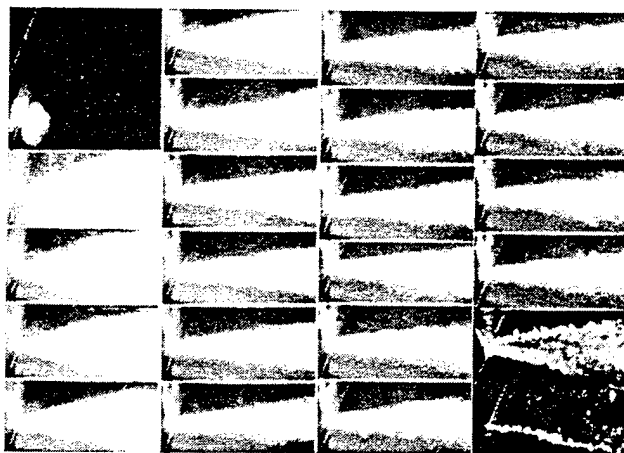
Fig. 10 Microscopic Visualization of EUI spray.
1500rpm, injection duration 10 crank angle degree,
Time between Frame: 0.04ms.
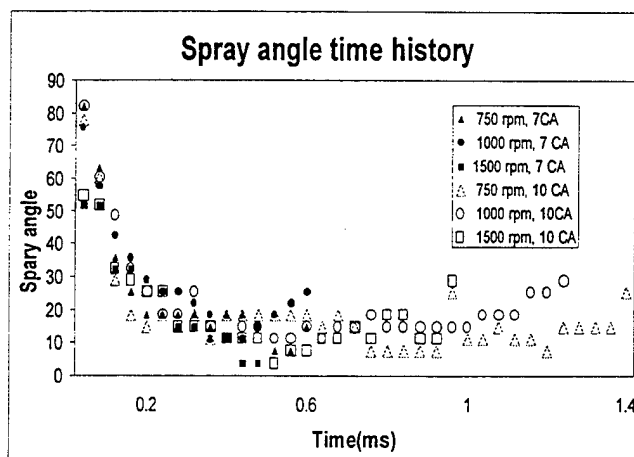
Fig. 11 Spray angle variation for EUI sprays.

PRIMARY BREAKUP MECHANISMS FOR VCOs

In order to investigate the primary breakup mechanisms, single-shot microscopic visualization using 35mm SLR camera is also carried out in order to get higher resolution and to avoid the vibration effect which could be introduced by the high-speed rotating drum camera. Figure 10 shows a collection of the microscopic photographs taken with a 35 mm SLR camera. The still-photography captures the overall spray boundary, and provides excellent contrast on black-and-white film. These close-ups were taken to catch the onset of spray formation, where the spray just exits the nozzle orifice. The photograph shows a very dynamic primary breakup processes very close to the injector. For the EUI injection system, the injection rate increases with engine speed. In addition, the peak pressure also increases with injection duration. Therefore, there might be slight difference with the two engine speeds tested; however, the difference may be too subtle to conclude.

Fig. 12 (Right) Still photographs of early spray development of EUI(VCO) sprays. top:1500rpm, bottom:750 rpm.
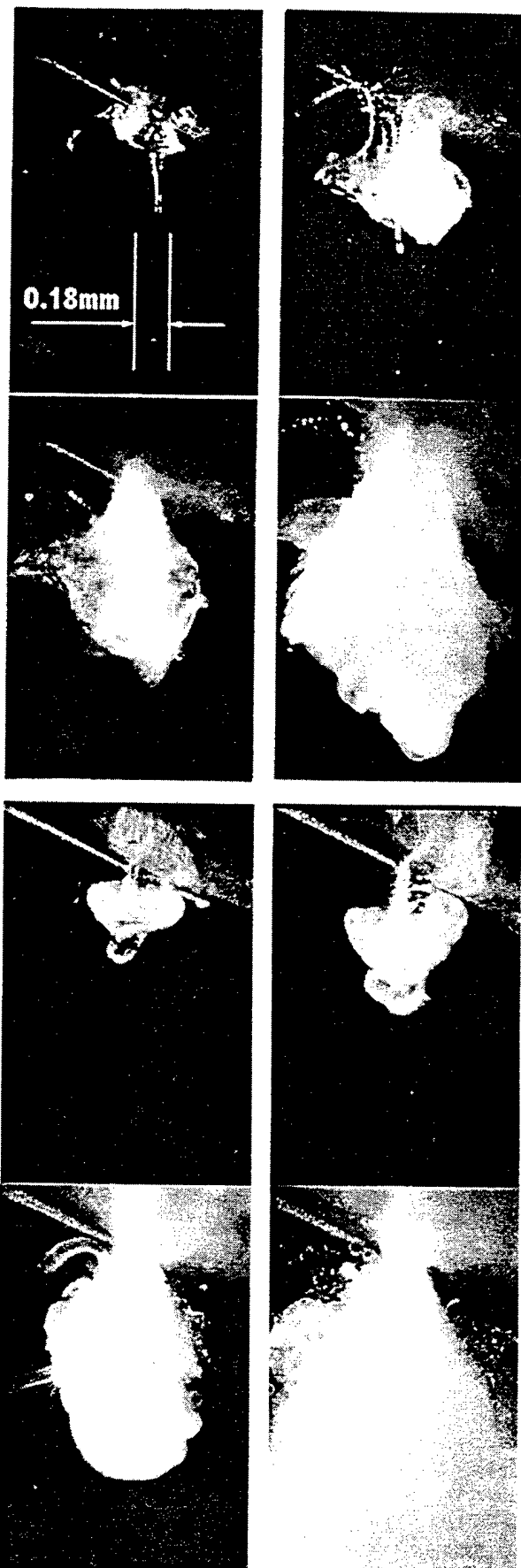
At the earliest instant that the camera was able to capture the spray exiting the nozzle, the liquid column appears to have a translucent potential core wrapped around by a separating boundary layer that tends to mushroom and roll up. The asymmetry of the spray structure is obvious in the early spray development. Further into spray development, the spray tends to have a very large cone-angle, as is evident in Figure 13.
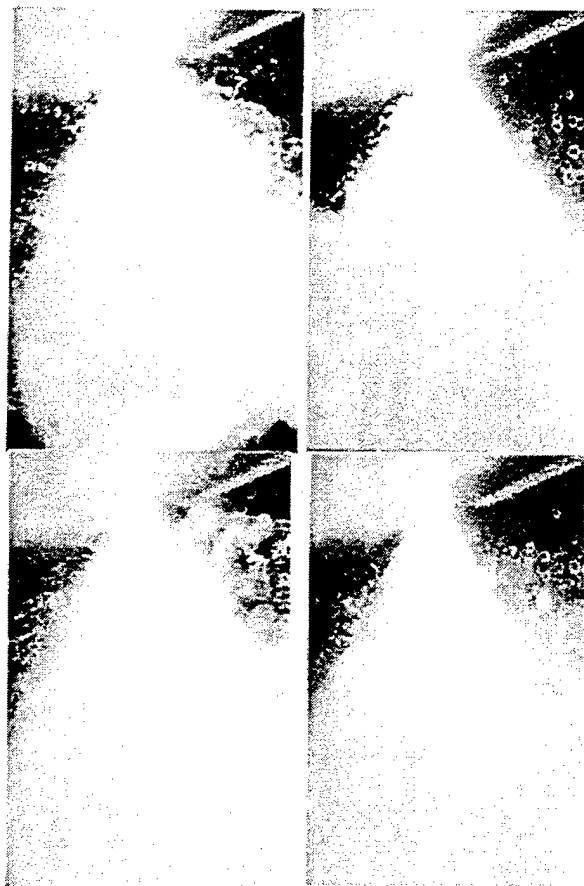
Fig. 13 Still photographs of early spray development of EUI(VCO) sprays.

Typical microscopic phtographs of the EUI spray at peak pressure are shown in Figure 14, which are taken at the maximum pressure of 200MPa. The spray shows a much smaller cone angle. The onset of spray breakup is immediately at the injector exit, indicating the presence of turbulent primary breakup (Dan and Lai, 1998). The bottom side of the spray shows some large droplet formation. Although some of which are not exactly focused, their diameters can be estimated to be 10-20% of that of the nozzle hole, corresponding to the turbulent integral scale within the nozzle. In comparison, the top side of spray does not show a symmetric and corresponding distribution of large droplets. In spite of possible light attenuation across the spray, it shows instead the formation of a very fine mist. An inverted microscopic visualization of the EUI spray is also shown in Figure 15 for clarity.
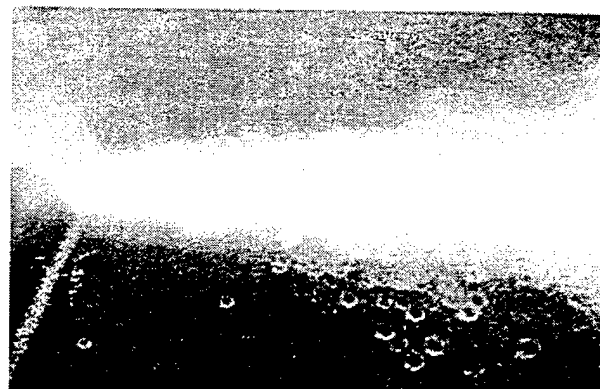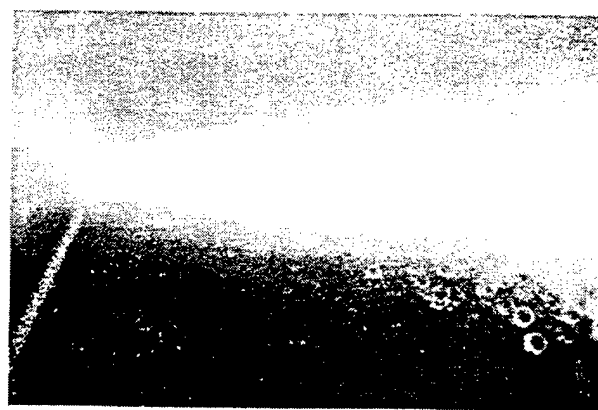
Fig. 14 Microscopic image of EUI spray at peak injection of 200 MPa.
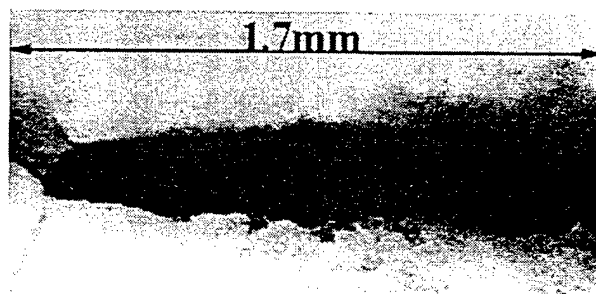
Fig. 15 Inverted microscopic image of EUI spray at peak injection of 200 MPa.

The nozzle internal flow direction is from top to bottom; therefore, the topside spray is directly downstream of the turn-around point, where nozzle internal flow passage dictates that fuel flow must negotiate a sharper inside turn into the VCO hole. The fine mist observed could be a direct confirmation of cavitation-enhanced breakup mechanism; however, more research is needed to verify these observations. Recently, Fath et al. (1997) reported the microscopic spray structure from a single-hole sac-type nozzle using a long-working-distance microscope, a laser sheet illumination, and a CCD camera. They proposed that the cavitation bubbles in jet could be obtained from the

6

intensity distribution of scattering light. And the new spray atomization concept was proposed, which the bubbles generated at nozzle hole's wall boundary region will enhance the disintegration of liquid at the ambient. The bubble sizes that they observed, however, are quite large, maybe due to the lower injection pressure and special nozzle-hole geometry.

EFFECTS OF NOZZLE GEOMETRY

For comparison, Figure 16 shows a collection of the close-ups of one of the spray from a HEUI mini-sac nozzle. At the onset of injection, the initially low-pressure fuel in the sac volume is squeezed out of the nozzle orifice like the shape of toothpaste. The initial liquid column has quite distinct and clear boundary, but it turns bubbly or milky, with a fussy boundary very quickly. Its surface also rolls up similar to that the eddy rollup processes observed in pure gas jet.

Close examination of the fussy interface suggests formation of very fine droplets as a result of micro-explosion or busting of bubbles; however, some optical artifacts can not be completely ruled out. Comparing the mini-sac nozzle sprays with those of the VCO's show that sac-type nozzle has less turbulent primary breakup and different cavitation breakup features, which is consistent with its internal flow characteristics. The sac-type nozzle, therefore, has better spray symmetry compared to the VCO in the spray cross-section. It is also well known to produce more even sprays, i.e., less hole-to-hole variability.

At a compatible injection pressure as the opening pressure of the mini-sac nozzle case shown in Figure 16, Figure 17 shows two typical transient microscopic visualization of the CR injector with VCO nozzle at the rail pressure of 300Mpa. A very fast transition from clear liquid column to milky or corrugated spray surface is also observed, on the order of 0.1-0.2 ms. This transition, however, is not observed at higher pressure cases.

Fig. 16 Early spray breakup photographs of HEUI sprays (mini-sac nozzle).
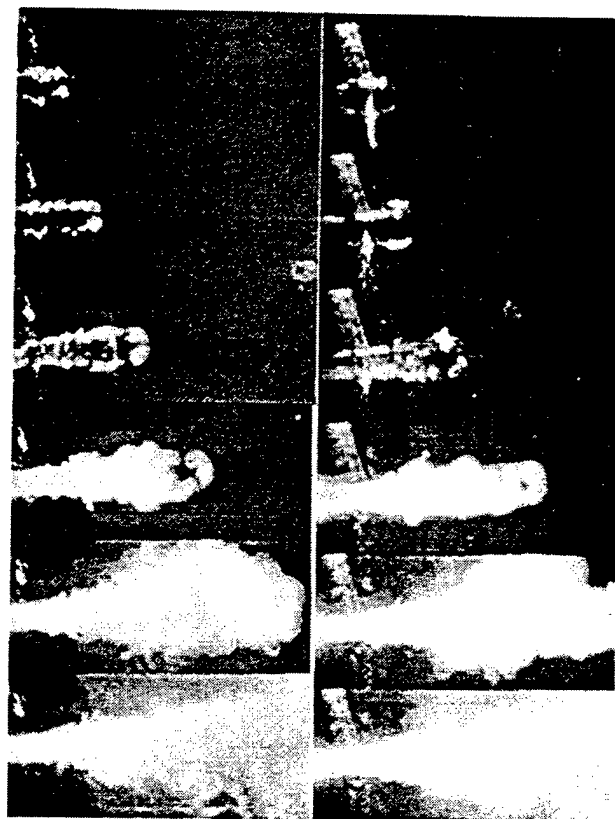
Fig. 17 Microscopic Visualization of CR spray. P_{inj}=300MPa, Injection Event: 0.3ms-pilot/0.45ms-dwell/1.2ms-main, Time between Frame: 0.04ms.

PHASE DOPPLER MEASUREMENTS An Aerometrics one-channel counter-type phase-Doppler particle analyzer (PDPA) system with an external digital clock was used to measure the droplet size, velocity and

7

time of arrival relative to the start of the injection event. Both 100- and 50-micorn slits were used to reduce the measuring volume and increase the validating rate for measuring the dense diesel sprays. The measurement location is fixed at the spray axis, 25 mm from the hole exit. This injection event consisted of a 0.45-ms pilot and a 0.7-ms main injection, with a 0.8-ms separation between the start of injection of the two events. In general, high-pressure diesel injection results in very dense sprays with very high droplet velocities, which makes the PDPA measurement close the nozzle quite difficult (Koo and Martin, 1991; Giorgio et al., 1995). Unfortunately, small diesel engines have small bowl diameters, and the region of interest in the sprays is quite close to the nozzle. The use of a smaller aperture in front of the receiving optics reduces measuring volume, which improves slightly the data validation rate but cuts down the overall data rate. In our case, changing the aperture from 100 microns to 50 microns reduced the data rate approximately 50%.

It is not possible to simultaneously measure in one run 0- to 20-micron densely-packed drops having a velocity range of 0-200 m/s. It was found necessary to measure the diesel spray for different velocity ranges in order to obtain the entire spectrum of droplet velocities. The PDPA data were time-windowed, using the arrival time logged by an external digital clock. Figure 18 contains the measured velocity history for this diesel injection event with five velocity ranges at 35 m/s increment. It is difficult to capture many validated drops during the very brief but dense pulses, particularly the 0.45-ms pilot; however, the data show the presence of the pilot and the main injection pulse and the slower-moving spray tail.

Because of the high-density of the spray body, measurement of the bulk spray is actually suppressed by poor validation. Only the leading and trailing edges of the pilot and main injections and the slow moving tail sections are captured; therefore, there appears to be four peaks for the faster moving droplets. The droplet velocity peaks at 200 m/s at 0.7 ms after the start of the injection logic pulse, and rapidly decays to less than 15 m/s for the tail of the spray, which lasts longer than 6 ms for this non-evaporating spray.

The data rate, validation rate, and velocity-windowed dropsize are summarized in Figure 19. It shows that the usual PDPA measurement of a dense diesel spray tends to significantly under-estimate velocity and somewhat under-estimate dropsize. The dropsize of the faster droplet could be 20% larger than the averaged dropsize measurement which is mostly in the spray tail. However, time-resolved, velocity-windowed PDPA measurements of the spray history at the bowl-impact distance can provide modelers with a valuable input regarding their predictions.
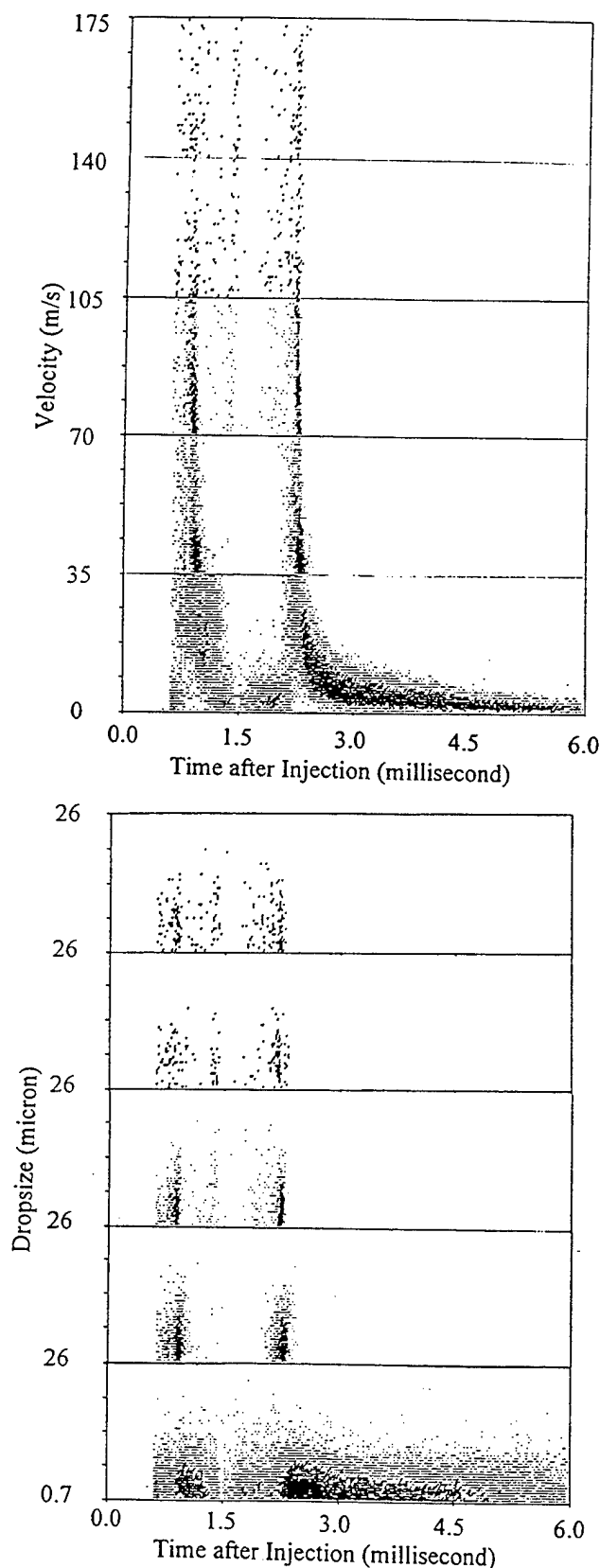
Fig. 18   PDPA data as a function of time of arrival at 25mm from nozzle, top: velocity, bottom: dropsize, P_{inj} = 100MPa, P_{amb}= 0.1MPa, t=0.45(pilot)/0.35(dwell)/0.7 (main) ms.

8
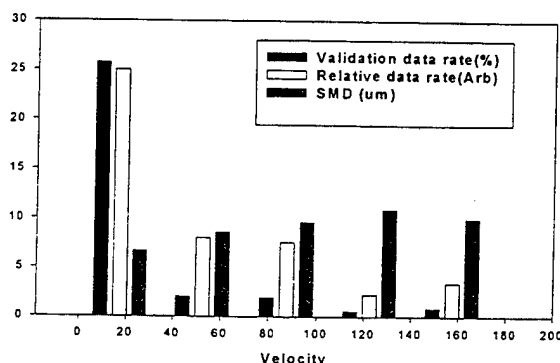
Fig. 19   Summary of velocity-conditioned PDPA measurements.

CONCLUSIONS

Representative advanced injection systems, such as the common-rail, cam-driven or hydraulic amplified electronic unit injectors are studied using microscopic high-speed visualization techniques. The microscopic visualization results provide very interesting and dynamic information on spray structure, showing spray angle variations, primary breakup processes, and spray asymmetry not observed using conventional macroscopic visualization techniques. The near-field spray behavior is shown to be highly transient, strongly depend on the nozzle geometry, needle lift and vibration, and injection pressure which is a function of the injection system. Specific conclusions are as follows:

1. The spray cone-angle observed for the unit injector is larger at the early transient stage of needle lift. For the high-pressure common rail system tested, the spray cone angle shows conspicuous oscillation during pilot or main injection period, possibly due to needle eccentricity and oscillation.

2. At the mid-injection period where injection is quasi-steady, spray breakup is shown commence at the nozzle exit, exhibiting behaviour due to turbulent primary breakup. Therefore, future spray modeling should consider the effects of transient three-dimensional turbulent flow and cavitation on the spray breakup processes.

3. PDPA measurement of the CR a diesel spray at bowl-impact distances in a small-bore engine are shown to be significantly influenced by the spray number density, with little or no data rate during the mid-portion of the injection pulse. This yields measured spray characteristics that are biased towards those of the spray tail. This under-predicts the mean dropsize and significantly under-predicts the mean drop velocity.

REFERENCES

Arcoumanis, C., Gavaises, M., Nouri, J. M., Abdul-Wahab, E., and Horrocks, R. W., (1998) "Analysisi of the Flow in the Nozzle of a Vertical Multi-Hole Nozzle Diesel Engine Injector," SAE 980811.

Dan. T., and Lai, M.-C. (1998) "Modeling Primary Turbulent Breakup Processes in Diesel Sprays," *ILASS AMERICAS '98*.

Dec, J. E., (1997) "A Conceptual Model of Diesel Combustion Based on Laser-Sheet Imaging," SAE 970873.

Fath A., Münch K. U. and Leipertz A., (1997) "Spray Break-up Process of Diesel Fuel Investigated Close to the Nozzle", *ICLASS - '97*, p. 513.

Giorgio, F., Laforgia, D., and Damiani, V., (1995) "Investigation of Drop Size Distribution in the Spray of a Five-Hole, VCO Nozzle at High Feeding Pressure," SAE 950087.

Harrington, D., and Lai, M.-C., (1998) "Characterization and Visualization of Hole-To-Hole Variation and Wall Impingement of Diesel Sprays," *ILASS AMERICAS '98*, pp. 106-110, Sacramento, May 17-20, 1998.

Koo, J.-Y., & Martin, J. K., (1991) "Comparisons of Measured Drop Sizes and Velocities in a Transient Fuel Sprays with Stability Criteria and Computed PDF's, SAE 910179.

Lai, M.-C., Henein, N. A., Xie, X., Chue, T.-H., Itoh, Y. and Bryzik, W., (1995) "Diesel Cold-Starting Study using Optically Accessible Engines," SAE paper 952366.

Sjoberg, H., Manneberg, G., Cronhjort, A., (1996) "Long-Working-Distance Microscope used for Diesel Injection Spray Imaging," Optical Engineering, Vol. 35(12) pp. 3591-3596.

Smith, D. P. (1997) "Cavitation in Diesel Fuel Injector Nozzles," Ph.D. Thesis, University of Wisconsin, Madison, Mechanical Engineering Department.

202

Correlating the Diesel Spray Behavior to Nozzle Design

Jian-Rong Qin, Tomohisa Dan and Ming-Chia Lai
Wayne State University

Craig Savonen
Detroit Diesel Corporation

Ernest Schwartz and Walter Brkyzik
US Army TARDEC

Correlating the Diesel Spray Behavior to Nozzle Design

Jian-Rong Qin, Tomohisa Dan and Ming-Chia Lai
Wayne State University

Craig Savonen
Detroit Diesel Corporation

Ernest Schwartz and Walter Brkyzik
US ArmyTARDEC

ABSTRACT

This paper studies the effect of nozzle geometry on the flow characteristics inside a diesel fuel injection nozzle and correlates to the subsequent atomization process under different operating conditions, using simple turbulent breakup model. Two kinds of nozzles, valve covered orifice (VCO) and mini-SAC nozzle, with various nozzle design parameters were studied. The internal flow inside the nozzle was simulated using 3-D computational fluid dynamics software with k-ε turbulence model. The flow field at the nozzle exit was characterized by two parameters: the fuel discharge coefficient Cd and the initial amplitude parameter $amp0$. The latter parameter represents the turbulence characteristics of the exit flow. The effects of nozzle geometry on the mean velocity and turbulent energy distribution of the exit flow were also studied. The characteristics of the exit flow were then incorporated into the spray model in KIVA-II to study the effect of nozzle design on diesel spray behavior. The results show that the nozzle geometry has a strong influence on the flow field inside the nozzle and the subsequent process of atomization.

INTRODUCTION

Despite its importance in applications, the mechanism of atomization is not yet well understood. Various proposed atomization mechanisms were evaluated by Reitz and Bracco [1], but none of them taken alone could explain their experimental results. Ranz [2] suggested the change in nozzle design could supply different initial disturbance levels to the flow, which could be one of the important mechanisms of atomization. Recent experimental and computational results [3-7] show nozzle geometry has a strong effect on the characteristics of the exit flow and the subsequent spray behavior.

The design of hole-type nozzle employed in internal combustion engines involves many parameters, including the aspect ratio of the nozzle (hole length / hole diameter),

the cone angle of the needle valve, the turning angle of the orifice, the sac shape and the needle valve lift amount. All these parameters can influence the performance of the nozzle. The detailed configuration, such as the wall surface roughness and the curvature of orifice entrance, also brings changes in the internal flow inside the nozzle. How to analytically correlate the nozzle design to the spray behavior remains largely unknown.

The discharge coefficient Cd and the turbulence characteristics of the exit flow are two important factors that influence the atomization of spray. Ohrn et al. [8] demonstrated that the shape and condition of the nozzle inlet have a strong effect on the discharge coefficient. Increasing the inlet radius has a pronounced effect on the internal flow pattern. Rounding the nozzle inlet increases the discharge coefficient. For nozzles with small inlet R/D ratios (below 0.20), the discharge coefficient is independent of Reynolds number throughout the range from 7,000 to 30,000. For nozzles having R/D values higher than 0.20, the discharge coefficient increases slightly with increase in Reynolds number up to 30,000. They [9] also reported that the effects of injection pressure, inlet radius, and length/diameter ratio on spray angle are highly coupled. Cone angle increases markedly with increase in injection pressure for nozzles featuring small inlet radius, especially for L/D's of around 4 to 5. But for large inlet radius cases, cone angle increases only slightly with the increase in injection pressure. In their study, they also found that nozzles with large inlet radiuses produce cone angles that decrease slightly with increasing L/D, whereas nozzles with smaller inlet radiuses produce cone angles that attain their maximum values at an L/D of around 4.

Bosch [10] applied hydro grinding process during VCO nozzle production to obtain smooth wall surfaces and rounded edges at the orifice entrance. Their experimental results show the hydro grinding process increases the discharge coefficient of the nozzle. Their numerical simulation shows the nozzles with larger entrance curvature produce more symmetrical velocity profile indicating less

shear stress and lower turbulence intensities in the orifice.

Using a dimensional analysis, Huh et al. [11] claimed that the gas inertia and turbulent stress were the two dominant forces of a comparable magnitude in atomization of a diesel spray. Experimental results [12, 13] also show that turbulence inside a nozzle has dominant effects on the primary breakup of liquid jets. These results show the atomization of a liquid jet is promoted greatly with the increase of disturbance inside the nozzle, and the liquid jet atomizes little for the cases of little disturbance inside the nozzle even under very high injection pressure conditions. Recently, Lai et al. [7] reported the spray behavior through VCO nozzles at the spatial region close to the nozzle by means of the microscope photography. Their experimental results show that the fuel jets breakup instantaneously at the nozzle exit, which indicates the seeds of atomization have been already sown in the flow inside of the nozzle.

Decrease in needle valve lift makes sprays spread more widely in the radial direction. But the fuel flow rate becomes less than that of full needle lift case [14]. This feature can be clearly seen in larger orifice diameter cases (D=0.4 mm). The reason is that the fuel flow rate in the cases of small needle lift is limited by the cross-sectional flow area at the valve seat region rather than by the cross-sectional area of the orifice. Thus the seat region of nozzle becomes the bottleneck and enhances the turbulence of the internal flow. This *duo contracta* effect suggests the important effect of turbulence on the atomization process.

This paper presented an extensive study on the effect of the change in nozzle geometry on the liquid flow inside the nozzle and the subsequent atomization process. The internal flows inside the nozzle were simulated as non-cavitating liquid. The calculation results were then correlated to the TAB spray model in KIVA-II code. Particularly, the turbulence characteristics of the exit flow were incorporated into the spray model by the parameter *amp0*, which represents the initial deforming rate of the drop surface. Although diesel injection is highly transient, only quasi-steady analysis has been carried out in order to simplify the analysis.

TAB MODEL AND TPB METHOD

TAB (Taylor analogy breakup) model is based on Taylor analogy. Details of this technique can be found in reference [15], therefore only a brief description is noted here. In accordance with the Taylor analogy, the displacement of the equator of the droplet from its equilibrium position, x, is governed by the equation of a damped, forced harmonic oscillator. Normalizing x by $C_b r$, we have

$$y = \frac{x}{C_b r}, \tag{1}$$

where C_b is a model constant which is equal to 1/2, r is the radius of the droplet. Droplet breakup occurs if and only if $y > 1$. For constant relative speed u between the gas and droplet, y can be described by the following equation.

$$y(t) = \frac{C_F}{C_k C_b} We + e^{-t/t_d} \left\{ \left(y_0 - \frac{C_F}{C_k C_b} We \right) \cos \omega + \frac{1}{\omega} \left(\dot{y}_0 + \frac{y_0 - \frac{C_F}{C_k C_b} W}{t_d} \right) \sin \omega \right\} \tag{2}$$

where y_0 and $\dot{y}_0$ represent initial displacement and velocity of the droplet oscillation, respectively, and the parameters

$$We = \frac{\rho_a u^2 r}{\sigma}, \quad \frac{1}{t_d} = \frac{C_d \mu_l}{2 \rho_l r^2}, \quad \omega^2 = C_k \frac{\sigma}{\rho_l r^3} - \frac{1}{t_d^2}, \tag{3}$$

where t_d is the damping time, ω is the oscillation frequency, μ_l is the liquid viscosity, ρ_l is the liquid density, and C_F, C_k, C_b and C_d are model constants. In TAB model, the initial deforming rate $\dot{y}_0$ is related to another model parameter *amp0* by

$$\dot{y} = amp0 \cdot \omega_0, \tag{4}$$

where ω_0 is the initial oscillation frequency for the droplet.

TPB (turbulent primary breakup) method [16] was previously applied to the calculation of port injections with TAB model in KIVA-II code and taken to gasoline direct injection analysis with good agreement with experimental result [17]. With the assumption of isotropic turbulent state of the exit flow of the nozzle, this method is intended to give a reasonable estimation for the model parameter *amp0*. Combining Eqs. (1) and (4), we have

$$\dot{y} = \frac{\dot{x}}{C_b r} = amp0 \cdot \omega_0, \tag{5}$$

where r_0 is the initial drop radius and $\dot{x}_0$ is the dimensional initial deforming rate of the drop surface. The TPB method correlates $\dot{x}_0$ to the flux-averaged kinetic turbulent energy of the exit flow, k_0, by

$$\dot{x} = \sqrt{\frac{2}{3} k_0}. \tag{6}$$

The initial oscillation frequency ω_0 in Eq. (5) is determined from Eq. (3).

$$\omega_0 = \sqrt{C_k \frac{\sigma}{\rho_l r_0^3} - \left(\frac{C_d \mu_l}{2 \rho_l r_0^2} \right)^2} \tag{7}$$

Substituting Eqs. (6) and (7) into Eq. (5), we have

$$amp0 = \frac{1}{C_b r_0 \omega_0} \cdot \dot{x} = \frac{1}{C_b r_0 \omega_0} \cdot \sqrt{\frac{2}{3} k_0}. \tag{8}$$

2

The parameter *amp0* can be used as an indication of the turbulence intensity of the exiting flow.

FUEL FLOW INSIDE A NOZZLE

MODEL DETAILS – The internal liquid flows inside VCO (valve covered orifice) and mini-sac nozzles were numerically studied using 3D CFD analysis. The possible effects of cavitation on the flow field were not taken into consideration in this study. The parameters studied here include the aspect ratio of the nozzle (L/D), the cone angle of the needle valve (α), the discharging direction (β), the normalized needle lift (H/D), the curvature of the orifice entrance (R/D) and the injection pressure. The down stream pressure at the nozzle exit was kept at atmospheric pressure. Figure 1 shows schematically the above mentioned parameters in a VCO nozzle. For the mini-sac case, the orifice was moved from the side down to the bottom of the nozzle.
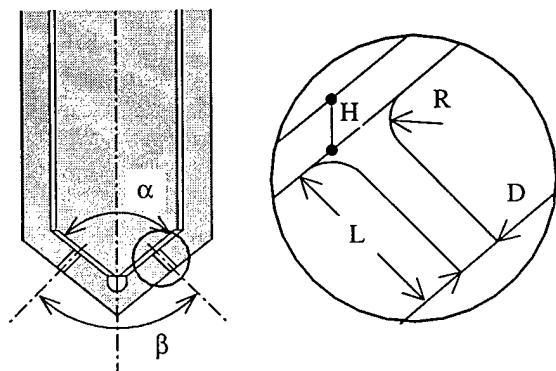
Figure 1. A schematic view of the VCO nozzle tip

The tip part of a typical mesh for VCO nozzle is shown in Fig. 2. There are three inlet holes at the top of the nozzle and eight exit orifices at the bottom. For computational economy, half of the flow domain was taken in our calculation.
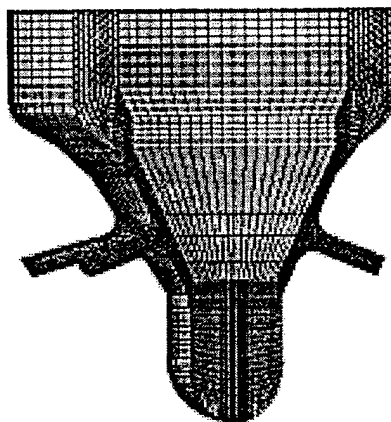
Figure 2. Perspective view of a typical mesh

The calculations were performed using SIMPISO algorithm, which is similar to SIMPLE algorithm but tolerates more mesh distortion, with standard k- ε turbulence

model. Figure 3 shows a distribution of kinetic turbulent energy of the flow field in the orifice. This computational result was obtained under the condition of L/D=4.7, H/D=0.14, α=60 degrees, β=145 degrees, ρ=840kg/m^3 and Δp=100MPa. The kinetic turbulent energy k and dissipation ε at the inlets are calculated based on the assumption of 10% turbulence intensity and a mixing length of one order of magnitude less than the inlet diameter.

The parameters studied in this paper are shown in Table 1. Unless other noted, the condition of the underlined refers to the analysis case.

Table 1. Parameters studied in this analysis.

D (mm)	L/D	H/D	R/D	α (°)	β (°)	ΔP (MPa)
0.160	4.7	0.14	0	60	145	50
0.184	5.2	0.42	0.1	90	156	100
	8.4	0.62	0.3			178
		1.4	0.5			
			0.6			
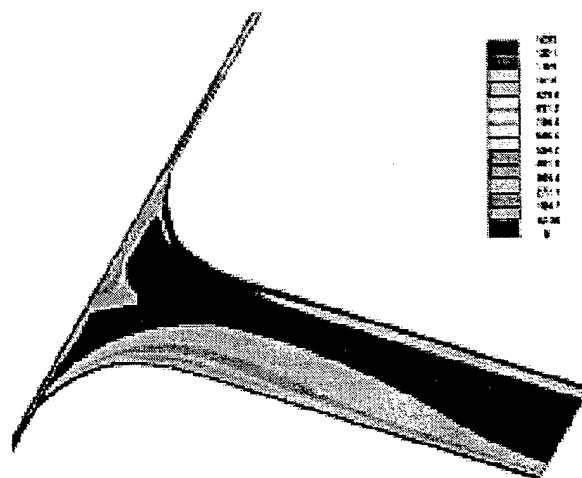
Figure 3. Turbulent kinetic energy distribution (D=0.18 4mm)

The computational results show that the nozzle design has a strong effect on its internal flow between the needle valve and its seat and the flow field in the orifices. The upper stream flow field of the nozzle changes very little during the parameter study. All the nozzle design parameters studied in this paper influence the flow pattern around the orifice entrance. Among these parameters, the needle lift has the most important influence on the internal flow characteristics. When the needle lift is large, e.g. H/D=1.4, the flow at the orifice entrance is relatively smooth and there is no obvious vortex. On the contrary, when the needle lift is small, e.g. H/D=0.14, a strong large vortex appears at the orifice entrance and most turbulence is generated between the needle valve and its seat rather than at the orifice entrance. The change of the curvature of the inlet entrance also has a significant influ-

3

ence on the internal flow, especially when R/D is small. Other parameters have a relatively smaller effect on the internal flow.

EFFECTS OF NOZZLE DESIGN ON C d AND *amp0* – Two important performance parameters of the nozzle, the fuel discharge coefficient Cd and the initial amplitude parameter *amp0*, were evaluated for different nozzle designs. The calculated discharge coefficient and *amp0* are plotted against needle lift for different injection pressures and aspect ratios of the orifice in Fig. 4 and Fig. 5, respectively. The initial amplitude parameter *amp0* is obtained from the flux averaged turbulent kinetic energy of the exiting flow. The discharge coefficient is defined by

$$Cd = \frac{\overline{V}}{\sqrt{2\Delta p / \rho_l}} , \qquad (9)$$

where $\overline{V}$ is the mean flow velocity at the nozzle exit, Δp is the pressure difference between the injector and outlet, an ρ_l is the density of the liquid. The Cd computed is larger than experimental value, mostly due to lack of transient and cavitation consideration.
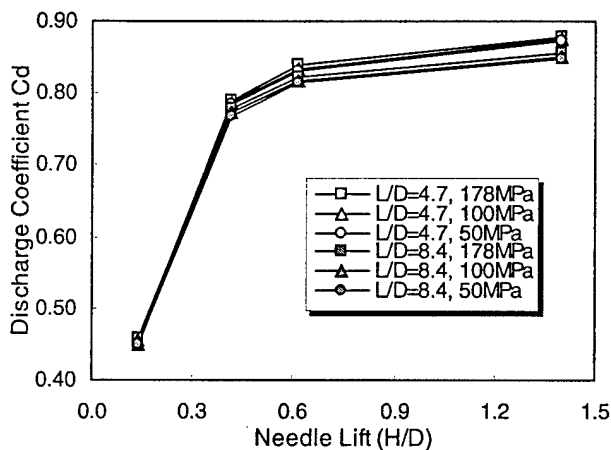
Figure 4. Variation of discharge coefficient with needle lift

As shown in Fig. 4 and Fig. 5, needle valve lift (H/D) has a strong effect on both Cd and amp0. For all cases, Cd increases at a decreasing rate with the increase of needle lift. This tendency agrees with the computational results of Oishi et al. [3]. Under the condition of large need lift (H/D > 0.5), Cd increases slightly with the increase of H/D. Under the condition of small needle lift (H/D < 0.5), Cd increases significantly with the increase of H/D, as shown in Fig. 4. This is because the throat of the nozzle is located between the valve and the seat rather than in the orifice for the cases of small needle lift.

The initial amplitude parameter *amp0* has the same tendency as that of Cd, as shown in Fig. 5. It increases with the increase of needle lift and increases more quickly at low needle lift conditions. When H/D changes from 0.6 to

1.4, *amp0* remains almost identical. But H/D has a strong influence on *amp0* when H/D is small.
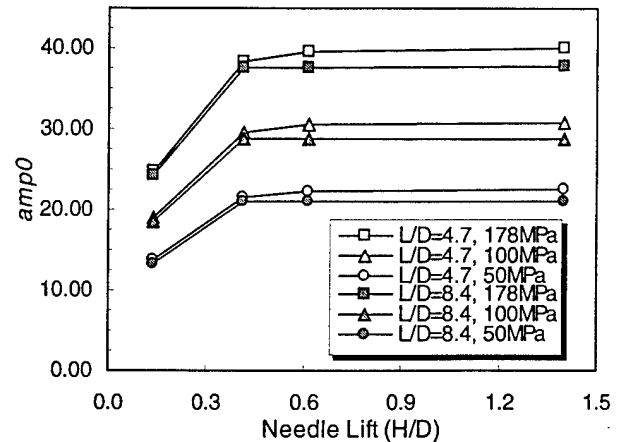
Figure 5. Variation of *amp0* with needle lift

Figure 4 and Fig. 5 also show the effects of injection pressure on Cd and amp0, respectively. Increase of injection pressure doesn't enhance discharge coefficient too much when injection pressure is high. As can be seen in Fig. 4, Cd increases less than 1.5% by increasing injection pressure difference from 50MPa to 178MPa. This agrees with the reults of Ohrn et al. [7]. Differing from Cd, amp0 increases significantly with the increase of injection pressure, as shown in Fig. 5. This is reasonable. Although Cd remains almost identical with the increase of injection pressure, the velocity of flow inside the orifice increases. So the shear stress increases along the boundary of the orifice, which leads to the increase of turbulent kinetic energy and amp0.

The aspect ratio of exit orifice, L/D, also influences Cd and amp0, especially under large needle lift conditions, as shown in Fig. 4 and Fig. 5. The discharge coefficient Cd decreases slightly with the increase of L/D (from 4.7 to 8.4). This is contributed to the friction between the fluid and the wall of the orifice. The initial amplitude parameter amp0 also decreases slightly with the increase of L/D.
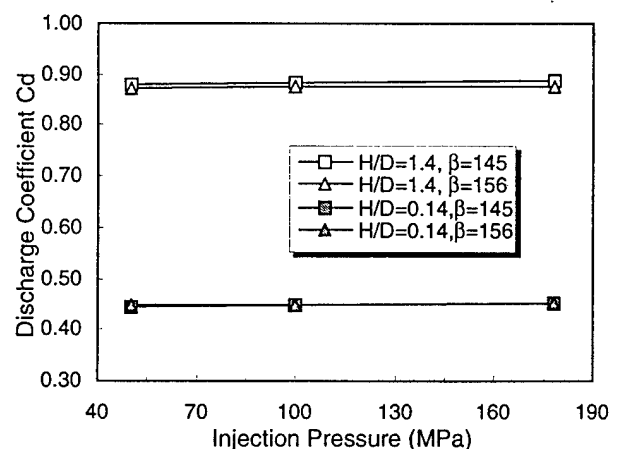
Figure 6. The effect of discharging direction on Cd
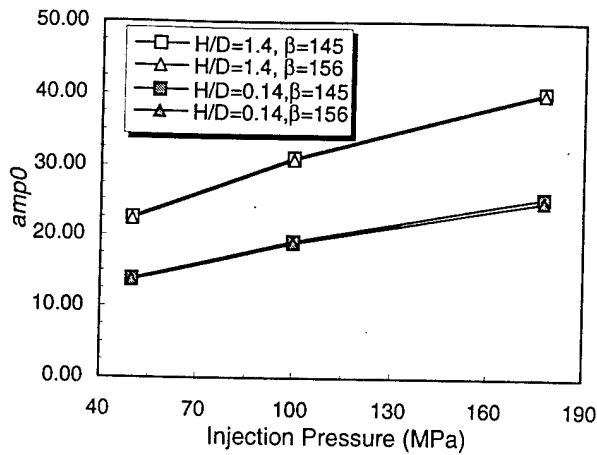
Figure 7.   The effect of discharging direction on *amp0*
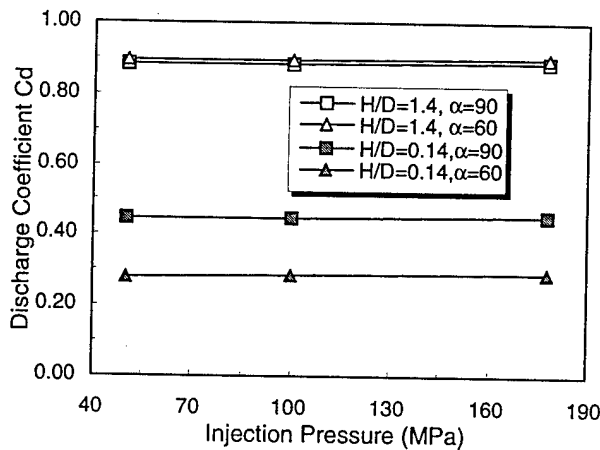
Figure 8.   Effect of valve cone angle on Cd
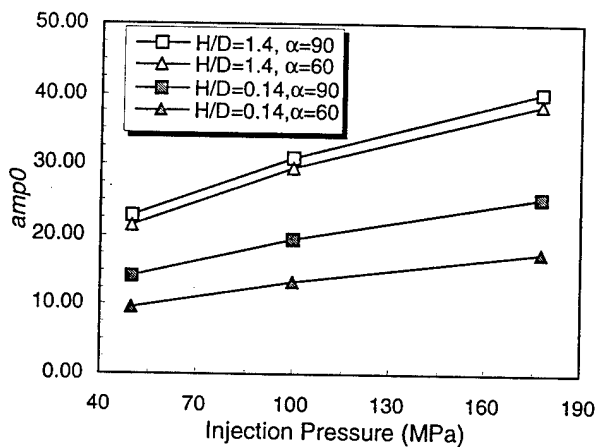
Figure 9.   Effect of valve cone angle on *amp0*

As can be seen in Fig. 2, turbulence is mainly generated at the inlet region of the exit orifice. So it is important to study the influence on the flow of the change in geometry at that region. The effect of change in discharging angles (β) on the discharge coefficient is displayed in Fig. 6. It shows that the nozzle with smaller discharging angle (β=145) has a larger discharge coefficient at high needle

lift (H/D=1.4). That is, the smaller in the turning angle from the seat to the orifice, the higher the flow speed of the fuel at the nozzle exit. Under the condition of low needle lift (H/D=0.14), however, the discharge coefficient is almost identical for two different turning angle cases. This is because the needle lift becomes the dominant effect on the discharge coefficient under small needle lift condition.

Figure 7 shows the effect of discharging direction (β) on *amp0*. The initial amplitude parameter *amp0* increases slightly with the decrease of discharging angle for both large and small needle lift cases.

Figure 8 shows the effects of change in valve cone angle (α) on the discharge coefficient. The discharge coefficient decreases with the increase of valve cone angle under the condition of large needle lift (H/D=1.4). This is contributed to the change in the turning angle from the seat to the orifice. Differing from the change in discharging angle (β), change in valve cone angle (α) influences the discharge coefficient considerably under the condition of small needle lift (H/D=0.14). As shown in Fig. 8, the discharge coefficient increases more than 50% when the valve cone angle is changed from 60 to 90 degrees. This is because the throat of the nozzle is between the seat and valve under these conditions and the clearance between them is determined by α as well as H. In contrary to the large needle lift case, the nozzle with large valve cone angle has large discharge coefficient for the small needle lift case.

Shown in Fig. 9 is the effect of change in the valve cone angle (α) on *amp0*. It can be seen that *amp0* is more influenced by the change in valve cone angle under the condition of small needle lift. Under the condition of large needle lift, although discharge coefficient decreases with increase of α, *amp0* increases with α. This is because the increase of α enhances the turbulence at the entrance of the orifice.
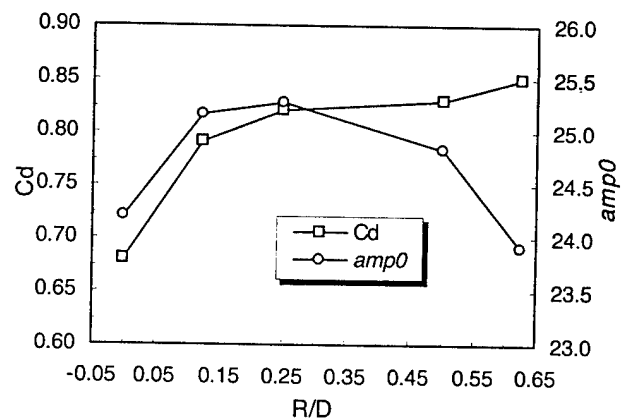
Figure 10. Effect of R/D on Cd and amp0

Figure 10 shows the effects of the change in the curvature of orifice inlet on discharge coefficient and *amp0*. The results were obtained under the conditions of

5

D = 0.16mm, L/D = 5.2, H/D = 1.6. As shown in Fig. 10, the discharge coefficient increases at a decreasing rate with the increase of inlet fillet radius. When R/D is small, it has a strong effect on the discharge coefficient. Increasing R/D can enhance the discharge coefficient by 20%, as shown in Fig. 10. This agrees with the results of Kampmann et al. [9]. The initial amplitude parameter *amp0*, however, has a maximum value at R/D = 0.2. This is because the increase of R/D tends to increase the mean flow velocity and enhance the turbulence, but the smoothness of the orifice entrance tends to generate less turbulence at the inlet of the orifice.

Figure 11 shows the discharge coefficients of mini-SAC and VCO nozzles under the full needle lift condition (H/D=1.4). It shows that the discharge coefficient of mini-SAC nozzles is much lower than that of VCO nozzles. This is caused by the sudden expansion of the flow passage at the entrance of the sac. It also shows that the curvature of the orifice entrance has a significant effect on the discharge coefficient.

Figure 12 shows the discharge coefficients for mini-SAC and VCO nozzles under small needle lift condition (H/D = 0.14). Differing from the large needle lift cases, the discharge coefficient of mini-SAC nozzles is much larger than that of VCO nozzles. This is because that the mini-SAC nozzle has only one orifice while the VCO nozzles have eight, and the critical flow area is located between the needle valve and the seat under smaller needle lift condition.

Figure 13 and 14 show the *amp0* for mini-SAC and VCO nozzles under full needle lift condition (H/D = 1.4) and small needle lift condition (H/D = 0.14), respectively. It can clearly be seen that VCO nozzles have much higher turbulence than mini-SAC nozzle under both full and small needle lift conditions. This indicates that sprays discharged from VCO nozzles will have wider angles. The effects of R/D on *amp0* for mini-SAC nozzles can also be seen in Fig. 13 and Fig. 14.

Figure 11. Discharge coefficient for different nozzles (H/D=1.4)
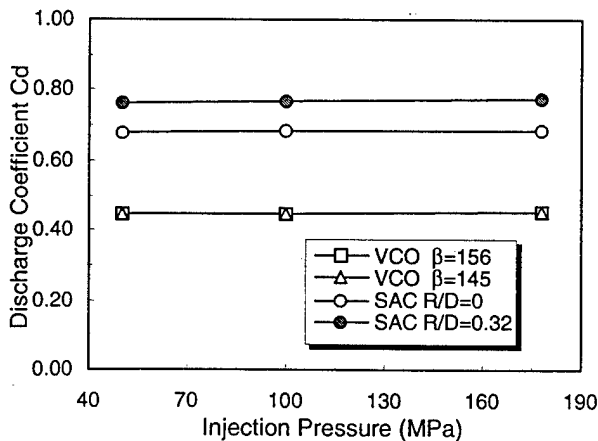
Figure 12. Discharge coefficient for different nozzles (H/D=0.14)

Figure 13. amp0 for different nozzles (H/D=1.4)
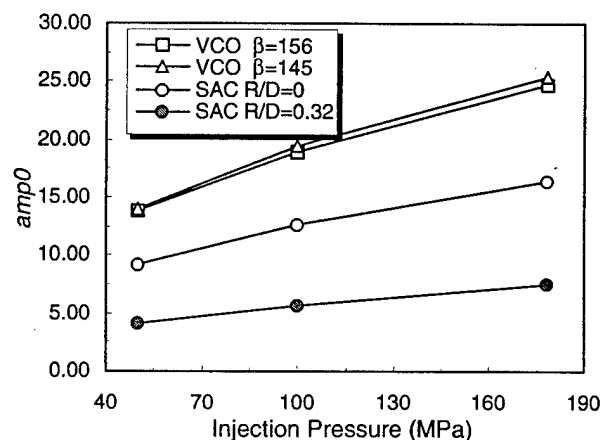
Figure 14. amp0 for different nozzles (H/D=0.14)

6
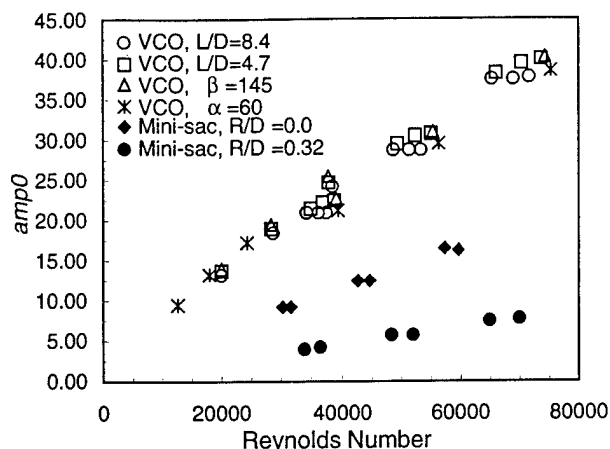
Figure 15. Variation of amp0 with Reynolds number

Figure 15 shows the value of the initial amplitude parameter plotted against its corresponding Reynolds number of the exit flow. All the R/D's of the VCO nozzles in Fig. 15 are about 0.4. It shows that the value of *amp0* of VCO nozzles is higher than that of mini-SAC nozzles. For a given type of nozzle (VCO or mini-SAC) and a given curvature of the orifice entrance, the *amp0*'s are correlated fairly well with the Reynolds number. This indicates an easy way to estimate the value of *amp0* for a nozzle under different operating conditions.

DISTRIBUTION OF VELOCITY AND TURBULENT ENERGY AT THE NOZZLE EXIT – Velocity profile rearrangement at the nozzle exit could be a mechanism of atomization [1]. Shown in Fig. 16 are the velocity profiles along the vertical diameter of orifice at the nozzle exit. The velocity is normalized by the corresponding mean ve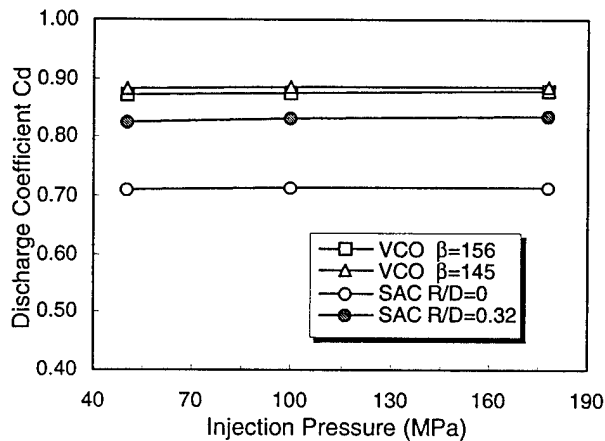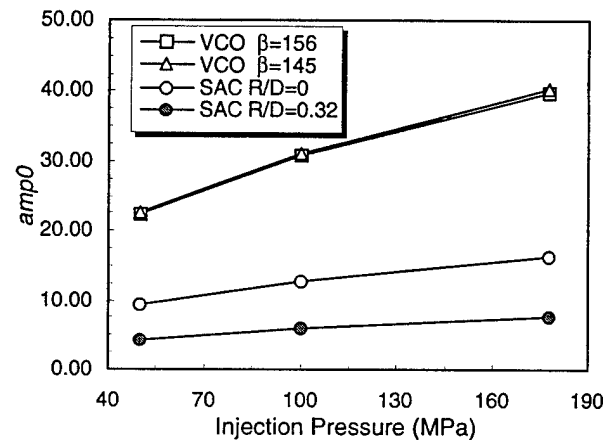locity of the exit flow. The horizontal axis is the location along the vertical diameter with 1.0 at the top and −1.0 at the bottom.

Figure 16(a) shows the velocity profiles for the baseline case (L/D=4.7, H/D=1.4, α=90, β=156) under different injection pressures. It shows injection pressure has little effect on the pattern of velocity distribution. It also can be seen that due to the turning angle inside VCO nozzle the velocity profiles are not symmetric, with more fluid discharged from the lower part of the orifice.

When L/D increases from 4.7 to 8.4, as shown in Fig. 16(b), the velocity profiles tend to be more symmetric. In this case, the velocity profiles are almost identical under different injection pressure conditions. The effect of L/D on the velocity profile can be clearly seen in Fig. 16(c).

The effect of needle valve lift on velocity profile is shown in Fig. 16(d). The velocity profile is strongly influenced by the amount of needle valve lift. As the needle valve lift decreases, more fluid is discharged through the upper part of the nozzle orifice. For the 10% needle valve lift case, there are actually two peaks on the velocity profile.

The effects of valve cone angle on velocity profile are shown in Fig. 16(e) and (f) for H/D = 1.4 and H/D=0.14, respectively. It can be seen that valve cone angle has

stronger effect on the velocity profile under larger H/D condition. Smaller valve cone angle tends to produce more symmetric spray. The effects of injection direction on velocity profile are relatively small, as shown in Fig. 16(g).

Figure 16(h) shows the velocity profile at the nozzle exit for mini-SAC nozzle, which is plotted against that of VCO nozzle under the same conditions. Since there is only one orifice for the mini-SAC nozzle considered and its geometry is symmetric, the velocity profile for mini-SAC nozzle is also symmetric.

The radial component of velocity in turbulent pipe flow could cause the immediate atomization of spray at the nozzle exit [18]. This phenomenon has been observed in experiment [7]. Figure 18 shows the turbulent energy distribution along the vertical diameter of the nozzle exit. The turbulent energy is normalized by its corresponding mean value.

Shown in Fig. 17(a) are the turbulent energy profiles for the baseline case under different injection pressures. With the increase of injection pressure, more turbulence is generated at the lower part of the orifice. Under the condition of longer L/D, the turbulent energy profiles tend to be identical, as shown in Fig. 17(b). The turbulent energy profiles for different L/D are compared in Fig. 17(c). Figure 17(d) shows the effect of H/D on the turbulent energy profile. It can be seen that more turbulent energy is generated at the upper part of the orifice as the needle valve decreases. The effect of valve cone angle on the turbulent energy profile is shown in Fig 17(e) and (f) for H/D=1.4 and 0.14, respectively. The decrease of valve cone angle tends to produce more symmetric turbulent energy profile. The injection direction doesn't influence the turbulent energy profile too much, as shown in Fig. 17(g). The turbulent energy profile for mini-SAC nozzle is plotted against that of VCO nozzle in Fig. 17(h). It shows that more turbulent energy concentrates at the wall boundary for mini-SAC nozzles.

APPLICATION IN SPRAY PREDICTION

CALCULATION CONDITIONS – A 2-dimensional cylindrically symmetric grid with cell dimensions of 2 mm in the axial direction and 1 mm in the radial direction was employed in our spray computations. The size of the computational domain was 40 mm in the radial direction and 120 mm in the axial direction. Time step was varied in the range of 0.5 to 10 μs. The standard k-ε turbulent model was used, and the TAB method was employed in the original formula with standard values for model constants, $C_b = 1/2$, $C_k = 8$, $C_d = 5$ and $C_F = 1/3$. Non-evaporating condition was considered.

Although we have studied the effects of nozzle design on Cd, *amp0*, velocity and turbulent energy profiles at the nozzle exit, it is difficult to consider all these factors in our spray modeling. In this paper, we focus on the effect of *amp0*, which represents the turbulence characteristics of the exit flow, on the atomization of spray. The value of
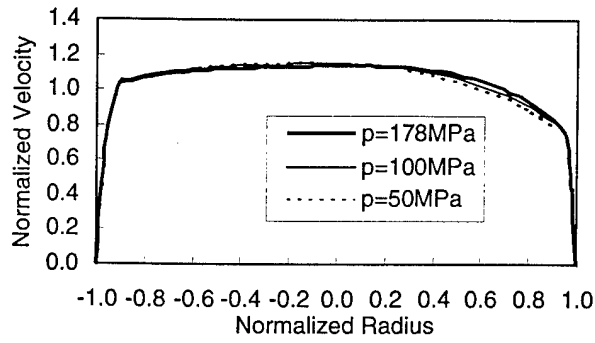
(a) L/D=4.7, H/D=1.4
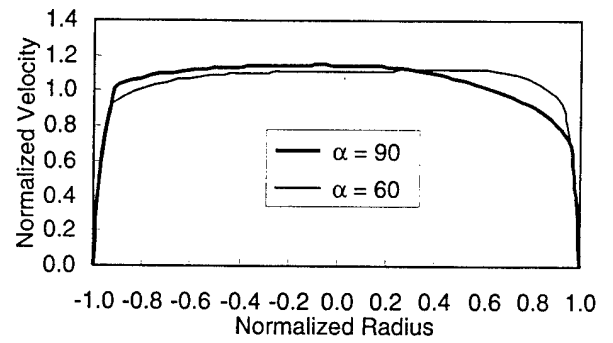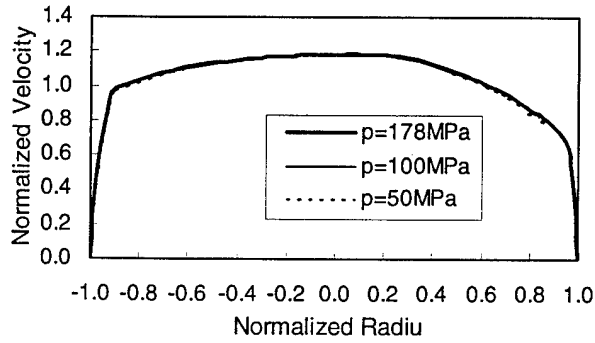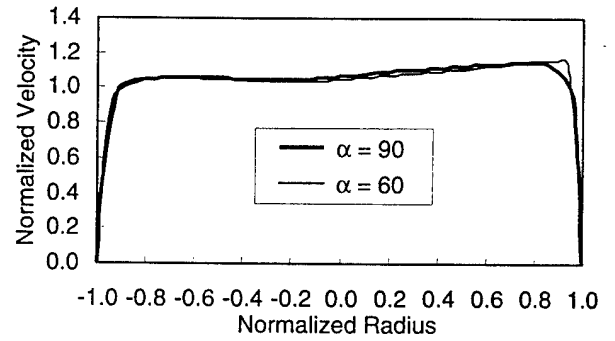
(b) L/D=8.4, H/D=1.4

(c) P=100MPa, H/D=1.4

(d) L/D=4.7, P=100MPa
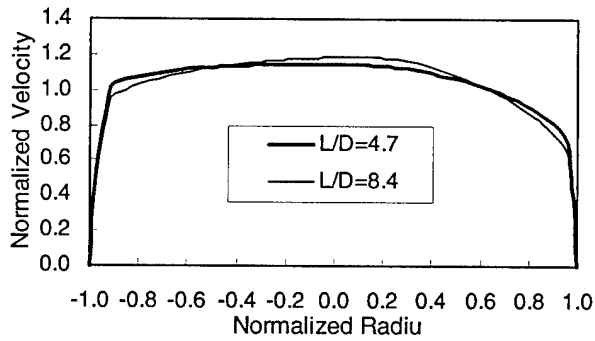
(e) L/D=4.7, P=100MPa, H/D=1.4
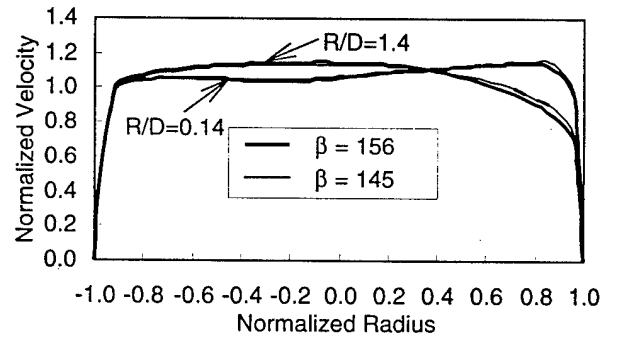
(f) L/D=4.7, P=100MPa, H/D=0.14
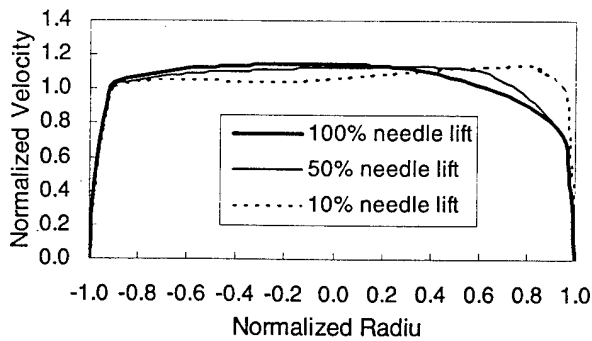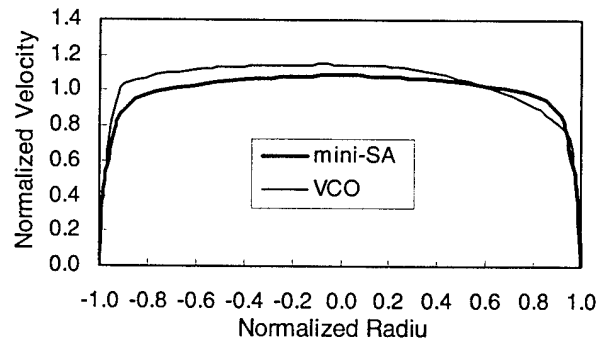
(g) L/D=4.7, P=100MPa

(h) L/D=4.7, P=100MPa, H/D=1.4

Figure 16.   Normalized velocity distribution at the orifice exit
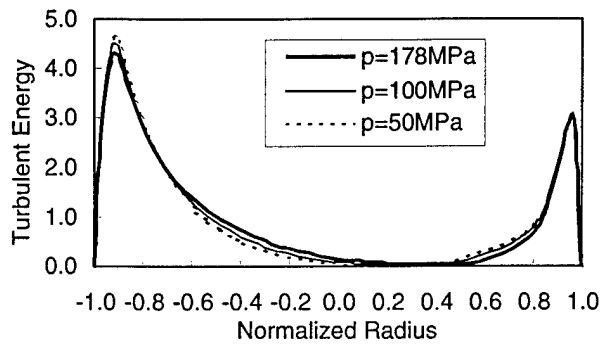
(a) L/D=4.7, H/D=1.4
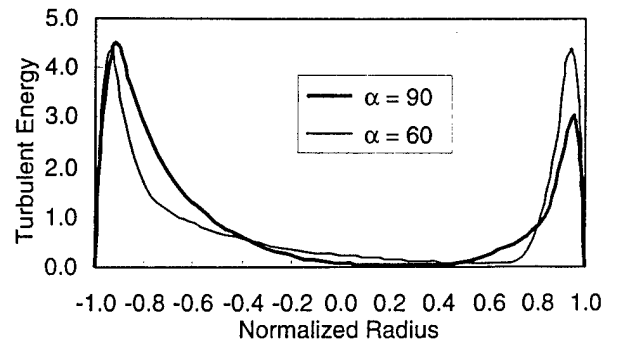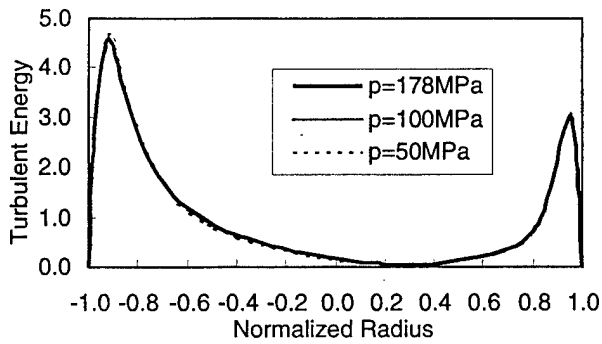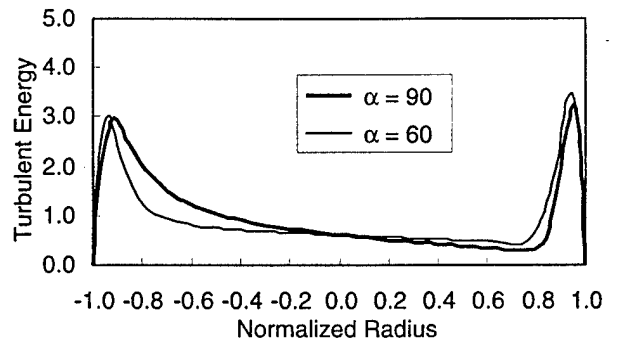
(b) L/D=8.4, H/D=1.4

(c) P=100MPa, H/D=1.4

(d) L/D=4.7, P=100MPa
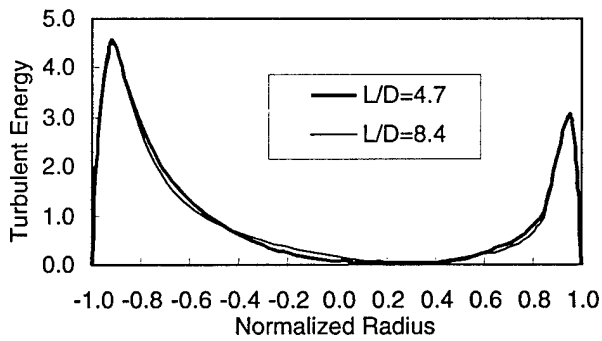
(e) L/D=4.7, P=100MPa, H/D=1.4
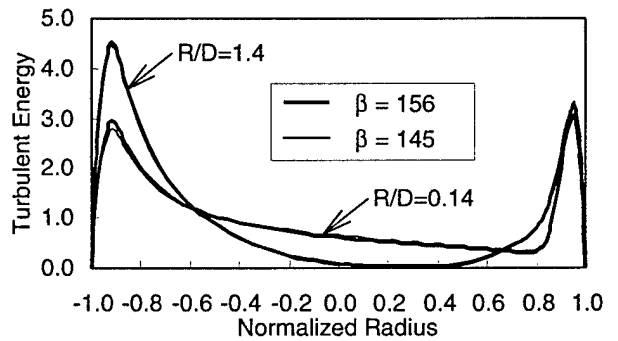
(f) L/D=4.7, P=100MPa, H/D=0.14
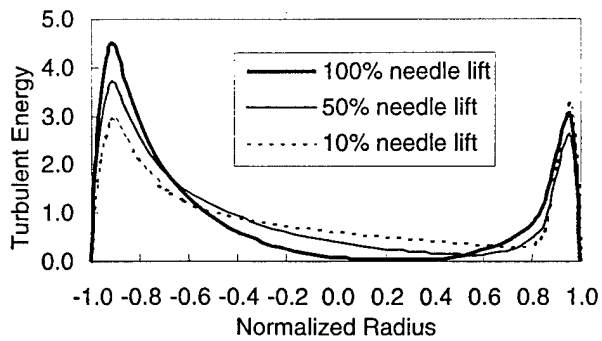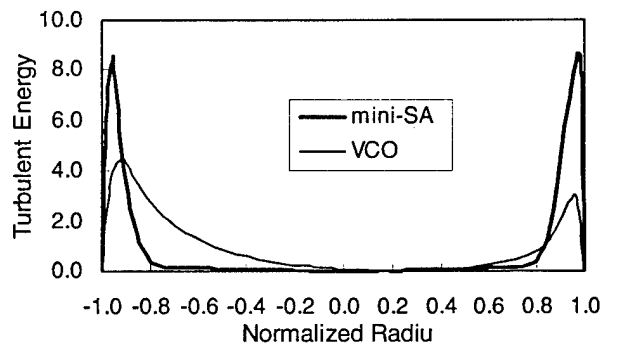
(g) L/D=4.7, P=100MPa

(h) L/D=4.7, P=100MPa, H/D=1.4

Figure 17.   Normalized turbulence distribution at the orifice exit

 amp0 was changed within a wide range from 0.0 to 50.0 in our computations. The spray injection velocity in the current modeling is shown in Fig. 18, which is taken from the results of our experiments.
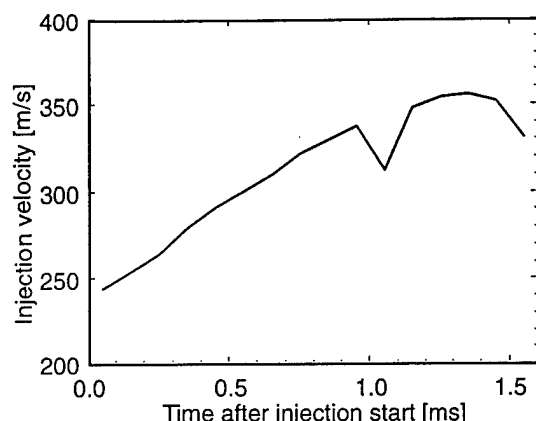
Figure 18. Injection velocity used in KIVA calculation

CALCULATION RESULTS – Shown in Fig. 19 are the parcel distributions of the sprays with different values of amp0 at 0.2 ms after the injection starts. These are the cases for lower ambient gas density (ρ_a=1.2kg/m^3). It can be seen that the spray structure is strongly influenced by the value of amp0. With the increase of amp0, the spray spreads more widely in the radial direction, but the penetration length becomes shorter. This indicates a nozzle with higher turbulent energy at the orifice exit will produce a spray with wider cone angle and shorter penetration.

Thus, all the change of the nozzle design that enhance the turbulent energy of the exit flow, such as the change from mini-SAC to VCO type and decrease of the radius of the nozzle orifice, will improve the spray cone angle. The tendency of the influence of the orifice entrance curvature on the spray cone angle agrees with the experimental result [12].

Changes in the drop size distribution are shown in Fig. 20 for different amp0 values at 0.4 ms after injection start. For each computation case, parcels are classified and plotted according to their size ranges. These figures also show that the spray outer shapes are determined mainly by the middle size parcels (5 < dp < 20 μm) for all the cases. Comparing these figures, we can see that more smaller size drops (dp < 5 μm) were produced for larger amp0. At the same time, the number of large size drops was reduced. Unbroken drops (dp = 188μm) exist for the case of no initial disturbances (amp0 = 0.0). With the increase in amp0, the small size drops (dp < 5μm) tend to appear more frequently at the upstream region of the spray (around z=10~30 mm). Thus, under the same condition of discharging rate and orifice diameter, VCO nozzles will produce finer droplets than mini-SAC nozzles; and sharp orifice entrance will enhance the quality of atomization (wider spray cone angle and finer droplets) for the same type of nozzle. Other parameters of nozzle design have relatively smaller effects on the quality of spray atomization.

Figure 19. Change in parcel distribution with initial disturbance (t=0.2 ms, ρ_a=1.2kg/m3)
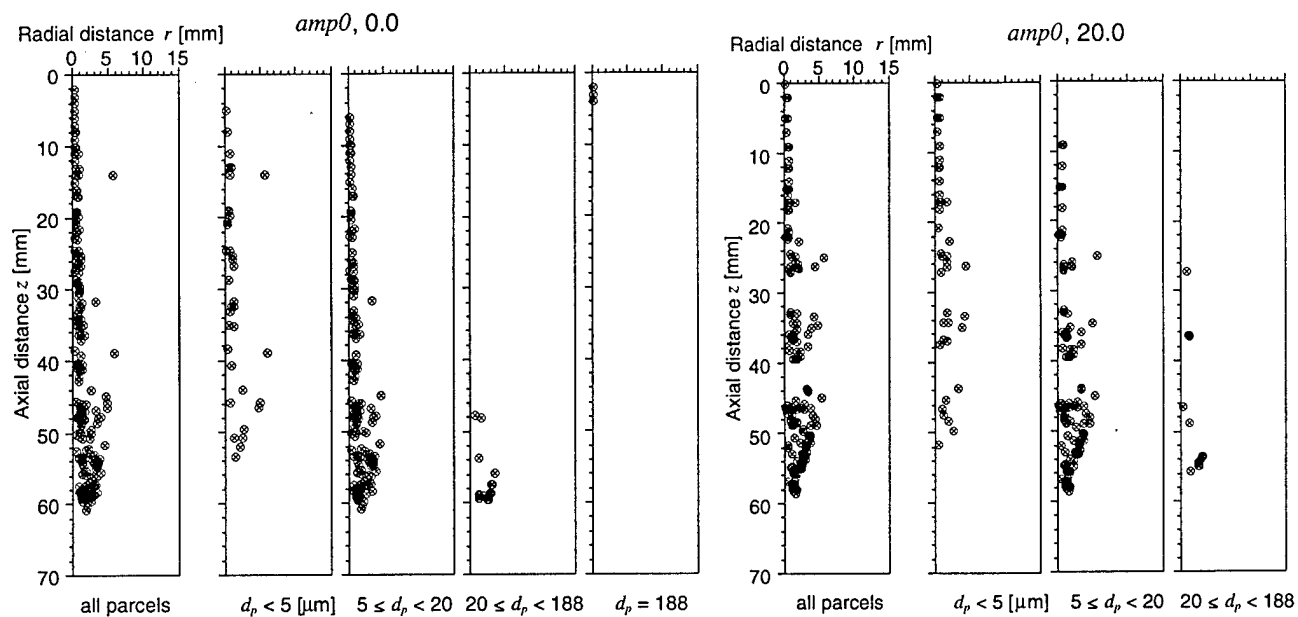
Figure 20.　Size classified distribution of parcels with initial disturbance (t=0.4 ms, ρ_a=1.2kg/m3)
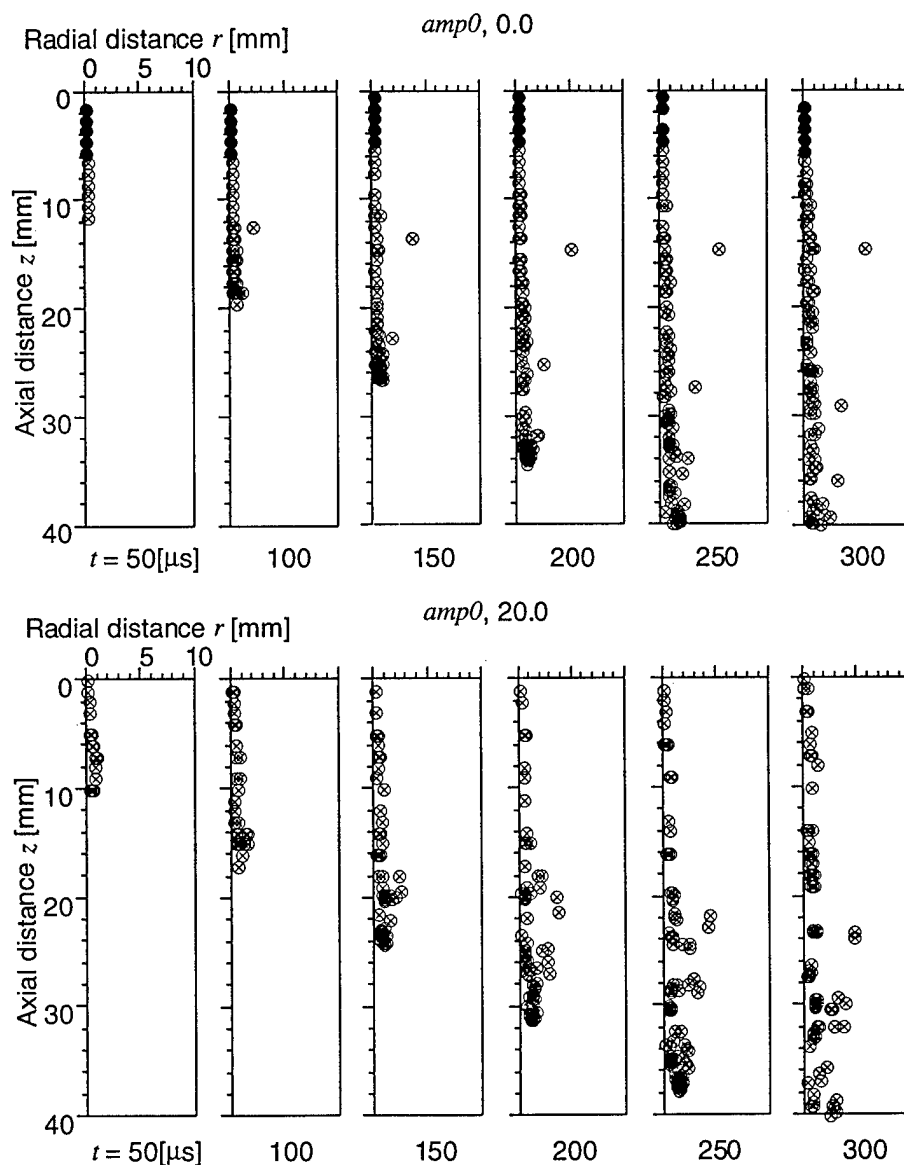
Figure 21.　Temporal change in parcel distribution with and without initial disturbance

Shown in Fig. 21 are the temporal changes in the parcel distribution for different *amp0* values at the early stage of spray injection. In the case of no initial disturbance, as shown in the upper side figure, unbroken drops remain at a space close to the nozzle exit (z < 5 mm). These unbroken drops indicated by solid circles can be seen for the entire time period. After breakup into droplets, the spray penetrates straightly toward downstream, except for a few fine droplets at z = 13 mm (3.7μm in diameter) and 22 - 29 mm (2.5μm). However, these small droplets have not sufficient momentum to penetrate toward the radial direction comparing to those drops at the spray tip. The almost straight penetration of the liquid injection under the condition of very low initial turbulence is in consistent with the experiments of Tamaki et al. [13].

When the exit flow is turbulent, e.g. *amp0* = 20, spray breaks up instantaneously at the nozzle exit, as shown in Fig. 21. This phenomenon agrees with the experimental results of Lai et al. [7]. These atomized droplets traverse in the radial direction as well as toward downstream. The spray has a much wider cone angle but a shorter penetration compared to the non-disturbance case.
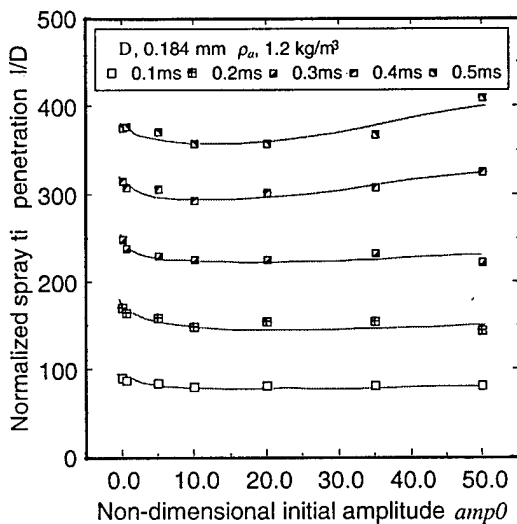
Figure 22. Change in normalized tip penetration
(ρ_a=1.2kg/m^3)

Figure 22 shows the development of tip penetration with time under different values of amp0. The penetrations are normalized by the diameter of the nozzle orifice. It can be seen that for small amp0 cases the tip penetration decreases with increase of amp0. For large amp0 cases, the tip penetration doesn't change with the value of amp0 at the early stage of injection. At the late stage of injection, sprays with large amp0 penetrate faster.

Figure 23 shows the spray simulation results against available experimental results. In this case, the ambient pressure ρ_a = 19.4 kg/m^3 and the initial deforming rate *amp0* = 20. The numerically predicted tip penetration agrees well with the experimental results.
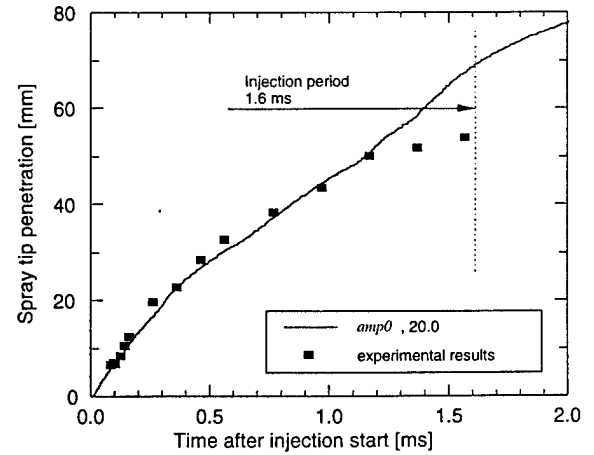
Figure 23. Spray tip penetration with amp0
(ρ_a=19.4kg/m^3)

DISCUSSIONS

In the present work, we just considered the effect of mean discharge coefficient and *amp0* at the nozzle exit in the spray modeling. The uneven distribution of velocity and turbulent energy at the nozzle exit could also influence the behavior of spray. How to take these factors into spray modeling is interesting and challenging.

Compared with our experimental results, the calculated discharge coefficients are a little higher. One possible reason is that the transient effect was not considered in our steady state simulations. Another possible reason is that the possible formation of cavitation was not taken into consideration in this study. In our calculation, the pressure in one small zone at the entrance of the nozzle orifice falls below the vapor pressure of the liquid. This indicates the flow at that area can be a two-phase flow. The occurrence of cavitation will reduce the effective cross-sectional area of the flow in the nozzle orifice and thus reduce the discharge coefficient [19, 20]. Further work needs to be done to study the effect of cavitation in the nozzle on the atomization of spray.

CONCLUSIONS

In the present study, the internal flows in VCO and mini-SAC nozzles were studied under different geometric and operating conditions. The calculation results were then incorporated into the TAB spray model in KIVA code to study the effect of nozzle design on the atomization of diesel spray

Change in nozzle geometry can influence its internal flow and consequently the atomization process. The discharge coefficient Cd and the initial amplitude parameter *amp0* are two important parameters influencing the spray behavior. They can both be improved by changing the nozzle aspect ratio, discharging direction, needle valve shape, curvature of the orifice inlet, and so on. Discharge

coefficient and *amp0* are also greatly influenced by changing the needle lift. Thus the nozzle performance can also be improved by controlling the history of needle lift.

Despite the changes in nozzle geometry, *amp0* of a nozzle (VCO or mini-SAC) with given curvature of the orifice entrance can be correlated fairly well to the Reynolds number based on the parameters of the exit flow. This indicates an easy way to obtain a good estimation of *amp0*.

The computational results of the internal flow of nozzle have been correlated to the TAB spray model in KIVA-II. The discharge coefficient and initial disturbance have a strong effect on spray cone angle and tip penetration. Increase of the initial disturbance of the exit flow can significantly enhance the atomization of a liquid jet. Larger initial disturbance tends to produce smaller droplets and wider spray cone angle.

ACKNOWLEDGEMENT

REFERENCES

1. Reitz, R. D. and Bracco, F.V., 1982, "Mechanism of Atomization of a Liquid Jet," Physics Of Fluids, Vol. 25, pp. 1730-1742.

2. Ranz, W. E., 1958, "Some Experiments on Orifice Sprays," The Canadian Journal of Chemical Engineering, Vol. 36, pp. 175-181.

3. Oishi, Y, Miura, A., Hamazaki, N. and Watanabe, Y., 1992, "A computational Study into the Effect of the Injection Nozzle Inclination Angle on the Flow Characteristics in Nozzle Holes," SAE Paper, No. 920580.

4. Arcoumanis, C. and Gavaises, M., 1998, "Linking Nozzle Flow with Spray Characteristics in a Diesel Fuel Injection System," Atomization and Sprays, Vol. 8(3), pp. 307-347.

5. Su, T. F., Farrell, P. V. and Nagarajan, R. T., 1995, "Nozzle Effect on High Pressure Diesel Injection," SAE Paper, No. 950083.

6. Potz, D., Kreh, A. and Warga, J., 1995, "Variable Orifice Geometry Verified on the Two-Phase Nozzle (VRD)," SAE Paper, No. 950081.

7. Lai, M. C., Wang, T. T.-C., Xie, X., Han, J. S., Henein, N. A., Schwartz, E. and Bryzik, W., 1998, "Microscopic Characterization of Diesel Sprays at VCO Nozzle Exit", SAE paper, No. 982542.

8. Ohrn, T. R., Senser, D. W. and Lefebvre, A. H., 1991, "Geometrical Effects on Discharge Coefficients for Plain-Orifice Atomizers", Atomization and Sprays, Vol. 1(2), pp. 137-153.

9. Ohrn, T. R., Senser, D. W. and Lefebvre, A. H., 1991, "Geometric Effects on Spray Cone Angle for Plain-Orifice Atomizers", Atomization and Sprays, Vol. 1(3), pp. 253-268.

10. Kampmann, S., Bittus, B., Mattes, P., and Kirner, M., 1996, "The Influence of Hydro Grinding at VCO Nozzles on the Mixture Preparation in a DI Diesel Engine," SAE Paper, No. 960867.

11. Huh, K. Y., Lee, E. and Koo, J. Y., 1998, "Diesel Spray Atomization Model considering Nozzle Exit Turbulence Conditions," Atomization and Sprays, Vol. 8(4), pp. 453-469.

12. Wu, P. K., Miranda, R. F. and Faeth, G. M., 1995, "Effects of Initial Flow Conditions on Primary Breakup of Nonturbulent and Turbulent Round Liquid Jets," Atomization and Sprays, Vol. 5(2), pp. 175-196.

13. Tamaki, N., Shimizu, M., Nishida, K. and Hiroyasu, H., 1998, "Effects of Cavitation and Internal Flow on Atomization of a Liquid Jet," Atomization and Sprays, Vol. 8(2), pp. 179-197.

14. He, L. and Ruiz, F., 1995, "Effect of Cavitation on Flow and Turbulence in Plain Orifices for High-Speed Atomization," Atomization and Sprays, Vol. 5(6), pp. 569-584.

15. O'Rourke, P.J. and Amsden, A. A., 1987, "The TAB method for the Numerical Calculation of Spray Droplet Breakup," SAE Paper, No. 872089.

16. Lai, M. C., Zhao, F. Q., Amer, A. A. and Chue, T. H., 1994, "An Experimental and Analytical Investigation of the Spray Structure from Automotive Port Injectors," SAE Paper, No. 941873.

17. Xu, M. and Markle, L. E., 1998, "CFD-Aided Development of Spray for an Outwardly Opening Direct Injection Gasoline Injector," SAE Paper, No. 980493.

18. Schweitzer, P. H., 1937, "Mechanism of Disintegration of Liquid Jets," Journal of Applied Physics, Vol. 8, pp. 513-521.

19. Schmidt, D.P. and Corradini, M. L., 1997, "Analytical Prediction of the Exit Flow of Cavitating Orifices," Atomization and Sprays, Vol. 7, pp. 603-616.

20. Nurick, W. H., 1976, "Orifiice Cavitation and Its Effect on Spray Mixing," Journal of Fluids Engineering, Vol. 98, pp. 681-687.

216

Direct Visualization of High Pressure Diesel Spray and Engine Combustion

Tsung-Cheng Wang, Joong-Sub Han, Xingbin Xie, Ming-Chia Lai and Naeim A. Henein
Wayne State Univ.

Ernest Schwarz and Walter Bryzik
TARDEC

Direct Visualization of High Pressure Diesel Spray and Engine Combustion

Tsung-Cheng Wang, Joong-Sub Han, Xingbin Xie, Ming-Chia Lai and Naeim A. Henein
Wayne State Univ.

Ernest Schwarz and Walter Bryzik
TARDEC

ABSTRACT

An experimental study was carried out to visualize the spray and combustion inside an AVL single-cylinder research diesel engine converted for optical access. The injection system was a hydraulically-amplified electronically-controlled unit injector capable of high injection pressure up to 180 MPa and injection rate shaping. The injection characteristics were carefully characterized with injection rate meter and with spray visualization in high-pressure chamber. The intake air was supplied by a compressor and heated with a 40kW electrical heater to simulate turbocharged intake condition. In addition to injection and cylinder pressure measurements, the experiment used 16-mm high-speed movie photography to directly visualize the global structures of the sprays and ignition process.

The results showed that optically accessible engines provide very useful information for studying the diesel combustion conditions, which also provided a very critical test for diesel combustion models. The high IMEP conditions were successfully achieved in the optical engine experiments, which show sensitivity to injection pressure, charge condition, and combustion chamber geometry. Sprays and combustion visualization for both single and multi-stage injections was conducted in this study. Nozzle hole flow area, injection pressure, and length of rate-shaping pipe are the dominating parameters that control the injection rate , and the rate shape is affected mainly by common rail pressure, especially the pressure rising rate, and length of rate-shaping pipe.

INTRODUCTION

High-pressure electronic-controlled fuel injection systems, such as electronic unit injector (EUI), hydraulic EUI (HEUI), and common rail (CR), are the heart of advanced diesel engines. These systems could provide features required by an advanced engine such as more precise injection quantity, more flexible injection timing, and higher injection pressure comparing to the conventional mechanical injection systems. High injection pressure combined with small hole diameter nozzle can provide, 1) better spray formation which is due to finer initial drops exiting the nozzle with higher velocity, 2) better air entertainment and air-fuel mixing, and 3) more homogenous mixture with lower local equivalence ratio and fewer over-rich regions. These three factors have been reported as the keys to generate a low smoke combustion process [1]. [2] Also showed that at high load engine operating conditions raising the injection pressure effectively reduces particulate emissions. As to how to optimize combustion chamber to cope with high-pressure injection, in-depth understanding of the cross influence between the injection and the configuration of combustion chamber is inevitable. Since evaporative and non-evaporative diesel spray behave quite differently in terms of spray penetration and dispersion. [3] reported that vaporization reduces penetration and dispersion by as much as 20% relative to non-vaporizing spray. Therefore, visualization of the formation process of diesel spray and its combustion in the combustion chamber of diesel engine has been recognized as one of the best ways to understand in-cylinder injection performance, spray characteristics and combustion for controlling emissions [4,5,6,7].

The objective of this work is to visualize and analyze in-cylinder spray and combustion and evaluate the effects of fuel injection and engine operating conditions on spray and combustion process. In this study, an AVL single cylinder optically accessible engine is used to visualize spray and combustion process directly from the engine bottom through a quartz window inserted in the piston top. The in-cylinder spray characterization items included penetration, dispersion, and uniformity of liquid-phase fuel in the chamber under different engine operating conditions, such as different charge air temperatures and pressures. Based on visualization, the effects of change of engine and injection operating conditions on ignition delays, ignition locations, and combustion process were

addressed and analyzed. The high-pressure fuel injection system used in the study was a prototype system fabricated at Wayne State University for the purpose of advanced diesel engine combustion research. The system is capable of high injection pressure up to 180 MPa and injection rate shaping. This HEUI (Hydraulic Electronic Unit Injector) System consists of a low pressure fuel supply pump, a high pressure oil pump, a common rail equipped with PWM (Pulse Width Modulation) pressure regulator, and an electronic-controlled intensified injector. The high-pressure oil pump is the source of system working pressure. It pressurizes and delivers the oil, the working fluid of the system, to the common rail that serves as pressure accumulator. The pressure regulator then maintains the pressure of the accumulator at a setting point that can be in the range of 207 to 380 bar . The pressurized oil is fed to the inlet of injector via the common rail. Once the injector being energized, a spool valve in the injector is opened to allow the pressurized oil flow through it and act on an intensified plunger which subsequently pressurizes the fuel and make an injection through the injection nozzle. The low-pressure fuel supply pump continuously delivers fuel to the injector with fuel pressure maintained at around 7 bar.

Intensive injection characterization had been conducted prior to the in-cylinder spray and combustion visualization work to obtain the characteristics of the injector, nozzle tips, and the associated fuel system used in the study. Based on the information obtained a proper set of injection conditions were then identified to match with the intent engine test conditions. The injection characterization items included injector delay (time between command and injection issued), injection pressure, injection quantity, and injection rate. Non-evaporative spray visualization was also being conducted beforehand to gain knowledge about the spray issued by the injection system in terms of spray penetration, spray symmetry, and start and end of injection.

EXPERIMENTAL SETUP

The experimental setup of the fuel injection system for injection characterization was shown in Figure 1. The specification of the nozzle tips used in this study was summarized in Table (1). The flow number- for example, 610 of the VCO nozzle- represents steady state volume flow rate in cubic centimeter within 30 seconds test period with 100 bar injection pressure. The optically accessible engine modified from an AVL single cylinder engine was shown in Figure 2. with specification summarized in Table(2). [8] The experimental setup for in-cylinder spray and combustion visualization consisted of a bottom-viewed optically accessible engine, 16-mm high-speed movie camera, HEUI fuel injection system, copper-vapor laser system, and Labview data acquisition and control system. The engine was equipped with Kistler 6043A60 cylinder pressure transducer, 720 ticks per revolution shaft encoder, inlet air temperature and pres-

sure transducers, 40kW inlet air heater, and supercharged air inlet system. For the fuel injection system installed on the engine cylinder head, a Kislter 4067A2000 Piezo-resistive pressure transducer was mounted at about 6.5 cm upstream of the inlet of the injection nozzle holder. The measured injection pressure was upstream injection pressure. The Labview system was implemented to operate the HEUI system for the test requirements such as the controls of injection pressure, injection timing, injection duration, and number of injections, and the synchronization between injection and data acquisition. The copper-vapor laser was operated at 25,000 Hz pulsing frequency to illuminate the in-cylinder spray from bottom of the piston. The high-speed movie camera was operated at 5,000 Hz framing speed for about 2 second period after triggered by a synchronization signal. The synchronization logic among the engine, injection system, high-speed camera, and data acquisition was implemented by the Labview programming and the associated hardware consisting of a Pentium computer system and National Instrument's PC compatible I/O devices such as timer/counter and data acquisition boards.
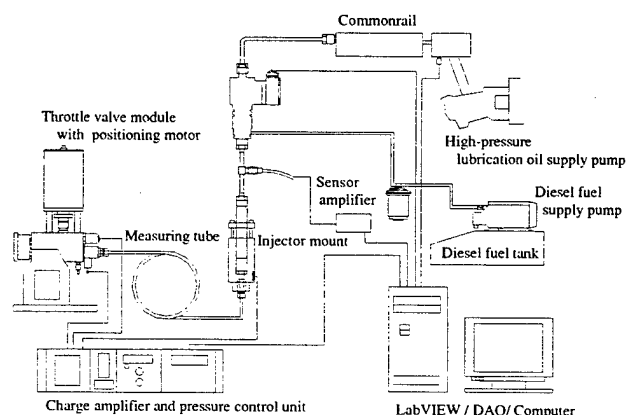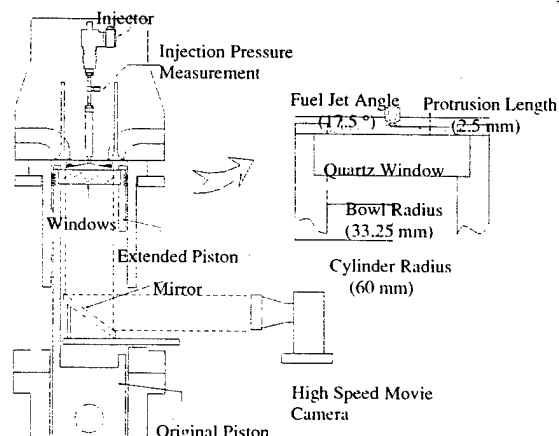

Figure 1. System for Injection Characterization

Figure 2. OAC Engine Experimental Setup

Table 1. Nozzle Tip Specification

Nozzle tip	No. of hole	Hole Diameter(mm)	Total hole flo area(m**2)	Cd (steady state flow)
610 VCO	6	0.218	2.24 E-7	0.58
620 Mini-sac	7	0.190	1.98 E-7	0.66
730 VCO	7	0.210	2.42 E-7	0.64

Table 2. OAC Engine Specification

Bore x Stroke (mm)	120 X 128	IVO (degree, BTDC)	13
Compression Ratio	16.7	IVC (degree, ABDC)	26
No. of valves	4	EVO(degree, BBDC)	48
Combustion chamber (mm)	66.5 (diameter)	EVC(degree, ATDC)	6
bowl-in-piston(mm)	16.5(deep)	Swirl Number	2.1

Cylinder pressure, injection pressure, and charge air pressure/temperature were acquired and recorded for each crankangle degree while the spray combustion pictures were being taken by the high-speed movie camera. The visualization films were then developed, digitized and processed for further analysis.

The test conditions were summarized in Table 3. For all of test cases the engine speed and injection timing were remained unchanged and set at 750 rpm and 10 degree BTDC respectively. However, other test variables, such as charge air conditions, Common Rail pressure, injection duration, length of rate shaping pipe, and type of nozzle tip were changed according to the test requirement. Table (4) detailed the conditions of each of the 7 test cases. Case A to E simulated full-load engine operating condition, while Case F and Case G simulated 65% load condition. In addition to the test conditions mentioned above, a test was specially arranged to study the spray and combustion process of a multi-stage fuel injection.
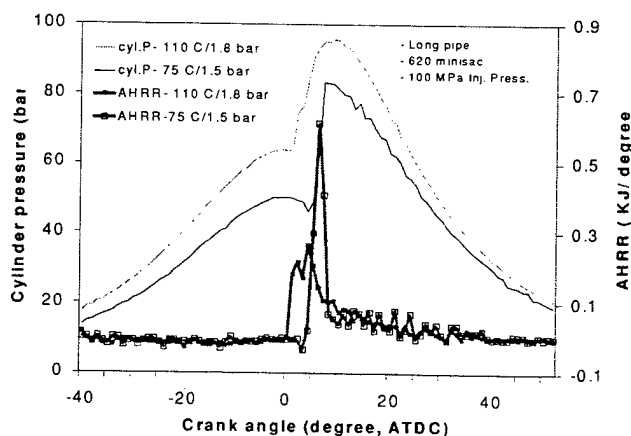
Figure 3. Case A vs. Case B

Table 3. Conditions of Case A to Case G

Engine speed	750 rpm
Injection timing	10 degree BTDC
Inlet Conditions(pressure/temperature)	1.5bar/75 C and 1.85 bar/110 C
Common Rail Pressure	27.6 MPa and 37.9 Mpa
Injection duration	1.70 ms and 2.25 ms
Length of rate shaping pipe	12 inches and 24 inches
Nozzle tip type	610vco,620mini-sac,and 730vco

Table 4. Comparison of Case A and Case B

Test case	Inj. Duration (ms)	Peak Inj. Pressure (MPa)	Inlet Temp. /Pressure (deg C/bar)	Type of Nozzle Tip	Length of Rate Shaping Pipe (inches)
A	2.25	101	110/1.85	620mini-sac	24
B	2.25	101	75/1.5	620mini-sac	24
C	2.25	106	75/1.5	610vco	24
D	2.25	134	75/1.5	610vco	12
E	2.25	84	75/1.5	730vco	12
F	1.7	75	75/1.5	730vco	12
G	1.7	109	75/1.5	610vco	12

RESULTS AND DISCUSSIONS

EFFECTS OF CHARGE AIR CONDITION – Case A and Case B were used as comparing cases to evaluate the effect of charge air condition on in-cylinder spray and combustion process. Figure 3 showed the traces of cylinder pressure and apparent heat release rates of both cases. The apparent heat release rate shown in the figure was calculated from the crank angle-based cylinder pressure data according to the first law of thermodynamics. Figure A-4 and Figure A-5 were the associated combustion images for Case A and Case B respectively. In Figure 3, the heat release of Case B showed that most of the energy was released by pre-mixed combustion and only small portion of the energy was released by diffusion-controlled combustion. As shown in Figure A-5, the images of Case B, the fuel delivery to the cylinder was started at about 2 degree BTDC and -based on the measured injection pressure data- the injection was ended at about 8 degree ATDC. First visible flame started at about 3.3 degree ATDC at the downwind edges of the 3 o'clock and 8 o'clock sprays near the wall of the combustion bowl. The in-cylinder air swirl was in the clockwise direction. The in-cylinder gas motion could be clearly observed in an animated movie. It is believed that at the downwind region of each spray the air and fuel mixing was enhanced by the swirl and, as shown in the picture of the 4.4 degree ATDC, those regions were the locations where the ignitions and initial stage of combustion

3

occurred. At 6 degree ATDC, the heat release reached its peak. At 7degree ATDC, the cylinder pressure reached its maximum pressure, 83.5 bar. Most soot formed in the spray overlapping regions. After 46 degree ATDC the flame became invisible.

As compared to Case B, Case A had much lower level of pre-mixed combustion heat release and most of the energy was released by diffusion-controlled combustion, which is a much more favorable combustion process in terms of reduction of NOx emissions and combustion noise. As shown in Figure A-4, the images of Case A, the fuel was introduced to the cylinder at about 2 degree BTDC and the fuel injection was ended at about 8 degree ATDC. The ignitions and flames started at the downwind regions of the fuel sprays, but as opposed to Case B they did not start at the near wall region. At 3.3 degree ATDC, Soot formed at the spray wall impingement regions. At 6.0 degree ATDC, soot formed in the spray overlapping regions. Most soot oxidized after 8.7 degree ATDC. After 30 degree ATDC, the flame became invisible. Apparently, the increase of temperature and pressure of the charge air of Case A had significant influence on the spray and combustion process. The higher temperature and pressure condition enhanced the liquid fuel droplet further break-up as the sprays proceeded outward and also accelerated the evaporation of the liquid fuel droplet as a result the atomization, fuel distribution and air-fuel mixing were improved. The combustion of Case A was more uniformly across the combustion chamber while the combustion of case B was more concentrated toward the near wall region forming a circular shape combustion flame. Based on the combustion images, both cases had portion of air at the center region near the nozzle exit was not being fully utilized.

Table 5. Comparison of Case A and Case B

Test Conditions an Results	High inlet temperatur and pressure	Low inlet temperature and pressure
Engine speed(rpm)	750	
Inlet conditions	110 deg C / 1.85 bar	75 deg C/ 1.5 bar
Peak motoring pressure(bar)	64	50
Injection timing (BTDC)	10	
Injection pressure(Mpa)	101	
Injection Quantity(mg)	94.8	99.2
Ignition delay(ms)	0.6	1.2
Total heat release(KJ)	2.28	2.20
Thermal efficiency	0.56	0.52
Peak heat release rate(KJ/ degree)	0.265	0.615
Maximum liqui penetration(mm)	21	27
Liquid phase penetration rate(m/sec)	26	26

Table (5) summarized the comparison between them. It showed the thermal efficiency of Case A is higher than that of Case B, which could be attributed to better fuel distribution, better air-fuel mixing, better air utilization and shorter ignition delay.

EFFECTS OF INJECTION PRESSURE – The Case D and E were used as the comparing cases to evaluate the effect of injection pressure on sprays and combustion process. For both cases, the injection pressures and nozzle specifications were carefully selected such that their injection quantity and injection rate were the same or closed enough to make a good base for case comparison. The average injection velocity of Case D was about 15% higher than that of Case E. Figure 4 showed the traces of cylinder pressure and apparent heat release rate. Both cases had similar heat release pattern. The combustion of Case E was about 5 crank-angle degree later than that of Case D. It was mainly due to longer injection delay caused by the lower injection pressure and partly due to that Case D with higher injection pressure had shorter ignition delay than that of Case E. Basically, sprays of higher injection pressure leave the nozzle holes with higher velocity and momentum. The higher velocity induced higher level of dispersion, and consequently better atomization and air/fuel mixing; more importantly when the higher momentum sprays collided with the wall of the combustion bowl higher level of spray rebound was generated, which enhances air entrainment rate. From the combustion observation pictures shown in Figure A-8, it was found that in Case E, the case of lower injection pressure, the air utilization at the center region of the combustion bowl was very poor. It was an evident that most of the vaporized fuel was distributed and stagnant around the near wall region. Table (6) summarized the comparison between Case D and Case E.
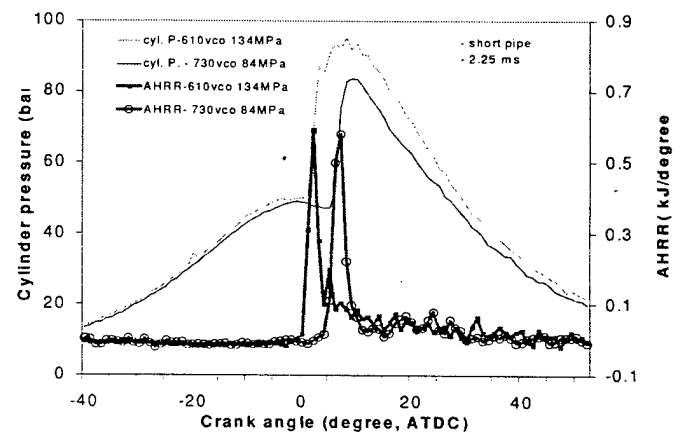

Figure 4. Case D vs. Case E

Table 6. Comparison of Case D and Case E

	High injection pressure	Low injection pressure
Engine speed(rpm)	750	
Inlet temperature and pressure	75 C / 1.5 bar	
Peak motoring pressure(bar)	57	
Injection timing (BTDC)	10	
Injection pressure(Mpa)	134	84
Injection Quantity(mg)	109	99.6
Ignition delay(ms)	1.2	1.4
Total heat release(KJ)	2.65	2.26
Thermal efficiency	0.57	0.53

EFFECT OF INJECTION DURATION – Figure 6 showed the comparison of Case E andF. Figure 7 showed the comparison of Case D and G. As shown in the combustion pictures of both Case F and G, the sprays and combustion of secondary injection was observed and most of the combustion occurred at the near wall region.
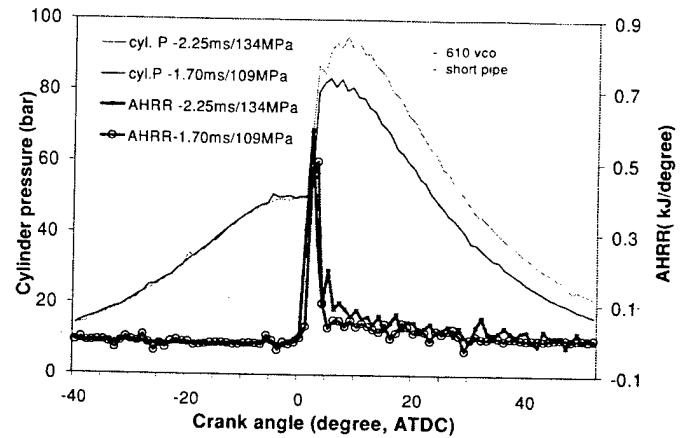
Figure 6.   Case E vs. Case F

Figure 5.   Case C vs. Case

EFFECTS OF NOZZLE CONFIGURATIONS – Two types of nozzle tip , 7-hole mini-sac(for Case B) and 6-hole VCO(for Case C), had been evaluated in the study. Non-uniform spray penetration of liquid phase fuel was found at the early stage of injection of the VCO nozzle. However, within short period of time, about 2 crankangle degree, the spray penetration became as uniform as that of the mini-sac nozzle. There is no difference found between these two types of nozzle in terms of the in-cylinder spray and combustion characteristics.

EFFECTS OF INJECTIONRATE SHAPE – The   rate shape of HEUI injection could be changed by changing the length of the rate shaping pipe which was a piece of high pressure steel tube connected the intensifier and the nozzle holder. The injection rate shape became smoother with length increase. In this study, 12" and 24" pipe were used. With increase of the length from 12" to 24", the rate of injection pressure decreased from 72 MPa/ms to 54 MPa/ms. The injection rate gradient of Case D was about 15% higher than that of Case C. As the cylinder pressure and heat release traces shown in Figure 5, the late combustion of Case C was mainly due to injection delay.

Figure 7.   Case D vs. Case G

PILOT INJECTION SPRAYAND COMBUSTION – Figure A-3 / A-11 showed the in-cylinder sprays and combustion process of a two-stage injection. The engine was running at 1000 rpm with 80 degree C and 1.48 bar charge air. The pilot with 0.8 ms duration was issued at 13 degree BTDC and ended at 9 degree BTDC. It was followed by a 2.25 ms duration main injection issued at 3 degree BTDC and ended at 10 degree ATDC. The time difference between the pilot and the main was 0.6 ms. The injection rate was shown as trace "a" in Figure 8. The peak injection pressures of the pilot and main were 65 MPa and 110 MPa respectively. At 8.2 degree BTDC, the ignition and start-of-combustion occurred simultaneously at several spots near the center of the combustion bowl. As the pilot flame proceeded its shape changed slightly by the clockwise swirl. At 3 degree BTDC the main injection was issued into the pilot flame and the main combustion started. After 5 degree ATDC, several heavy sooted

combustion zones were found at the spray wall impingement regions. The cylinder pressure and heat release curves of the pilot injection combustion along with needle lift signal were shown as Figure 9. It demonstrated that a mild pre-mixed combustion followed by a strong and smooth diffusion-control combustion was achieved by the two-stage injection. However to optimize the combustion process, the timing, quantity, and dwell time of the pilot injection need to be further refined.
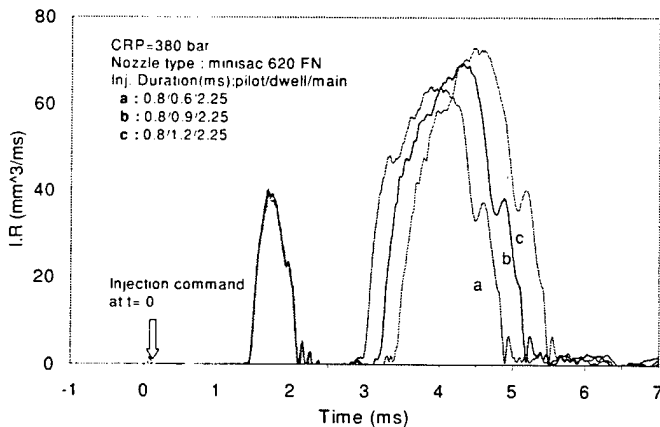
Figure 8. Injection Rate of Injection with pilot and main
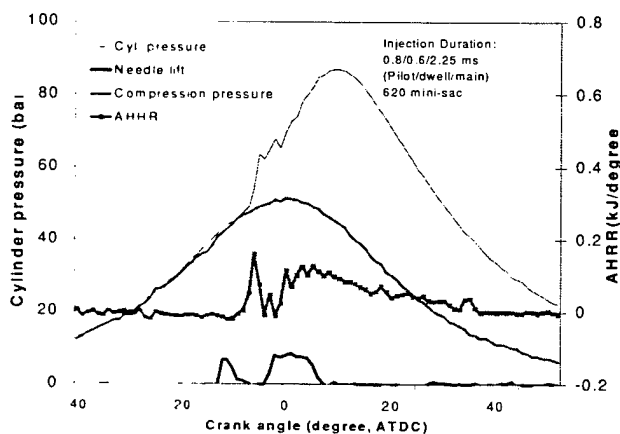
Figure 9. Combustion with Pilot and Main Injections

NON-EVAPORATIVE SPRAY CHARACTERISTICS – Non-evaporative spray visualization and characterization had been conducted for two nozzle tip used in the in-cylinder combustion visualization work, which were the 610vco and the 620 mini-sac. In the non-evaporative spray visualization test the injection was issued into a non-heated Nitrogen-filled pressurized chamber. Figure 10 showed the pictures of sprays development in time sequence. The spray pattern of the 610VCO nozzle was highly asymmetry as compared to that of the 620 mini-sac nozzle. Similar asymmetry behavior of the 610 VCO nozzle was also found in the pictures of in-cylinder sprays and combustion visualization, as shown in Figure A-6. Figure 11 showed the comparison of the penetration of non-evaporative and evaporative sprays of the 620mini-sac nozzle. For the non-evaporative spray visualization, the injection was issued into a pressurized chamber with

its density similar to that of the compressed air at TDC. The 17 bar and 25 degree C condition of the pressurized chamber was used to simulate the TDC air density of Case B.
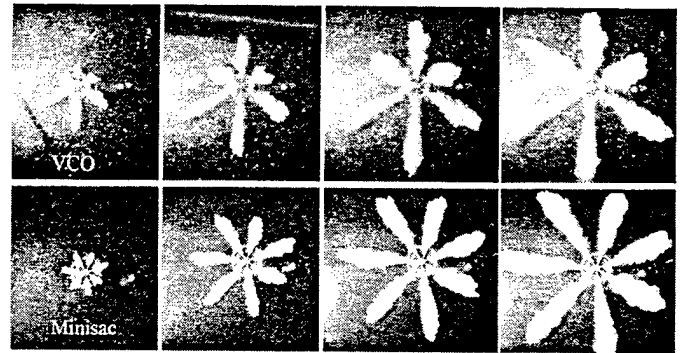
Figure 10. Non-evaporative spray tip development (Time between each frame is approximately 0.08 ms)
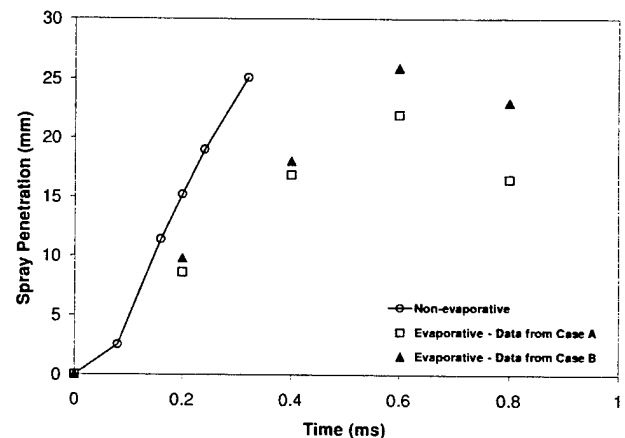
Figure 11. Comparison of a liquid spray penetration
Evaporative–Case A
(OAE Engine ran with 1.8 bar / 110 C Charge Air)
Evaporative–Case B
(OAE Engine ran with 1.5 bar / 75 C Charge Air)
Non-evaporative–
(17 bar / 25 C Nitrogen-filled Pressurized Chamber)

CONCLUSIONS

1. Direct in-cylinder visualization of global sprays and combustion process of single and multi-stage high-pressure direction injection were conducted in this study. The visualization results associated with measured cylinder pressure and calculated apparent heat release rate provided useful information for studying of Diesel combustion. Especially, this method could be applied to optimizing the application of pilot injection in terms of injection rate, quantity, and timing to best match it with the main injection under a variety of engines operating conditions.

2. At high load condition the pilot injection significantly reduced the peak heat release rate of the pre-mixed combustion, which is favorable to the reduction of NOx emissions and combustion noise. With pilot injection, the pre-mixed combustion of the main injec-

tion was not observable. It seemed that the diffusion-controlled combustion of the main injection got started right after the main injection was issued. How would the sprays of main injection interact with pilot flame would be an interesting subject for future study.

3. By increase of pressure and temperature, up to 1.85 bar and 110 degree C, of the charge air, the maximum liquid fuel penetration was reduced by about 20% for the case of injection with 100 MPa peak pressure, and the air utilization of the combustion was also improved. Therefore, it could be an effective approach to avoid liquid fuel impingement on the wall of combustion bowl and to improve fuel distribution, atomization, and air-fuel mixing, especially for high load and high-pressure injection engine operating condition.

4. At 65% load condition, with 1.5 bar and 75 degree C charge air the high pressure injection tended to distribute the fuel to the near wall region, which could cause rich combustion around the wall and lean combustion at the center region. The situation was getting worse by adopting nozzle with larger hole flow area.

5. With high-pressure injection the ignition and start of combustion most likely occurred at the sprays' downwind where the air-fuel mixing was enhanced by swirl.

ACKNOWLEDGEMENT

REFERENCE

1. T.Kato, T. Tsujimura, M.Shintani, T.Minami and I. Yamaguchi, "Spray Characteristics and Combustion Improvement of D.I. Diesel Engine with High Pressure Fuel Injection", SAE Paper 890265,1989

2. D. A. Pierpont and R. D. Reitz, "Effects of Injection Pressure and Nozzle Geometry on D.I. Diesel Emissions and Performance", SAE Paper 950604,1995

3. J. D. Nabers and D. L. Siebers, "Effects of Gas Density and Vaporization on Penetration And Dispersion of Diesel Sprays", SAE Paper 960034, 1996

4. K. K. Rao, D. E. Winterbone, and E. Clough, "Influence of Swirl on High Pressure Injection in Hydra Diesel Engine", SAE Paper 930978,1993

5. L. Zhang, T. Tsurushima, T. Ueda, Y. Ishii, T. Itou, T. Minami, and K. Yokota, "Measurement of Liquid Phase Penetration of Evaporating Spray in a DI Diesel Engine", SAE Paper 971645, 1997

6. C. Espey and J. E. Dec, "The Effect of TDC Temperature and Density on the Liquid-Phase Fuel Penetration in a D.I. Diesel Engine", SAE Paper 952456, 1995

7. T. Shiozaki, H. Nakajima, H. Yokota, A. Miyashita, "The Visualization and its Analysis of Combustion Flame in a DI Diesel Engine", SAE Paper 980141, 1998

8. M.-C. Lai, N. A. Henien, X. Xie, T.-H. Chue, Y. Itoh and W. Bryzik, "Diesel Cold-Starting Study using Optically Accessible Engines," SAE paper 952366
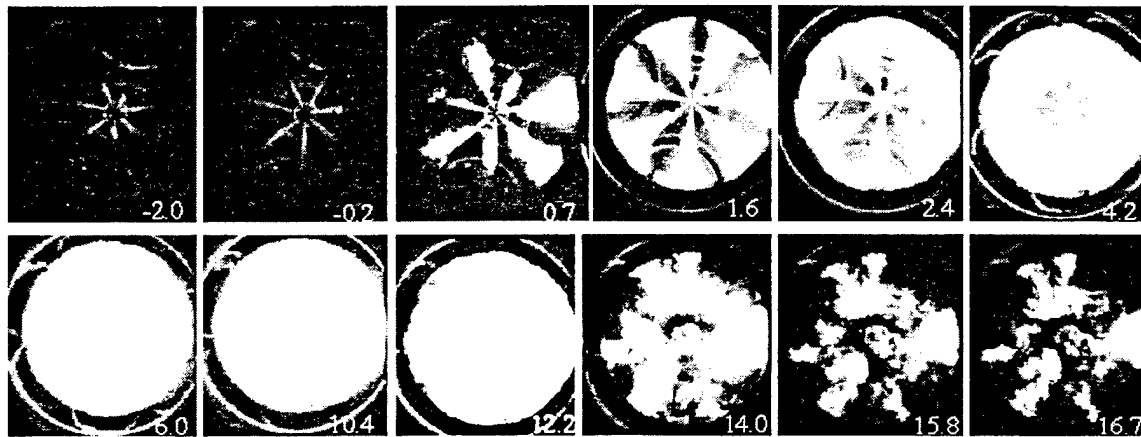
Figure A1.   High-speed movies of spray and combustion (time sequence is not constant)
Test condition: 750 rpm, 10 degree BTDC injection timing, 2.25 ms injection duration, 110 C/ 1.85 bar inlet air, 101 MPa peak injection pressure, 620 mini-sac nozzle tip, 24" rate shaping pipe
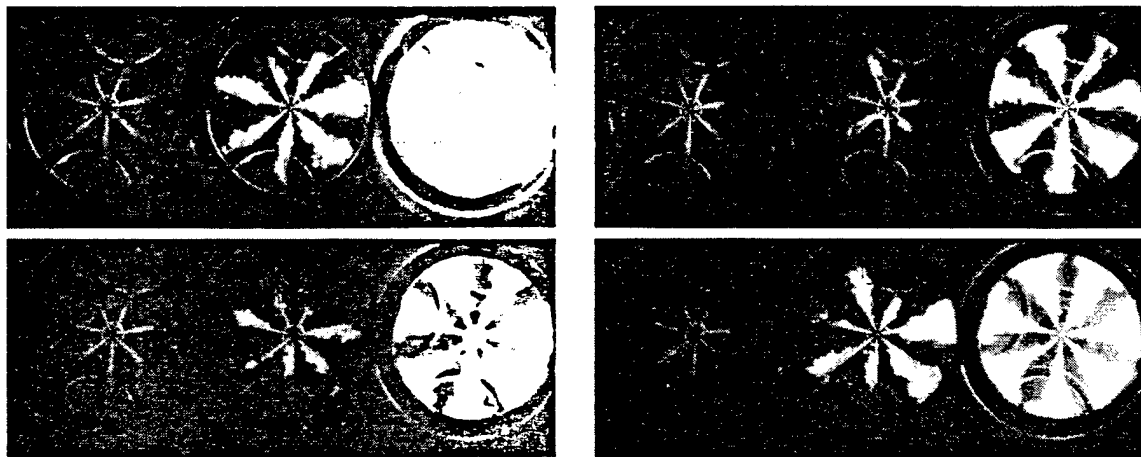
Figure A2.   High-speed movies of start of combustion for four consecutive combustion cycles. (Time between each frame is approximately 0.2 ms) Test condition is same with Figure A-1.
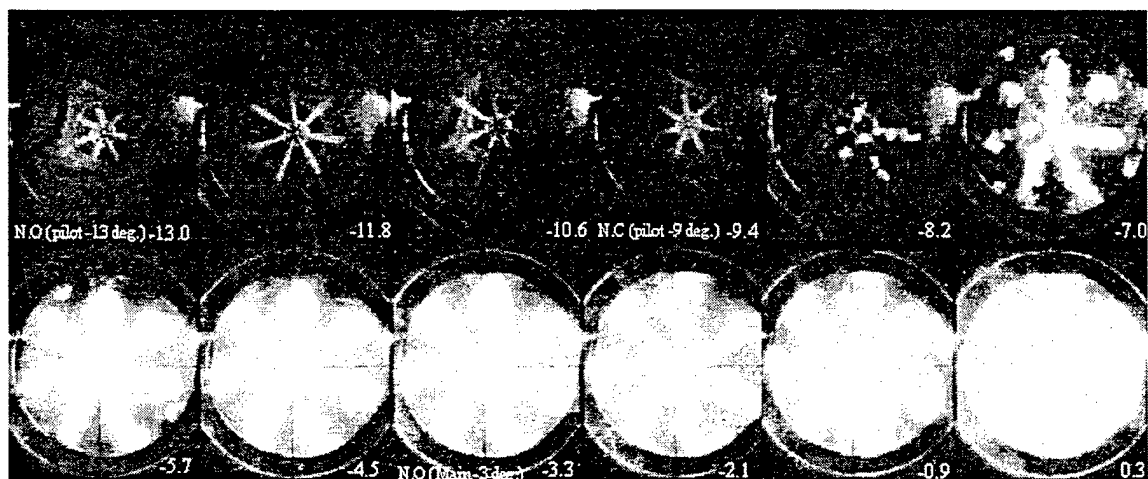
Figure A3.   High-speed movies of spray and combustion with a pilot injection (Time between each frame is approximately 0.2 ms)
Test condition: 1000 rpm, 20 degree BTDC injection timing, 0.8 / 0.6 / 2.25 ms injection duration, 80 C/ 1.6 bar inlet air, 620 mini-sac nozzle tip, 12" rate shaping pipe

Figure A4.   Combustion images (CASE A)
Test condition: 750 rpm, 10 degree BTDC injection timing, 2.25 ms injection duration, 110 C/ 1.85 bar inlet air, 101 MPa peak injection pressure, 620 mini-sac nozzle tip, 24" rate shaping pipe
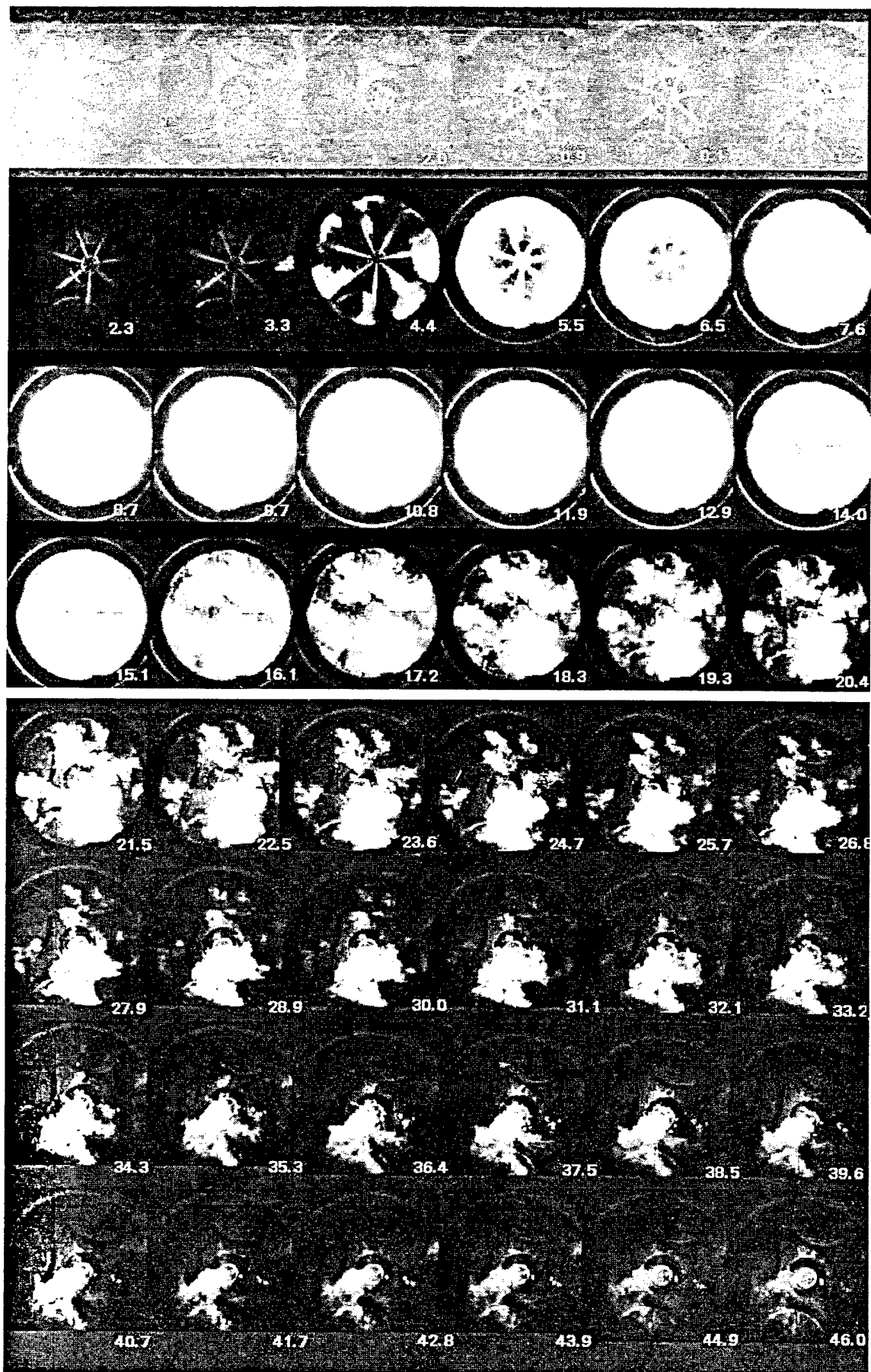
Figure A5.   Combustion images (CASE B)
Test condition: 750 rpm, 10 degree BTDC injection timing, 2.25 ms injection duration, 75 C/ 1.50 bar inlet air, 101 MPa peak injection pressure, 620 mini-sac nozzle tip, 24" rate shaping pipe
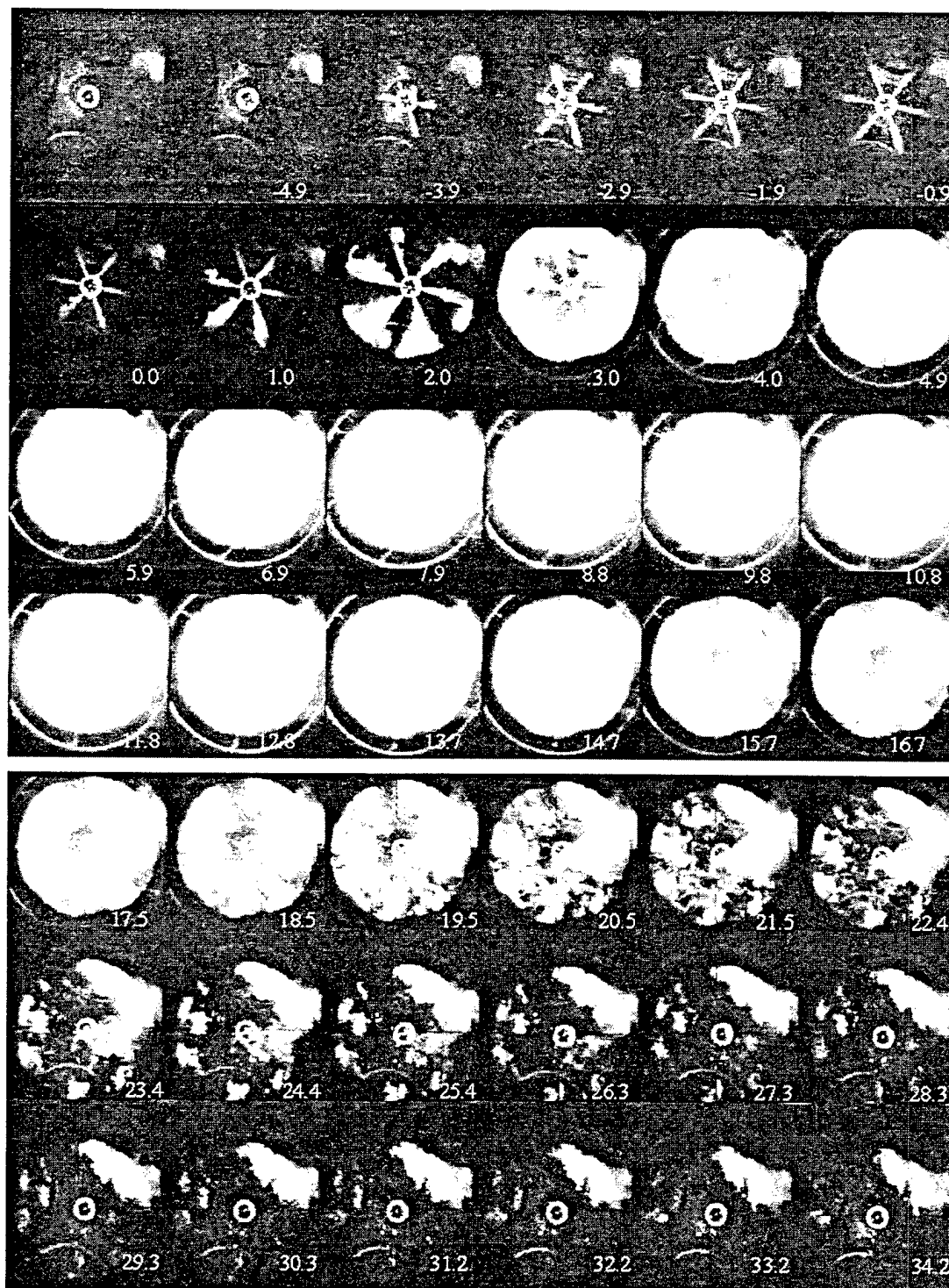
Figure A6.   Combustion images (CASE C)
Test condition: 750 rpm, 10 degree BTDC injection timing, 2.25 ms injection duration, 75 C/ 1.50 bar inlet air, 134 MPa peak injection pressure, 610VCO nozzle tip, 24" rate shaping pipe
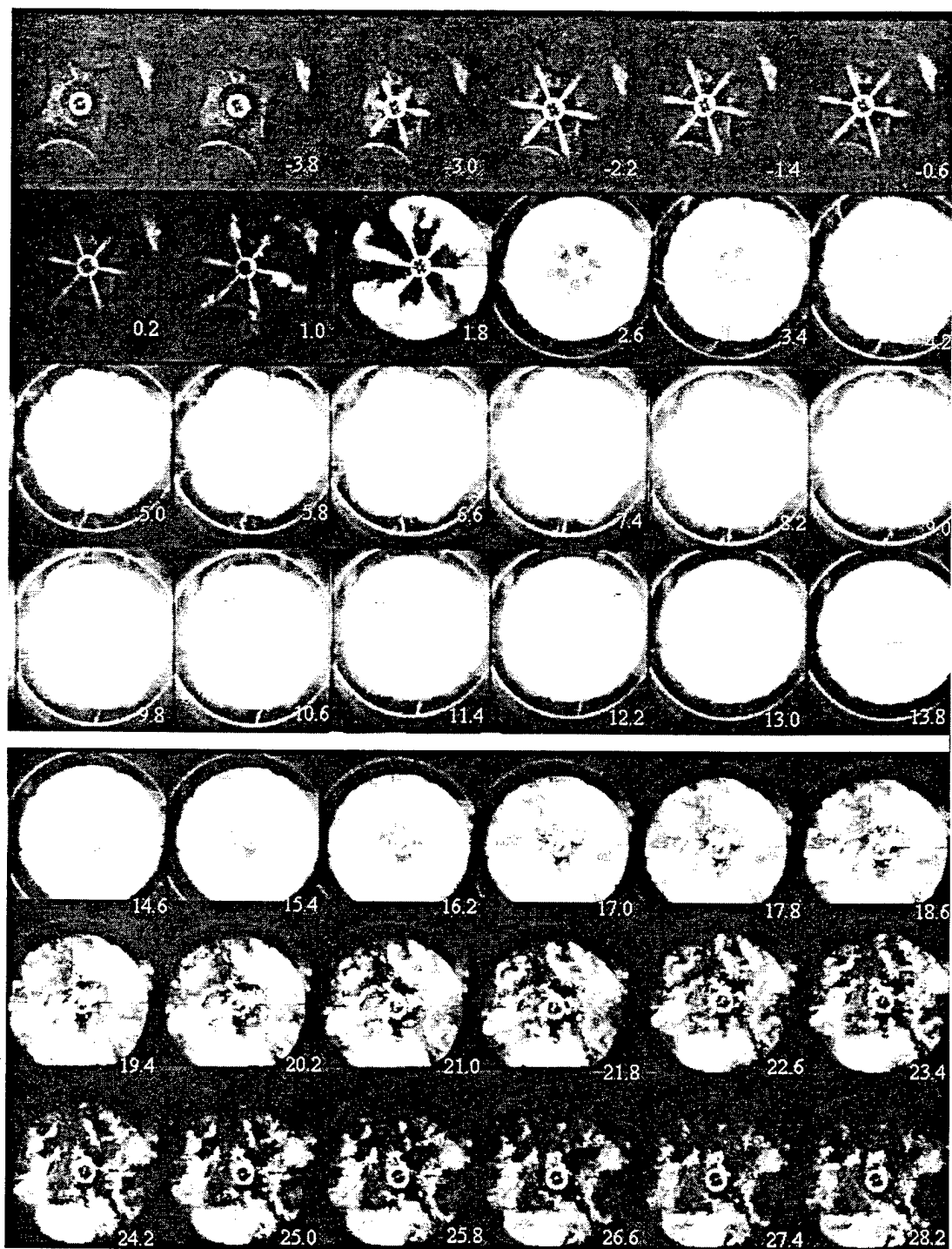
Figure A7.   Combustion images (CASE D)
Test condition: 750 rpm, 10 degree BTDC injection timing, 2.25 ms injection duration, 75 C/ 1.50 bar inlet air, 134 MPa peak injection pressure, 610VCO nozzle tip, 12" rate shaping pipe

12
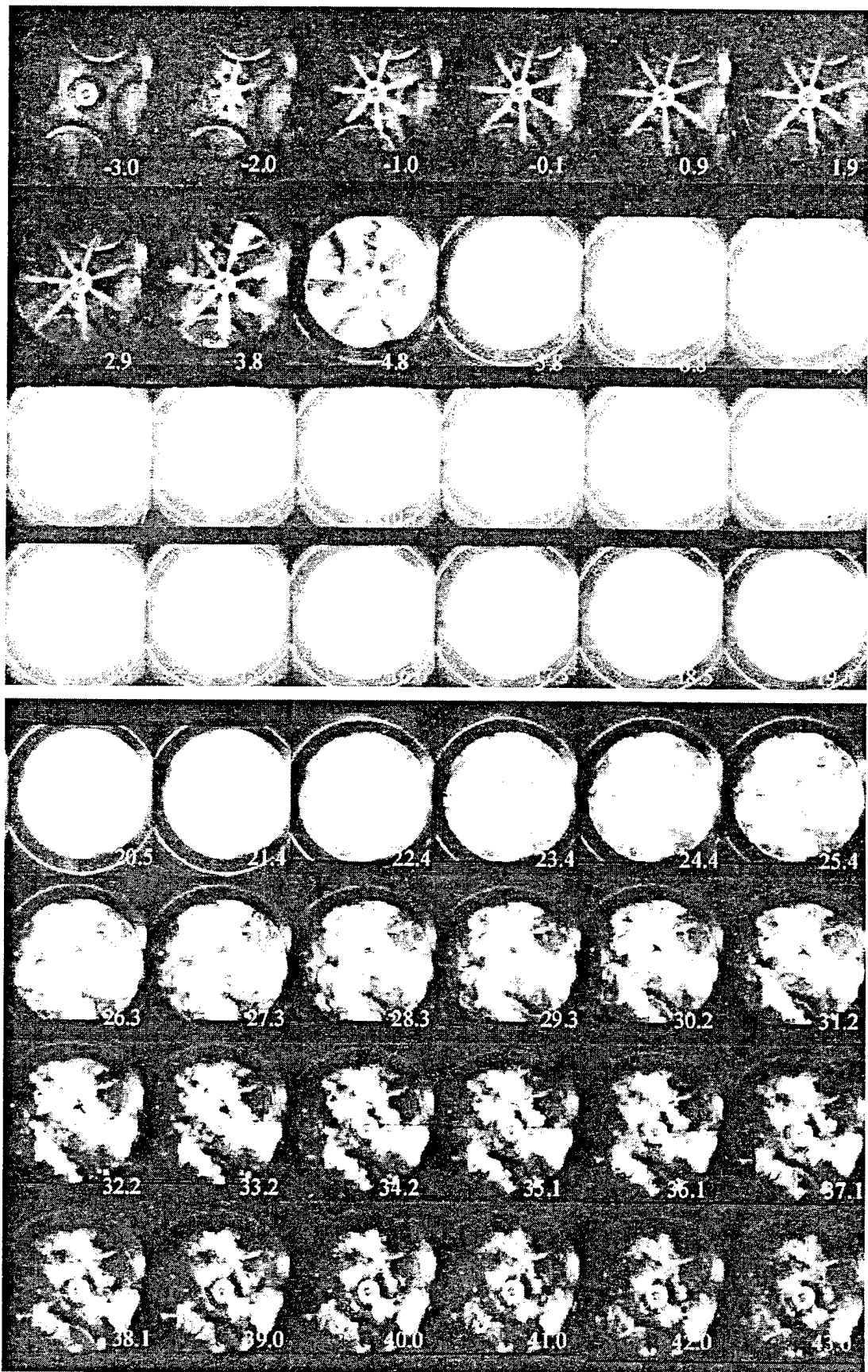
Figure A8. Combustion images (CASE E)
Test condition: 750 rpm, 10 degree BTDC injection timing, 2.25 ms injection duration, 75 C/ 1.50 bar inlet air, 84 MPa peak injection pressure, 730VCO nozzle tip, 12" rate shaping pipe
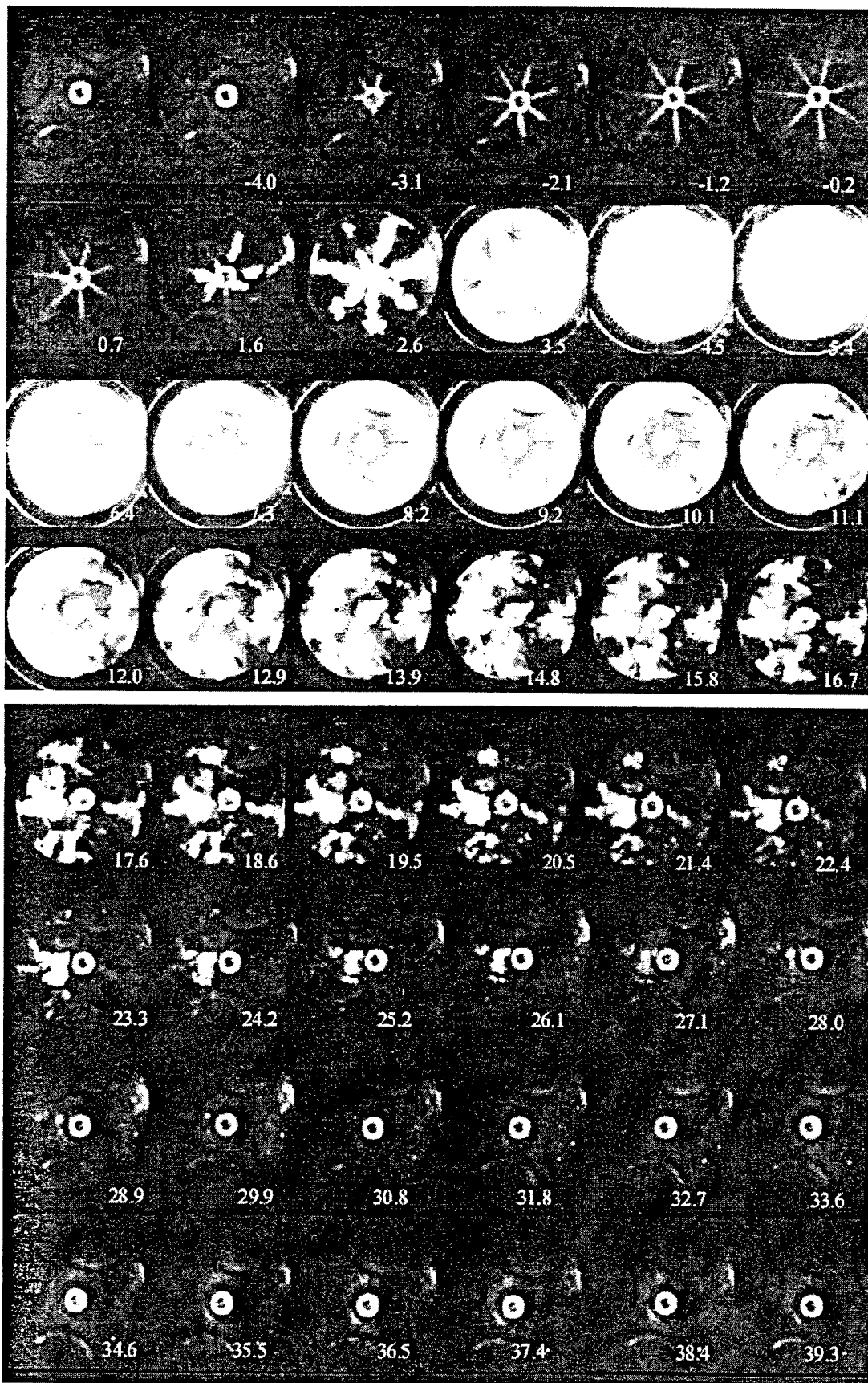
Figure A9. Combustion images (CASE F)
   Test condition: 750 rpm, 10 degree BTDC injection timing, 1.70 ms injection duration, 75 C/ 1.50 bar inlet air, 75 MPa peak injection pressure, 730VCO nozzle tip, 12" rate shaping pipe

14
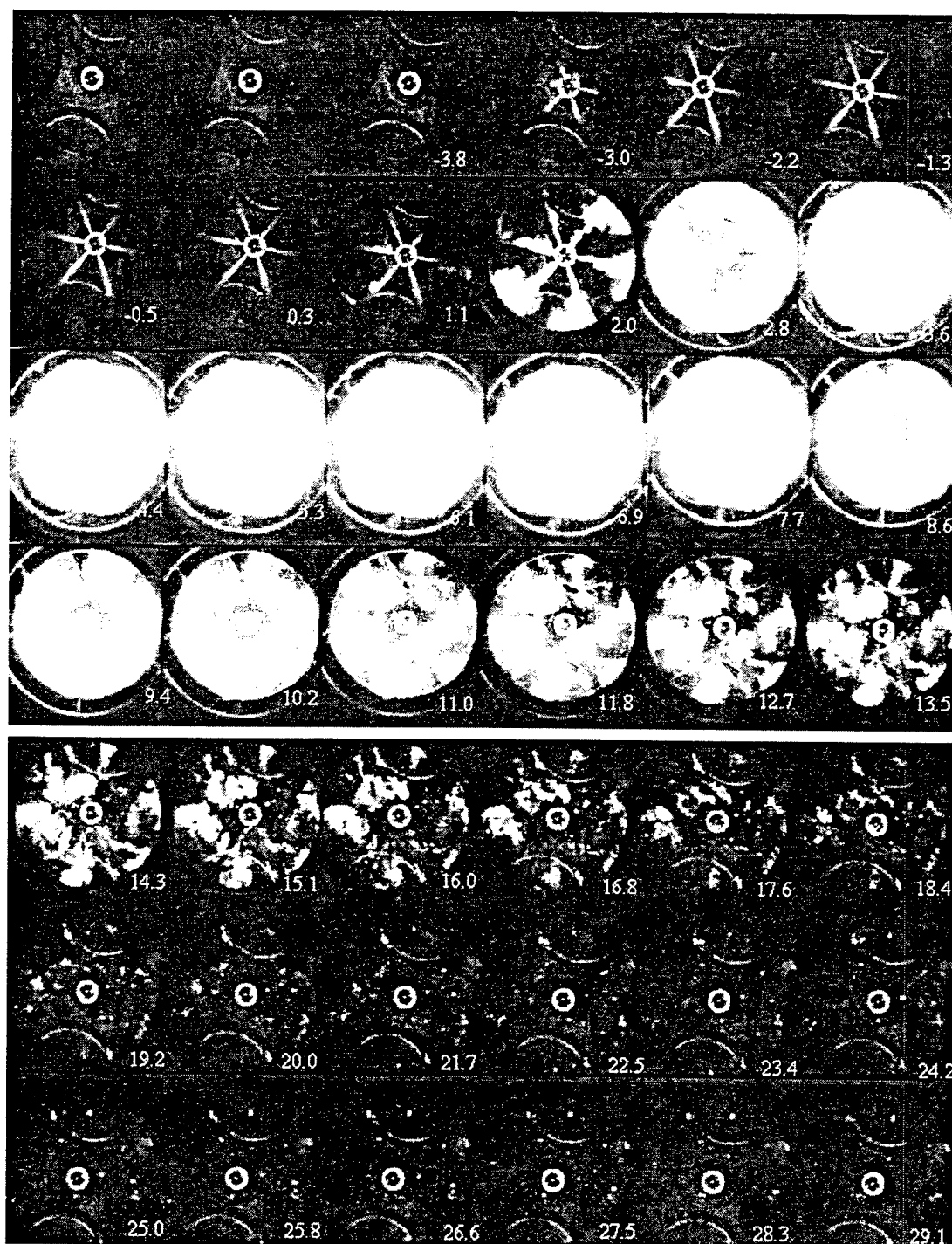
Figure A10.   Combustion images (CASE G)
Test condition: 750 rpm, 10 degree BTDC injection timing, 1.70 ms injection duration, 75 C/ 1.50 bar inlet air, 109 MPa peak injection pressure, 610VCO nozzle tip, 12" rate shaping pipe
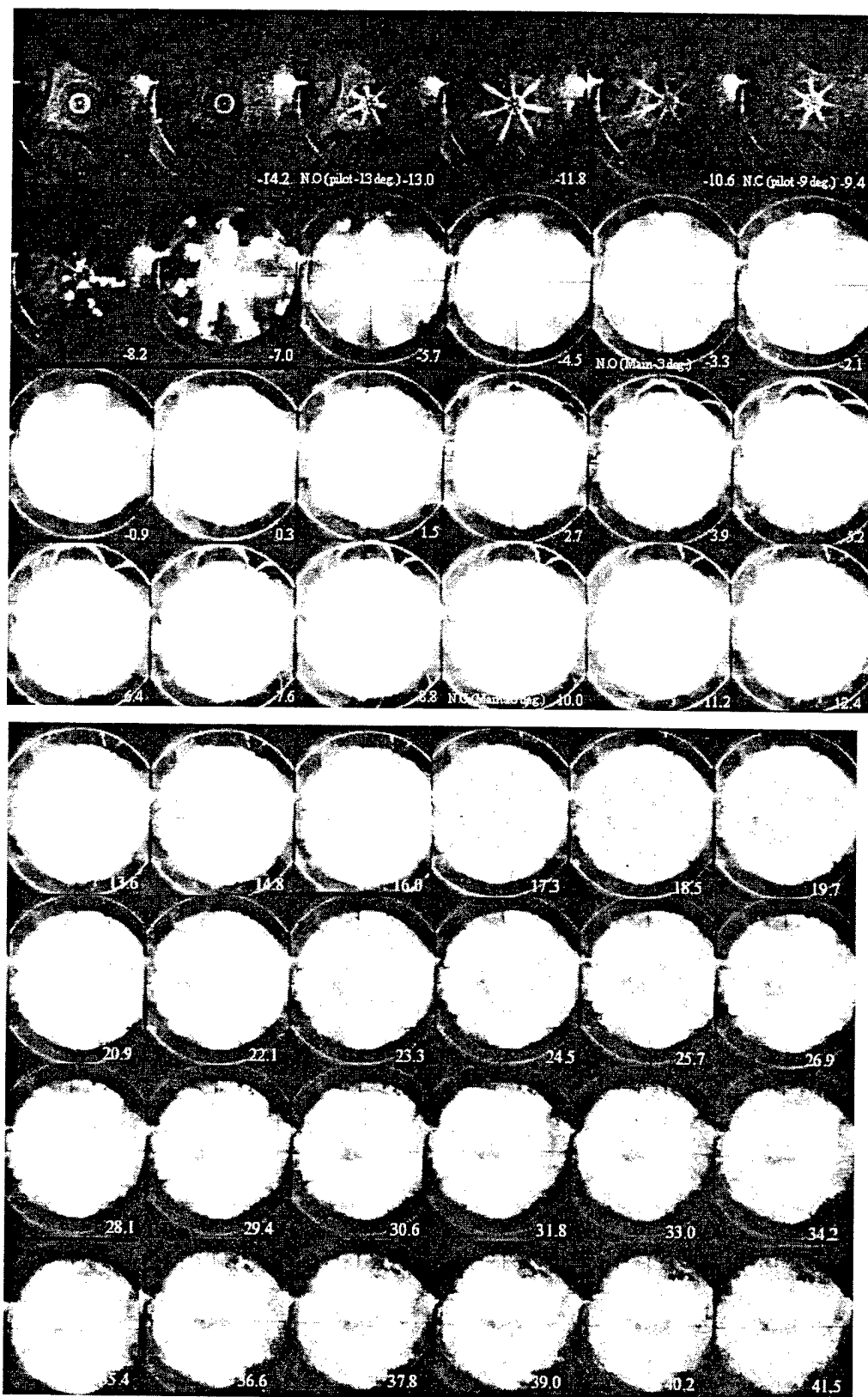
Figure A11. Combustion images (CASE with Multiple Stage Injection)
Test condition: 1000 rpm, 20 degree BTDC injection timing, 0.8 / 0.6 / 2.25 ms injection duration,
80 C/ 1.6 bar inlet air, 620 mini-sac nozzle tip, 12" rate shaping pipe

2 33

1999-01-3554

Direct Calculations of Cavitating Flows in Fuel Delivery Pipe by the Space-Time CE/SE Method

Jian Rong Qin, S. T. John Yu and Ming Chia Lai
Wayne State University

Direct Calculations of Cavitating Flows in Fuel Delivery Pipe by the Space-Time CE/SE Method

Jian Rong Qin, S. T. John Yu and Ming Chia Lai
Wayne State University

ABSTRACT

In this paper, we report direct calculations of cavitating pipe flows by the method of Space-Time Conservation Element and Solution Element, or the CE/SE method for short. The tenet of the CE/SE method is treating space and time as one entity, and the calculation of flow properties is based on the local and global space-time flux conservation. As a contrast to the modern upwind schemes, no Riemann solver is used, thus the logic of the present scheme for cavitating flows is much simpler. Two numerical examples are reported in this paper: (1) a hydraulic shock problem, and (2) a cavitating pipe flow. For the hydraulic shock problem, we demonstrate the capability of the CE/SE method for capturing contact discontinuities in cavitating fluids. For the pipe flows, a two-phase homogeneous equilibrium cavitation model is employed. In both cases, numerical results compared favorably with the experimental data and analytical solution.

INTRODUCTION

Transient hydraulic pressure wave propagation in a pipe is of practical importance in automotive systems, including fuel delivery, power steering, anti-lock brake, engine cooling, and automatic transmission. Under certain conditions, such as a sudden open or closure of a valve, vapor bubbles may form when the static pressure in the liquid drops to its vapor pressure. The collapse of these bubbles will generate high pressure waves propagating through the pipe, which will lower the performance of the system, produce vibration and noise, and even cause damage to the pipe and valve surfaces [6]. Many researchers [4, 9, 10] have attempted to simulate the transient wave propagation in the pump-line-nozzle system, which is widely used in diesel engine. But they didn't consider the possible formation of cavitation and its effect on the transient flows. While the maximum pressure generated at the valve can be analytically predicted by neglecting the fluid resistance [3], detailed hydrodynamic simulation can only be achieved by numerical methods. However, numerical simulation of cavitating flows poses unique challenges both in modeling the physics and in developing a robust numerical methodology. Because of the tremendous density difference between the vapor and liquid, it is necessary to construct a numerical scheme with high resolution for the region of cavitation. The numerical scheme should also be robust enough to deal with the enormous instability problems caused by the cavitating flows. Various numerical methods, such as the method of characteristics [8] and high resolution upwind schemes for capturing the interface of two phase flows [11], have been developed to study cavitating flows.

In this paper, we employed the CE/SE method originally developed by Chang [1]. The method is substantially different in both concept and methodology from the traditional methods. It enforces both local and global flux conservation in space-time domain and has remarkable ability to resolve discontinuity interfaces. In automotive industry, the CE/SE method has been successfully used by Onorati and Ferrari [5] to simulate one-dimensional flows in internal combustion engines.

The rest of this paper is organized as follows. In Section 2, we discuss the theoretical model of the flow equations to be solved. In Section 3, the essence of the CE/SE method will be illustrated. In Section 4, we present numerical results of two examples. We then give the concluding remarks.

2. THEORETICAL MODEL

2.1 FLOW EQUATIONS – For the compressible liquid flow in a pipe, the governing equations are

$$\frac{\partial \mathbf{Q}}{\partial t} + \frac{\partial \mathbf{E}}{\partial x} = \mathbf{S} . \qquad (2.1)$$

The flow variable vector, flux vector, and the source vector are

$$\mathbf{Q} = \begin{pmatrix} \rho \\ \rho u \end{pmatrix} \quad \mathbf{E} = \begin{pmatrix} \rho u \\ \rho u^2 + p \end{pmatrix} \quad \mathbf{S} = \begin{pmatrix} 0 \\ -\dfrac{fu|u|\rho}{2D} \end{pmatrix} \qquad (2.2)$$

in which ρ is density, u is velocity, p is pressure, D is the diameter of the pipe, and f is the Darcy friction factor. In Eq. (2.1), the first equation is the continuity equation and the second one is the mementum equation. The density

and pressure are related by the acoustic velocity a of the liquid, such as

$$\frac{dp}{d\rho} = a^2.$$ (2.3)

The source term in the momentum equation models the viscous friction of fluid flow.

2.2 CAVITATION MODEL – When cavitation occurs, the density in the flow equations is treated as a "psuedo density", which is related to the gas and liquid density by

$$\rho = \alpha \rho_g + (1-\alpha)\rho_l ,$$ (2.4)

where α is the void fraction. The relation between density, pressure and the speed of sound, Eq. (2.3), needs to be modeled. In this paper a two-phase homogenous equilibrium cavitation model [7] was adopted. The acoustic velocity of the two-phase homogeneous fluid is given by Wallis [12] as

$$a = \left\{ \left[\alpha \rho_g + (1-\alpha)\rho_l \right] \cdot \left[\frac{\alpha}{\rho_g \cdot a_g^2} + \frac{(1-\alpha)}{\rho_l \cdot a_l^2} \right] \right\}^{-1/2}.$$ (2.5)

Substituding Eq. (2.5) into Eq. (2.3) and integrating pressure as a function of void fraction from the saturated liquid state, we have

$$p = p_l^{sat} + \beta \cdot p_{gl} \cdot$$

$$\log \left[\frac{\rho_g \cdot a_g^2 \cdot (\rho_l + \alpha \cdot (\rho_g - \rho_l))}{\rho_l (\rho_g \cdot a_g^2 - \alpha \cdot (\rho_g \cdot a_g^2 - \rho_l \cdot a_l^2))} \right]$$ (2.6)

where p_{gl} a constant given by

$$p_{gl} = \frac{\rho_g \cdot a_g^2 \cdot \rho_l \cdot a_l^2 \cdot (\rho_g - \rho_l)}{\rho_g^2 \cdot a_g^2 - \rho_l^2 \cdot a_l^2}.$$ (2.7)

The parameter β ($10^{-3} > \beta > 10^{-5}$) is a model constant. The simulation results are independent of the values of β as long as it is in the range.

3. THE CE/SE METHOD

In this section, we give a brief description of the CE/SE method. Equation (2.1) can be written in the form of

$$\frac{\partial q_m}{\partial t} + \frac{\partial f_m}{\partial x} = s_m(q_1, q_2) ,$$ (3.1)

where m equals 1 and 2, representing the continuity equation and momentum equation, respectively. The source term $s_m(q_1, q_2)$ ion of q $_1$ and q_2. Let x_1 (= x) and x_2 (= t) be the coordinates of a two-dimensional Euclidean space E_2. Thus Eq. (3.1) becomes

$$\nabla \cdot \mathbf{h}_m = s_m(q_1, q_2)$$ (3.2)

in which the current density vector is $\mathbf{h}_m = (f_m, \ q_m)$. By using Gauss' divergence theorem in the space-time domain E_2, it can be shown that Eq. (3.1) is the differential form of the integral conservation law:

$$\oint_{S(R)} \mathbf{h}_m \bullet d\vec{s} = \int_R s_m(q_1, q_2)dR$$ (3.3)

Figure 1 shows a schematic of Eq. (3.3).
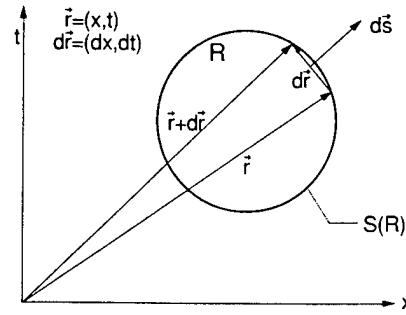
Figure 1.   A schematic of the space-time integral

Here S(R) is the boundary of an arbitrary space-time region R in E_2, $d\vec{s} = d\sigma\vec{n}$ with $d\sigma$ d   , $\vec{n}$ spectively, being the area and the outward unit normal of a surface element on S(R), and dR is the volume of a space-time region inside S(R). Note that $\mathbf{h}_m \bullet d\vec{s}$ is the space-time flux of hm leaving the region R through the surface element $d\vec{s}$ nd all mathematical operations can be carried out since E_2 is an ordinary two-dimensional Euclidean space. We remark that space and time are treated on an equal footing manner. Therefore, there is no restriction on the space-time geometry of the conservation elements over which the space-time flux is imposed.

In the light of the method of treating stiff source terms proposed by Yu and Chang [13], we discretized the space-time domain into rectangular elements in stead of rhombic ones, and associated the source term with the old time step variables. These treatments enable explicit time marching of this scheme. This is a good approximation, since the source term in Eq. (2.1) is not stiff.

4. NUMERICAL EXAMPLES

In this section, two numerical examples are reported. The first problem is a hydraulic shock problem, which demonstrates the capability of the CE/SE method for capturing contact discontinuities. The second problem is the transient waves in a cavitating pipe flow.

4.1 HYDRAULIC SHOCK PROBLEM

4.11 Analytical Solution – Consider an infinitely long tube with a diaphragm located at a certain place. The diaphragm separates two initially quiescent liquid states at different pressures and densities. When the diaphragm is suddenly broken at time t = 0, an expansion fan will be formed and propagate to the high-pressure liquid, simultaneously a shock will be formed and propagate to the low-pressure region, as shown in Fig. 2. In this figure, the diaphragm is placed at the lower center and the pressure of the liquid to the left of this diaphragm is higher than that to the right.
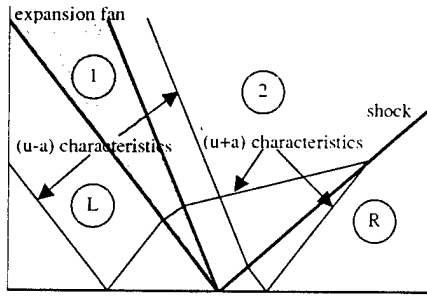
Figure 2.   A description of hydraulic shock problem

In our analysis, we didn't take the source term in Eq. (2.1) into consideration. The initial conditions were set such that no bubble will form during the transient process. With this simplification, Eq. (2.1) can be written as

$$\frac{\partial \mathbf{Q}}{\partial t} + \mathbf{A}\frac{\partial \mathbf{Q}}{\partial x} = 0 , \tag{4.1}$$

where $\mathbf{A}$ is the jacobin matrix given by

$$\mathbf{A} = \begin{bmatrix} 0 & 1 \\ a^2 - u^2 & 2u \end{bmatrix} . \tag{4.2}$$

This jacobin matrix $\mathbf{A}$ can be diagonized by a matrix, say, $\mathbf{M}$. Multiplying the inverse $\mathbf{M}^{-1}$ to both sides of equation (4.1), we can get the characteristic form

$$\frac{\partial \hat{\mathbf{Q}}}{\partial t} + \Lambda\frac{\partial \hat{\mathbf{Q}}}{\partial x} = 0 . \tag{4.3}$$

Where Λ a diagonal matrix given in Eq. (4.4), and $\hat{\mathbf{Q}}$ is related to $\mathbf{Q}$ by Eq. (4.5).

$$\Lambda = \mathbf{M}^{-1}\mathbf{A}\mathbf{M} = \begin{bmatrix} u+a & 0 \\ 0 & u-a \end{bmatrix} \tag{4.4}$$

$$\frac{\partial \hat{\mathbf{Q}}}{\partial \mathbf{Q}} = \mathbf{M}^{-1} \tag{4.5}$$

By selecting appropriate matrix $\mathbf{M}$ and integrating Eq. (4.5), we have

$$\begin{cases} \hat{q}_1 = u + a\ln\rho + C_1 \\ \hat{q}_2 = u - a\ln\rho + C_2 \end{cases}, \tag{4.6}$$

where C1 and C2 are two integration constants. Eqs. (4.3) and (4.6) indicate that $u \pm a\ln\rho$ are two constants along the two characteristics $\frac{dx}{dt} = u \pm a$, respectively. In the expansion fan area, area $\mathbf{1}$ in Fig. 2, we have

$$\begin{cases} u_1 + a\ln\rho_1 = u_L + a\ln\rho_L \\ u_1 - a\ln\rho_1 = const. \quad along \quad \frac{dx}{dt} = u_1 - a \end{cases} \tag{4.7}$$

From equation (4.12), we know u_1 is a constant along $\frac{dx}{dt} = u_1 - a$. Thus, we get the solution $u_1 = \frac{x - x_0}{t} + a$.

area $\mathbf{1}$, where x_0 is the initial position of the diaphragm. Density ρ_1 and other properties can then be obtained using Eq. (4.7). In the area $\mathbf{2}$ in Fig. 2, we have

$$\begin{cases} u_2 + a\ln\rho_2 = u_L + a\ln\rho_L \\ \rho_2(u_2 - C) = \rho_R(u_R - C) \\ \rho_2(u_2 - C)^2 + p_2 = \rho_R(u_R - C)^2 + p_R \end{cases}, \tag{4.8}$$

where C is the speed of the shock. By assuming constant acoustic velocity a, intergration of Eq. (2.3) gives

$$p = a^2\rho + const.. \tag{4.9}$$

Combining Eqs. (4.8) and (4.9) leads to

$$\begin{cases} \dfrac{\rho_2 - \rho_R}{\sqrt{\rho_2\rho_R}} + \ln\rho_2 = \ln\rho_L \\ u_2 = \dfrac{\rho_2 - \rho_R}{\sqrt{\rho_2\rho_R}}a \\ C = \dfrac{\rho_2 u_2}{\rho_2 - \rho_R} \end{cases}. \tag{4.10}$$

This is the exact solution in area $\mathbf{2}$. The flow properties in area $\mathbf{L}$ and $\mathbf{R}$ are not changed from their initial value.

4.12 Numerical Results – To demonstrate the ability of the CE/SE to capture discontinuity interfaces, we first compute the hydraulic shock problem described above. In this case, our computation domain is from x = 0m to x = 1.0m. The diaphragm is initially located at x = 0.5m. The initial velocity is 0 everywhere in the tube. The left and right boundaries are set as non-reflect boundaries. At the bursting of the diaphragm, at time t = 0, a rarefaction wave moves to the left and a shock moves to the right.

Figure 3 shows the numerical results plotted against the analytical solutions. In this case, the initial pressure of the liquid (water) to the left of the diaphragm is 2.0MPa and the pressure to the right of the diaphragm 0.1Mpa. As shown in Fig. 3, the numerical results agree with the analytical results very well. Two discontinuity steps were successfully captured by the space-time CE/SE scheme. The left step is an expansion fan and the right step is a shock. Since the compressibility of water is very small, the expansion fan looks like a shock.

As the initial pressure difference between the two sides of the diaphragm becomes larger, the expansion fan can be seen more clearly. Shown in Fig. 4 are the numerical and analytical results under the condition of large pressure difference. In this case, the left side pressure is 500MPa, and right side pressure is 1.0MPa. The left side expansion was captured by three points, and the right side shock was captured by one point. The numerical results also agree with analytical results very well.
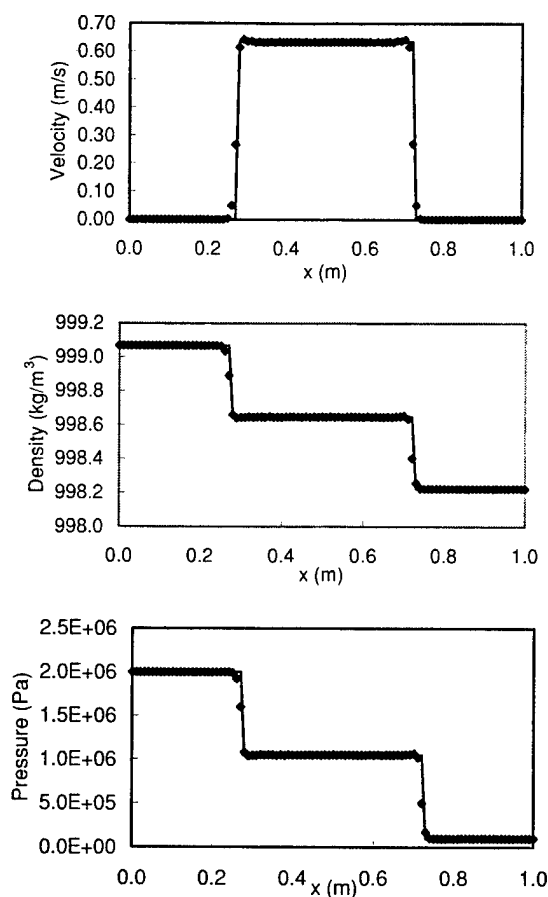
Figure 3.   The CE/SE solution of hydraulic shock problem (t= 0.15x10^{-3} sec.)

Figure 4.   The CE/SE solution of hydraulic shock problem (t= 0.15x10^{-3} sec.)

4.2 CAVITATING PIPE FLOWS – In this case, the calculation is initiailized by a pipe flow at a steady state. When t=0, an upstream valve is suddenly closed . Due to the inertia of the liquid flow, however, the liquid continues to flow in the pipe. Thus, a vacuum region (cavitation) occurs in the neighborhood of the valve. The low pressure of the vacuum region imposes an adverse pressure gradient to the pipe flow, and eventually causes the liquid to flow in a reverse direction back to the valve. The collapse of the cavitation region creates a pressure surge. As a result, fluid flow changes the direction again and flows away from the valve. The back and forth oscillations of the pipe flows is the phnomenon that we want to simulate by using the CE/SE method.

Figure 5 shows the series of the pressure distribution along the pipe with an interval of 0.185 seconds. The horizontal axis represents the pipe and vertical axis represents the pressure head. A logarithmic (base 10) scale is used for the vertical axis from 0.1m to 100m. The arrows in this figure indicate the wave propagation directions. It's

interesting to see that wave propagation speed varies considerably during the first 4.5 seconds after the valve closure. This is because the sonic speed of two phase flow is very sensitive to the void fraction of the flow. The sound speed of mixture of water and its vapor can be as low as 20m/s.

Figure 6 shows the pressre history on the valve surface with (a) as the experimental data and (b) the numerical results by the CE/SE method.   The numerical results compared favorably with the experimental data in terms of the pressure pick and the oscillation period. We remark that in the later stage of the flow development, experimental data showed more damped condition. This is due to fact that the use of a simple one-dimensional viscous model in our model, Eq.(2.2), is inadequate to represent the real mechanism of flow friction, which is by and large caused by the boundary layer effect.

4
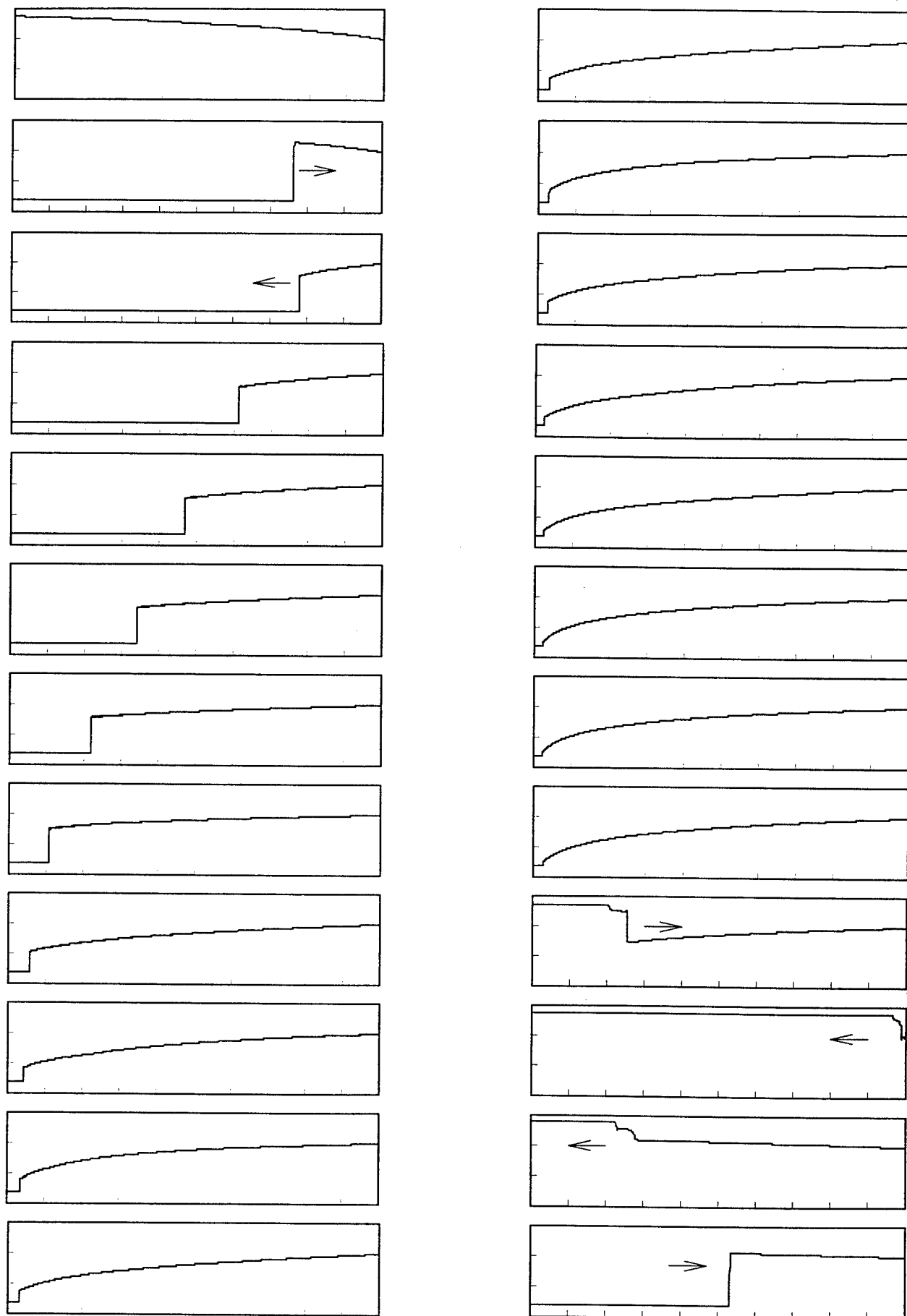
Figure 5. Series of the pressure distrbution along the pipe (interval time = 0.185sec.)
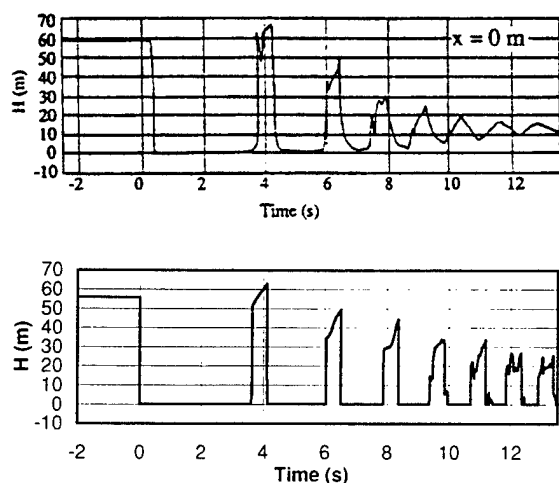
Figure 6. Cavitation caused by an upstream closing valve: (a) Experimental result, (b) Numerical simulation results.

Figure 7 shows the pressure history of a cavitating flow, where the valve is located at the downstream of the pipe. Again, the comparison is very favorable.
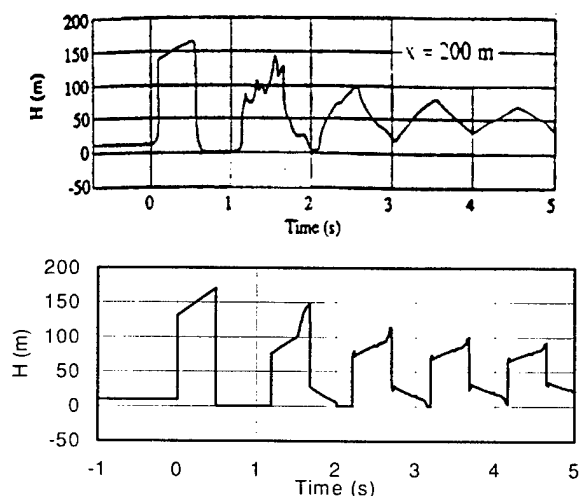
Figure 7. Cavitation caused by a downstream closing valve: (a) Experimental result, (b) Numerical simulation result.

5. CONCLUDING REMARKS

In this paper, we reported the extension of the CE/SE method to calculate cavitating flows. The CE/SE method is simple, accurate, and very efficient in calculating the complicated flow phenomenon of cavitation. Two examples are reported: (1) a hydraulic shock problem and (2) a cavitating pipe flows. In both cases, the CE/SE was capable to capture all salient features of the flow field, and the numerical results compared favorably with the experimental data and analytical solution.

REFERENCES

1. Chang S. C., 1995, "The Method of Space-Time Conservation Element and Solution Element – A New Approach for Solving the Navier-Stokes and Euler Equations," Journal of computational Physics, Vol. 119, pp. 295-324.
2. Chen Y. and Heister S. D., 1995,"Two-Phase Modeling of Cavitated Flows," Computers and Fluids, Vol. 24, No. 7, pp. 799-809.
3. Li W. H. and Walsh J. P., 1964, "Pressure Generated by Cavitation in a Pipe," Journal of the Engineering Mechanics Division, Proceedings of the American Society of Civil Engineers, pp. 113-133.
4. Marcic M. and Kovacic Z., 1985, "Computer Simulation of the Diesel Fuel Injection System," SAE Paper 851583.
5. Onorati A. and Ferrari G., 1998, "Modeling of 1-D Unsteady Flows in I.C. Engine Pipe Systems: Numerical Methods and Transport of Chemical Species," SAE Paper 980782.
6. Ozol J., Kim J. H. and Healzer J., 1994, "Cavitation Experience with Control Valves in Nuclear Power Plants," FED-Vol. 190, Cavitation and GAS-Liquid Flow in fluid Machinery and Devices, ASME.
7. Schmidt D. P., 1997, "Cavitation in Diesel Fuel Injector Nozzles," Ph. D. Thesis.
8. Shu J. -J., Edge K. A., Burrows C. R., and Xiao S., 1993, "Transmission Line Modelling with Vaporous Cavitation," Presented at the ASME Winter Annual Meeting, 93-WA/FPST-2.
9. Sobel D. R. and Lehrach RP. C., 1987, "A Hydro-Mechanical Simulation of Diesel Fuel Injection Systems," SAE Paper 870432.
10. Strunk R. D., 1991, "The Dynamics of Pump-Line-Nozzle Fuel Injection Systems," SAE Paper 91181.
11. Tang H. S. and Huang D., 1996, "A Second-Order Accurate Capturing Scheme for 1D Inviscid Flows of Gas and Water with Vacuum Zones," Journal of Computational Physics, 128, pp. 301-318.
12. Wallis G. B., 1969, One-dimensional Two-phase Flow, McGraw-Hill Book Company.
13. Yu S. T. and Chang S. C., 1997, "Treatments of Stiff Source Terms in Conservation Laws by the Method of Space-Time Conservation Element and Solution Element," AIAA 97-0435.

Parametric Characterization of High-Pressure Diesel Fuel Unit Injection Systems

Tsung-Cheng Wang, Joong-Sub Han, Xing-Bin Xie, Ming-Chia Lai and Naeim A. Henein
Wayne State University
Detroit, MI USA

Ernest Schwarz, Walter Bryzik
US TARDEC
Detroit, MI USA

ABSTRACT

Characterization of high-pressure Hydraulic Electronic Unit Injector (HEUI) and Electronic Unit Injector (EUI) diesel injection systems was conducted in this study. The characterization items included injection pressure, injection rate, injector response time, needle lift. start-up injection transient, dynamic discharge coefficient of the nozzles and macro- and micro-scopic spray visualizations. The effects of injection conditions and nozzle configurations on injection characteristics were reviewed. Nozzle sac pressure was measured to correlate with up-stream injection pressure. A LabVIEW data acquisition and controls system was implemented to operate the injection systems and to acquire and analyze data. For HEUI system, based on the results of the study, it can be concluded that common-rail pressure and length of the injection rate-shaping pipe determine injection pressure, while pressure rising rate and injection duration determine peak injection pressure; it was also found that nozzle flow area, common-rail pressure, and the length of rate-shaping pipe are the dominating parameters that control the injection rate, and the rate shape is affected mainly by common-rail pressure, especially the pressure rising rate, and length of rate-shaping pipe. Both injection pressure and ambient pressure affected the spray tip penetration significantly. The penetration increased corresponding to the increase of injection pressure or decrease of ambient pressure. The variation of spray penetration depends on type of injection system, nozzle configuration, and ambient pressure. The large penetration variation observed on the HEUI sprays could be caused by eccentricity of the VCO nozzle. The variation of mini-sac nozzle was 50% less than that of the VCO nozzle. The near-field spray behavior was shown to be highly transient and strongly depended on injector design, nozzle configuration, needle lift and oscillation, and injection pressure.

INTRODUCTION

High-pressure electronic-controlled fuel injection systems, such as electronic unit injector (EUI), hydraulic EUI (HEUI), and common-rail (CR), are key technology of advanced diesel engines. These systems could provide features required by an advanced engine such as more precise injection quantity, more flexible injection timing, better air-fuel mixing, and higher injection pressure comparing to the conventional mechanical injection systems. High injection pressure combined with small hole diameter nozzle can provide, 1) better spray formation which is due to finer initial drops exiting the nozzle with higher velocity, 2) better air entertainment and air-fuel mixing, and 3) more homogenous mixture with lower local equivalence ratio and fewer over-rich regions. These three factors have been reported as the keys to generate a low smoke combustion process (Pierpont, D.A. et al, 1995). Also Kato et al. (1989) showed that at high load engine operating conditions raising the injection pressure effectively reduces particulate emissions. This paper describes the injection and spray characteristics of high-pressure HEUI and EUI injection systems.

The HEUI system used in the study was an IRI prototype high-pressure injection system for advanced diesel engine combustion research. The system consists of a low-pressure fuel supply pump, a high-pressure oil pump, a common-rail equipped with PWM (Pulse Width Modulation) pressure regulator, and an electronic-controlled hydraulic amplify-lifted injector. The high-pressure oil pump is the source of system working pressure. It pressurizes and delivers the oil, the working fluid of the system, to the common-rail that serves as pressure accumulator. The pressure regulator then maintains the pressure of the accumulator at a setting point that can be in the range of 207 to 380 bar .The pressurized oil is fed to the inlet of injector via the common-rail. Once the injector being energized,

a spool valve in the injector is opened to allow the pressurized oil flow through it and act on an intensified plunger which subsequently pressurizes the fuel and make an injection through the injection nozzle. The low-pressure fuel supply pump continuously delivers fuel to the injector with fuel pressure maintained at around 7 bar.

The EUI system used in the study consists of a low-pressure fuel supply pump, a cam-driven rocker arm, and electronic-controlled mechanical driven injector. In the injector, a plunger is continuously actuated by the rocker arm when engine is running, and keeps pumping the fuel in the plunger chamber. Once the solenoid of the injector is energized, the solenoid-driven poppet control valve closes the channel that connects the plunger chamber to the low pressure returning fuel gallery. Subsequently, the pressure of the plunger chamber starts to increase. When the chamber pressure is greater than nozzle opening pressure, fuel injection starts and continues until the solenoid is de-energized and chamber pressure drops below the opening pressure, which is 34.5 bar for the nozzle used in the study. A strain gage is installed on the surface of the rocker arm for measuring the injection pressure indirectly.

In this study, the items of injection characterization included injection pressure, injection rate, injector response time, and needle lift. Based on these measured characteristics, other useful information can be derived, such as dynamic discharge coefficients of the nozzles. Meanwhile, the items of spray characterization included penetration, overall structure, hole-to-hole variation, initial spray break-up, spray at end of injection, spray at peak-pressure injection, and near-nozzle-exit spray cone angle. Both macroscopic and microscopic visualization methods were applied for the characterization of the HEUI and EUI sprays.

The stability and asymmetry of the fuel sprays from high-pressure nozzles, especially the VCO type nozzle, has significant influence on the combustion and emission performance of diesel engines, mainly resulting from the decreased air utilization efficiency for the greater degrees of asymmetry. The variation in spray penetration and spray cone angle from hole to hole must be quantified both before and after the injector tip is utilized on the engine if emissions and combustion variations are to be understood and correlated. In this study, the spray characterization was carried out by injecting fuel into a room-temperature nitrogen-filled pressurized chamber or atmosphere ambient. The chamber pressure was adjusted to simulate the air density at the end of compression stroke of Compression Ignition engine. In a real engine operating condition, fuel is injected to combustion chamber at the timing closed to end of a compression stroke. Hence, it is reasonable to assume that the fuel sprays issued into the pressurized chamber encounters similar drag force as it did in a real engine. Since the chamber was filled up with room temperature nitrogen gas, the fuel sprays mostly were in the form of liquid droplets and could be treated as non-evaporative

sprays. By high-speed photography technique, the time-evolved structure and characteristics of non-evaporative fuel sprays could be recorded and analyzed. The characterization items of macroscopic visualization carried out in this study included penetration, overall structure, and hole-to-hole variation. This method could be used to measure the performance of nozzle tip, injection unit, or injection system in terms of their capability of distributing fuel as far as temporal and spatial concerns. Although under same ambient density condition both the penetration and dispersion of an evaporative spray could be much less than those of a non-evaporative one, the characteristics obtained from a non-evaporative test condition still provides good indication of the performance of a fuel injection

The characterization items of microscopic visualization of this study included initial spray break-up, spray at end of injection, spray at peak-pressure injection, and near-nozzle-exit spray cone angle. Although some research had been carried out to characterize the near exit spray behavior, most previous work is limited to use single-hole nozzle which could not produce similar turbulence flow that could simulate those of multi-hole nozzles, or limited to scale-up models which could not exactly match the force-ratios and time scales in practical diesel sprays. As far as photograph technique concerns, most previous work is limited to single-image-per-injection photography technique, either using CCD or traditional still camera. To improve the situations, In this study, standard multi-hole nozzles were used to avoid misleading result; meanwhile, both still camera and high-speed drum camera associated with long distance microscope were applied to obtain more insight of near exit spray dynamics.

EXPERIMENTAL SETUP

The experimental setup for the characterization of HEUI injection system was as shown in Figure 1. A Kislter 4067A2000 Piezo-resistive pressure transducer was mounted at about 6.5 cm upstream of the inlet of the injection nozzle holder. The measured pressure was an upstream injection pressure. A Bosch type injection rate meter recorded injection rate by measuring the pressure wave that is produced by an injector when it issues an injection into a length of compressible fluid-diesel fuel. A LVDT (Linear variable differential transformer) displacement sensor with its ferromagnetic moving core mounted on the pressure pin of injection nozzle holder detected the needle lift. A special made nozzle tip was instrumented with pressure transducer, as shown in Figure 2, for the measurement of sac pressure that represents down stream injection pressure. By comparing the upstream and downstream injection pressure the pressure drop and the fuel transportation time across the nozzle holder assembly was obtained. A LabVIEW Data acquisition and controls system was implemented to operate the HEUI system for all kinds of test

requirements in terms of injection pressure, injection duration, number of injections, and synchronization between injection and data acquisition. The LabVIEW system was also used to record and analyze test data. The specification of the nozzle tips used in this study was summarized in Table 1. The flow number, for example, 610 of the VCO nozzle, represents steady state volume flow rate in cubic centimeter within 30 seconds test period with 100 bar injection pressure.

The experimental setup for macroscopic spray visualization included copper-vapor laser system (Oxford CU15), 35-mm still camera or high-speed drum camera, pressurized chamber and its peripheral, and LabVIEW data acquisition and control system. The copper-vapor laser was expanded into a thin light sheet using cylindrical lens and functioned as an optical shutter with 12.5-kHz pulsing frequency and with exposure time as short as 10 ns. The drum camera was operating at 250 revolutions per second with 1/15-second shutter speed. A LabVIEW Data Acquisition and Control System controlled the fuel injection pressure, timing and quantity. At the same time, the LabVIEW system also executed data acquisition and system synchronization among the laser, photography and fuel injection systems. The injection pressure was recorded along with injection and laser command signals, while the images were being taken by the photography system. The experimental setup was shown as Figure 3. Two levels of chamber pressure, 17.2 and 27.6 bar, were used to evaluate the effect of ambient density condition on penetration and dispersion. For the study of HEUI sprays, two types of nozzle with similar flow number, 620 mini-sac and 610VCO, were arranged in the test to analyze the effect of nozzle configuration on spray symmetry. Calculated spray tip penetration based on the model proposed by Hiroyasu et al.(1983) was incorporated in the analysis to correlate with the measured data.

The optical system setup for microscopic visualization included a long-distance microscope, copper-vapor laser (Oxford CU15), and still or high-speed drum camera. To obtain better image resolution, still camera photography with 35x24-mm photographic film, long-distance microscope, and single-shot laser as the light source was the method for the visualization of initial spray break-up peak-pressure injection, and end of injection. To obtain more insight of spray dynamics, high-speed drum camera photography with 10x24-mm photographic film, long-distance microscope, and 25kHz pulsed copper laser as optical shutter was the method for near nozzle exit spray characterization. The copper laser was expanded into a thin sheet with thickness less than 0.09mm by using cylindrical lens. It was used as the optical shutter, one shot or 25-kHz shots, with the exposure time as short as 10 ns. The drum camera was operating at 250 revolution-per-second with 0.16-second shutter speed. The long-distance microscope, similar to the ones used by other researchers (Sjoberg et al., 1996; Fath et al, 1997), was used to magnify the diesel spray structure very close to the nozzle exit. With its lens 8.75 inches

away from the observed object, the amplification factor was about 17.4. The diffraction-limit resolution can be as small as 1-2 micron. The optical setup provided great resolution in both time and space, as shown in Figure 4.
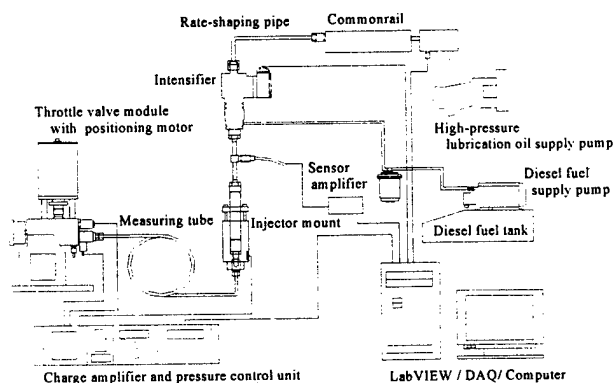

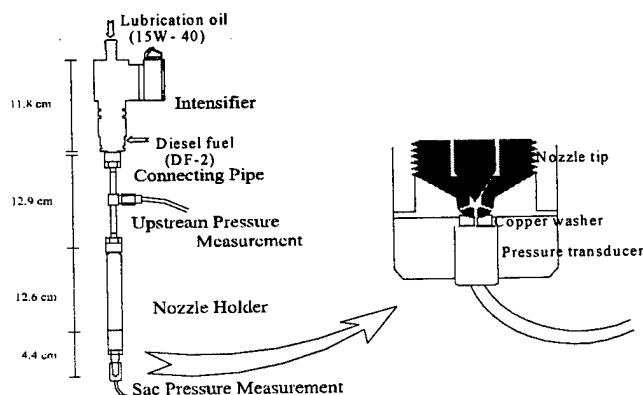Figure 1 Schematic diagram of the experimental set-up and fuel system

Figure 2 Injection pressure measurement for both up-stream and sac pressure

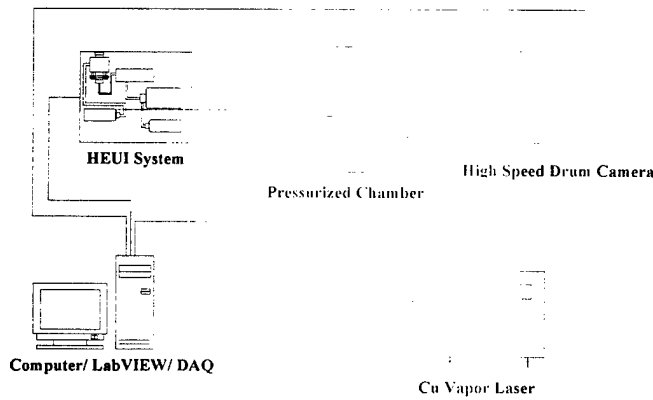| Nozzle tip	No. of hole	Hole Diameter(mm)	Total hole flow area(m**2)	Cd (steady state flow)
610 VCO	6	0.218	2.24 E-7	0.58
620 Mini-sac	7	0.190	1.98 E-7	0.66
730 VCO	7	0.210	2.42 E-7	0.64

Table 1 Nozzle specifications

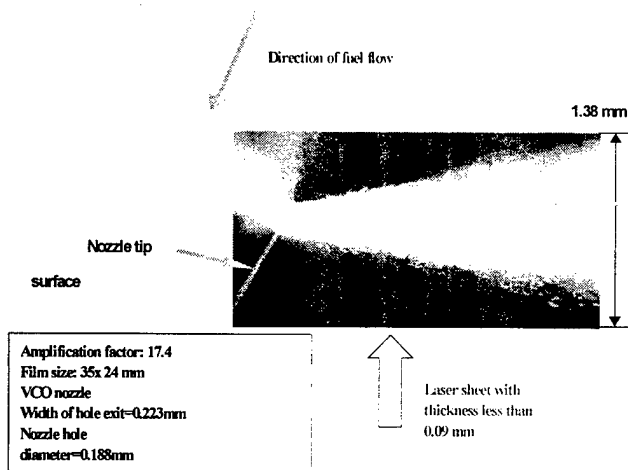Figure 3 Schematic of the experimental setup of non-evaporative spray visualization

Figure 4 Schematic of microscopic visualization of VCO nozzle of EUI system

RESULTS AND DISCUSSION

1.Characterization of the HEUI system

Injection Pressure

The injection pressure of HEUI system mainly depended on the common-rail pressure and injection duration. As shown in Figure 5, with injection duration remained at 2.25 ms, the injection pressures increased as common-rail pressures increased. With 2.25 ms injection duration and 380-bar common-rail pressure, the system was able to issue injection with pressure up to 1300 bar. The intensified ratios, the ratio of injection pressure to common-rail pressure, of the injector for three common-rail pressure settings, 207, 276, and 380 bar, were 3.71, 3.80, and 3.44 respectively. Figure 6 showed the effect of injection duration on injection pressure; one

millisecond increase of injection duration contributed to 290-bar increase in peak injection pressure. The thickness of the pressure adjusting shim inside nozzle holder also affected the injection pressure. With shim thickness increased from 1.95 to 3.24 mm, the peak injection pressure increased 4 to 6 percent.

Injector Response Time

Injector Response Time, defined as the time between injection command and start-of-injection (SOI), was in the range of 1.4 to 1.8 ms. The injector was driven by peak-and-hold type driver powered by 70-volt power supply. The injector response time consisted of two parts; part one is the time required for energizing of the solenoid that drives the spool valve, and part two is the time required for the spool valve to move to the open position and the line pressure to build up. The former depends on the power supply voltage applied to the driver, the latter depends mainly on common-rail pressure and length of the rate-shaping pipe. The results summarized in Table 1 and Table 2 showed that long rate-shaping pipe, low common-rail pressure, and reduced pressure adjusting shim thickness increased the injector response time. On the contrast, short rate-shaping pipe, high common-rail pressure, and additional shim thickness reduced the injector response time.
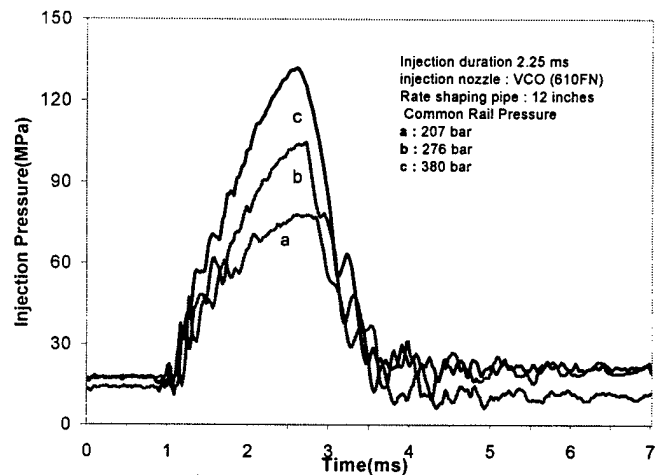

Figure 5 The effect of common-rail pressure on injection pressure

Common-rail Pressure (bar)	Response time (ms)	
	24 inches shaping pipe	12 inches shaping pipe
207	2.0	1.8
276	1.7	1.6
380	1.5	1.4

Table 2 The effect of C.R.P. and length of rate-shaping pipe on response
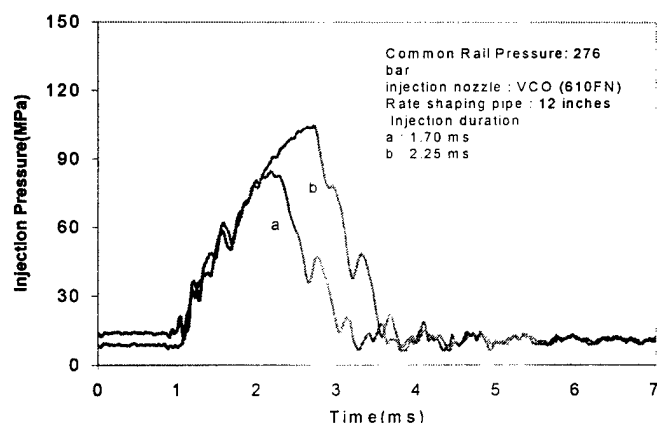
Figure 6 The effect of injection duration on injection pressure

Common-rail Pressure (bar)	Response time (ms)	
	3.24mm shim thickness	2.16mm shim thickness
207	1.6	1.8
276	1.5	1.6
380	1.4	1.4

Table 3 The effect of C.R.P. and shim thickness on response

Injection Rate and Needle Lift

Injection Rate mainly depended on the common-rail pressure, needle lifting, nozzle hole area, and length of the rate-shaping pipe. Figure 7 showed that higher common-rail pressure provided higher rising rate of injection pressure and consequently higher injection rate. Figure 8 showed that with 24 inches rate-shaping pipe the pressure rising rate became slower and the needle was lifting slower, both of which resulted in lower injection rate. Figure 9 showed the effect of nozzle hole area on injection rate. As the nozzle flow area increased, the injection rate increased but there was no significant effect on the shape of injection rate. Injection duration, type of nozzle tip (VCO or Mini-sac), or thickness of the pressure-adjusting shim had little effect on injection rate. Maximum needle lift of the nozzles used in the tests is 0.31mm that was measured from needle seat to fully open position. The pressure in the nozzle pressure chamber and the pressure applied to the top of the needle determine the behavior of needle lift. In the case of HEUI nozzles, the pressure applied to the top of needle was equivalent to the atmosphere pressure therefore the pressure in the nozzle pressure chamber dominated the pattern of needle lift. As shown in Figure 8, with 12 inches rate-shaping pipe and 380 bar common-rail pressure, it took 0.2 ms for the needle to reach fully open position. However, with longer injection rate-shaping pipe (24 inches pipe) and lower common-rail pressure (276 bar), the needle lift time increased from a regular 0.2 ms to 0.6 ms. The test result also showed that increase of the pressure

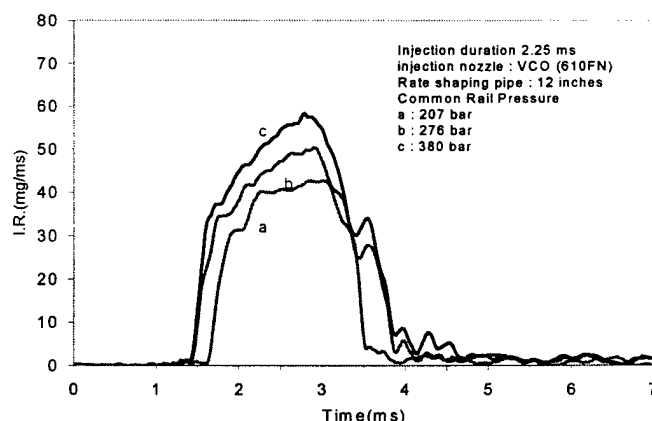adjusting shim thickness reduced needle bounce.

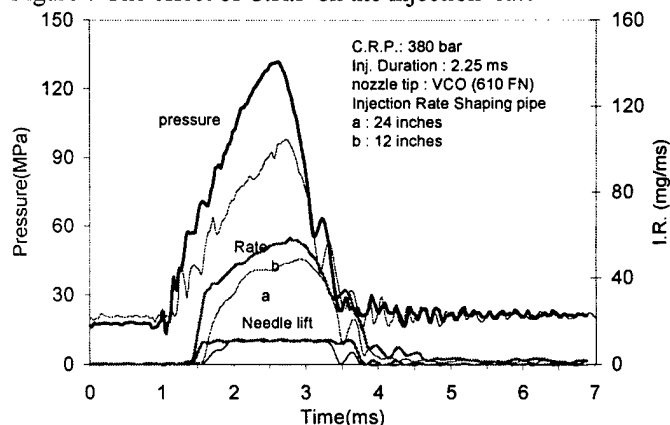Figure 7 The effect of C.R.P on the injection -rate

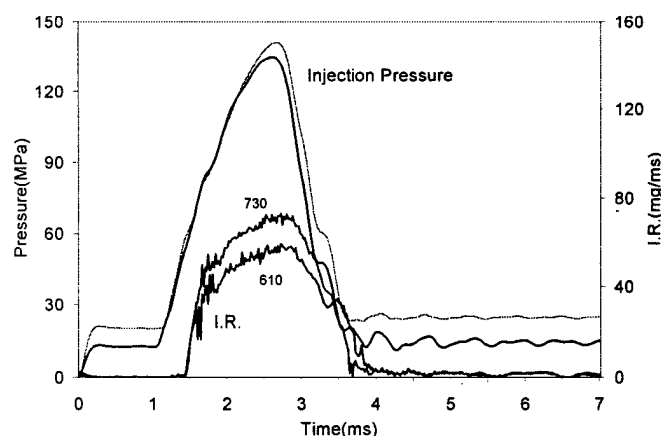Figure 8 The effect of length of rate-shaping pipe on the injection

Figure 9 The effect of nozzle flow area on the injection-rate

Nozzle Discharge Coefficient

The steady-state Discharge Coefficients of the

nozzles, as those in Table 1, were calculated from the nozzle data based on the following formula.

$$Cd = \frac{Q}{A \times \sqrt{\dfrac{2 \times P}{\rho}}}$$

Where,	Q	= Volume flow rate, m³/sec
	A	= Nozzle flow area, m²
	P	= Injection pressure, MPa
	ρ	= Fuel density, Kg/m³

On the other hand, the dynamic Discharge Coefficients of the nozzle can also be calculated by the same formula, but instead using the measured up-stream pressures and injection rates. Figure 10 to Figure 12 showed the dynamic Cd traces for the nozzles used in the study associated with the measured injection pressure, injection rate, and needle lift. Each of the Cd trace shown in the figures can be divided into three segments, which can be corresponding to three phases of needle lift, opening, full lift, and closing. For example, in Figure 10, when the needle was opening the Cd increased from 0 to about 0.57. Once the needle reached the full lift position the Cd gradually approached 0.62 and maintained at the same value until needle started to close. When the needle was closing, the Cd decreased from 0.62 to 0. Needle bouncing was observed in this example. The calculated dynamic discharge coefficient, 0.62, at needle full-lifted condition is about 6 percent lower than the steady-state discharge coefficient, 0.66.
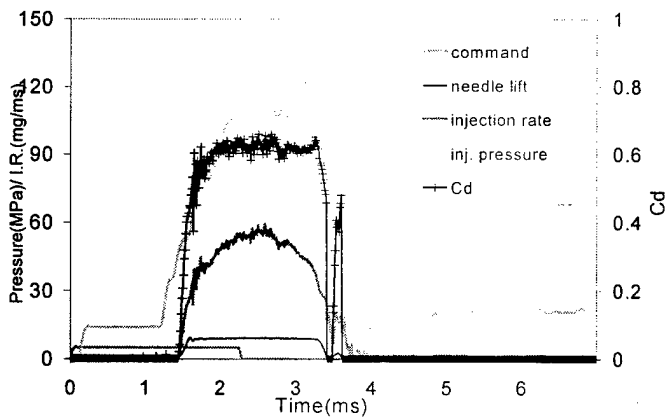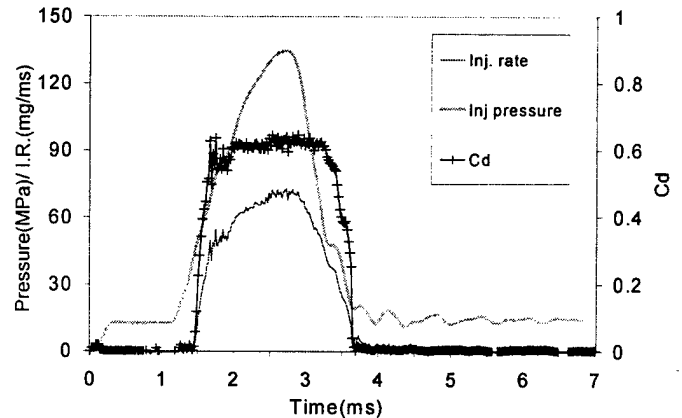

Figure 11 Dynamic Discharge Coefficient - 730 VCO nozzle

Injection System Startup Behavior

Figure 13 and 14 showed the transient injection pressure and injection rate at system startup. With common-rail pressure maintained steadily at 380 bar, the injection system took 3 to 4 injections to build up the pressure in both the intensifier and high-pressure line before a nominal injection was issued. The injection pressure, injection rate, and injection quantity became stable and repeatable after the 3rd injection was issued. The test results were summarized in Table 4. For the 1st injection, its pressure reached 56 percent of the nominal (140 MPa) and its quantity reached 71 percent of the nominal (101mg).

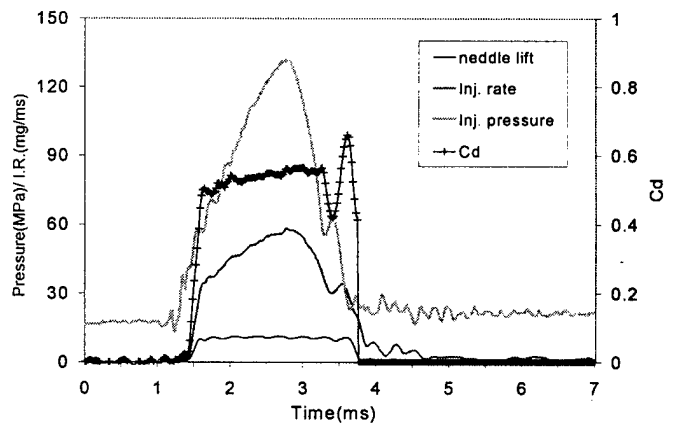Figure 10 Dynamic Discharge Coefficient - 620 minisac nozzle

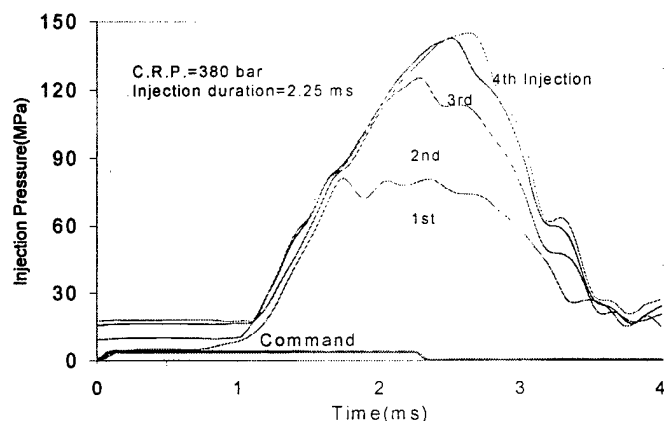Figure 12 Dynamic Discharge Coefficient - 610 VCO nozzle

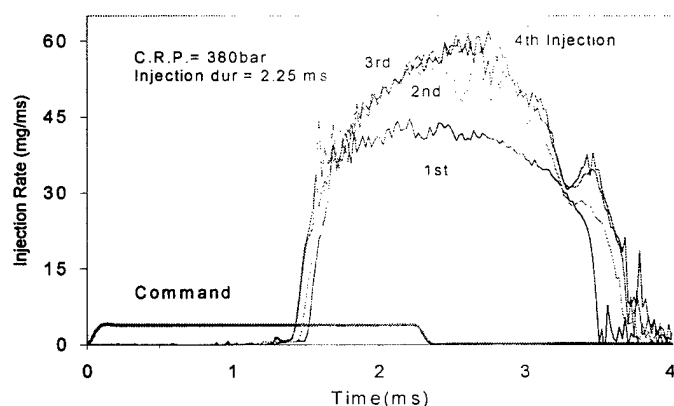Figure 13 Injection pressure transient at system start-up

Figure 14 Injection-rate transient at system start-up

Injection since engine start-up	Injector Response Time(ms)	Peak Injection Pressure(MPa)	Injection Quantity(mg)
1st	1.5	80	72
2nd	1.44	127	90
3rd	1.38	143	99
4th	1.4	145	101
5th	1.38	140	101

Table 4 Transient of HEUI injection during system startup period

Pilot Injection

The system was capable of delivering pilot injection, however the operating range of pilot injection in terms of its duration and dwell time was quite limited. The low limit of injection duration for pilot injection was 0.6 ms. The injector could not perform pilot injection with duration shorter than this. The dwell time, defined as the time between issue of pilot and main injection, could not be shorter than 0.6 ms. Figure 15

showed a typical measurement of the injection rate and needle lift for injection with pilot and main. Figure 16 and 17 showed the effect of dwell time on main injection in terms of injection rates and needle lift. With shorter dwell time the peak pressure, rate, and quantity of on injection were lower than those of an injection with a longer dwell time. It could be due to the slow pressure recovery in the common-rail after a pilot was delivered. Figure 18 showed the effect of dwell time on injection quantity. As dwell time decreased the injection quantity of the main injection decreased.

Figure 19 showed that the peak pressures of main injections were decreased with increase of peak pressure of pilot injection. Because the system could not make a pilot injection with 0.5-ms duration, the condition 'a' did not lead to a pilot injection. This resulted in a higher main peak injection pressure, as the trace "a" shown in the figure. If the pressure of pilot injection increased due to a longer duration, a decrease of peak pressure of the main injection could be observed, as trace "b" and "c" shown in the figure.
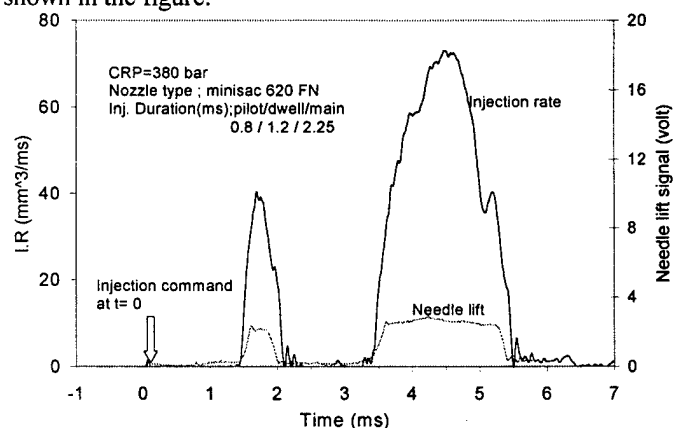

Figure 15 Injection-rate and needle lift measurement for pilot/main
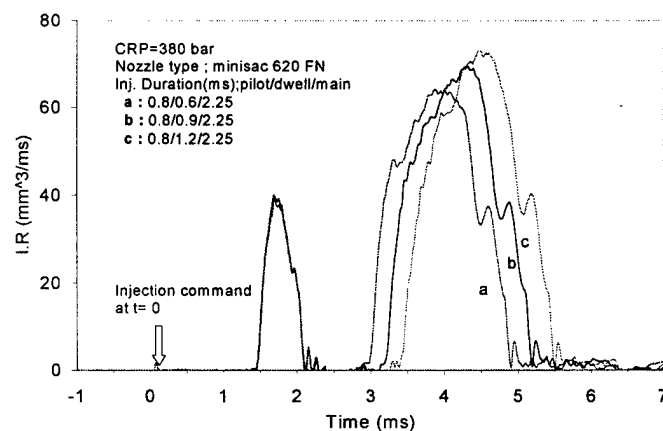

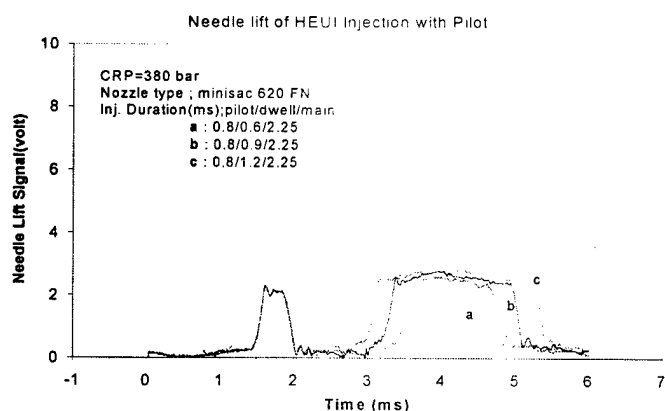Figure 16 The effect of dwell time on injection-rate of the main injection

46

Figure 17 The effect of dwell time on needle lift of the main injection

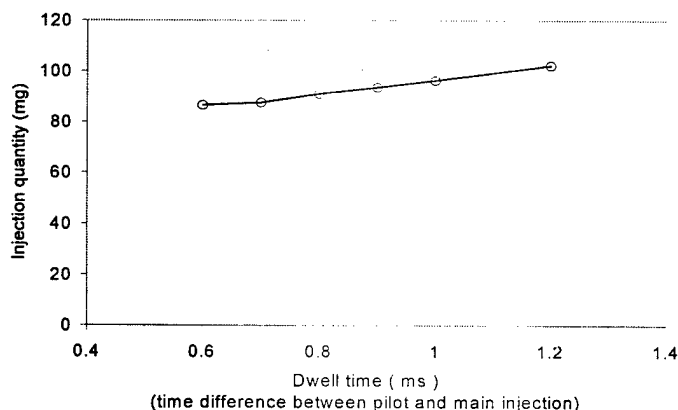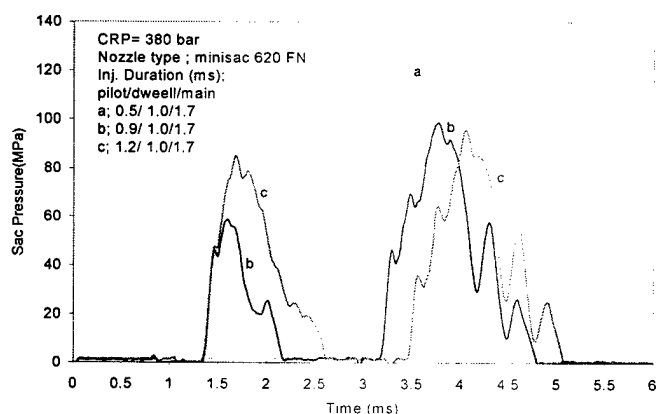Figure 18 The effect of dwell time on quantity of the main injection

Figure 19 The effect of pilot injection pressure to main injection pressure

Sac Pressure and Upstream Pressure

In this injection characterization study, the injection

pressure was measured at 6.5cm upstream of the fuel inlet of injection nozzle holder. To understand the correlation between the upstream pressure and the sac pressure (the pressure in the sac chamber of nozzle tip), a special instrumented nozzle tip and adapter were made such that pressure transducer can directly get access to the sac chamber of the nozzle tip. The upstream and sac pressures were measured at the same time. The test cases and results were summarized in Table 5. Figure 20 and 21 showed the pressure traces for two of the test cases. The pressure drops between the upstream and the sac chamber were in the range of 5 to 10 MPa. It is believed that the pressure drop occurred mainly at the needle seat region when high-pressure high-velocity fuel flowed through it. The pressure transportation lags were in the range of 0.1 to 0.14 ms. There is no correlation found between the operation conditions (common-rail pressure and injection duration) and pressure drops and transportation lags.
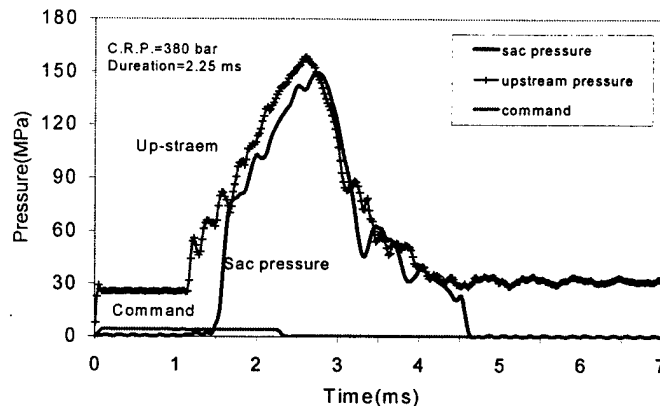

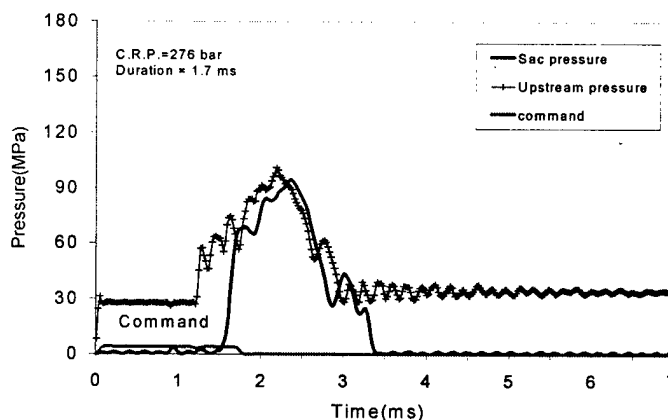Figure 20 Sac pressure and up-stream pressure with 380 bar C.R.P and 2.25 ms duration

Figure 21 Sac pressure and up-stream pressure with 276 C.R.P and 1.7 ms duration

Common Rail Pressure(MPa)	Injection Duration(ms)	Peak Upstream	Peak Sac Pressure(MPa)	Pressure Drop (MPa)	Time Lag (ms)
380	2.25	158	149	9	0.12
380	1.70	126	121	5	0.14
276	2.25	114	108	6	0.14
276	1.70	101	91	10	0.1

Table 5 Summary of sac pressure measurement

2.Characterization of EUI system

The injection pressure of the EUI system was determined mainly by engine camshaft speed, cam profile and injection duration. As shown in Fig 22, with 500-rpm camshaft speed, the pressure rising rate was 50 MPa per millisecond; with 25 crank angle injection duration, the peak injection pressure could reach 160 MPa. The injection pressure decreased as the speed of the camshaft decreased, as shown in Fig 23. The injector response time increased from 1.6 ms to 2.1 ms corresponding to the decrease of camshaft speed from 600 rpm to 300 rpm.
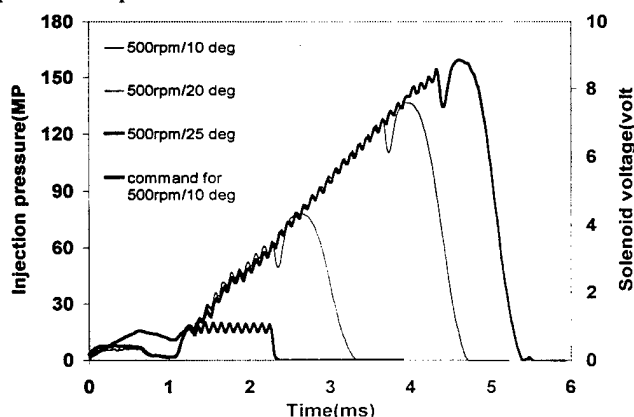

Figure 22 Injection pressure of EUI system, with various injection duration and 1000-rpm engine speed (500-rpm camshaft speed)
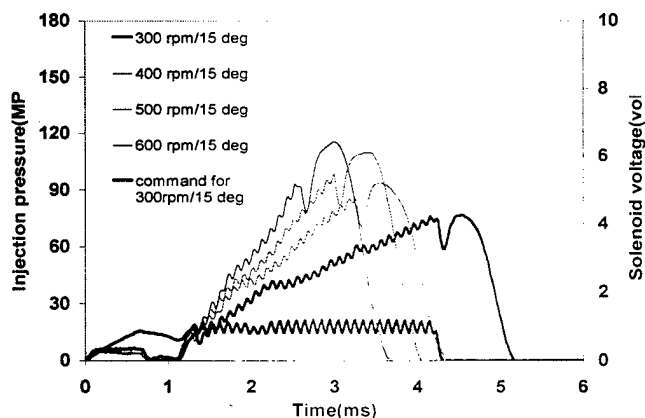

Figure 23 Injection pressure of EUI system, with various camshaft speeds and 15-degree injection duration

3.Macroscopic Spray Visualization

Spray Penetration and Correlation with Empirical Model

Figure 24 to 28 demonstrated how the tip penetration of HEUI and EUI sprays change with various ambient pressures. On average, increase of the ambient pressure from 17.2 to 27.6 bar reduces the penetration by 24 % for the HEUI sprays and by 10 % for the EUI sprays.

Figure 29 showed the correlation between the measured and calculated penetration for the HEUI sprays under various ambient conditions The calculated penetration was based on empirical model proposed by Hiroyasu et al.(1983). Input data for the calculation included nozzle specifications, injection quantity, injection rate, density of ambient gas, and density of fuel. Value of 0.8 was used as the Coefficient of Spray Contraction for the calculation of average injection velocity, which was carried over from the study of Kuo (1987). To best fit with the measured data 0.55 had been chosen as the values of Coefficient of Effective Injection Velocity for the calculation of penetration of HEUI sprays. In general, the model correlated fairly well with the measured data. However, the model tended to over predict the early phase of the penetration and under predict that of the later phase.

Figure 30 showed the maximum penetration of pilot injection of HEUI system under various peak injection pressures. With peak pressure of 25 MPa and ambient pressure of 27 bar, the maximum penetration of the pilot injection was 22 mm. The maximum penetration increased corresponding to the increase of peak injection pressure. As the peak pressure increased to 50 MPa, the maximum penetration reached 50 mm.
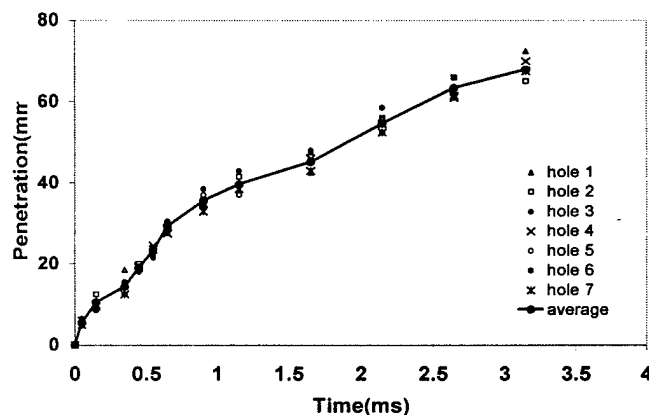

Figure 24 Hole-to-hole penetration variation of the HEUI sprays, with 620 mini-sac nozzle, pressure of 77 MPa, duration of 2.85 ms, and ambient pressure of 27.6 bar.

Figure 25 Hole-to-hole penetration variation of the HEUI sprays, with 620 mini-sac nozzle. pressure of 77 MPa, duration of 2.85 ms, and ambient pressure of 17.2 bar.

Figure 28 Hole-to-hole penetration variation of the EUI sprays, with 0.188-mm VCO nozzle, pressure of 80 MPa, duration of 2.3 ms, and ambient pressure of 17.2 bar.

Figure 26 Hole-to-hole penetration variation of the HEUI sprays, with 610 VCO nozzle. pressure of 126 MPa, duration of 2.25 ms, and ambient pressure of 27.6 bar.

Figure 29 Correlation between measured and modeled penetration of the HEUI system, with pressure of 77 MPa, duration of 2.25 ms, 620 mini-sac nozzle, and ambient pressures of 17.2 and 27.6 bar.
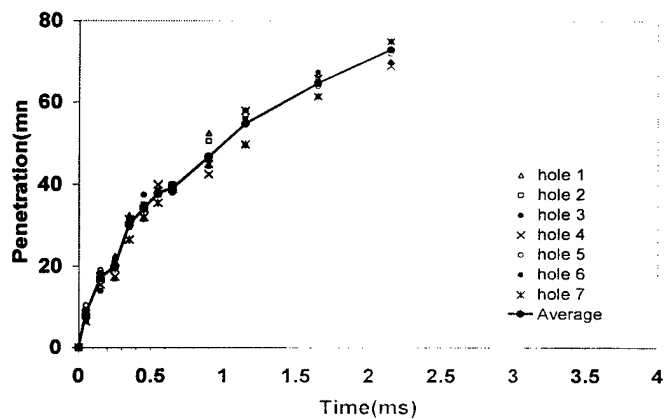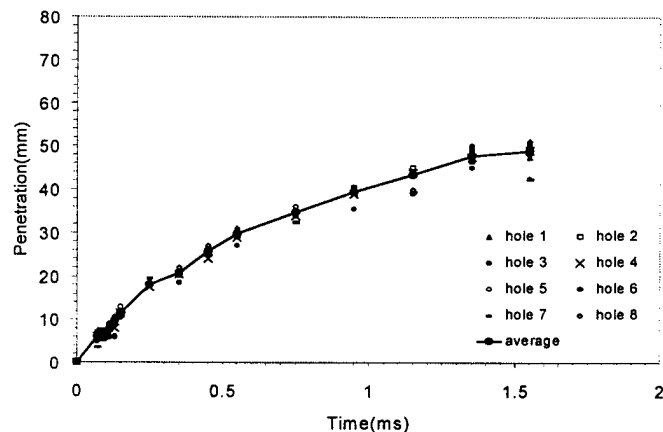

Figure 27 Hole-to-hole penetration variation of the EUI sprays, with 0.188-mm VCO nozzle. pressure of 80 MPa. duration of 2.3 ms, and ambient pressure of 27.6 bar
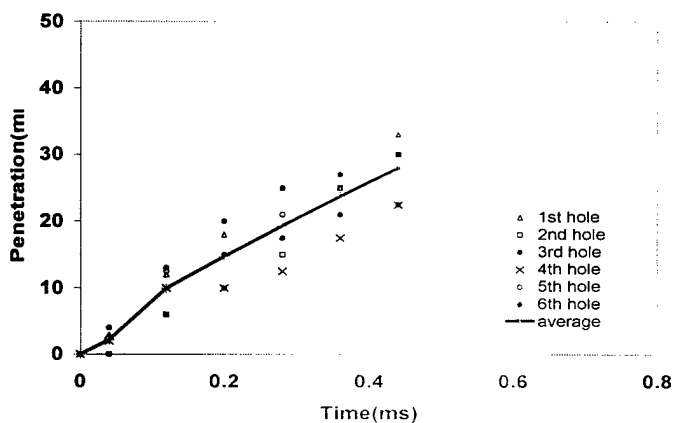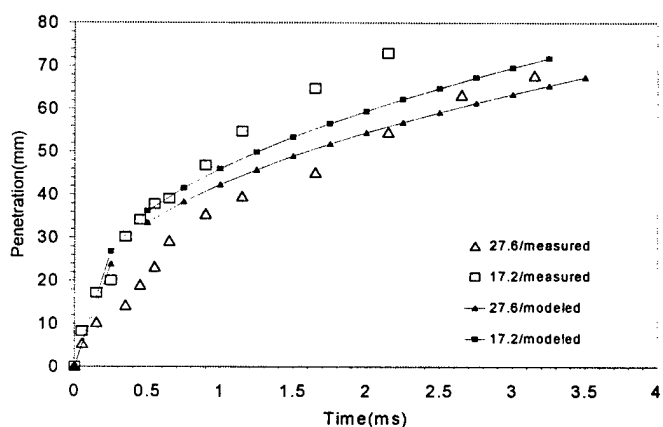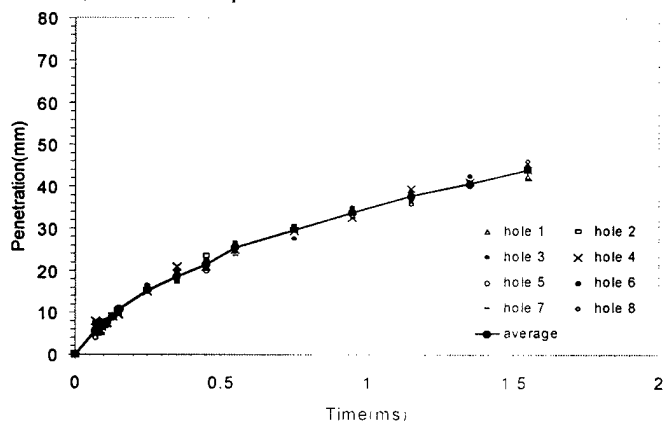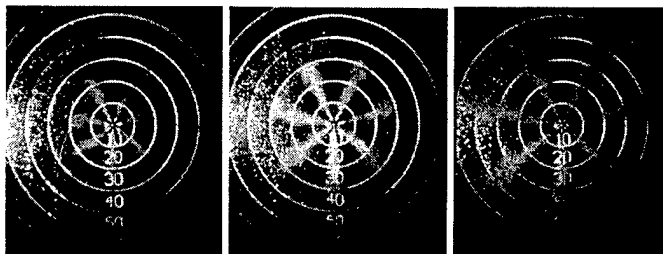

Figure 30 Maximum penetration length of pilot injection with various peak pilot injection pressure; 25Mpa (Left), 30 MPa (Middle), and 50 MPa (Right)

Hole-to-hole Spray Variation and Spray Structure

Figure 31 illustrated the early spray development of injections with common-rail pressure of 380 bar. These time-sequence photographs were taken using a drum camera with the laser pulsing at 12.5 kHz. At atmospheric ambient pressure, sprays of the minisac nozzle showed an extremely asymmetric pattern (Figure 31, L1 to L4). As the ambient pressure increased to 27 bar, the spray pattern became more symmetric and, at the same time, a substantial decrease of the penetration could be observed (Figure 31, M1 to M4). As compared to the minisac nozzle, the VCO nozzle showed significant hole-to-hole variation (Figure 31, R1 to R4). The mini-sac nozzle demonstrated more uniform spray penetration and structure. Asymmetry and puffy structure were observed on the sprays of the VCO nozzle. Significant hole-to-hole variation in cone angle of the sprays of the VCO nozzle was also observed, especially at the early stage of spray development. The fastest spray of the VCO nozzle appeared in the 11 o'clock direction, while the slowest one was right on the opposite side, in the 5 o'clock direction. In addition, puffy structure along the edges of the sprays was also observed for the 1-, 3-, 5-, and 7-o'clock sprays. Therefore, it would be reasonable to conclude that the needle-to-seat eccentricity was most severe upon the 5 o'clock nozzle hole, which consequently reduced the flow area of the corresponding hole at the early stage of spray development. The puffy structure at the early development of these sprays may be categorized as hollow cone spray with characteristics of wide angle as the type of the spray Soteriou et al.(1995) identified in their study. These early-developed sprays with puffy structure were surpassed and penetrated by the later coming solid cone sprays after 0.24 to 0.32 ms from start of injection.

Figure 24 to 28 also showed the penetration variation for the sprays of HEUI and EUI systems under two ambient pressure settings. As summarized in Table 7, the variation of spray penetration depended on type of injection system, nozzle configuration, and ambient pressure. Overall speaking, the EUI system equipped with VCO nozzle had the best performance in terms of penetration variation. The EUI system used in the test is for heavy-duty engine; it has a sturdy injector construction with a larger nozzle, which generally results into more symmetric spray. As to the case of HEUI system, the variation of the Mini-sac nozzle is about 47% less than that of the VCO nozzle. The result also showed that increase of ambient pressure slightly reduced the magnitude of variation for all test cases.
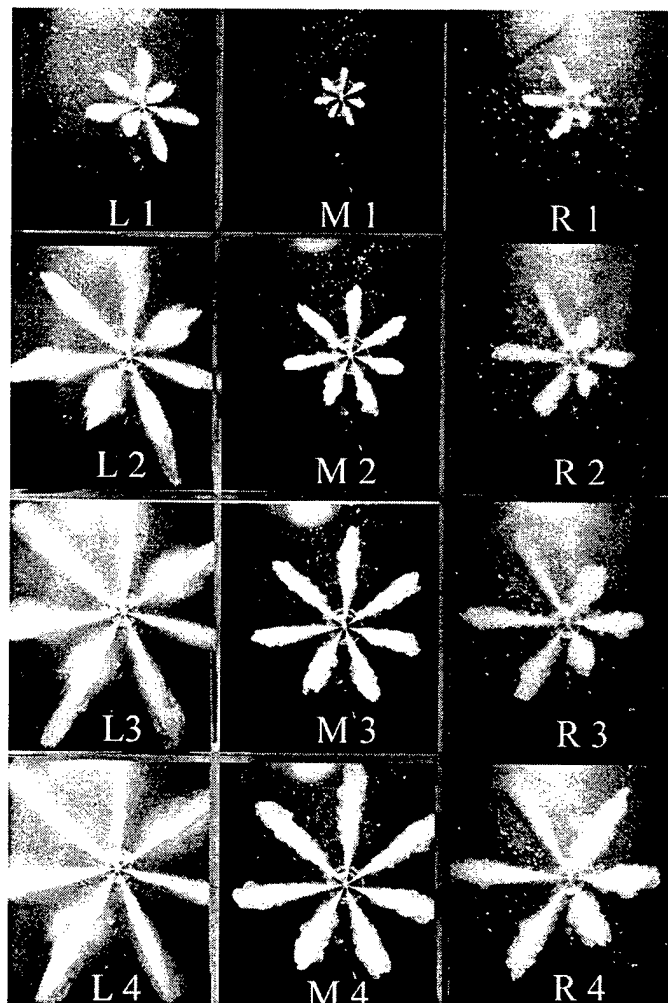
Figure 31 Early spray development

	Nozzle type	C.R.P	Ambient P.	Inj. Duration	Injection P.
Left	minisac 620 FN	380 bar	Atmosphere	2.25 ms	130 Mpa
Middle	minisac 620 FN	380 bar	27 bar	2.25 ms	133 Mpa
Right	VCO 610 FN	380 bar	27 bar	2.25 ms	127 Mpa

Table 6 Description of macroscopic visualization of Figure 31

Injection System	Nozzle tip/ hole diameter	Ambient pressure(bar)	Variation of penetration (mm)
EUI	VCO/0.188mm	17.2	1.3
		27.6	1.0
HEUI	Mini-sac/0.190mm	17.2	2.2
		27.6	1.8
HEUI	VCO/0.210mm	17.2	3.8
		27.6	3.7

Table 7 Comparison of hole-to-hole penetration variation of the injection systems
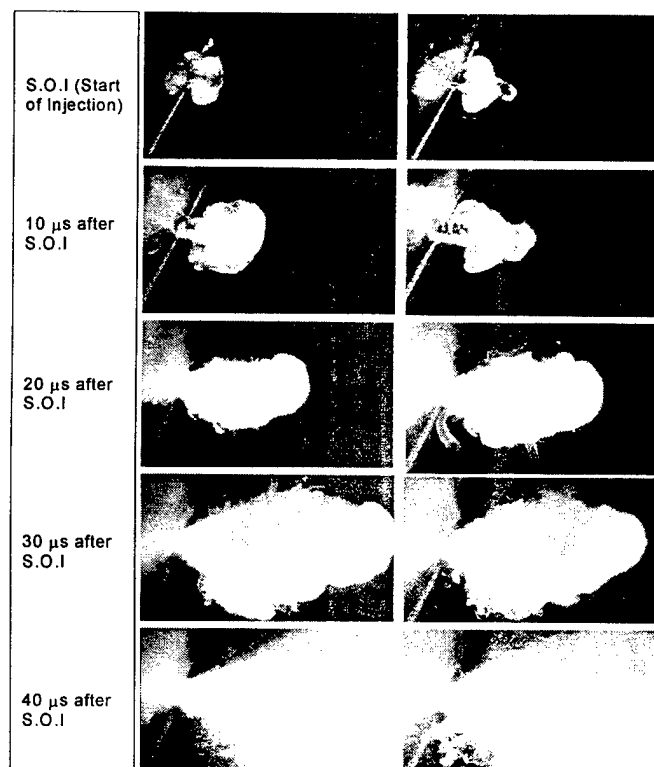
Figure 32 Still photographs of early development of EUI sprays, with 0.188-mm VCO nozzle, 1500 rpm engine speed, and duration of 10 degree.
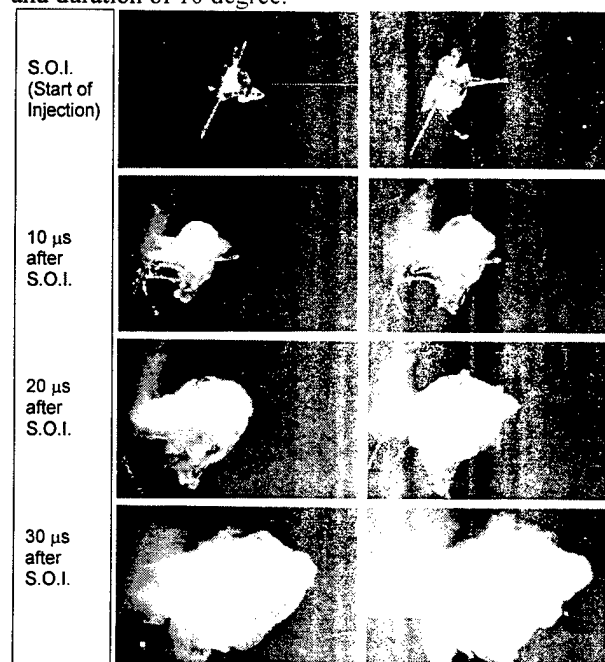
Figure 33 Still photographs of early spray development of EUI

sprays, with 0.188-mm VCO nozzle, 750 rpm engine speed, and injection duration of 10 degree.
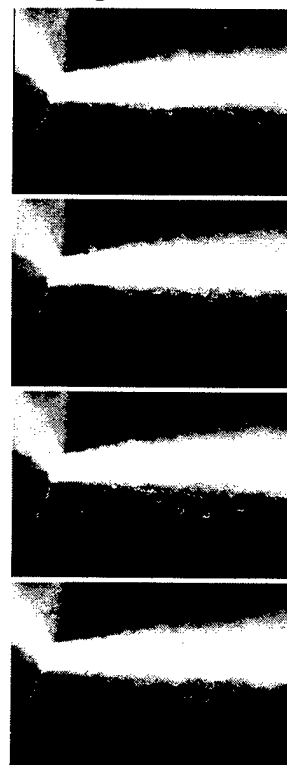
Figure 34 Still photographs of EUI spray at peak injection of 200 MPa, with 1500 rpm engine speed and injection duration of 25 degree.

4.Microscopic Spray Visualization

Initial Spray Breakup

In order to investigate the primary breakup mechanisms, the method of single-shot microscopic visualization using 35-mm still camera was used to get higher resolution pictures and to avoid the vibration effect which could be introduced by the high-speed rotating drum camera. Figure 32 and 33 showed a collection of the microscopic photographs of EUI spray for initial spray development right after SOI, which were taken with a 35-mm still camera. The still-photography captured the overall spray boundary and provided excellent contrast on black-and-white film. These close-ups were taken to catch the onset of spray formation, where the spray just exited the nozzle orifice. The photograph showed a very dynamic primary breakup processes very close to the injector. For the EUI injection system, the injection pressure and its rising rate are directly proportional to engine speed. Figure 32 showed the primary breakup process of EUI spray with 1500-rpm engine speed and 10- degree injection duration.

At the earliest instant that the camera was able to capture the spray exiting the nozzle, the liquid column appeared to have a translucent potential core wrapped around by a separating boundary layer that tends to mushroom and roll up, as shown on the 10-μs image of Fig 32. The asymmetry of the spray structure was obvious in the early spray development. Further into the spray development, at 40 μs after start of injection, the spray evolved to have a very large cone-angle: meanwhile, a cluster of fuel particles with sizes as large as 55 μm could be observed at the left bottom corner of the images. Fig 33 showed similar test case but with lower pressure rising rate resulting from reducing engine speed to 750 rpm. As the pressure rising rate reduced in a half, the early spray development process also slowed down. The shape of the sprays in the early spray development was more irregular as compared to the case of 1500 rpm. At these early spray developments, the spray penetration velocity was about 40 m/s, while the injection pressure was around or slightly higher than the needle opening pressures of 34.5 MPa.

Microscopic photographs of EUI spray at peak-pressure injection were shown in Figure 34, which were taken at the maximum injection pressure of 200MPa from four individual injections with 1500-rpm engine speed and 25- degree injection duration. The sprays showed a much smaller cone angle. The onset of spray breakup was immediately at the injector exit, indicating the presence of turbulent primary breakup (Dan and Lai, 1998). The bottom side of the spray showed the formation of large droplets. The sizes of the droplet increased as the distance from the nozzle exit increased. Although some of which were not exactly focused, their diameters could be estimated to be 10-20% of that of the nozzle hole, corresponding to the turbulent integral scale within the nozzle. In comparison, the top side of the sprays did not show a symmetric and corresponding distribution of large droplets, but instead suggested the formation of a very fine mist, in spite of possible light attention across the spray. The nozzle internal flow direction was from top to bottom: therefore, the topside spray was directly downstream of the turn-around point, where nozzle internal flow passage dictates that fuel flow must negotiate a sharper inside turn into the VCO hole. The fine mist observed could be a direct confirmation of cavitation-enhanced breakup mechanism: however, more research is needed to verify these observations.

pray Cone Angle and Its Oscillation

High-speed microscopic visualization results of EUI sprays were shown in Figure 35 for two injection conditions. The spray cone-angle oscillation phenomena were observed on both of the EUI and HEUI sprays. For the HEUI sprays, as shown in Figure 36, wider spray angle was observed at the early development of the injections, within 0.2 ms from start of injection, for injection pressures of 64, 80, and 124 MPa. As

referred to data of Fig 8, with 12-inch rate-shaping pipe, the time for needle full open was about 0.2 ms, which is in line with period of time in which wider spray cone angle was observed. Hence, it can be concluded that the wider spray cone angle at early development of the spray is induced by needle opening. The result could also be verified by Figure 37, which showed that under the condition of same pressure rising rate, even with different injection duration's and types of nozzle, all cases showed wider spray cone angle at the early development of the sprays, which is about 0.2-ms period after SOI. Similarly, for the case of EUI spray, wider spray cone angle was observed at the early development as well as prior to the end of injection; as shown in Figure 38 and Figure 39. The sprays started with 80-degree spray cone angle. Within 0.2 ms after start of injection, their cone angle decreased to about 20 degree and stabilized at the same angle through the mid-injection period until the end of injections at which the cone angles kicked up to about 30 degree. As a conclusion of the analysis on the spray cone angle oscillation of EUI and HEUI injection, it is suggested that the opening and closing of needle induce the wide spray cone angle. In the mid-injection period, both EUI and HEUI sprays were devoid of the significant oscillation, which may be attributed to their quick needle opening and settling at the full open position.

Spray Characteristics at End of Injection

In the microscopic visualization, spray trickled down and formed larger drops or liquid ligament was observed at end of injections. Figure 40 showed the end of injections of EUI sprays for four injection conditions. All images in the figure showed that at the end of injection, the spray trickled down and formed larger drops. Fig 41 showed the captured images by still camera with better resolution, which were taken just prior to end of injection of two individual EUI injections with 1500-rpm engine speed and 10-degree duration. Both figures showed that large drops were formed at the edges of spray as well as and in the spray. The size of the larger drops could be as large as 100 μm; these large drops were moving with slow speed that could be as low as 12 m/s.

Figure 42 and 43 compared the end of injections of the mini-sac and VCO nozzles of the HEUI system. The mini-sac nozzle tended to produce larger ligaments and drops at end of injection (and consequently higher HC emission in engine tests); as compared to the minisac nozzle the VCO nozzle showed some improvement. For both injection conditions, pressure of 70 and 98 MPa, secondary injection due to needle bouncing were observed. As a result, the period of injection with poor atomization was extended. As shown in Figure 43, the width of the ligament formed at end of injection of a mini-sac nozzle was about 110 μm that is 60% of the size of the nozzle hole. On average, the moving velocity of the drops formed at end of injection of HEUI injection is about 3 to 4 m/s. Figure 44

showed the spray penetration of a secondary injection caused by needle bounce. The maximum penetration of secondary injection could be as large as 5 mm.

375-rpm camshaft speed & 7 degree duration

750-rpm camshaft speed & 10 degree duration

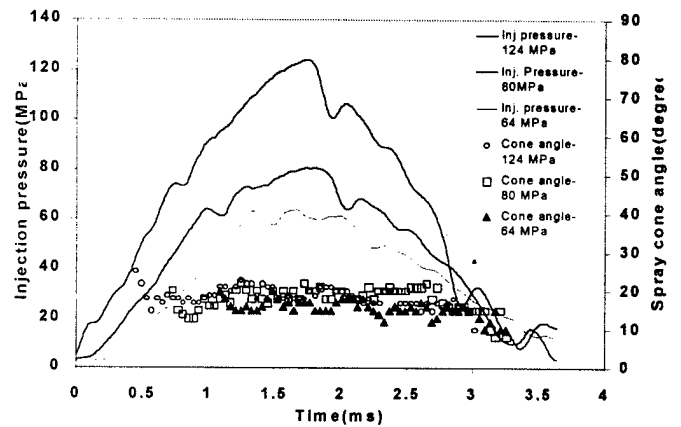Figure 35 Microscopic visualization of EUI spray.

Figure 36 Spray cone angle and injection pressures of HEUI spray, with fixed duration of 2.25 ms and 610 VCO nozzle.
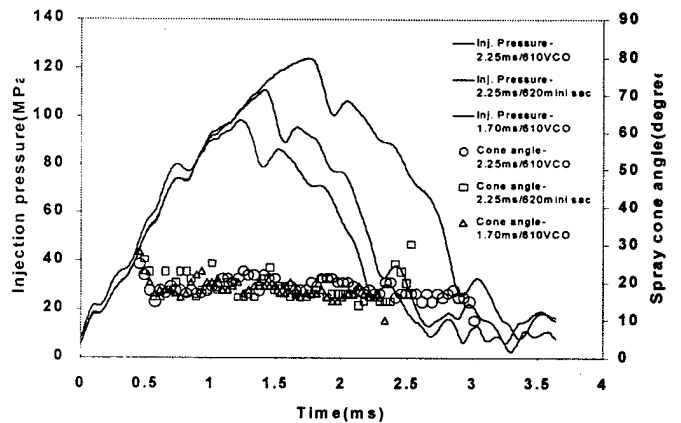
Figure 37 Spray cone angle and injection pressure of HEUI spray, with fixed common-rail pressure of 379 bar.
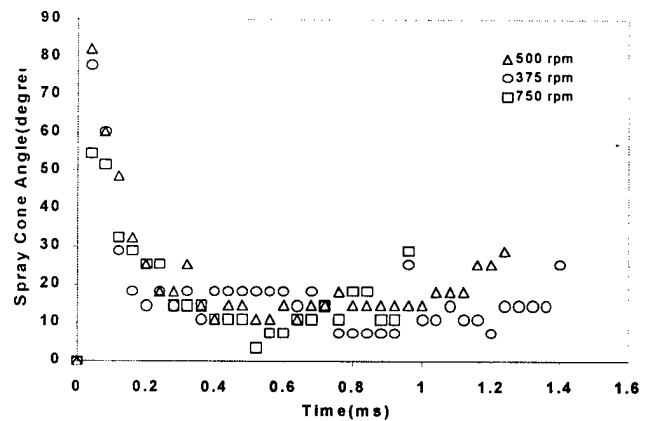
Figure 38 Spray cone angle of EUI spray with various cam shaft speeds.
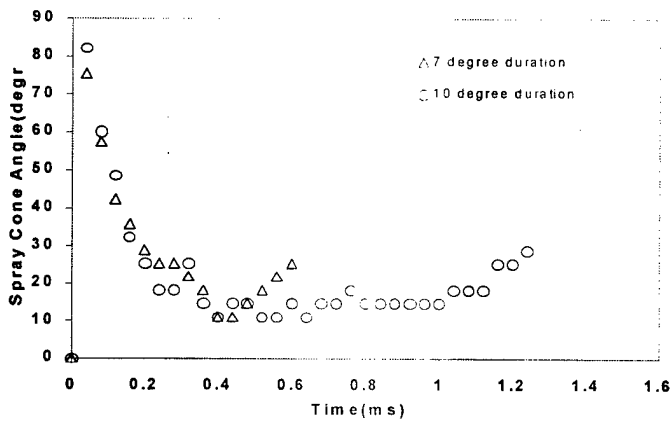
Figure 39 Spray cone angle of EUI spray with fixed camshaft speed of 500 rpm and injection duration of 7 and 10 crank-angle degree.

Figure 41 Still photographs of end of injection of EUI system, with 1500-rpm engine speed and 10-degree duration.

750 rpm 7 degree   375 rpm 7 degree

750 rpm 10 degree   500 rpm 10 degree
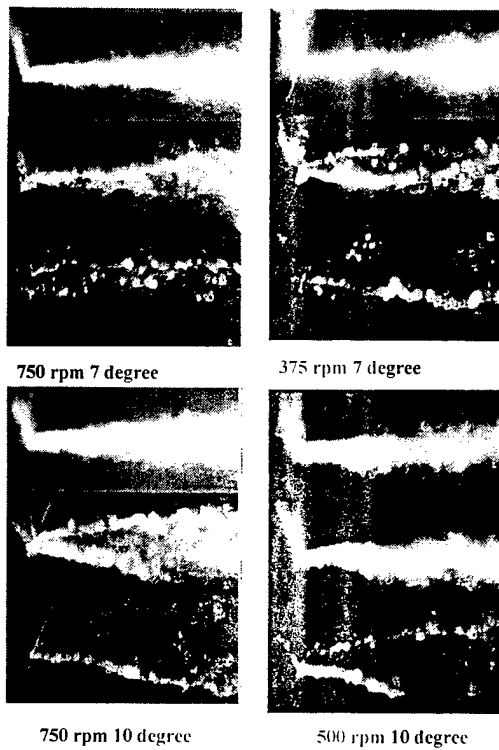
Figure 40 End of injections of EUI system under various camshaft speeds and injection duration.
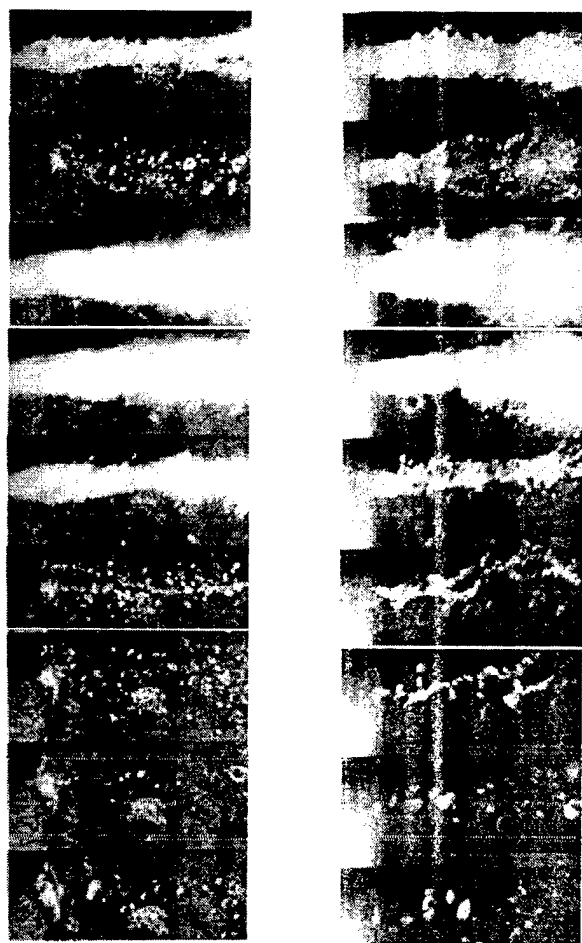
610 VCO nozzle.
98 MPa peak
injection pressure &
1.7 ms duration

620 Mini-sac nozzle.
97 MPa peak
injection pressure &
1.7-ms duration

610 VCO nozzle,
69 MPa peak
injection pressure &
1.7 ms duration

620 Mini-sac nozzle,
71 MPa peak
injection pressure &
1.7-ms duration

Figure 42 Effect of nozzle configuration on end of injection of HEUI system. (610 VCO vs.620 mini-sac), with common-rail pressure of 379 bar
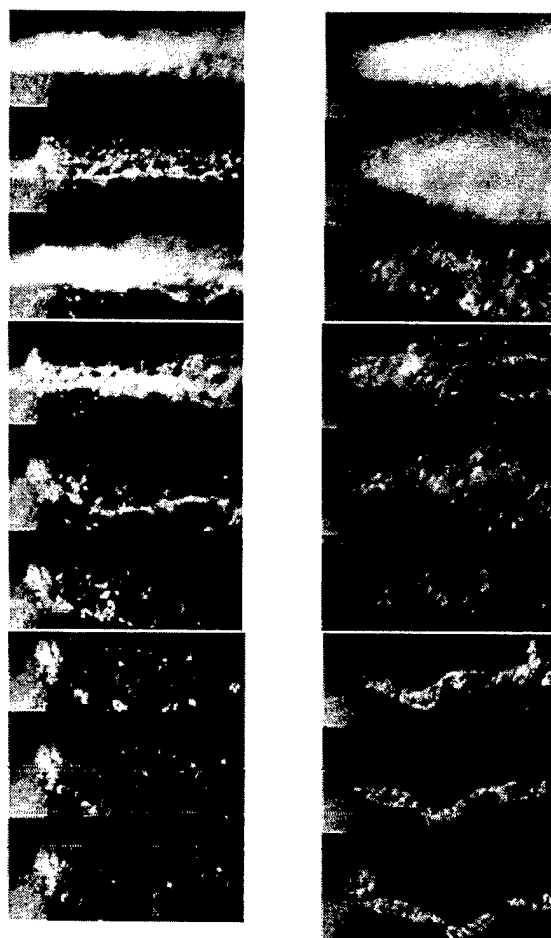
Figure 43 Effect of nozzle configuration on end of injection of HEUI system.(610 VCO vs. 620 mini-sac), with common-rail pressure of 276 bar.

Figure 44 Secondary injection (Needle valve bouncing)

CONCLUSIONS

1. Specific findings for the characterization of HEUI injection system were summarized as follows.
   - Common-rail pressure and length of the injection rate-shaping pipe determine injection pressure while pressure rising rate and injection duration determines peak injection pressure.
   - Nozzle flow area, common-rail pressure, and length of rate-shaping pipe affect injection rate. The rate shape is affected mainly by common-rail pressure, especially the pressure rising rate, and length of rate-shaping pipe.
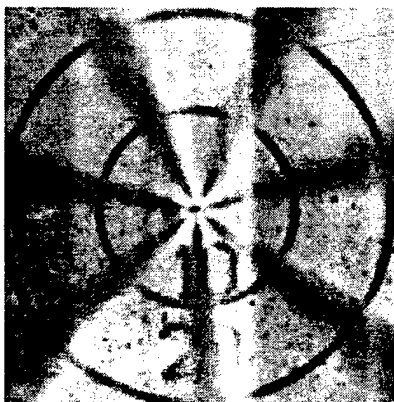   - Injection response time is in the range of 0.1 to 0.18 ms and mainly depends on common-rail pressure, length of rate-shaping pipe, and shim thickness.
   - Dynamic Discharge Coefficient derived from measured up-stream injection pressure and injection rate is about 6 percent lower than Static Discharge Coefficient derived from static flow data.
   - Start-up Injection transient was observed. At system start-up, it took 3 to 4 injections to establish line pressure in the high-pressure section of the system. Afterward, stable and repeated injection can be issued.
   - The pressure drop across nozzle seat flow area is in the range of 5 to 10MPa and transportation lag between upstream and nozzle sac chamber is in the range of 0.1 to 0.14 ms, which are independent of common-rail pressure and injection duration.
2. Based on the study of HEUI and EUI sprays, both injection pressure and ambient pressure affect the spray tip penetration significantly. The penetration increases corresponding to increase of injection pressure or decrease of ambient pressure.
3. The spray tip penetration model correlate fairly well with the measured data of HEUI sprays under various injection and ambient pressures. However, the model tends to over predict the early phase of the penetration and under predict

that of the later phase.
4. The variation of spray penetration depends on type of injection system, nozzle configuration, and ambient pressure. The large variation observed on the HEUI sprays could be caused by eccentricity of the VCO nozzle. From the visualization results of the HEUI sprays, the variation of mini-sac nozzle is 50% less than that of the VCO nozzle.
5. The spray cone-angle oscillation phenomena were observed on both of the the EUI and HEUI sprays. It is suggested that the opening and closing of needle induce the wide spray cone angle. In the mid-injection period, both EUI and HEUI sprays are devoid of the significant oscillation, which may be attributed to their quick needle opening and settling at the full open position.

REFERENCE

1. Bosch, Wilhelm, (1966) "The Fuel Rate Indicator; A new Measuring Instrument For Display of the Characteristics of Individual Injection," SAE 660749.
2. Bruni,G. and Fiore, A. Laforgia, D. and Fiorentino, L. (1995) "3-D Analysis of the Flow through a multihole V.C.O for D.I Diesel Engine," SAE 950085.
3. Dan, T., Lai, M.-C., Wang, T.-C., Xie, X., (1998) " Transient Characterization of High-Pressure Diesel Sprays", COMODIA 98
4. Dan, T., Takehiro Yamamoto, Jiro Senda, and Hajime Fujimoto, (1997) " Effect of Nozzle Configurations for Characteristics of Non-Reacting Diesel Fuel Spray," SAE paper 970355
5. Fath A., Munch K. U. and Leipertz A., (1997) "Spray Break-up Process of Diesel Fuel Investigated Close to the Nozzle", ICLASS - '97, p.513
6. Han J.S, Wang, T.C. Xie, X.B Lai, M.-C and Henein, N.A. "Dynamics of Multiple-Injection Fuel Sprays in a Small-bore HSDI Diesel Engine", SAE paper 2000-01-1256, 2000
7. Han, J.S. Wang, T.C and Lai, M.-C., "Common-Rail Diesel Fuel Injection System Dynamics and Spray Characterization," ILASS AMERICAS '99. pp. 201-205.
8. Harrington, D., and Lai, M.-C., (1998) "Characterization and Visualization of Hole-To-Hole Variation and Wall Impingement of Diesel Sprays," ILASS AMERICAS '98, pp. 106-110.
9. Hiroyasu, H., and Kadota, T., and Arai, M., "Development and Use of a Spray Combustion Modeling to Predict Diesel Engine Efficiency and Pollutant Emission", Bulletin of the

JSME. Vol 26, No. 214, April 1983.

10. Kato, T. ,Tsujimura, K., Shintani, M.,Minami, T. and Yamaguchi, I.,"Spray Characteristics and Combustion Improvement of D.I. Diesel Engine with High Pressure Fuel Injection", SAE Paper 890265,1989.

11 Kuo, T.W., "Evaluation of a Phenomenological Spray-Combustion Model for Two Open-Chamber Diesel Engines", SAE paper, Nov. 2-5, 872057, 1987.

12 Qin,J.R, Dan ,T. Lai, M.C (1999) "Correlating the Diesel   Spray Behavior to Nozzle Design," SAE 1999-01-3555.

13 Lai, M.-C., Wang, T.-C., Xie. X., Han, J., Henein, N. A., Schwarz, E., and Bryzik, W., (1998) "Microscopic characterization of Diesel Sprays at VCO Nozzle Exit" SAE 982542.

14 Pierpont,D.A.and.Reitz.R.D."Effects of Injection Pressure and Nozzle Geometry on D.I. Diesel Emissions and Performance",SAE Paper 950604,1995

15 Sjoberg, H., Manneberg. G.. Cronhjort, A., (1996) "Long-Working-Distance Microscope used for Diesel Injection Spray Imaging," Optical Engineering, Vol. 35(12) pp. 3591-3596.

16 Soteriou, C.,   Andrews, R.. and Smith, M.. "Direct Injection Diesel Sprays and the Effect of Cavitation and hydraulic Flip on Atomization", SAE Paper 950080, 1995.

17 Wang, T. C. Han, J.S. Xie, X.B. Lai, M.C, Henein N.A(1999) "Direct Visualization of High Pressure Diesel Spray and Engine Combustion." SAE 1999-01-3496.

Dynamics of Multiple-Injection Fuel Sprays in a Small-bore HSDI Diesel Engine

Joong-Sub Han, T.C. Wang, X.B Xie, Ming-Chia Lai and Naeim A. Henein
Wayne State University

David L. Harrington, John Pinson
General Motor Research & Development Center

Paul Miles
Sandia National Laboratories

ABSTRACT

An experimental study was conducted to characterize the dynamics and spray behavior of a wide range of minisac and Valve-Covered-Orifice (VCO) nozzles using a high-pressure diesel common-rail system. The measurements show that the resultant injection-rate is strongly dependent on common-rail pressure, nozzle hole diameter, and nozzle type. For split injection the dwell between injections strongly affects the second injection in regards to the needle lift profile and the injected fuel amount. The minisac nozzle can be used to achieve shorter pilot injections at lower common-rail pressures than the VCO nozzle.

Penetration photographs of spray development in a high pressure, optical spray chamber were obtained and analyzed for each test condition. Spray symmetry and spray structure were found to depend significantly on the nozzle type. The minisac class of diesel nozzle definitely exhibits superior characteristics regarding hole-to-hole spray symmetry, whereas the VCO class of diesel nozzles produce a more asymmetric, but more dispersed spray plume, with potentially better fuel-air mixing performance than the minisac nozzle. The dual-guided VCO class of nozzle does not significantly improve the spray symmetry over that of the single-guided nozzle. However measurement of spray tip penetration length shows that the dual-guided VCO nozzle provides higher spray-tip velocities than is achieved for single-guided tips. The results obtained show that the liquid spray tip penetration mainly depends on nozzle type, needle guiding strategy, injection pressure, and ambient gas pressure.

Close to nozzle exit spray dynamics observation was carried out. The microscopic visualization results provide very interesting and dynamic information on spray structure, showing spray angle variations, injection-to-injection variation, and primary breakup processes not observed using conventional macroscopic visualization techniques. The near-field spray behavior is shown to be highly transient, strongly depend on the injector design, nozzle geometry, needle lift and vibration, and injection pressure which is a function of the injection system.

INTRODUCTION

Because of the associated high thermal efficiency and reduced CO_2 emissions, the small-bore, high-speed, direct-injection (HSDI) diesel engine is achieving an extended application in worldwide passenger car markets. It is also a major candidate for the power plant of the partnership-for-new-generation vehicle (PNGV). Increasing the injection pressure and optimizing the injection-rate profile have been focused technologies in the development-advanced diesel engines. For small bore diesel engines the combination of high rail pressure and an injection nozzle tip having small holes and low sac volume is critical to achieving successful fuel-air mixing in the HSDI combustion chamber. The high-pressure common-rail (HPCR) injection system, with its independent pressure control and electronic injection-rate shaping capabilities, is an important enabling technology for the HSDI engine. Although diesel fuel sprays have been studied extensively over many decades, the combined effect of nozzle geometry, needle design and multiple injection events on the spray dynamics of HPCR systems is largely unknown. The objectives of this study are to characterize the dynamics and spray behavior of the high-pressure diesel common-rail (HPCR) systems, and to compare the spray characteristics of minisac, single-guided VCO and dual-guided VCO nozzles. The experimental data includes needle lift, injection pressure, injection-rate, spray plume images and liquid spray tip penetration.

showed the effects of injection pressure and ambient pressure on the spray resulting from multiple injections. However a detailed parametric study is required to provide definitive guidelines for HSDI engine designer

The VCO spray structure and its asymmetry were investigated by Lai et al. [9] using a long-working-distance microscope and laser sheet illumination. It was shown that the near-field spray behavior strongly depends on the nozzle geometry, needle lift and vibration, and the injection pressure.

EXPERIMENTAL SETUP

1) Injection-Rate Measurement

Experimental apparatus consists of high-pressure electronically-controlled common-rail (HPCR) fuel injection systems, an injection-rate meter (IAV model – Bosch type [1]) and an electronic weight balance to analyze the injection-rates and total injection quantity. Figure 1 shows the schematic of the test facility. The common-rail injection system utilized was capable of providing an injection pressure of up to 1350 bar; however, a maximum of 1200 bar was used for injection-rate measurement to ensure rail pressure stability. An electronically-controlled injector having a two-way valve was used. As the needle lifts, a proximity sensor registers the needle shaft stem expansion and needle lift. Details of the design of the diesel common-rail injection system are discussed by Renner et al [10], Boner et al [2] and Hoffmann et al [6]. The experimental sequencing and data acquisition are under PC control using LabVIEW software. The injection quantity for each nozzle was varied by a combination of a common-rail pressure and the pulse width duration.
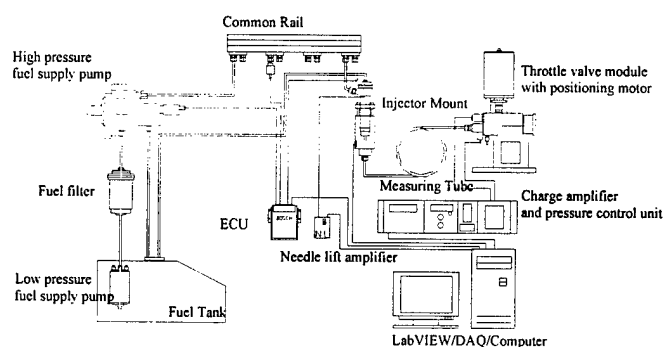

Figure 1. Fuel Injection-rate Measurement Setup

2) Spray Penetration Visualization

The diesel fuel spray pattern and penetration was investigated using an optical spray chamber pressurized by nitrogen. For the spray visualization, a short-duration stroboscope and copper-vapor laser system (Oxford CU15) served as the light source. The spray images were photographed using a 35mm still camera and a high-speed drum camera, and a waveform analyzer was used to capture the needle lift signal. The injection pressure, injection duration and ambient pressure are varied in the experiment. Because orifice and nozzle geometry significantly affects

the spray, a significant range of designs and nozzle geometries were tested. Table 1 summarizes the test matrix for the experiment.
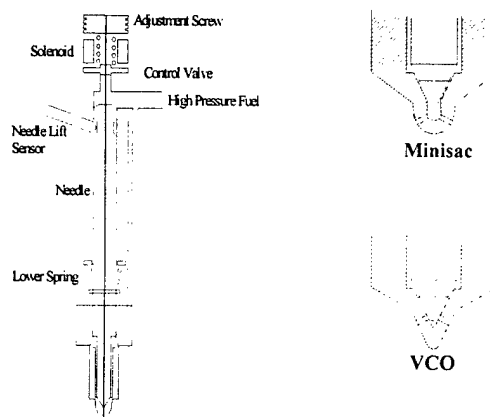

Figure 2. Configuration of Tested Unit Injector and Nozzles

Injector type	Prototype No1.	Prototype No2.
Nozzle type	Minisac	VCO
Guide type	Single Guide	Single Guide, Dual guide
Hole to hole bending angle	Minisac 140, 145, 150 deg.	VCO 145 deg.
Hole number	Minisac 5,6,7	VCO 6
Hole diameter (mm)	0.147 (390 *) 0.158 (430) 0.164 (470)	0.162 (390) 0.171 (430) 0.180 (470)
Injection Pressure (bar)	From 250 to1350	
Tip	Optimized & normal needle seat, Coated & Non-coated needle-guidance	
Injection duration (ms)	Varied with & without pilot injection	
Ambient N2 pressure (bar)	From 0 to 27	

Table 1. Summary of Nozzle Geometry and Test Conditions

3) Close to Nozzle Exit Spray Dynamics Observation

The optical system setup includes a long-distance microscope, a copper-vapor laser (Oxford CU15), and a high-speed drum camera. The copper laser is expanded into a thin sheet with thickness less than 0.09mm using cylindrical lens. It is used as the optical shutter, operating at 25-kHz with exposure time as short as 10 ns. The drum camera is operating at 250 revolution-per-second with 0.16 -second shutter speed. The long-distance microscope is used to magnify the diesel spray structure very close to the

---

* The number denotes flow number (FN), representing volume flow rate in cubic centimeters for 30 seconds of continuous injection under 100 bar injection pressure.

nozzle exit. With its lens 8.75 inches away from the observed object, the amplification factor is about 17.4. The diffraction-limit resolution can be as small as 1-2 micron.

RESULTS AND DISCUSSIONS

1. Injection-Rate Measurement

The injection-rate is defined as the instantaneous rate of fuel mass exiting from the nozzle tip. In order to control the COV of IMEP, the injection-rate, injection pressure and injection duration must be repeatable. Figure 3 shows the measured 50-injection variability at a common-rail pressure of 1200 bar, with a 54.88mg average injected quantity. The injection variation for a typical HPCR system was found to be +/-2 %(Maximum injected fuel amount was 55.99 mg and minimum injected fuel amount was 53.92mg).

50-shot cycle variability at 1200bar
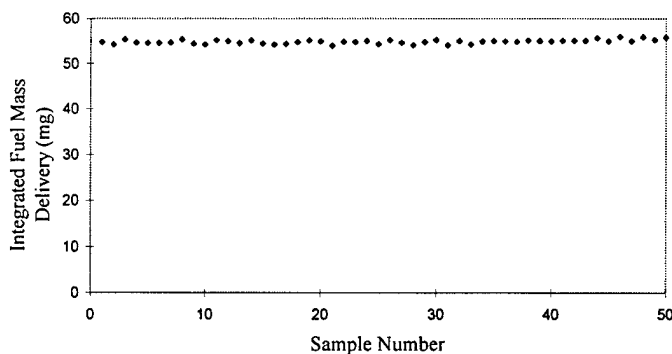54.88mg Average Injection

Figure 3. 50 Shot Cycle Variability of the Injector

(a) Effect of Back Pressure on the Injection-rate Measurement

The chamber pressure of the injection-rate meter before the start of injection is defined as the backpressure. The effect of backpressure and cavitation on the injection-rate measurement accuracy must be determined before measurements are conducted. The injection-rate was first measured by changing the backpressure in the range from 11 bar (162psi) to 37.5bar (550psi) with injection pressures ranging from 300 bar to 1200 bar. Tests with an injection duration of 2.0 ms (without a pilot injection) and 1.2/1.0/2.0 ms (with a pilot injection) indicate that the injection-rate displays the same wave form for a range of back pressures from 27 bar to 37.5 bar. At a lower range of backpressure a fluctuating waveform due to cavitation can be observed immediately after the start of injection. In order to achieve precision injection-rate measurements, the backpressure for this study was maintained at 27 bar.

(b) Effect of Common-rail Pressure & Nozzle Hole Diameter

The injection-rate is a strong function of the common-rail pressure. The injected fuel quantity is found to be nearly proportional to the square root of the sac pressure, which closely tracks the injection pressure, and the effective opening area. The rise in injection-rate for a

higher common-rail pressure is clearly shown in Figure 4. The data were obtained for a 6-hole (0.18mm diameter)-dual guided VCO nozzle. The injection pressure was varied from 300 bar to 1200bar. For 1200 bar, the initial rise rate is the highest, and the start of injection is also earlier than for the lower common-rail pressure cases.
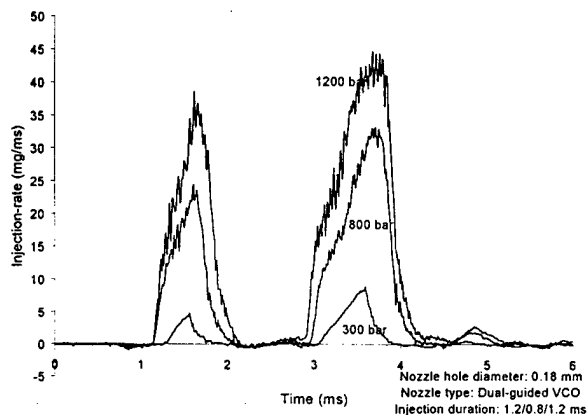

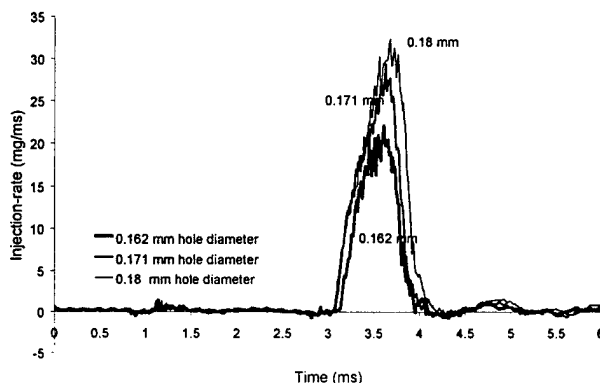Figure 4. Comparison of Initial Injection-rates

Figure 5. Effect of Nozzle Hole Size on Measured Injection-rate

The effect of the nozzle hole diameter on the injection-rate also was investigated. Figure 5 shows the injection-rate for a dual-guided VCO nozzle for hole diameters from 0.162 to 0.18mm. Under a constant 800-bar injection pressure, the injection-rate was found to increase as shown with increasing hole size.

(c) Maximum Needle Valve Lift

Due to working principle of the common-rail system, the needle lift time of common-rail injector is much longer and is strongly affected by the injection pressure. For three different common-rail pressures, the maximum needle lift was found to be different for each case. The location of the hall effect needle lift sensor may perhaps explain why the indicated maximum lift is different. Because the location of the lift sensor is at the top of the injector, which is quite far from the needle seat, there is a significant extension of the long needle before any actual opening of the nozzle.

The relationship of the needle lift and injection command signal without pilot injection is illustrated in Figure 6. As the common-rail pressure is increased, the delay time from injection command to maximum needle lift becomes shorter. For maximum needle lift, the measured

delay time is 2.3ms, 1.88 ms, 1.77 ms respectively for 300-bar, 800-bar, 1200-bar injection pressure.

These results explain why a rapid increase in the initial injection rate is possible with a higher common-rail pressure. The anomalous hump observed in lift-time curves during the opening periods is mostly likely a result of needle compression and the distant location of the needle lift sensor. The actual time for the spray to exit the nozzle as determined by spray visualizations corresponds very closely with the injection-rate measurement

The relationship between the common-rail pressure and the needle lift under pilot injection condition is shown in Figure 7. The injection duration was 1.2 / 1.2 /2.0 ms with the same 0.18mm hole diameter VCO nozzle. The dynamic characteristics of the needle-closing event are similar for all of the tested pressures; however, for the lowest rail pressure (300bar) a slightly faster needle valve closing was detected.

Figure 8, Figure 9 and Figure 10 show the injection rate and needle lift for the No 2-prototype injector with various injection duration's and pressures. Due to the design and working principle, the injector is operating in partial needle lift condition regularly, especially for injection with short duration and low pressure. This result was well matched with spray penetration result, which will be shown at Figure 25.
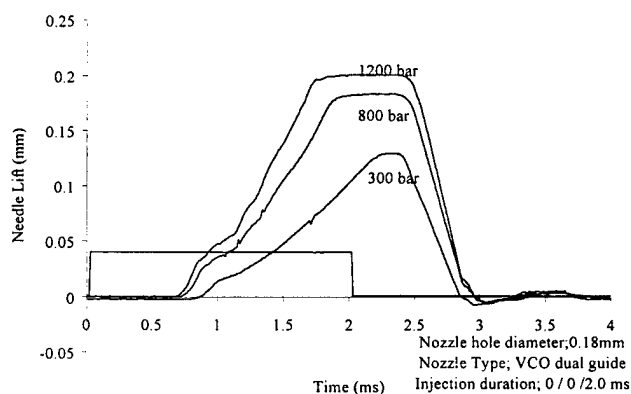

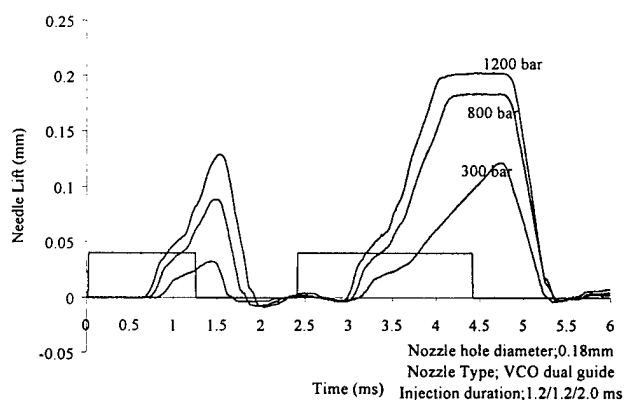Figure 6. Maximum Needle Lift without Pilot Injection

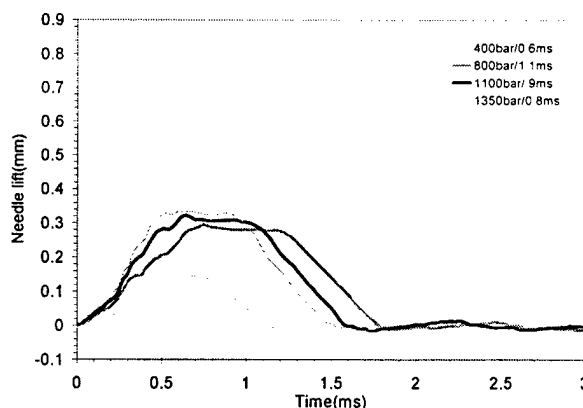Figure 7. Maximum Needle Lift with Pilot Injection

Figure 8. Effect of Common-rail Pressure on Needle Lift of the Common-rail System, with 0.33-mm Maximum Needle Lift, and 390 FN VCO Nozzle (6 holes, 0.162-mm hole diameter, single-guide, and 6.173 L/D ratio)
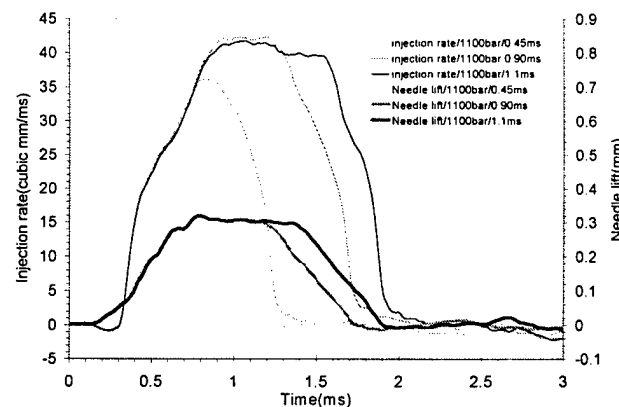

Figure 9. Injection-rate and Needle Lift of the Common-rail System under Conditions of Different Injection Duration with Common-rail Pressure of 1100 bar and 390 FN VCO nozzle
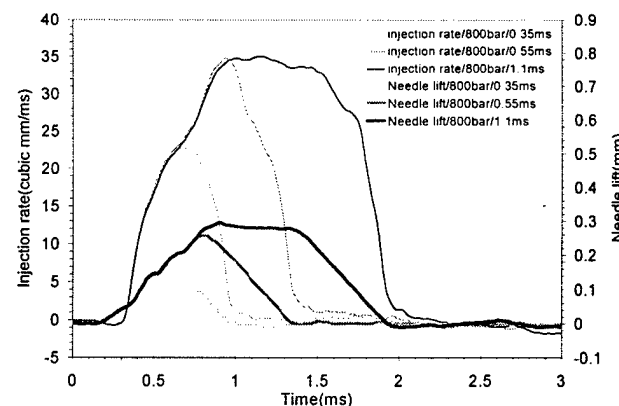

Figure 10. Injection-rate and Needle Lift of Common-rail System under Conditions of Different injection Duration, with Common-rail Pressure of 800 bar and 390 FN VCO Nozzle

(d) Injection-Rate Comparison for Minisac and VCO Nozzles

Figure 11 through 14 show the needle lift and injection-rate data for two types of nozzles; a 390-FN VCO

No

nozzle and a 390-FN minisac nozzle, having 0.162mm (L/D=6.173) and 0.147mm hole-diameter (L/D=4.082), respectively. The discharge coefficients (Cd) were 0.48 and 0.58 for the VCO nozzle and the minisac nozzle respectively. These values were computed from the flow number definition. The energy losses due to the flow turning angle at the orifice inlet could explain why the VCO nozzle has the lower discharge coefficient. Figures 11 and 12 show the injection-rate comparison with 1.2/1.2/1.5 ms pilot injection timing at a lower rail pressure of 300bar. The VCO nozzle was found to exhibit a shows smaller pilot injection in terms of needle lift and injection-rate.
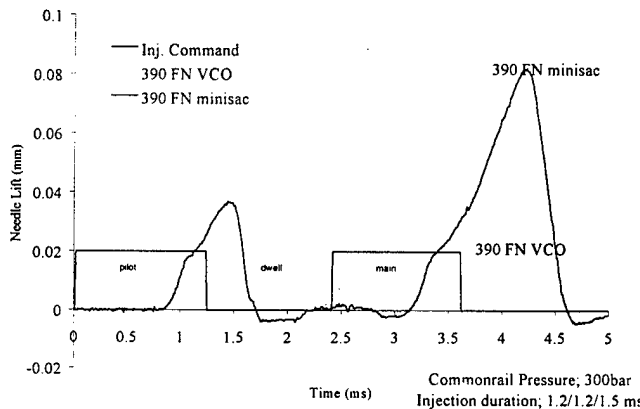

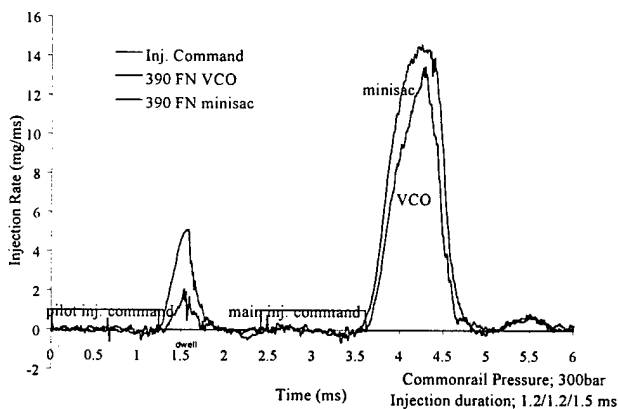Figure 11. Minisac and VCO Nozzle Comparison- Needle Lift

Figure 12. Minisac and VCO Nozzle Comparison – Injection-rate

In general, the minisac nozzle can be used at a lower rail pressure and shorter pilot injection duration than the VCO nozzle. Due to higher discharge coefficients, the minisac nozzle tip delivers more fuel quantity at the shorter pilot injection duration. Examples of this are shown in Figures 13 and 14. Even though both needle lifts are identical, the injected fuel amount is different for a pilot injection in Figure 14, in which the injection pressure was 800 bar and the commanded injection duration sequence was 1.2/1.2/2.0ms

Figure 15 plots the instantaneous discharge coefficient history. The discharge coefficient is computed from the upstream pressure measured at the injector inlet, and the injection-rate measurements. While static discharge coefficients were 0.58 and 0.48 for the minisac and VCO nozzles respectively, Figure 15 shows that the maximum discharge coefficient of the minisac is nearly 0.7 while the

VCO nozzle is nearly 0.6. This is consistent with the fact that the flow resistance is considerably larger for the VCO nozzle (Qin et al. [8]).
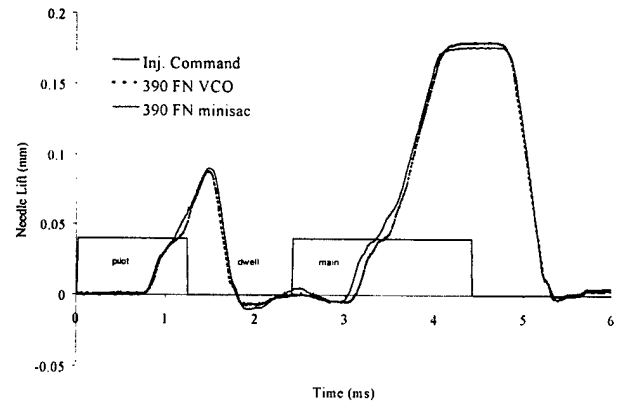

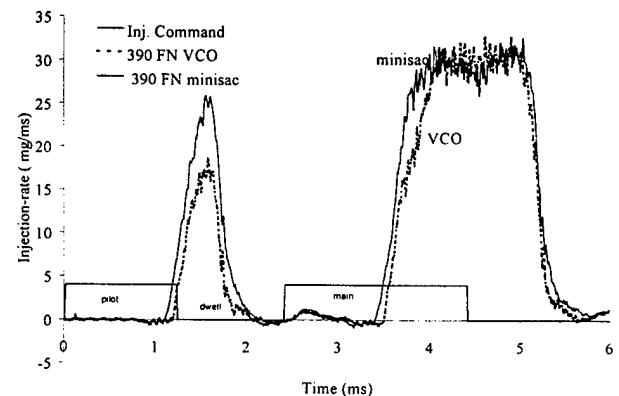Figure 13. Minisac and VCO Nozzle Comparison Fully Opened Needle Case –Needle Lift

Figure 14. Minisac and VCO Nozzle Comparison Fully Opened Needle Case –Injection-rate
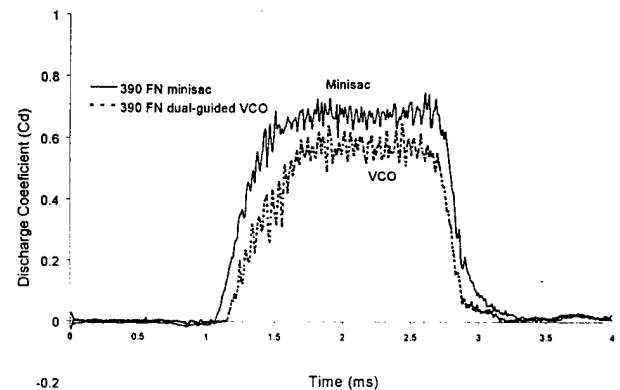

Figure 15. Discharge Coefficient Comparison - Minisac & VCO nozzle

(e) Pilot Injection

Due to the interaction of injection line hydraulics and the injector dynamics, the pilot injection and dwell duration between injections could significantly affect the needle lift and delivered fuel quantity of the secondary injection. Figure 16 shows a pilot separation sweep of needle lift for a 300-bar common-rail pressure. For this sweep the injection duration for the main injection is maintained at 0.8 ms and the pilot injection duration is maintained at 0.7 ms, but the dwell period was changed from 0.2ms to 1.0ms.

The same pilot injection duration produces an unchanging pilot needle lift. However, the needle lift for the main injection changes as the dwell period is increased. Until 0.8ms dwell period, the needle lift amount decreases as the dwell decreases. But for a dwell period of less than 0.8ms, the needle lift amount increased again. The variation of the total injection-rate amount is shown in Figure 18 to be as large as 100 percentage over the separation sweep. The integrated injection-rate from injection-rate trace is very close to the mass measured using the electronic weight balance. The corresponding injection-rate is shown in Figure 17.

The measured characteristics of the needle lift with a change in dwell period were the same for No2-prototype injector. Figure 19 shows the result of a pilot separation sweep of needle lift for No2-prototype injector. This unit exhibits a slightly improved consistency, but still shows variations

A pilot separation sweep with a fully open needle condition for the main injection is shown in Figures 20 and 21. The pilot injection duration is 1.2 ms and the main injection duration is 2.0 ms for an injection pressure of 800 bar. A minisac and a VCO nozzle, both with 430 flow-numbers are used. As illustrated in Figure 22, the minisac and VCO nozzles show the same tendency regarding variations in the injected fuel quantity.
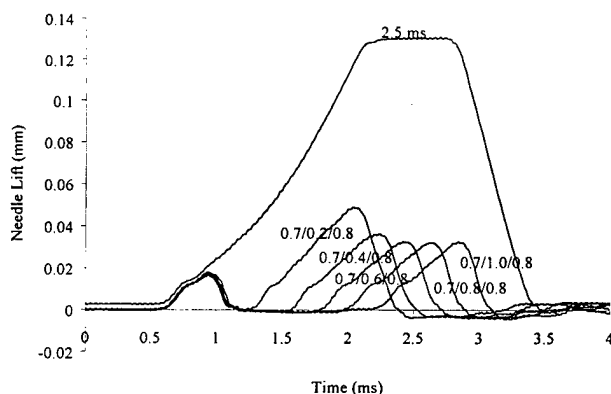

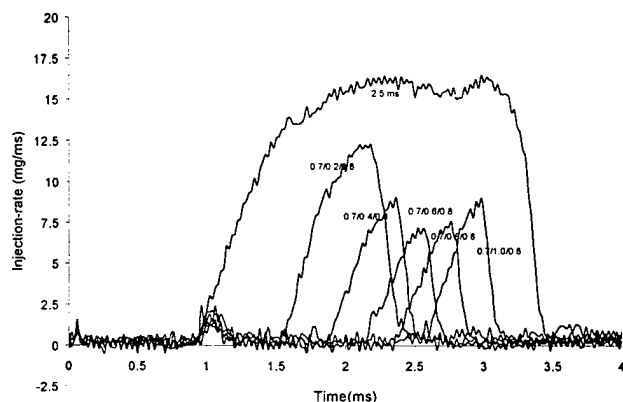Figure 16. Pilot Separation Sweep – Needle Lift (300 bar)

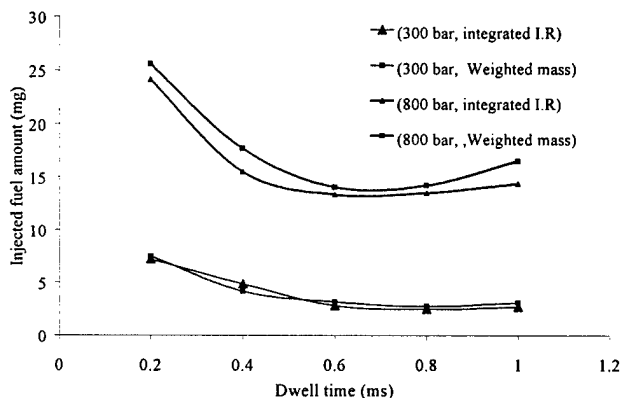Figure 17. Pilot Separation Sweep – Injection-rate at 300 bar for 430 FN minisac

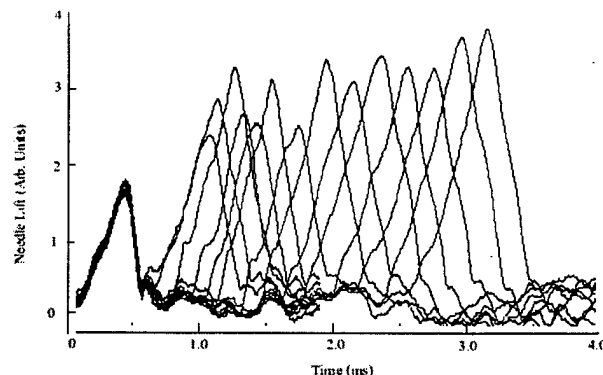Figure 18. Injected fuel Amount Variation (300 & 800 bar, 430 FN minisac)

Figure 19. Injector Separation Sweep Plot – Needle Lift of No 2- Prototype Injector at 400 bar Common-rail Pressure
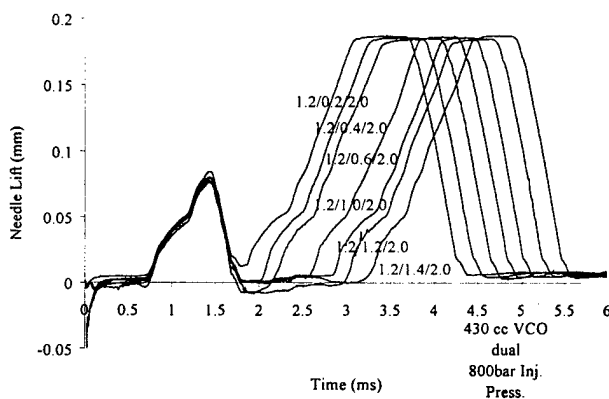

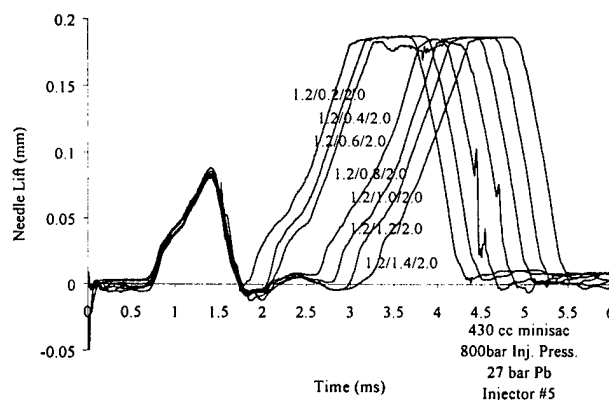Figure 20. Pilot Separation Sweep – Needle Lift (VCO)

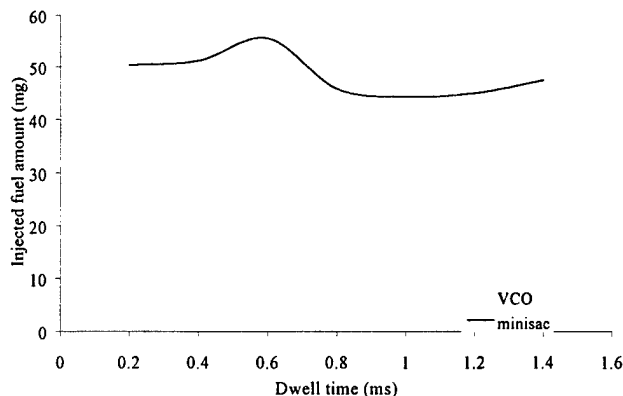Figure 21. Pilot Separation Sweep – Needle Lift (minisac)

Figure 22. Injected fuel Amount Variation
- Minisac & VCO nozzle

2. Spray Penetration Visualization

In the study of spray penetration visualization, the spray visualization was carried out by injecting fuel into a room-temperature nitrogen-filled pressurized chamber .The chamber pressure was adjusted to simulate the air density at the end of compression stroke of Compression Ignition engine. In a real engine operating condition, fuel is injected to combustion chamber at the timing closed to end of a compression stroke. Hence, it is reasonable to assume that the fuel sprays issued into the pressurized chamber encounters similar drag force as it did in a real engine. Since the chamber is filled up with room temperature nitrogen gas, the fuel sprays will mostly be in the form of liquid droplets and can be treated as non-evaporative sprays.

The characterization items carried out in this study include penetration, overall structure, and hole-to-hole variation. This method could be used to measure the performance of nozzle tip, injection unit, or injection system in terms of their capability of distributing fuel as far as temporal and spatial concerns. Although under same ambient density condition both the penetration and dispersion of a evaporative spray could be much less than those of a non-evaporative one, the characteristics obtained from a non-evaporative test condition still provides good indication of the performance of a fuel injection.

(a) Spray Symmetry

The symmetry of the fuel spray was found to vary significantly with the nozzle type. The spray development for a minisac nozzle and a VCO nozzle are illustrated in Figure 24 and Figure 31. The VCO spray penetration exhibits a very asymmetric spray plume. These spray asymmetric images for the VCO nozzle tip validates the needle lift eccentricity. Furthermore, the dual-guided VCO nozzles were also not free from needle lift eccentricity (Figure 33). These data are obtained for an identical injection pressure of 800 bar and ambient pressure of 13.5 bar.

(b) Spray Structure

The VCO nozzle shows significant puffy spray structure, larger spray angle, better spray spread and potentially better fuel-air mixing. Lai et al. [9] reported the spray angle oscillation of VCO nozzle, which results in a puffy spray structure. It was shown that the near -field spray behavior strongly depends on the nozzle geometry, needle lift and vibration. The minisac nozzle shows a thinner spray angle and a better symmetric spray penetration. This tendency is affected by the hole's inlet curvature from the seat region to the hole region. Figure 32 shows the comparison between minisac and VCO nozzle liquid spray tip penetration.

(c) Hole-to-Hole Spray Variation and Spray Structure

Significant hole-to-hole variation in penetration of the sprays of the VCO nozzle was observed, especially at the early stage of spray development, as shown in Figure 23. For this test No 2-prototype injector was used. As shown in Figure 26, with 300 bar injection pressure, the 2- and 5-o'clock sprays do not appear for the whole injection period. Based on the results obtained from the needle lift measurements, as shown in Figure 8, with 300 bar injection pressure, the needle just barely opens with little needle lift and injection rate; under this circumstance four holes are open, however the other two holes, 2- and 5-o'clock holes, remain covered by the needle. This is an evidence of needle eccentricity. As injection pressure increases to 800 bar, the injection rate and needle lift increase accordingly. The 5-o'clock hole starts to issue injection after a 0.16-ms lag time. The fastest spray is locating on the opposite side of the slowest spray. Therefore, it would be reasonable to conclude that the needle-to-seat eccentricity is most severe upon the 5 o'clock nozzle hole, which consequently reduces the flow area of the corresponding hole at the early stage of spray development. Puffy structure is observed on the 2-, 6-, 8- and 12-o'clock sprays. The puffy structure at the early development of these sprays may be categorized as hollow cone spray with characteristics of wide angle as the type of that spray Soteriou et al.[15] identified in their study . As shown in Figure 26, these early-developed sprays with puffy structure are surpassed and penetrated by the later coming solid cone sprays after 0.24 to 0.32 ms from start of injection.
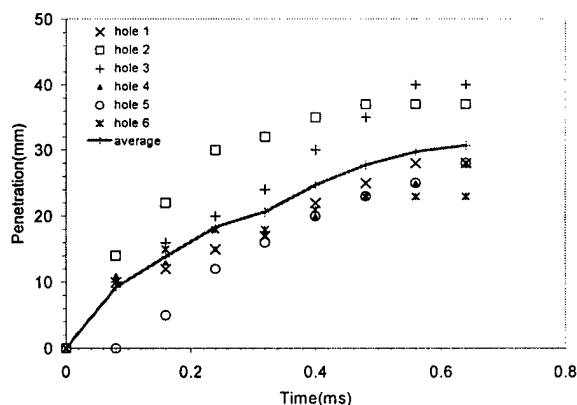

Figure 23 Hole-to-Hole Penetration Variation of the Common-rail Sprays, with Single-guide 390 FN VCO Nozzle, Common-rail Pressure of 800 bar, Duration of 0.3 ms, and Ambient Pressure of 17.2 bar.

Figure. 24 Comparison of Fuel Spray Development
for Minisac and VCO Nozzles.

Nozzle Flow Number = 390
P_{inj}=800 bar,
P_{ch}=13.5 bar
t_{inj}=1ms.

Left : Minisac
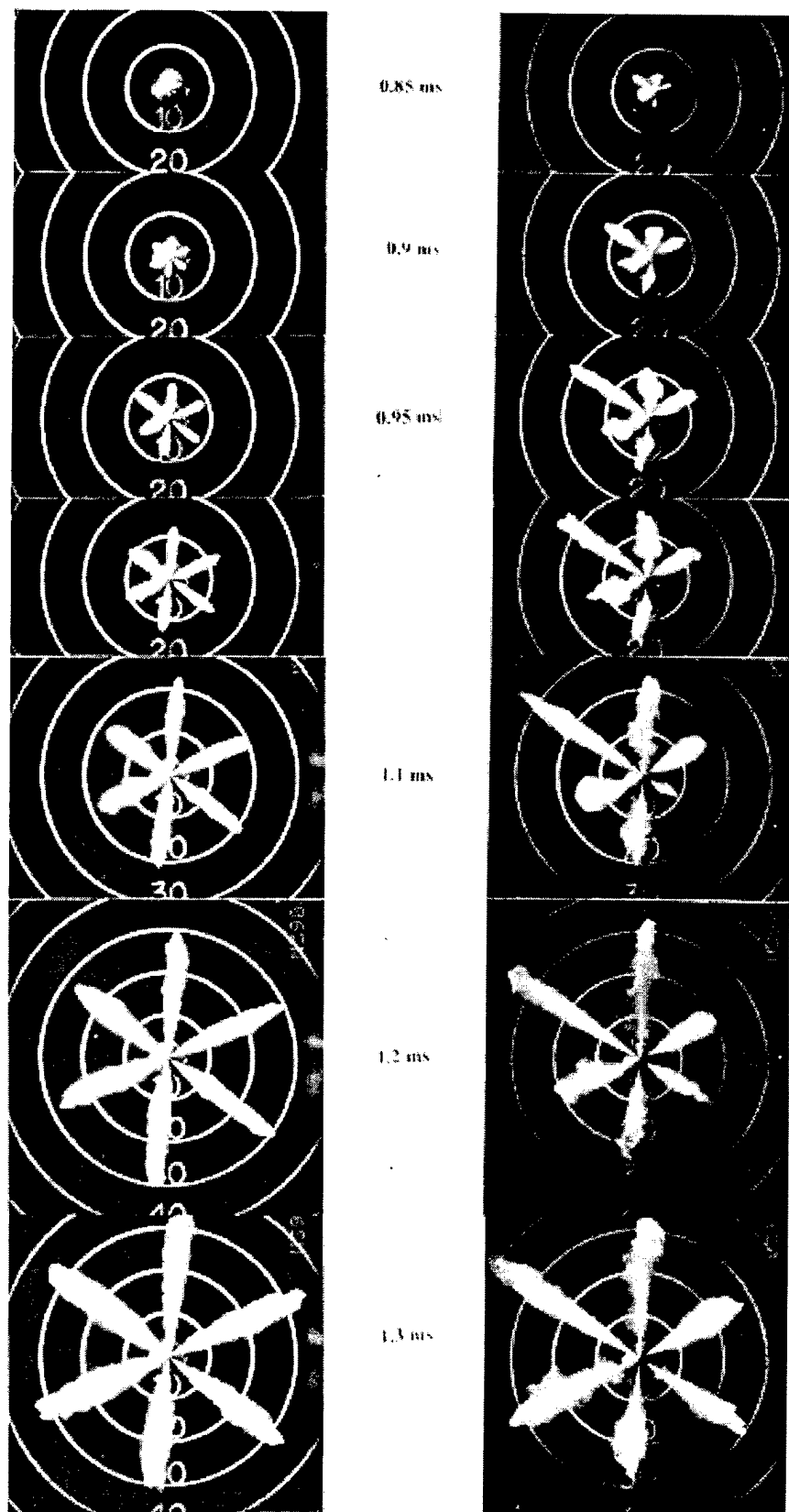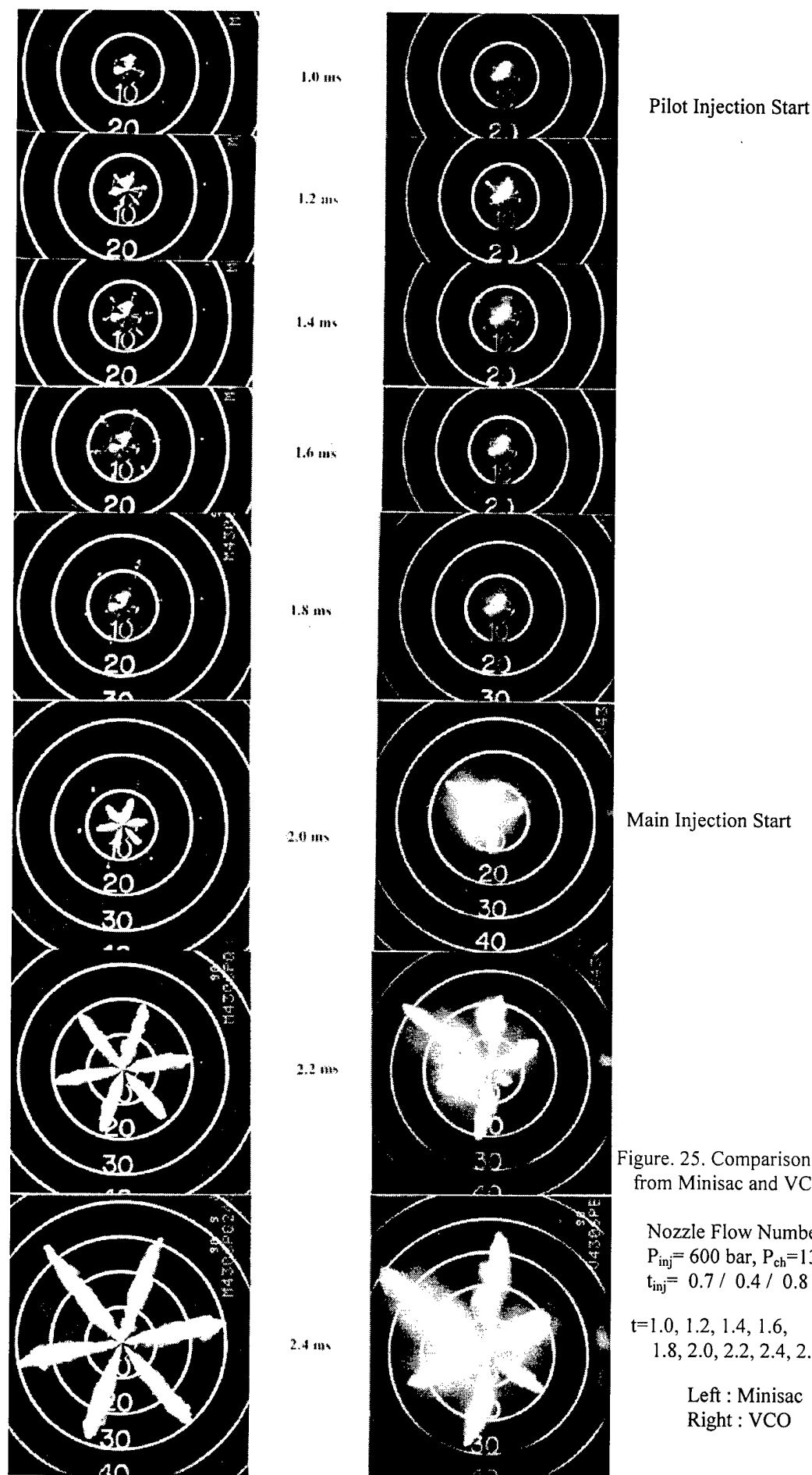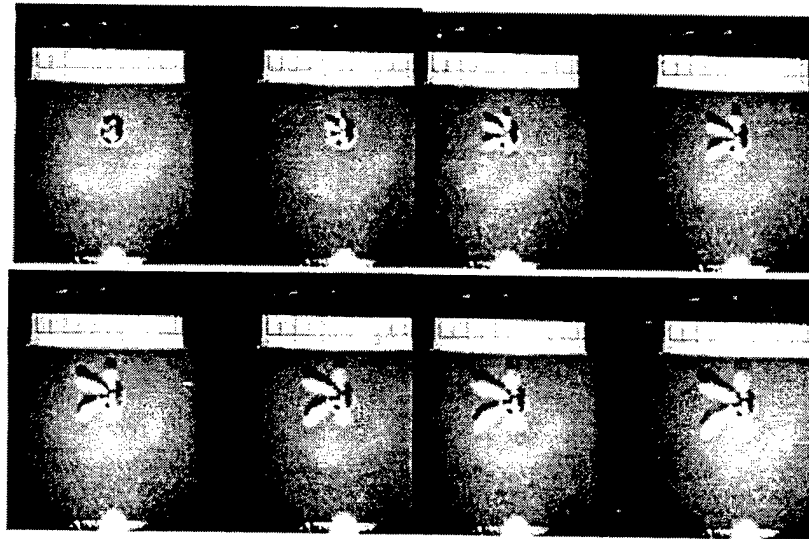Right : VCO

Pilot Injection Start

Main Injection Start

Figure. 25. Comparison of Fuel Spray Development
from Minisac and VCO Nozzles.

Nozzle Flow Number = 430
P_{inj}= 600 bar, P_{ch}=13.5 bar,
t_{inj}= 0.7 / 0.4 / 0.8 ms.

t=1.0, 1.2, 1.4, 1.6,
1.8, 2.0, 2.2, 2.4, 2.6ms.

Left : Minisac
Right : VCO

300 bar Common-rail Pressure
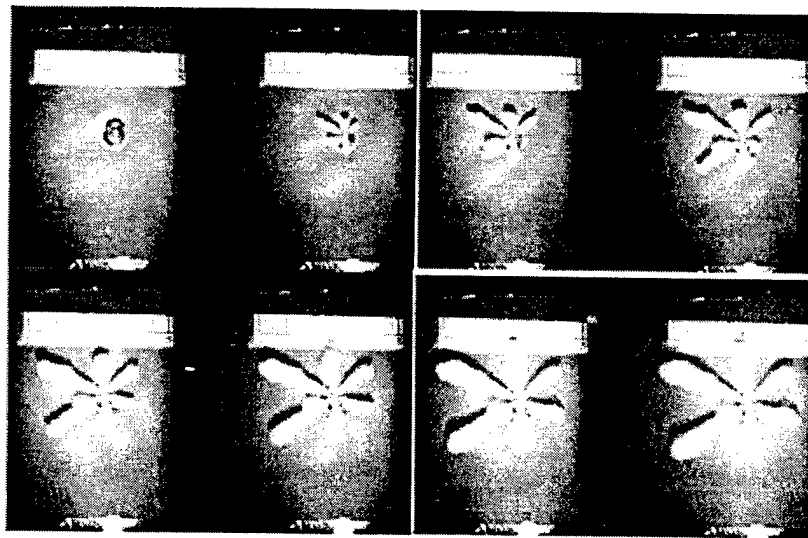
800 bar Common-rail Pressure

1350 bar Common-rail Pressure

Figure 26 Sequences of Development of the Common-rail
Sprays with Single-guide 390 FN VCO Nozzle,
Duration of 0.3 ms, Ambient Pressure of 27.6 bar;

Interval of 0.08-ms between Each Frame
Upper rows for Common-rail Pressure of 300 bar;
Center rows for Common-rail Pressure of 800 bar;
Bottom rows for Common-rail Pressure of 1350 bar;

(d) Spray Penetration

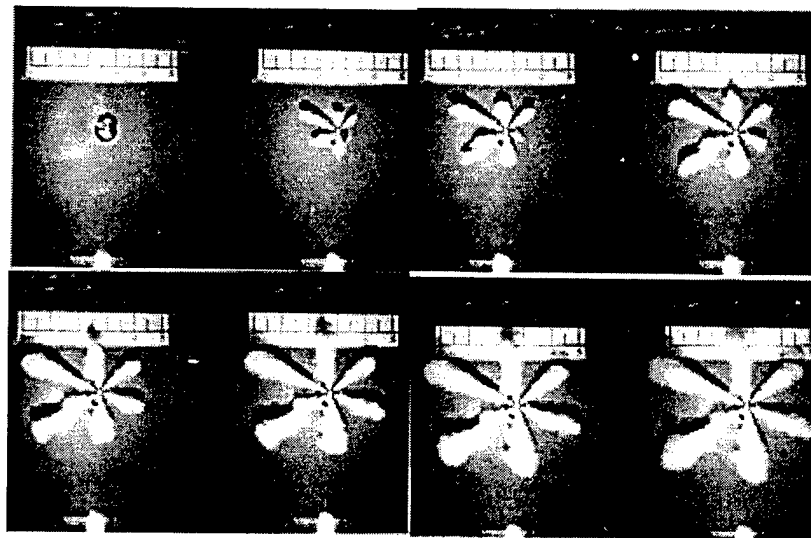Figure 25 shows spray tip penetration employing a pilot injection. The pilot injected spray stays at a certain length and does not penetrate any more to the axial direction but starts to evaporate to the radial direction. Following main injection takes over the pilot injection.

In this split injection mode, the main (second) injection penetrates more rapidly than the pilot (first) injection, and quickly overtakes the earlier pilot spray and passes through it. This can be explained by the lower amount of needle valve opening for the pilot injection. This gives an increased pressure loss across the seat opening. Therefore the pilot penetration data shows slower penetration (Figure 27)
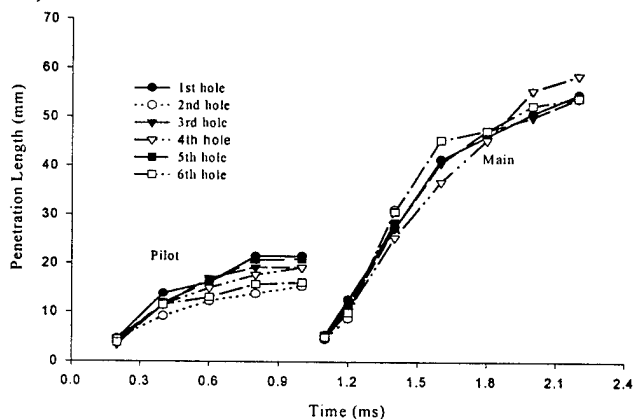

Figure 27. Spray Penetration with Pilot

(e) Spray Penetration and Correlation with Empirical Model

Figure 28, Figure 29, and Figure 30 summarize the correlation between the measured and calculated penetration under various injection and ambient pressures. The calculated penetration is based on empirical model proposed by Hiroyasu et al.[13]. Input data for the calculation include nozzle specifications, injection quantity, injection rate, density of ambient gas, and density of fuel. Value of 0.8 is used as the Coefficient of Spray Contraction for the calculation of average injection velocity, which is carried over from the study of Kuo [14]. To best fit with the measured data, 0.8 has been chosen as the values of Coefficient of Effective Injection Velocity for the calculation of penetration. In general, the model correlate fairly well with the measured data. However, the model tends to over predict the early phase of the penetration and under predict that of the later phase. The calculated penetration of CR sprays with injection pressure of 300 bar is far less than the measured data, which may indicate that the model does not apply to injection with low needle lift and low injection rate.

Orifice geometric parameters such as needle angle, L/D, curvature edge sharpness, and discharge coefficient significantly affect the rate of spray tip penetration. To investigate a needle type effect and a discharge coefficient effect, minisac and single-guided, dual-guided VCO nozzles are investigated by differentiating the injection pressure and the chamber pressure.
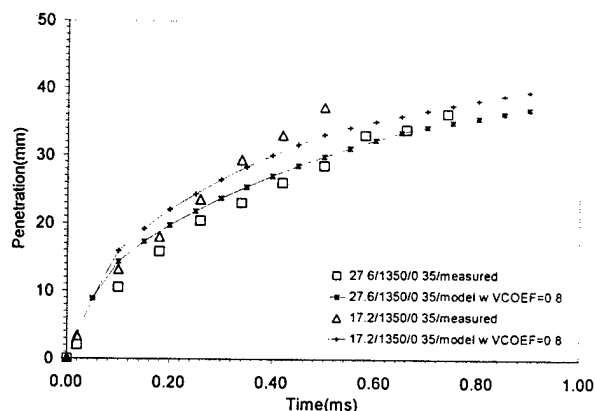

Figure 28 Correlation between the Measured and Modeled Penetration of the Common-rail System, with Pressure of 1350 bar, Duration 0f 0.35 ms, 390 FN VCO Nozzle, and Ambient Pressures of 17.2 and 27.6 bar.
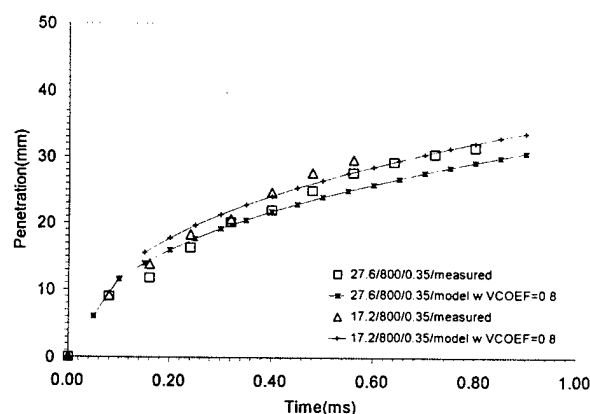
Figure 29 Correlation of Measured and Modeled Penetration of the Common-rail System, with Pressure of 800 bar, Duration of 0.35 ms, 390 FN VCO Nozzle, and Ambient Pressures of 17.2 and 27.6 bar.
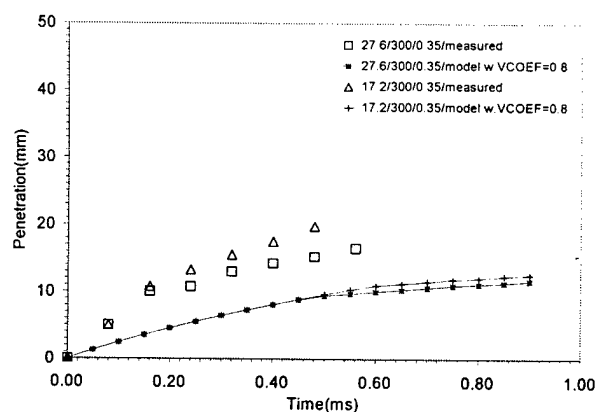
Figure 30 Correlation of Measured and Modeled Penetration of the Common-rail System, with Pressure of 300 bar, Duration of 0.35 ms, 390 FN VCO Nozzle, and Ambient Pressures of 17.2 and 27.6 bar.

(f) Penetration Comparison of Minisac & VCO

The minisac nozzle design is found to provide a fairly uniform spray penetration among the various holes, but the VCO nozzle generally provides asymmetric spray penetration. The VCO nozzle's large variation could be caused by eccentricity of the VCO nozzle inside and exaggerated by the low needle lift under low injection

pressure operating condition. This is clearly illustrated in Figure 31.
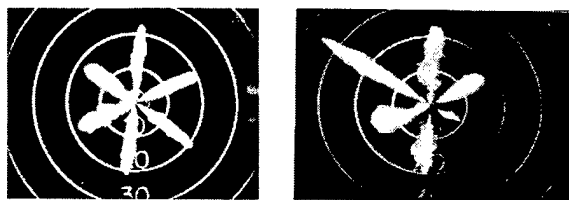
Figure 31. Minisac (left) and VCO (right) Nozzle Spray Image. (Both images were taken 0.3ms after injection start)
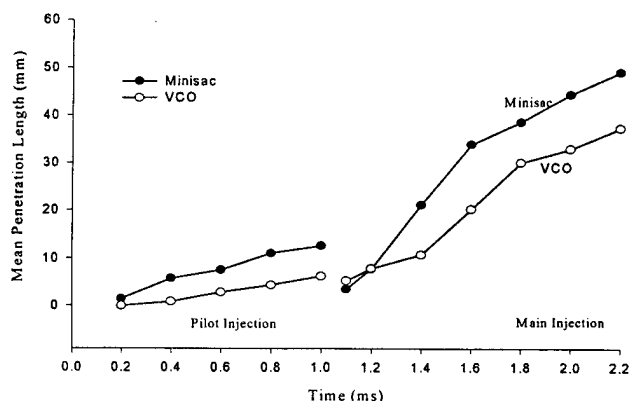
Figure 32. Penetration Comparison of Minisac & VCO Nozzles

Figure 32 shows a direct comparison of the mean minisac and VCO nozzle tip penetration for both 390 FN nozzles with pilot injection. This shows that the minisac nozzle has a higher rate of penetration for the same injection conditions. This tendency is possibly due to the higher discharge coefficient of the minisac nozzle.

(g) Effect of Single and Dual guide to penetration

The dual-guided VCO nozzle did not significantly improve the poor spray asymmetry of the single-guided VCO nozzle. This tendency is observed both with and without pilot injection. As illustrated in Figure 34, the measurement of the spray penetration length shows that the dual-guided VCO nozzle provides a faster spray tip penetration. (Figure 33, 34)
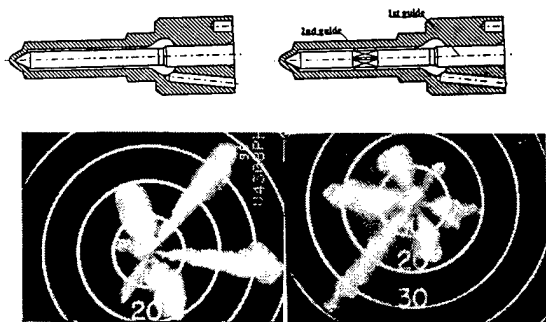
Single guide VCO   Dual guide VCO

Figure 33. Different Nozzle Guide Type and its Spray Pattern

(h) Effect of Common-rail Pressure to Penetration

Injection pressure is a key parameter in controlling the spray penetration. Figure 35 and 37 show that a higher common-rail pressure results in a more rapid spray tip penetration. For Figure 35 test data were obtained for common-rail pressures of 600 bar, 800 bar, and 1200 bar for the VCO nozzle. The chamber pressure was maintained at 13.5 bar.

Figure 34. Different Nozzle Guide Type Spray Tip Penetration Comparison

Figure 35. Effect of Common-rail Pressure to Penetration

Figure 36. Effect of Ambient Gas Pressure to Penetration

Figure 37 Effect of Injection Pressure and Ambient
Pressure on the Spray Penetration of the Common-rail
System, with Duration of 0.35 ms, Ambient Pressures of
17.2 and 27.6 bar, and Injection Pressures of 300, 800,
and 1350 bar
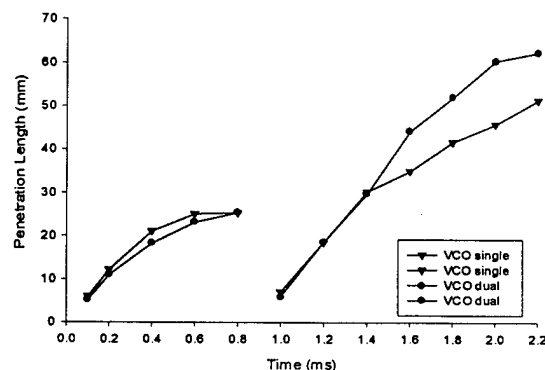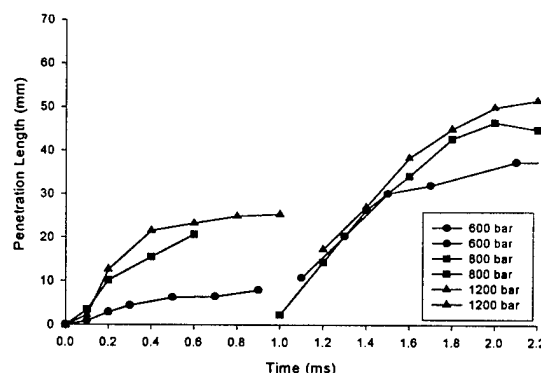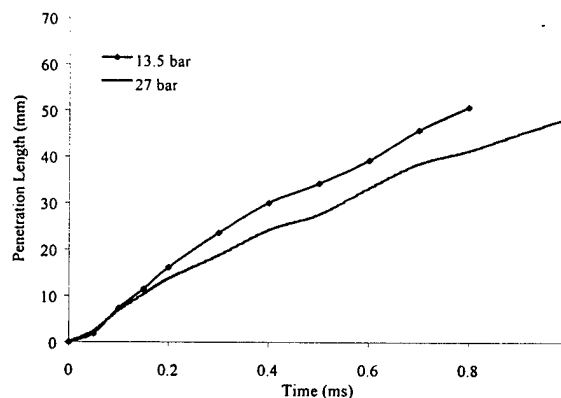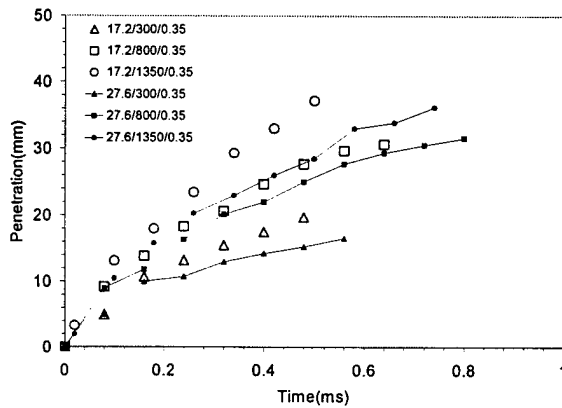
(i) Effect of Ambient Gas Pressure on Penetration

Independent of the injection pressure, the spray tip
penetration speed is reduced, as the ambient density is
increased (Figure 36 & Figure 37). The increased droplet
drag that is associated with higher gas density yields
reduced penetration rates for both pilot and main sprays.
The ambient nitrogen gas was pressurized to 17 bar, and to
27 bar with the temperature at 20 oC

3. Close to Nozzle Exit Spray Dynamics Observation

Recent implementation of laser diagnostics has
been shown to provide insight into the diesel spray
processes. The motivation of this study is to visualize the
spray structure of advanced diesel injection systems very
close to the nozzle exit in an attempt to correlate the
microscopic spray structure to the injection system
performance and nozzle design. In the microscopic
observation, the spray visualization was carried out by
injecting fuel into atmosphere ambient condition or a room-
temperature nitrogen-filled pressurized chamber.

(a) Spray Cone Angle and its Oscillation

Figure 38 shows a typical microscopic spray
visualization results. The result shows rapid temporal
variation of spray angle, which result into the puffy spray
structure at the edge of the spray as observed in the
macroscopic visualization in Figure 26. The results of the
inclusive spray angles measured from all test cases are
plotted in Figure 39, Figure 40 and Figure 41 for various
injection pressures. Figure 39 shows spray angles of three
tests with identical injection conditions. During the needle
opening and closing period, the spray cone angles vary
from test to test, however, during the needle fully open
period, the spray angles stay fairly stable in the range of 30
to 50 degree. Similar result is found for the case of
injection with 800 bar, as shown in Figure 40. During the
needle fully open period, the spray angles are stable and in
the range of 20 to 40 degree. For both of the cases injection
with low pressure, as shown in Figure 41, the injection
duration is not long enough for the needle to reach its fully
open position; as a result, the needle is only partly open

and the spray angle oscillates from start to end of injection.
This inconsistency and oscillation of spray angle could be
attributed to uncertainty of needle positioning in horizontal
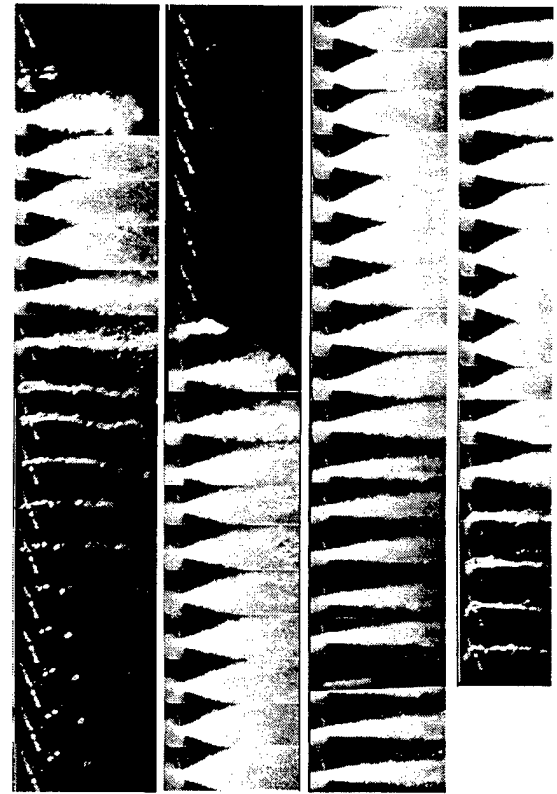direction that establishes inconsistent internal flow within
the nozzle.

Figure 38 Microscopic Visualization of Common-rail
Spray; Injection pressure: 300 bar, Injection event:
0.3ms-Pilot/1.0ms-Dwell/1.2ms-Main, Time between
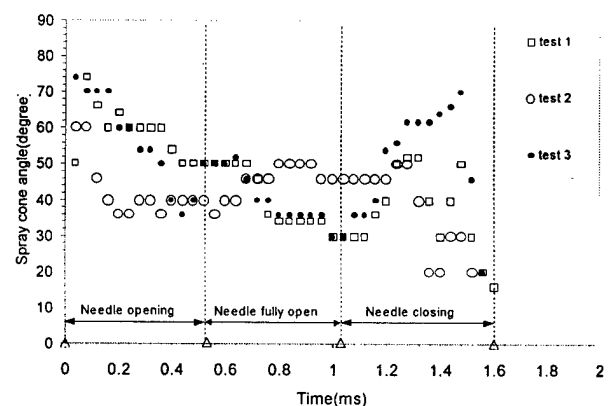Frame: 0.04ms. (Frame 19 to 24 skipped)

Figure 39 Correlation between Spray Cone Angle and
Needle Lift of Common-rail Pressure of 1350 bar and
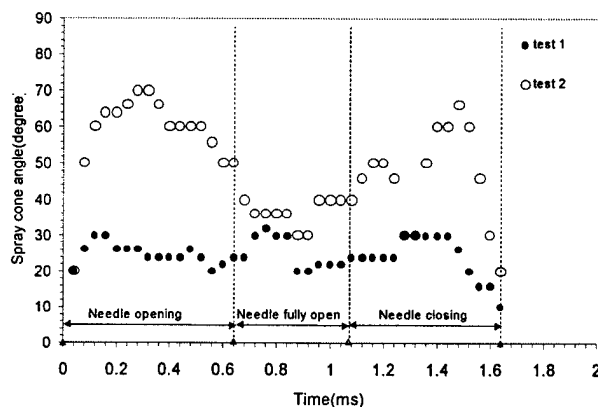Duration of 1.2 ms.

Figure 40 Correlation between Spray Cone Angle and Needle Lift of Common-rail Pressure of 800 bar and Duration of 1.2 ms.
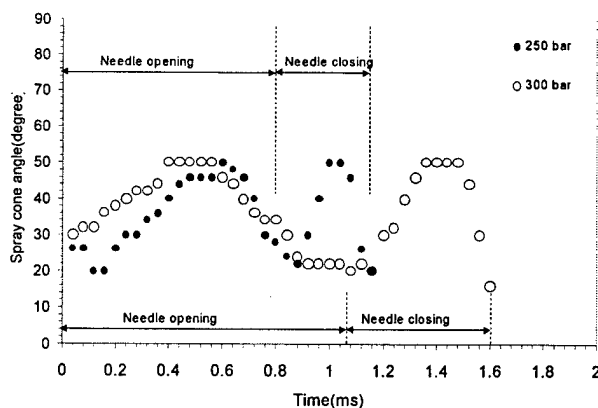
Figure 41 Correlation between Spray Cone Angle and Needle Lift of Main Injection of Common-rail System, with Pressure of 250 and 300 bar and Duration of 1.0 and 1.2 ms.

(b) Spray Characteristics at Start of Injection

Figure 42 shows two typical transient microscopic visualization of the VCO nozzle at 300-bar common-rail pressure. A very fast transition from clear liquid column to milky spray was also observed, which, however, was not observed at higher-pressure cases. The penetration velocity of these early development sprays is ranging from 4 to 12 m/s.
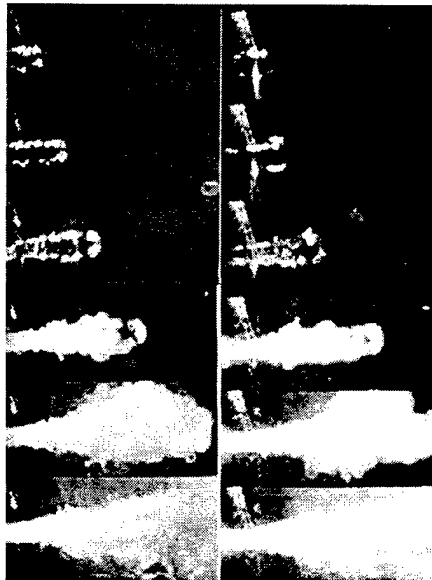
Figure 42 Initial Spray Breakup of Common-rail Spray, with Injection Pressure of 300 bar; Injection Event: 0.3ms-Pilot/0.45ms-Dwell/1.2ms-Main; Time between Frame: 0.04 ms.

(c) Spray Characteristics at End of Injection

Figure 43 shows the visualization results of end of injection with common-rail pressure of 300, 800, and 1350 bar, respectively. Significant liquid ligament sustaining for long period of time, about 0.32 ms, was observed in the case of low-pressure injection. Large size drops moving with low velocity, about 6 m/s, are also observed. As the pressure increase to 800 and 1350 bar, the situation is improved. The number and size of drops and the hanging-around period of liquid ligament are reduced as the injection pressure increases.
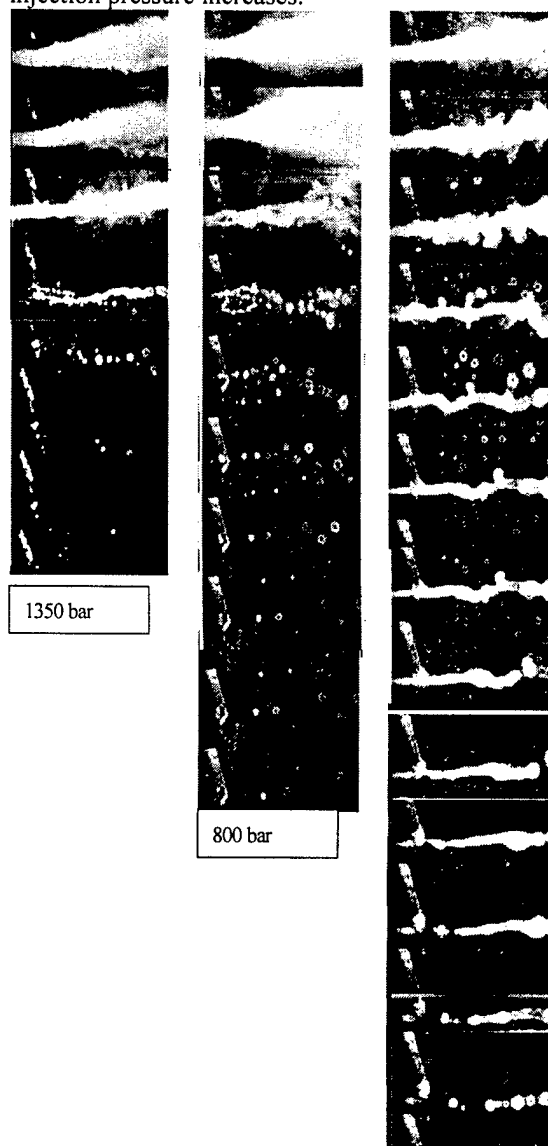
Figure 43 Effect of Injection Pressure on End of Injection of Common-rail System; 390 FN VCO Nozzle, Injection Duration: 1.2ms-Main Injection.
Left :   1350 bar Common-rail Pressure
Middle : 800 bar Common-rail Pressure
Right: 300 bar Common-rail Pressure

CONCLUSIONS

Both injection-rate measurement and spray visualization were performed to investigate injection dynamics and spray structure of minisac and VCO nozzle using HPCR system under high injection pressure. The deduced results are as follows:

1. The injection-rate is strongly dependent on the common-rail pressure, the nozzle hole diameter, and the nozzle type.
2. Pilot injection and dwell duration strongly affect the main injection in terms of needle lift and the injected fuel amount.
3. The maximum needle lift and initial needle opening rate are functions of the common-rail pressure.
4. The minisac nozzle has a higher discharge coefficient (Cd) than the VCO nozzle tip. The minisac nozzle can be utilized at a lower rail pressure and a shorter pilot injection duration, whereas the VCO nozzle cannot provide a consistent pilot injection at lower rail pressures.
5. The spray symmetry and spray structure depends on nozzle type. In general, the VCO nozzle has an asymmetric spray plume, but exhibits better spray spread and fuel-air mixing, as indicated by the observed larger spray angle. The large variation observed on the common-rail sprays could be caused by eccentricity of the VCO nozzle inside and exaggerated by the low needle lift under low injection pressure operating condition. The minisac nozzle exhibits a more symmetric spray penetration and a faster spray penetration rate.
6. The VCO dual-guided nozzle does not significantly improve the spray symmetry over that obtained with the VCO single-guided nozzle. However, the dual-guided nozzle does exhibit a faster average spray penetration than does the single-guided nozzle.
7. The spray tip penetration model correlates fairly well with the measured data of common-rail sprays under various injection and ambient pressures, except for the common-rail sprays with injection pressure of 300 bar. Meanwhile, for the spray, the model tends to over predict the early phase of the penetration and under predict that of the later phase.
8. The nozzle orifice geometry significantly affects the liquid spray-tip penetration. The data obtained show that the liquid spray tip penetration mainly depends on the nozzle tip type, needle guide type, injection pressure, ambient gas pressure.
9. For the high-pressure common rail system tested, the spray cone angle shows conspicuous oscillation during pilot or main injection period, possibly due to needle eccentricity and oscillation.

REFERENCES

1. Bosch, Wilhelm, (1966) "The Fuel Rate Indicator; A new Measuring Instrument For Display of the Characteristics of Individual Injection," SAE 660749.

2. Boehner, W. Hummel, K. (1997) "Common Rail Injection System for Commercial Diesel Vehicles," SAE 970345.

3. Dan, T., Takagishi, S. Senda, J. and Fujimoto, H. (1997) "Effect of Ambient Gas Properties for Characteristics of a Non-Reacting Diesel Fuel Spray," SAE paper 970352

4. Farrell, P.V. Chang, C.T. and Su, T.F (1996) " High Pressure Multiple Injection Spray Characteristics ," SAE 960860

5. Harrington, D., and Lai, M.-C., (1998) "Characterization and Visualization of Hole-To-Hole Variation and Wall Impingement of Diesel Sprays," *ILASS AMERICAS '98*, pp. 106-110.

6. Hoffmann, V.L.H Hummel, K Maderstein, T. and Peters A.(1997) "Das Common-Rail-Einspritzsystem-ein neues Kapitel der Dieseleinspitztechnik," MTZ 10/97 P572 – P582.

7. Han, J.S, Wang T.C and Lai, M.-C., "Common-Rail Diesel Fuel Injection System Dynamics and Spray Characterization," *ILASS AMERICAS '99*. pp. 201-205.

8. Qin,J.R, Dan ,T. Lai, M.C (1999) "Correlating the Diesel Spray Behavior to Nozzle Design," SAE 1999-01-3555.

9 Lai, M.-C., Wang, T.-C., Xie, X., Han, J.S, Henein, N. A., Schwarz, E., and Bryzik, W., (1998) "Microscopic characterization of Diesel Sprays at VCO Nozzle Exit" SAE 982542.

10. Renner, G. Koyanagi,K. and Maly R.R. (1998) " Effect of Common-rail Injector Design on the Emission Characteristics of Passenger Car DI Diesel Engines", COMODIA 98, P 477 - P 482

11. Siebers, D.L. "Scaling Liquid -Phase Fuel Penetration in Diesel Sprays Based on Mixing -Limited Vaporization," SAE paper 1999-01-0528

12. Wang, T. C Han, J.S. Xie, X.B. Lai, M.C, Henein N.A (1999) "Direct Visualization of High Pressure Diesel Spray and Engine Combustion," SAE 1999-01-3496.

13. Hiroyasu, H., and Kadota, T., and Arai, M., (1983) "Development and Use of a Spray Combustion Modeling to Predict Diesel Engine Efficiency and Pollutant Emission", Bulletin of the JSME. Vol 26, No. 214, April 1983.

14. Kuo, T.W.,(1987) "Evaluation of a Phenomenological Spray-Combustion Model for Two Open-Chamber Diesel Engines", SAE paper, Nov. 2-5, 872057, 1987.

15. Soteriou, C., Andrews, R., and Smith, M.,(1995) "Direct Injection Diesel Sprays and the Effect of Cavitation and hydraulic Flip on Atomization", SAE Paper 950080, 1995

REFERENCES

1. Arcoumanis, C., Gavaises, M., and French, B., "Effect of Injection Processes on the Structure of Diesel Sprays", SAE Paper 970799,1997.

2. Arcoumanis, C., Cossali, E., Paal, G., and Whitelaw, J.H., "Transient Characteristics of Multi-Hole Diesel Sprays", SAE Paper 900480, 1990.

3. Arcoumanis,C., Cutter, P.A., Foulkes, D.,and Tabaczynski, R. ,"Spray, combustion, and heat transfer studies in a Ricardo hydra direct-injection diesel engine", IMechE S433/013/96,1996.

4. Bosch, W., "The Fuel Rate Indicator; A new Measuring Instrument For Display of the Characteristics of Individual Injection," SAE Paper 660749, 1966.

5. Boehner, W. and Hummel, K., "Common Rail Injection System for Commercial Diesel Vehicles," SAE Paper 970345, 1997.

6. Bruni,G., Fiore, A. Laforgia, D. and Fiorentino, L., "3-D Analysis of the Flow through a multi-hole V.C.O for D.I Diesel Engine," SAE Paper 950085, 1995.

7. Canaan, John E. Dec, and Green, R.M., Daniel T. Daly, "The Influence of Fuel Volatility of the Liquid-Phase Fuel Penetration in a Heavy-Duty D.I. Diesel Engine", SAE Paper 980510, 1998.

8. Chen, S.K., Chen, S.X., and Gebert, K.,"Modelling of Advanced Electronic Fuel Injection Systems: Part 1 Theory, Assumptions, and Features," ICE-Vol. 25-2, 1995 Fall Technical Conference, Volume 2, ASME 1995.

9. Chen, S.K., Chen, S.X., Suder, T., and Wong, H.C.,"Modelling of Advanced Electronic Fuel Injection Systems: Part 2 Validation and

Application," ICE-Vol. 25-2, 1995 Fall Technical Conference, Volume 2, ASME 1995.

10. Chigier, Norman, "Spray Science And Technology", Key Note, ASME Winter Annual Meeting, New Orleans, December, 1993.

11. D. Laforgia, F., and Starace, G., "Experimental Investigation of the Sprays of an Axi-Symmetric Nozzle of a Common-Rail High Pressure Electro-Injector", SAE Paper 970054, 1998.

12. Dan, T., Yamamoto, T., Senda, J., and H. Fujimoto, " Effect of Nozzle Configurations for Characteristics of Non-Reacting Diesel Fuel Spray", SAE Paper 970355, 1997.

13. Dan, T., Lai, M.-C., Wang, T.-C., and Xie, X., "Transient Characterization of High-Pressure Diesel Sprays", COMODIA 98, 1998.

14. Date, K., Manabe, M., Kano, H., and Kato, M., "Contribution of Fuel Flow Improvement in Nozzle to Spray Formation", SAE Paper 920622, 1992.

15. Dec, J. E., (1997) "A Conceptual Model of Diesel Combustion Based on Laser-Sheet Imaging," SAE 970873.

16. Dec, J.E., Green, R.M., and Daniel T. Daly, "The Influence of Fuel Volatility of the Liquid-Phase Fuel Penetration in a Heavy-Duty D.I. Diesel Engine", SAE Paper 980510, 1998.

17. Espey, C. and Deck, J.E.,"The Effect of TDC Temperature and Density on the Liquid-Phase Fuel Penetration in a D.I. Diesel Engine", SAE Paper 952456, 1995.

18. Farrell, P.V., C. T. Chang, and T.F. Su, "High Pressure Multiple Injection Spray Characteristics", SAE Paper 960860, 1996.

19. Fath, A., Münch, K.-U., and Leipertz, A., "Spray Break-up Process of Diesel Fuel Investigated Close to the Nozzle", Proceeding of ICLASS-'97, pp. 513-520.

20. Ferguson. C. R., "Internal Combustion Engines", 1986.

21. Furuhama, S. and Tada, T., " On the flow of the Gas through the Piston-Rings(1st Report, the Discharge Coefficient and Temperature of Leakage Gas)," Bulletin of JSME, Vol. 4, No. 16, pp. 684-690, 1961.

22. Gatowski, J.A., Balles, E.N., Chun, K.M., Nelson, F.E., Ekchian, J.A., and Heywood, J.B., "Heat Release Analysis of Engine Pressure Data", SAE paper 841359.

23. Hames, R., Straub, R., and Amann, R., "DDEC Detroit Diesel Electronic Control," SAE Paper 850542, 1985.

24. Han, J.S, Wang, T.C. and Lai, M.-C., "Common-Rail Diesel Fuel Injection System Dynamics and Spray Characterization," *ILASS AMERICAS '99*. pp. 201-205.

25. Harrington, D., and Lai, M.-C., "Characterization and Visualization of Hole-To-Hole Variation and Wall Impingement of Diesel Sprays," *ILASS AMERICAS '98*, pp. 106-110, 1998.

26. Heywood, J.B., "Internal Combustion Engine Fundamental", McGraw-Hill, 1988.

27. Hiroyasu, H., Arai, M., and Shimizu, M., "Effect of Internal Flow conditions Inside Injector Nozzles on Jet Breakup Processes", AIAA Series 1995, Chapter 7 p.p. 173.

28. Hiroyasu, H., and Kadota, T., "Fuel Droplet Size Distribution in Diesel

Combustion Chamber", SAE paper 740715, 1974.

29. Hiroyasu, H., and Kadota, T., "Models for Combustion and Formation of Nitric Oxide and Soot in Direct Injection Diesel Engines", SAE paper 760129, 1976.

30. Hiroyasu, H., Kadota, T., and Arai, M., " Development and Use of a Spray Combustion Modeling to Predict Diesel Engine Efficiency and Pollutant Emissions (Part 1 Combustion Modeling)", Bulletin of JSME Vol.26 No. 214, Paper No. 214-12, April 1983.

31. Hiroyasu, H. and Nishida, K., "Fuel Spray Trajectory and Dispersion in a D.I. Diesel Combustion Chamber," SAE Paper 890462, 1989.

32. Hiroyasu, H., Shimizu, M., and Arai, M., "The Breakup of High Speed Jet in a High Pressure Gaseous Atmosphere", Proceeding of 2nd ICLASS, 1982, P.69.

33. Hosoya, H. and Obokata, T., "Effect of Nozzle Configuration on Characteristics of Steady-State Diesel Spray", SAE Paper 930593, 1993.

34. Ishikawa, N. and Niimura, L., "Analysis of Diesel Spray Structure Using Magnified Photography and PIV", SAE Paper 960770, 1996.

35. Kadota, T and Hiroyasu, H., Trans. of JAME, 42-365(1971), 1216, (in Japanese).

36. Kadota, T and Hiroyasu, H., and Ohya, H., Trans. of JAME, 41-348(1975), 2475, (in Japanese).

37. Kampmann, S., Dittus, B., Mattes, P., and Kirner, M., "The Influence of Hydro Grinding at VCO Nozzles on the Mixture Preparation in a DI Diesel Engine", SAE Paper 960867, 1996.

38. Kato, T. ,Tsujimura, K., Shintani, M.,Minami, T. and Yamaguchi, I.,"Spray Characteristics and Combustion Improvement of D.I. Diesel Engine with High Pressure Fuel Injection", SAE Paper 890265,1989.

39. Kuo, T.W., "Evaluation of a Phenomenological Spray-Combustion Model for Two Open-Chamber Diesel Engines", SAE paper, Nov. 2-5, 872057, 1987.

40. Lai, M.-C., Henein, N. A., Xie, X., Chue, T.-H., Itoh, Y. and Bryzik, W., (1995) "Diesel Cold-Starting Study using Optically Accessible Engines", SAE paper 952366.

41. Lai, M.-C., Wang, T.-C., Xie, X., Han, J.S, Henein, N.A., Schwarz, E., and Bryzik, W., "Microscopic Characterization of Diesel Sprays at VCO Nozzle Exit," SAE Paper 982542, 1998.

42. Matsumoto, I., Kawamoto, K., and Ohishi, T., " Spray Formation Improvement of a VCO Nozzle for DI Diesel Smoke Reduction", IMechE Seminar – Diesel Fuel Injection Systems, April 1992.

43. Nabers, J.D., and Siebers, D.L., "Effects of Gas Density and Vaporization on Penetration And Dispersion of Diesel Sprays", SAE Paper 960034, 1996.

44. Namaziam, M., " Studies of Combustion and Crevice Gas Motion in a Flow-Visualization Spark-Ignition Engine," Ph.D. Thesis, Massachusetts Institute of Technology, 1981.

45. Namazian, M., and Heywood, J.B., "Flow in the Piston-Cylinder-Ring Crevices of a Spark-Ignition Engine: Effect on Hydrocarbon Emissions, Efficiency and Power", SAE paper 820088.

46. Niven, H., Webber J. V., (1996) The Design of Tomorrow's Compact High Power Diesel Engine, 1996 ASME ICE Division Spring Technical Conference , ASME ICED-Vol. 26-2, pp. 15-20.

47. Payri, F., Desantes, J.M., and Arregle, J., "Characterization of D.I. Diesel Sprays in High Density Conditions", SAE Paper 960774, 1996.

48. Payri, F., Benajes, J., and Tinaut, F.V., "A phenomenological combustion model for direct-injection, compression-ignition engines," Appl. Math. Modelling, Vol.12, June 1988.

49. Pierpont, D.A., and Reitz, R.D., "Effects of Injection Pressure and Nozzle Geometry on D.I. Diesel Emissions and Performance", SAE Paper 950604,1995.

50. Pitcher, G., and Wigley, G., "The Effect of Needle Opening Pressure on the Atomization of Diesel Sprays", The Second Seminar on Experimental Methods in Engine Research and Development, 1991.

51. Potz, D., Kreh, A. and Warga, J.,"Variable Orifice Geometry Verified on the Two-Phase Nozzle (VRD)," SAE Paper 950081, 1995.

52. Rao, K.K.,Winterbone, D.E., and Clough, E., "Influence of Swirl on High Pressure Injection in Hydra Diesel Engine", SAE Paper 930978,1993.

53. Reitz, R.D., "Computer Modeling of Sprays", Spray Technology Short Course Notes, 1996.

54. Reltz, R.D.and Kuo, T.W., "Modeling of HC Emissions Due to Crevice Flows in Premixed-Charge Engines", SAE paper 892085, 1989.

55. Renner, G., Koyanagi,K. and Maly R.R.,"Effect of Common-rail Injector Design on the Emission Characteristics of Passenger Car DI Diesel